



On Clay Minerals: Adsorption and Modification

Finian John Allen

Department of Chemistry
University of Cambridge

This thesis is submitted for the degree of
Doctor of Philosophy

St Catharine's College

September 2020

Declaration

This thesis is the result of my own work and includes nothing which is the outcome of work done in collaboration except as declared in the Preface and specified in the text. It is not substantially the same as any that I have submitted, or, is being concurrently submitted for a degree or diploma or other qualification at the University of Cambridge or any other University or similar institution except as declared in the Preface and specified in the text. I further state that no substantial part of my thesis has already been submitted, or, is being concurrently submitted for any such degree, diploma or other qualification at the University of Cambridge or any other University or similar institution except as declared in the Preface and specified in the text. It does not exceed the prescribed word limit for the relevant Degree Committee.

Finian John Allen
September 2020

Abstract

On Clay Minerals: Adsorption and Modification

Finian John Allen

Clay minerals are prevalent in nature and are a key component of sandstone-based oil reservoirs. Understanding the behaviour of organic components at clay mineral surfaces is therefore important for elucidating the mechanisms of oil recovery. These clay - organic interactions are of interest both in the context of oil components adsorbed to clay minerals, and for the action and attrition of surfactant packages employed in enhanced recovery.

The surprising adsorption of anionic molecules onto the anionic mica surface from aqueous solution, mediated by specific cations, has been investigated. A key variation in cation behaviour down group 1A was demonstrated, where the caesium salt of the surfactant bis(2-ethylhexyl) sulfosuccinate (AOT) showed adsorption to mica, in contrast to the lack of adsorption of the sodium salt. This 'cation bridging' by monovalent ions is a novel finding of the work. Further investigations with added cations revealed potassium to also mediate adsorption, and probed the importance of the ratio of cations in solution. The sodium salts of carboxylic acids were found to adsorb to mica, representing a significant difference between the behaviour of these acids and the sulfonate head-grouped AOT.

The behaviour of an adsorbed layer of the cationic surfactant didodecyldimethylammonium bromide (DDAB) adsorbed on mica was studied on exposure to different species in solution, including anionic and non-ionic surfactants. Very different behaviour was seen depending on the nature of the solution species. The effect of the anionic surfactant sodium dodecyl sulfate was found to be particularly complex; below the CMC there was partial layer replacement but a thickening of the total organic layer, but significantly at the CMC complete desorption of all adsorbed material occurred. This may represent an approach to remove such strongly bound cationics.

As many surface techniques require large and very flat clay surfaces, methods to produce flat surfaces on a macroscopic scale with different surface charge densities were investigated. Two candidate approaches were shown to result in modified charges. Cation exchange then heat treatment of mica was shown to partially neutralise the surface charge, in line with the literature, and sodium aluminate treated silica was shown to display an imparted negative charge.

Finally, the technique of fluorescence microscopy was developed as an alternative experimental method for investigation of adsorption to mica. Through different imaging regimes, species in solution and on the surface were selectively imaged. Adsorption of cationic dyes was explored, and the surface mobility was investigated using bleach recovery measurements.

Acknowledgements

My first and greatest thanks must of course go to Stuart, for the fantastic supervision he has provided over the past 4 years. His unending enthusiasm and encyclopaedic knowledge have been invaluable, and he has provided constant motivation. I couldn't have asked for a better supervisor. A big thanks must also be given to Perry for moral and physical support on countless experiments, and staying up later than all of us to keep an eye on the beam. His brief foray into snowsports was a highlight in what was an otherwise awful experiment.

I am very grateful to EPSRC and BP for the funding that made my project possible, as well as the conversations and direction provided in particular by Stephanie Houston and Isabella Stocker. The beamline committees and instrument scientists at ISIS and the ILL have provided valuable assistance, with particular thanks to Becky Welbourn, Philipp Gutfreund, and Jos Cooper.

I am grateful to Steve Lee and Aleks Ponjavic for their time and assistance with fluorescence experiments, and Philip Camp and Georgia Tsagkaropoulou for their excellent simulations and good conversations.

I owe a huge thanks to many members of the Clarke group, past and present. Much of my work has only been possible due to the prior efforts and diligence of Lucy Griffin and Kate Browning. Chris Truscott has helped me enormously, as well as providing much needed entertainment.

The community that the BPI has provided has made the last 4 years so enjoyable, and special mention must be made to the cycle of office mates I have been entertained by: Stefano, Rich, Pond, Marcus, Scott, Paddy, and Sia.

My family have been very supportive throughout the process, for which I am very thankful. A final and very special thanks must go to Cara, who has supported and looked after me throughout the process. I have no doubt that without her I would have struggled.

Publications

An Anionic Surfactant on an Anionic Substrate: Monovalent Cation Binding

Allen, F.J., Griffin, L., Alloway, R.M., Gutfreund, P., Lee, S.Y., Truscott, C.L., Welbourn, R.J.L., Wood, M.H., Clarke, S.M., 2017. *Langmuir* 33, 7881–7888.

Anionic surfactant induced desorption of a cationic surfactant from mica

Allen, F.J., Truscott, C.L., Welbourn, R.J.L., Clarke, S.M., 2018. *Appl. Clay Sci.* 160, 276–281.

Potassium, calcium, and magnesium bridging of AOT to mica at constant ionic strength

Allen, F.J., Truscott, C.L., Gutfreund, P., Welbourn, R.J.L., Clarke, S.M., 2019. *Langmuir* 35, 5753–5761.

Self-assembly and adsorption of cetyltrimethylammonium bromide and didodecyldimethylammonium bromide surfactants at the mica–water interface

Tsagkaropoulou, G., **Allen, F.J.**, Clarke, S.M., Camp, P.J. 2019. *Soft Matter* 15, 8402-8411.

A p53-dependent checkpoint induced upon DNA damage alters cell fate during hiPSC differentiation

Eldridge, C.B., **Allen, F.J.**, Crisp, A., Grandy, R.A., Vallier, L., Sale, J.E. 2020. *Stem Cell Reports* 15, 1-9.

Contents

| | | |
|----------|---|-----------|
| 1 | Introduction | 1 |
| 1.1 | Clay Minerals | 1 |
| 1.1.1 | Structure | 1 |
| 1.1.2 | Muscovite Mica | 4 |
| 1.1.3 | Montmorillonite | 4 |
| 1.1.4 | The Hofmann-Klemen Effect | 5 |
| 1.2 | Surfaces and Surface Charge | 5 |
| 1.2.1 | Origins of Surface Charge | 5 |
| 1.2.2 | Electrical Double Layer | 6 |
| 1.3 | Surfactants | 8 |
| 1.4 | Adsorption and Adsorption Isotherms | 9 |
| 1.5 | Oil Recovery Mechanisms | 11 |
| 1.6 | Thesis Overview | 13 |
| 2 | Experimental Methods | 15 |
| 2.1 | Neutron Reflection | 15 |
| 2.1.1 | Neutron Reflection Theory | 16 |
| 2.1.2 | Instrumentation | 24 |
| 2.1.3 | Neutron Reflectivity Data Analysis | 31 |
| 2.2 | X-Ray Reflectivity | 35 |

| | | |
|--------|---|----|
| 2.2.1 | X-Ray Reflectivity Theory | 35 |
| 2.2.2 | Instrumentation | 36 |
| 2.2.3 | X-Ray Data Analysis | 37 |
| 2.3 | Powder X-Ray Diffraction | 37 |
| 2.3.1 | Theory | 37 |
| 2.3.2 | Experimental | 38 |
| 2.4 | Zeta Potential Measurements | 40 |
| 2.4.1 | Zeta Potential Theory | 40 |
| 2.4.2 | Experimental | 41 |
| 2.5 | Streaming Potential Measurements | 41 |
| 2.5.1 | Theory | 41 |
| 2.5.2 | Experimental | 42 |
| 2.6 | Surface Charge Calculations | 46 |
| 2.7 | Inductively Coupled Plasma - Atomic Emission Spectroscopy | 47 |
| 2.8 | AOT Counter-Ion Exchange | 47 |
| 2.8.1 | Salt Metathesis | 47 |
| 2.8.2 | Ion Exchange Column | 48 |
| 2.8.3 | AOT Exchange Results | 48 |
| 2.9 | UV-O ₃ Cleaning | 49 |
| 2.10 | Cation Exchange Capacity Measurements | 49 |
| 2.10.1 | CEC - Methylene Blue Method | 50 |
| 2.10.2 | CEC - Cu ^{II} Method | 51 |
| 2.11 | Mica Powder Modification | 52 |
| 2.12 | Mica Ion-Exchange Isotherms | 53 |
| 2.12.1 | Initial Potassium Saturation | 53 |
| 2.12.2 | Exchange Isotherm Protocol | 53 |
| 2.13 | Fluorescence Microscopy | 54 |

| | | |
|----------|---|------------|
| 2.13.1 | Background | 54 |
| 2.13.2 | Imaging Methods | 55 |
| 2.13.3 | Instrumentation | 57 |
| 2.13.4 | Substrates | 57 |
| 3 | Surfactant Adsorption at the Mica - Aqueous Solution Interface | 59 |
| 3.1 | Adsorption of Anionics to Mica | 59 |
| 3.1.1 | Background | 59 |
| 3.1.2 | CsAOT on Mica | 60 |
| 3.1.3 | AOT Adsorption from Mixed Salt Solutions | 67 |
| 3.1.4 | Carboxylate Adsorption | 84 |
| 3.1.5 | Discussion | 91 |
| 3.2 | Adsorption of Non-Ionic Surfactants to Mica | 93 |
| 3.2.1 | Background | 93 |
| 3.2.2 | C ₁₂ E ₅ Adsorption to Mica | 93 |
| 3.3 | X-Ray Reflectivity from Mica | 99 |
| 3.3.1 | Cell Design and Experimental Setup | 99 |
| 3.3.2 | Results | 101 |
| 3.4 | Adsorption Comparison with Simulations | 104 |
| 3.4.1 | The Mica - Water Interface | 106 |
| 3.4.2 | CTAB Adsorption | 107 |
| 3.4.3 | DDAB Adsorption | 110 |
| 3.4.4 | Summary | 114 |
| 3.5 | The Influence of Surface Treatment on Adsorption Behaviour | 114 |
| 3.5.1 | Experimental Evidence | 114 |
| 3.5.2 | Discussion | 116 |
| 4 | Induced Desorption of Surfactants at the Mica - Aqueous Solution Interface | 119 |

| | | |
|----------|--|------------|
| 4.1 | Background | 119 |
| 4.1.1 | Cationic Adsorption | 119 |
| 4.1.2 | Mixed Surfactant Adsorption | 120 |
| 4.1.3 | Surfactant Influence on Pre-Adsorbed Layers | 120 |
| 4.2 | Induced Desorption of DDAB by SDS | 121 |
| 4.2.1 | Background | 121 |
| 4.2.2 | SDS at the CMC | 121 |
| 4.2.3 | SDS Below the CMC | 124 |
| 4.2.4 | Discussion | 129 |
| 4.2.5 | Surfactant Interaction in Organoclays | 132 |
| 4.3 | Diacid Effect on Pre-Adsorbed DDAB | 136 |
| 4.4 | Induced Desorption of DDAB by AOT | 138 |
| 4.4.1 | Induced Desorption | 138 |
| 4.4.2 | Concentration Dependence | 139 |
| 4.4.3 | Discussion | 140 |
| 4.5 | Interaction of Adsorbed DDAB with C ₁₂ E ₅ | 140 |
| 4.5.1 | Mixed Layer Formation and Partial Desorption | 140 |
| 4.5.2 | Layer Re-Formation | 141 |
| 4.5.3 | Discussion | 143 |
| 4.6 | Comparison of Adsorbed Layer Behaviour | 148 |
| 5 | Modification of Surface Charge | 151 |
| 5.1 | Modification of Mica | 152 |
| 5.1.1 | Powder Characterisation | 152 |
| 5.1.2 | Powder Modification to Reduce the Surface Charge of Mica | 154 |
| 5.1.3 | Mica Ion Exchange Isotherms | 156 |
| 5.2 | Isomorphic Substitution of Silica Surfaces | 163 |

| | | |
|----------|---|------------|
| 5.2.1 | Colloidal Silica Characterisation | 164 |
| 5.3 | Flat-Surface Charge Measurements | 165 |
| 5.3.1 | Silica Results | 165 |
| 5.3.2 | Mica Results | 167 |
| 5.4 | Future Work | 169 |
| 6 | Fluorescence Study of Adsorption | 171 |
| 6.1 | Background | 171 |
| 6.2 | Dye Cation Exchange | 172 |
| 6.2.1 | Cation Exchange Process and Imaging | 173 |
| 6.2.2 | Bleach Recovery | 176 |
| 6.2.3 | Interaction with SDS | 178 |
| 6.3 | Method Development | 179 |
| 6.4 | Future Work | 182 |
| 7 | Conclusions and Future Work | 183 |
| 7.1 | Conclusions | 183 |
| 7.2 | Future Work | 185 |
| | References | 193 |
| | Appendix A Beamtime experiments and DOIs | 205 |

Chapter 1

Introduction

1.1 Clay Minerals

Clay minerals are abundant in nature, and of industrial relevance in fields ranging from agriculture to ceramics to lubricants. Behaviour at the surfaces of clay minerals is of particular interest in oil recovery, as clays are present in many sandstone reservoirs and can be pore lining minerals¹. This means that the solid surfaces contacting the oil residing in pores will in part be clay surfaces. There is also evidence that the presence of clays is linked to determining which reservoirs show incremental recovery from lowered salinity water flooding², a process discussed in more detail in Section 1.5.

1.1.1 Structure

Clays minerals are phyllosilicates (layered silicates), composed of sheets of silicon atoms tetrahedrally coordinated by oxygens and sheets of octahedrally coordinated aluminium or magnesium atoms³. These sheets are combined differently in different clays.

The structure of the tetrahedral sheet is shown in Figure 1.1a. Of the four oxygens forming each tetrahedron, three are shared with neighbouring tetrahedra and one apical oxygen oriented away from the plane, upwards as shown in the figure. In the octahedral sheet the metal ions are coordinated by six oxygen or hydroxyl groups which are shared by adjacent octahedra, as shown in Figure 1.1b. These types of sheets can associate by sharing of the apical oxygens from the tetrahedral sheet with octahedra in the octahedral sheet, as shown in Figure 1.1c. This can occur on just one side of the octahedral sheet as shown,

which results in a 1:1 clay (also referred to as ‘TO’), or on both sides of the octahedral sheet resulting in a 2:1 clay (‘TOT’). These combinations of sheets form layers which then stack to give the three-dimensional clay structure.

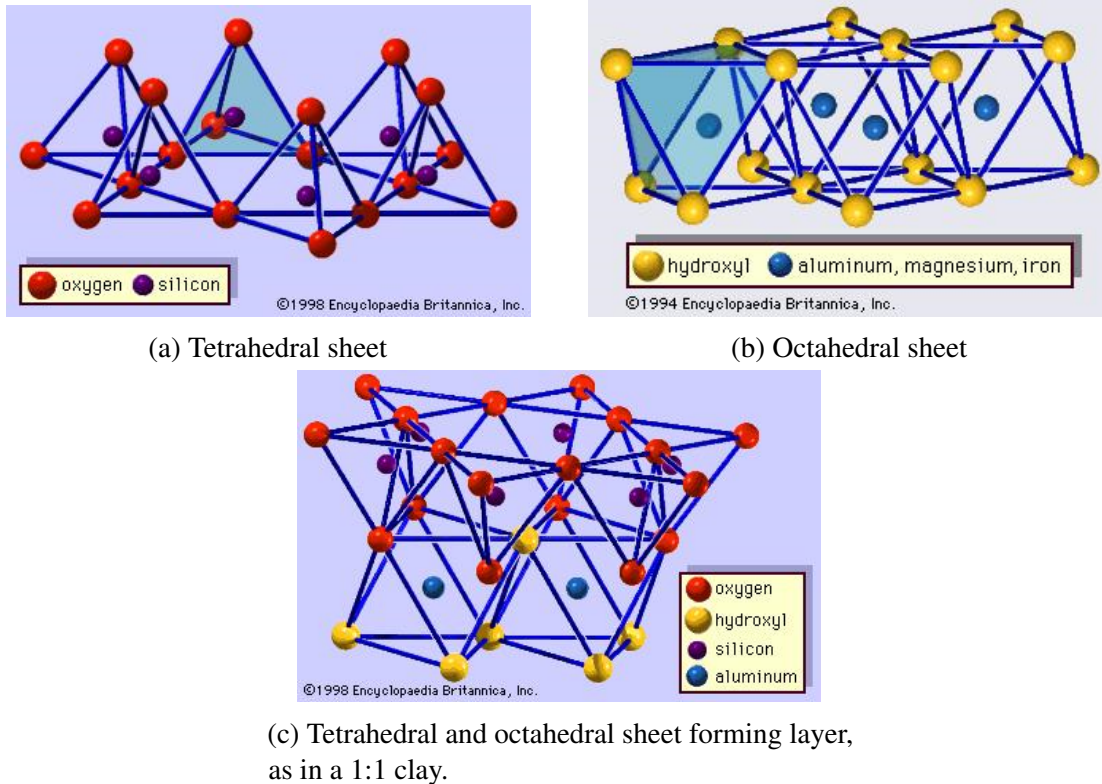


Fig. 1.1 Structures of tetrahedral and octahedral structures in clay minerals. (Images reproduced from Encyclopaedia Britannica⁴.)

The occupation of the octahedral metal ion site in the sheet varies; if the metal ions are trivalent Al^{3+} ions then only two of each three positions will be filled and the clay is termed *dioctahedral*, whereas if the ions are divalent Mg^{2+} then all three positions are filled and the clay is *trioctahedral*³. The 2:1 mineral with complete dioctahedral occupancy and no further substitutions is *pyrophyllite*, and in the case of complete trioctahedral occupancy the mineral is *talc*. The lack of isomorphic substitution in these clays leads to idealised neutral structures.

As discussed in Section 1.2.1, isomorphic substitution in the clay structure gives a permanent structural negative charge, compensated by cations occupying positions between the clay layers and on exposed surfaces. The nature of the cations and the degree of substitution are important in determining aspects of the behaviour of the clay. Depending on the structure of the clay, some minerals may incorporate water in the interlayers and expand

or even exfoliate into their component sheets, and these are termed *swelling* clays⁵. Clays which do not do this are termed *non-swelling*.

Swelling of clays may be of two types: limited hydration of the interlayer cations and surfaces, termed *intracrystalline* swelling, or unlimited hydration of the interlayers from the osmotic pressure due to the high effective ion concentration in the interlayer, termed *osmotic* swelling⁶. The extent of isomorphic substitution also has a profound effect on the clay particle flocculation behaviour when dispersed in water.

The surface cations may be exchanged for other cations in solution, and if the clay swells when in contact with water then the interlayer cations also become accessible to exchange. These cations are termed exchangeable cations, and the cation exchange capacity (CEC) of a clay is the number of exchangeable cations per unit mass. As the cations are present to neutralise the structural charge, the CEC gives a measure of surface charge. Care must be taken with interpretation of this quantity as non-swelling clays can only exchange cations on their exposed surfaces.

Isomorphic substitution can occur in either the tetrahedral or the octahedral sheet, and this distinction can influence surface behaviour. If the charge sites are in the tetrahedral layer, which is closest to the surface, the localisation of the charge site will be felt more strongly by an adsorbate due to the greater proximity. If the substitution is in the octahedral layer, and therefore below the outer most silicate layer, there will be less localisation of the charge on the surface⁷. The extent of substitution and resulting charge varies between classes of clay mineral and within each class depending on the specific sample of naturally occurring material.

The behaviour of the basal planes of clay mineral particles differs strongly from the behaviour of the edges of the plates. As described earlier, the surfaces carry a negative and mostly pH independent charge due to isomorphic substitution in the crystal structure. The edges however are made up of 'broken' edges of the clay sheets with dangling hydroxyl bonds: aluminol and silanol. The edges may therefore display behaviour of both these groups. The point of zero charge of alumina has been reported in the pH range 7-9, so at pH values below this components of edge sites might be expected to carry a positive charge^{8,9}.

1.1.2 Muscovite Mica

Muscovite mica is the focus of this project, and is a 2:1, non-swelling clay which occurs naturally in much larger crystals than most other clays. Muscovite provides a convenient model system for the study of the basal surface of clay minerals. Mica has been utilised extensively as a substrate for many surface techniques due to the perfect basal cleavage that the crystal exhibits. This can yield surfaces which are atomically flat over the order of square centimetres in area¹⁰. Mica carries a negative surface charge from isomorphous substitution of Si^{4+} by Al^{3+} in the tetrahedral layer of the mineral, giving a negative charge site per 47 \AA^2 area¹¹, or -0.33 C/m^2 charge density¹². In the natural material this charge is compensated by K^+ present between the mica sheets and on the exposed basal surfaces. In aqueous solution these ions can dissociate or be exchanged for other cations. The surface charge of mica is generally higher than other common clays.

In addition to the wide employment of mica as a substrate or substrate support for techniques such as atomic force microscopy (AFM) and sum frequency generation spectroscopy (SFG), there are also various industrial applications which make use of the high thermal and electrical insulating properties of the structure.

1.1.3 Montmorillonite

Montmorillonite is also a 2:1 clay mineral but unlike mica it is a swelling clay. Montmorillonite typically exists as a fine powder with particles of approximately $1 \mu\text{m}$ in diameter. No large crystals are readily available. Isomorphous substitution of Mg^{2+} for the Al^{3+} in the octahedral layer results in the layer charge, and the exchangeable cations are typically Na^+ and Ca^{2+} . In a given montmorillonite sample generally there is one predominant exchangeable cation. The surface charge density has been estimated as -0.1 C/m^2 from CEC measurements¹³.

Amongst other uses, montmorillonite is employed in pharmaceuticals preparations, catalysts, and as a precursor for organically modified clays¹⁴. The nature of the counter ion is central to the swelling and represents a subtle balance between binding to the charged clay surface and the extent of hydration that can restrict close approach of the ions to the clay, weakening the attraction. Related effects will be relevant in this work.

1.1.4 The Hofmann-Klemen Effect

The fixation of small cations, specifically Li^+ and Mg^{2+} , into clay minerals and associated reduction in layer charge and related properties was first reported in 1950 by Hofmann and Klemen¹⁵ and this effect has since occasionally been referred to in the literature as the Hofmann-Klemen effect. Nishimura *et al.*¹⁶ investigated this effect on mica and observed with atomic force microscopy (AFM) that the basal plane was not damaged by the cation fixation, and proposed that the cations were fixated in the hexagonal cavities on the mica basal plane. Various other studies using IR spectroscopy of treated montmorillonites have suggested that the cations in fact migrate to, or near to, vacant octahedral sites^{17,18}.

1.2 Surfaces and Surface Charge

1.2.1 Origins of Surface Charge

Surface charge at the solid - aqueous solution interface may arise from different physical processes, which can result in differing behaviour. Charge may originate from structural considerations, pH dependent groups, or from preferential dissolution of one ion over another. The specifics of each of these are discussed in more detail below, with particular reference to clay minerals which are the subject of this thesis.

Structural Charge

The form of structural charge of interest here typically originates from elemental substitution in the crystal lattice. Isomorphic (or isomorphous) substitution is the replacement of one element for another, without significant alteration of the crystal structure. If the substituting species has a lower valency this substitution results in a negative charge. As described in Section 1.1, clays have a layered structure and this isomorphic substitution leads to negatively charged layers. The charge is compensated by cations which sit between the layers in the stack and on exposed surfaces. The extent of substitution and resulting charge varies between classes of clay mineral and within each class depending on the specific sample of naturally occurring material.

pH Dependent Groups

Surface groups capable of being protonated or de-protonated will also give rise to a surface charge. Unlike charge arising from structural origins, this charge will depend on the pH of the solution in contact with the surface.

Phyllosilicates will be expected to have some surface silanol groups ($-\text{SiOH}$). These groups can be protonated ($-\text{SiOH}_2^+$) or de-protonated ($-\text{SiO}^-$), depending on the pH of the solution, resulting in a charged surface. At a given pH value the surface will be net neutral; this is termed the Point of Zero Charge (PZC) when determined by acid-base titration. The pH at which the charge at the plane of shear in electrokinetic measurements, discussed further in Sections 2.4 and 2.5, is zero is termed the Iso-Electric Point (IEP)⁹.

The degree to which pH dependent charges play a role in clay mineral behaviour will depend on the extent of surface hydroxylation.

Preferential Dissolution

Charge can arise from preferential dissolution. In an ionic solid in contact with a solvent, unequal chemical activity of the ionic species can result in enhanced dissolution of one ion relative to the others. This will leave the surface with the charge of the less soluble ion, and magnitude determined by solution conditions. The classic example of this effect is for silver chloride, in which silver ions preferentially dissolve to yield a surface with a negative surface charge.

Clearly the same arguments may be applied to precipitation from saturated solution as to dissolution, and pH dependent charging could be considered as a specific example of this effect involving the hydrogen and hydroxide ions. Preferential dissolution of ions other than H^+ and OH^- does not play a major role in the charge behaviour of clay minerals under the studied conditions.

1.2.2 Electrical Double Layer

When a charged surface is exposed to an electrolyte solution, a structure known as the electrical double layer (EDL) forms. The double layer was first proposed by Helmholtz who considered counterions bound to the charged surface giving a linear potential variation from the surface. This model was developed by Gouy and Chapman to include the effects of

thermal motion and co-ions, resulting in a model with an exponential decay of the potential from the surface into the bulk¹⁹. Finite size of the ions is neglected in this model. Stern²⁰ combined these theories into the model that is described here.

The variation in potential away from the surface is schematically illustrated in Figure 1.2. A layer of tightly bound unhydrated (or unsolvated) ions forms at the surface, and the inner Helmholtz plane (IHP) is defined by a plane through the centre of these ions. The potential falls linearly and steeply in this region due to the high counterion density, and the ions in this region are considered fixed to the surface. Beyond this is a layer of hydrated ions which are not specifically adsorbed to the surface and these define the outer Helmholtz plane (OHP)²¹. Together the IHP and OHP are often referred to as the Stern layer. Beyond this is the diffuse layer extending into the bulk, which balances the remaining Coulombic charge of the surface. The potential decays exponentially in this region.

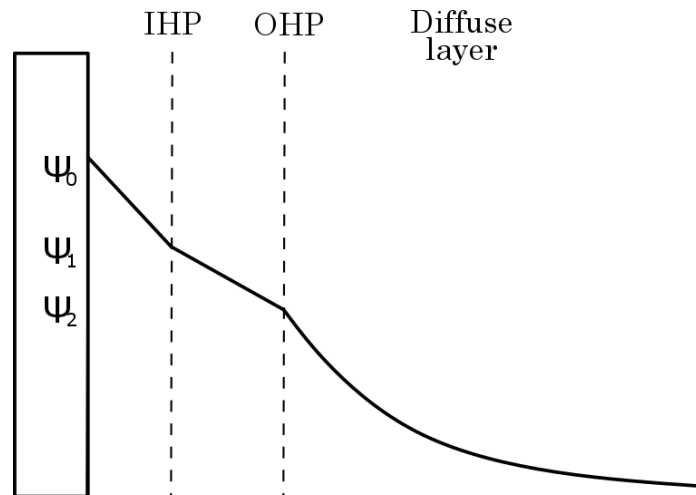


Fig. 1.2 Variation in potential of the electrical double layer as described by the Stern model. The surface has potential Ψ_0 , the inner Helmholtz plane (IHP) has potential Ψ_1 , outer Helmholtz plane (OHP) has potential Ψ_2 , and diffuse (Gouy) layer are shown.

The diffuse layer structure may be described by the Poisson-Boltzmann equation, Equation 1.1^{22,23}, where $\Psi(r)$ is the potential at the distance r from the OHP, ϵ_0 the permittivity of free space, ϵ_r the dielectric constant, n_i^0 is the number density of species i as $\Psi \rightarrow 0$ (in the bulk), z_i is the valency of species i , and e , k_b , and T are the electronic charge, Boltzmann constant, and temperature respectively. This equation can only be solved analytically in specific cases, and neglects any solvent-ion interactions. The equation performs well for monovalent ions at low concentrations but does not adequately describe the behaviour of multivalent ions²³.

$$\nabla^2\Psi(r) = -\frac{1}{\epsilon_0\epsilon_r} \sum_i n_i^0 z_i \exp\left(\frac{-ez_i\Psi(r)}{k_bT}\right) \quad (1.1)$$

In the limit of low potentials ($|\Psi| < 25\text{mV}$)²², the Poisson-Boltzmann equation can be linearised to give the Debye-Hückel theory result, shown in Equation 1.2. The Debye length, κ^{-1} , is a characteristic length scale of the system and at this distance away from the OHP the potential has fallen to e^{-1} (e now referring to Euler's number) of its value at the OHP. I is the ionic strength, given by $I = \frac{1}{2} \sum_i c_i z_i^2$ where c_i is the concentration of species i with valency z_i . At higher ionic strength the Debye length is smaller so the potential decays more rapidly, over a shorter length scale. This is due to the higher electrolyte concentration more effectively screening the surface charge.

$$\nabla^2\Psi(r) = \kappa^2\Psi(r) \quad \text{where} \quad \kappa = \sqrt{\frac{2e^2I}{\epsilon_0\epsilon_r k_bT}} \quad (1.2)$$

1.3 Surfactants

Surfactants are amphiphilic molecules which have an affinity for interfaces. Typically they contain a hydrophilic head-group and at least one hydrophobic tail, which is often an alkyl chain. Above a certain concentration in solution, and solubility constraints withstanding, surfactants self-assemble into aggregates. The structure of these aggregates can be considered to depend on the relative volumes of the head and tail sections of the molecule.

The molecular packing parameter can be calculated for a surfactant molecule and used to predict the aggregate structure in solution²⁴. The formula for the packing parameter (pp) is given in Equation 1.3, where V_c is the volume of the surfactant tail, a the cross-sectional area of the head group, and l_c the extended tail length. An example of a generic surfactant molecules, with these parameters labelled, is shown in Figure 1.3.

$$pp = \frac{V_c}{al_c} \quad (1.3)$$

For $pp \leq \frac{1}{3}$ spherical micelles are favoured, when $\frac{1}{3} < pp \leq \frac{1}{2}$ cylindrical micelles are favoured, and when $\frac{1}{2} < pp$ vesicles or bilayers are favoured²⁴.

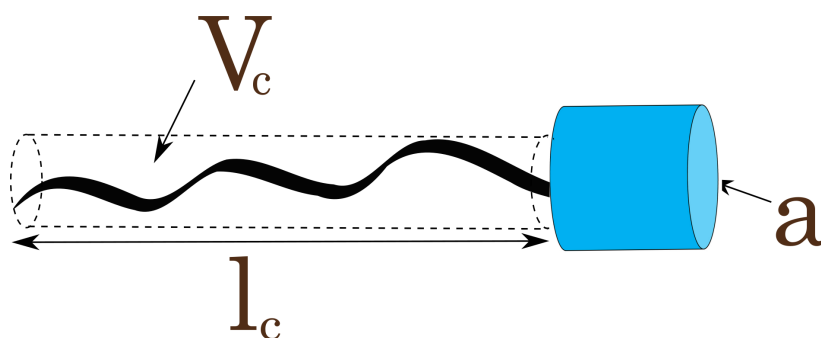


Fig. 1.3 A schematic of a surfactant, with the head group shown as a blue cylinder. The parameters used to calculate the packing parameter are labelled; the cross-sectional area of the headgroup ' a ', the extended tail length ' l_c ', and the tail volume ' V_c '.

The concentration at which micelles form is known as the *critical micelle concentration*, or CMC. Below this concentration there is insufficient driving force from the hydrophobicity of the tails for aggregates to form. The CMC value depends on the structure of a given surfactant and conditions. It is expected that at the CMC the driving force for aggregate assembly on a surface also increases, and adsorption becomes more likely. Adsorption of a molecule below the CMC suggests a specific interaction between the surface and adsorbate.

1.4 Adsorption and Adsorption Isotherms

Molecules adsorbing to surfaces may do so in different ways. If the molecule is held at the surface by attraction arising from weak forces, such as Van der Waals forces, this is termed *physisorption*. Xenon adsorbing to graphite is an example of physisorption²⁵. If however a chemical bond forms between the molecule and the surface then this is known as *chemisorption* and the interaction is much stronger than physisorption. An example of chemisorption is thiols adsorbing to a gold surface, where the gold chemically bonds to the sulphur and hydrogen is released. A binding energy of > 50 kJ/mol is generally considered to be classified as chemisorption²⁶.

Adsorption isotherms are descriptions of the amount of adsorbed species at an interface as a function of either the pressure in the gas phase or concentration in solution, at a constant temperature. Measurements of adsorption isotherms can be made in one of two broad ways, either measuring amount adsorbed at the surface or the amount depleted from solution. In many cases depletion studies are a relatively straightforward method and a powerful experimental tool for investigating a system. Further fitting of the data can reveal the

thermodynamics of the system, as well as the area per adsorbate molecule and thus the molecular orientation by inference.

A variety of models exist to describe the many possible isotherm shapes corresponding to different adsorption characteristics¹⁹. A widely applied and simple model is the Langmuir isotherm²⁷. This model is based on the assumptions that adsorption does not proceed above monolayer coverage, all sites are equivalent, and that there are no inter-adsorbate interactions. The Langmuir equation, which can be derived from these assumptions, is given in Equation 1.4, where θ is the fractional coverage, p is the equilibrium partial pressure of adsorbate or concentration if in solution, and K is the equilibrium constant for adsorption defined as $\frac{k_a}{k_d}$ where k_a and k_d are the rates of adsorption and desorption respectively. A schematic plot of the Langmuir isotherm is shown in Figure 1.4. Note the rapid rise in adsorption to a high concentration plateau.

$$\theta = \frac{Kp}{1 + Kp} \quad (1.4)$$

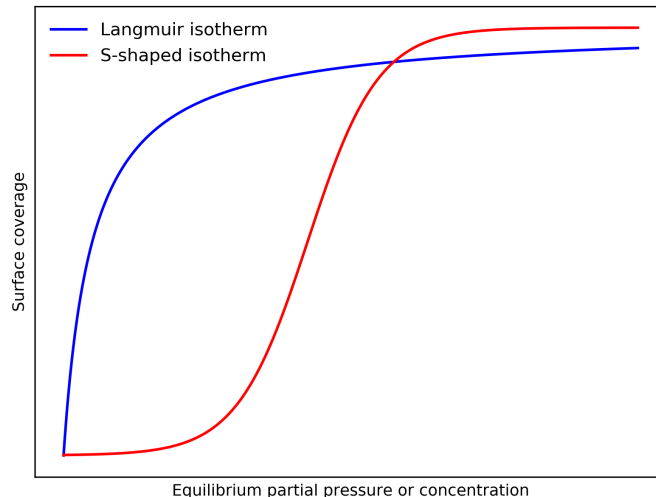


Fig. 1.4 Simulated isotherms for adsorption following a Langmuir (blue) and an S-shaped isotherm (red), plotted according to the Meghea equation²⁸.

In the case of an adsorbate showing strong inter-adsorbate interactions, the behaviour will deviate strongly from the Langmuir model. For strongly co-operative adsorption, where an adsorbate molecule on the surface increases the driving force for further molecules to adsorb as is often the case for surfactants in solution, S-shaped isotherms can occur. In this

case there is little or no adsorption up to some concentration, but a further small increase in equilibrium concentration leads to a large increase in adsorbed amount. This can occur at or close to the CMC for a surfactant solution. Various models exist for fitting S-shaped isotherms^{29,30}. A simple example without physical basis is the Meghea equation²⁸ which has been used to plot the example of an S-shaped isotherm shown in Figure 1.4.

1.5 Oil Recovery Mechanisms

There are broadly three stages to current conventional oil recovery³¹:

1. Primary recovery is the oil produced directly from the natural pressure of the formation. This can continue for some time depending on the pressure of the given reservoir.
2. Secondary recovery involves increasing the pressure in the reservoir once primary recovery has slowed or stopped. The pressure is generally increased using water flooding, though gas and other material can be injected. For offshore oil wells seawater is often used. Recovery rates after primary and secondary recovery have been implemented are mostly in the range 40-50%.³²
3. Tertiary recovery refers to 'enhanced' or 'efficient' methods of oil recovery (often referred to as Enhanced Oil Recovery, EOR). There are various methods of EOR, including the use of surfactants³³, polymers³⁴, and more recently, low salinity water flooding³⁵.

There is still much about the mechanisms of EOR techniques that is not well understood, and considerable work is being done to elucidate these processes. In addition to greater understanding allowing development of new and furthering of current EOR techniques, a key question is the prediction of how individual reservoirs will respond to different EOR techniques and where implementation is worthwhile. During the transition from fossil fuels to renewable energy, EOR will continue to be at least as important as it is currently; nearly all models of the energy transition include a reliance on fossil fuels for the next decade and beyond, used with increasing levels of carbon capture and storage (CCS). During this transitional period it will be vastly more carbon efficient and environmentally friendly to produce more oil from established fields, rather than development of new assets with all the associated environmental and fiscal costs of discovery, mapping, and production infrastructure.

A specific EOR method of interest here is the use of low salinity water flooding, as in the LoSal™ method developed by BP plc.^{35,36} This process involves flooding using water of significantly reduced salinity, and specifically lowered concentrations of divalent ions. Many mechanistic theories have been proposed for the method of action for enhanced recovery with this process. It has been reported that the effectiveness of reduced salinity water flooding is linked to the presence of clays in the reservoir³⁷.

One of the proposed mechanisms of enhanced recovery is the replacement of divalent cations, which are reported to ‘bridge’ between anionic oil molecules and anionic clay surfaces, with monovalent cations which it is assumed cannot bridge in this way³⁸. This has been termed ‘multivalent ion exchange’, or MIE. A schematic of this effect is shown in Figure 1.5. The release of adsorbed polar components is then proposed to release oil associated hydrophobically with these species, often described as the rock surface transitioning from ‘oil-wet’ to ‘water-wet’. Cation bridging is discussed further in Section 3.1.1.

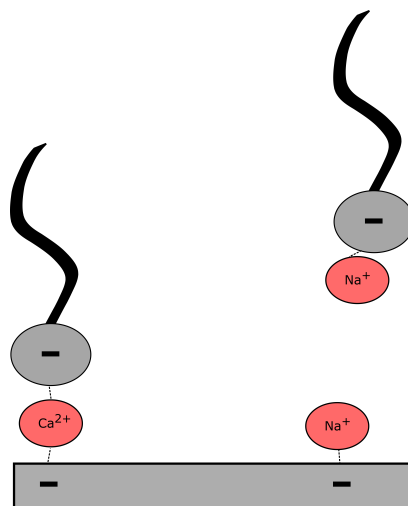


Fig. 1.5 Schematic of one of the suggestions for the mechanism for low salinity oil recovery, Multivalent Ion Exchange (MIE). On the left the divalent ion can bridge between the anionic clay surface and the anionic oil molecule, but when replaced with the monovalent ion, as shown on the right, bridging does not occur and the oil molecule is liberated from the surface.

An alternative mechanism which has been suggested is ‘double layer expansion’, or DLE³⁸. This postulated mechanism is that as the ionic strength is decreased on introduction of lowered salinity water, the expansion in the electrical double layer from the increase in Debye length is sufficient to move organic molecules bridged by cations in this layer further from the mineral surfaces and into the sweeping flow.

The incredibly complex and varied nature of both reservoirs and crude oils makes study of these effects difficult. Core flooding experiments, where rock cores either from real reservoir rock or more commonly a substitute, are the closest laboratory analogue³⁹. Generally more model systems are utilised to attempt to glean the key parameters and driving forces, and develop fundamental insight.

1.6 Thesis Overview

In this thesis I will outline my findings and developments in the fields of surfactant adsorption and interaction at the mica surface, with reference to the relevance of these effects to enhanced oil recovery. The main objectives are to further the understanding of behaviour of charged organic species at clay mineral interfaces, and develop new techniques with which to study these systems experimentally. The content of the remaining chapters is given below:

- Chapter 2: the principles and specifics of the experimental techniques used in this work.
- Chapter 3: results and discussion relating to adsorption of anionic and non-ionic surfactants to the mica surface from aqueous solution, including the effect of inorganic cations on anionic adsorption.
- Chapter 4: the complex interplay of surfactants in solution with a pre-adsorbed and strongly bound surfactant layer on mica, and the relative driving forces for layer removal or addition are discussed.
- Chapter 5: attempts to measure and control surface charge of macroscopic ultra-flat surfaces.
- Chapter 6: the application of fluorescence microscopy to adsorption studies.
- Chapter 7: conclusions and potential avenues for further study.

Chapter 2

Experimental Methods

2.1 Neutron Reflection

Behaviour at ‘buried’ interfaces, such as the solid - liquid interface, is experimentally difficult to access. Many of the techniques capable of investigating interfaces of this type operate by introducing a second interface into the system. Examples of this are the tip in AFM, where deflection or frequency response of a cantilever is measured as it traverses a region, or the second surface in the use of the surface force apparatus, where the attractive or repulsive force is recorded as a function of separation between two surfaces approaching or retracting. The use of an external solid probe has the potential to perturb the system either by inducing ordering through ‘frontal confinement’^{40,41} or by removal of transiently bound species.

Neutron reflectivity is a well established technique which has been used extensively as a non-invasive probe for studying behaviour at a number of interfaces, including the solid - liquid⁴²⁻⁴⁵. A particular advantage of neutron reflectivity is the ability to resolve organic molecules in aqueous or organic solvents. An advantage of neutron over X-ray reflectivity is that the former does not suffer from the problems of radiation damage, which can be induced by high intensity X-ray sources^{46,47}.

Plainly a neutron source is required for experiments to be carried out. Different types of source exist, as discussed further in Section 2.1.2. Experimental time is granted in cycles via an application process with a peer review panel. Because of this limited availability significant preparation and planning must be conducted before any neutron experiment.

2.1.1 Neutron Reflection Theory

Classical Optics

Reflection of neutron waves can be treated using classical optics, as for electromagnetic radiation. For a wave traversing an interface between two media with refractive indices n_1 and n_2 , the incident and transmitted angles are related using Snell's Law⁴⁸, as given in Equation 2.1. The angles are defined as between the plane of the interface and the wavevector, as illustrated in Figure 2.1, and it is noted that this definition is not the same as the convention for optics where the angle with the surface normal is usually used.

$$\frac{n_1}{n_2} = \frac{\cos \theta_2}{\cos \theta_1} \quad (2.1)$$

The neutron reflectivity work described in this thesis is the result of specular neutron reflection. In specular reflection, intensity is measured at an angle of reflection equal to the angle of incidence on to the sample. The information content in specular reflection relates purely to the structure of the sample in the direction normal to the interface (z-direction), and an in-plane (xy) average structure is seen. Other techniques, such as off-specular diffuse scattering and grazing incidence scattering, can give some information about in-plane structures and ordering, but have not been employed here.

A schematic of a neutron wavevector interacting with a single interface between two phases is shown in Figure 2.1. In this case there is both a reflected wave, with wavevector k_R , and a transmitted wave, with wavevector k_T . For specular reflection $\theta_I = \theta_R$.

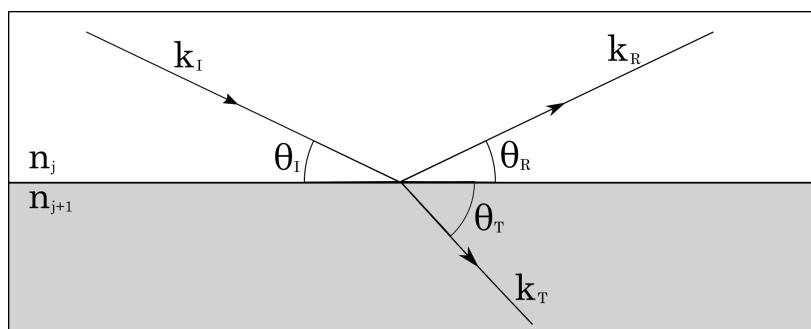


Fig. 2.1 A schematic representation of a wave interacting with a single interface between phases with refractive indices n_j and n_{j+1} respectively. Some of the wave is reflected, and some transmitted into the second medium.

Neutrons interact with the nuclei of atoms, unlike the more common technique of X-ray scattering where X-rays interact with the electron density surrounding the nuclei. The potential neutrons experience on interacting with a bound nucleus is described in Equation 2.2, where m_n is the neutron mass, and b is the neutron scattering length.

$$V(r) = \frac{2\pi\hbar}{m_n}b \quad (2.2)$$

The scattering length is composed of both a coherent and incoherent component, comprising the real and imaginary parts respectively. When the neutron is passing through a medium the potential described is modified to the one given in Equation 2.3, where ρ is the scattering length density (SLD) defined as $\rho = \frac{1}{\text{volume}} \sum_i b_i$ for a unit volume. The SLD may therefore be calculated for a given material from the molecular volume, which can usually be calculated from the bulk density, and the molecular formula.

$$V(r) = \frac{2\pi\hbar}{m_n}\rho \quad (2.3)$$

The scattering length varies in a pseudo-random manner across the periodic table, and between isotopes of the same element. This provides a useful tool in the ability to distinguish between chemically very similar species through selective isotopic substitution. In particular, the scattering lengths of ^1H and ^2H (deuterium, D) are very different, at -3.74 and 6.67 fm respectively⁴⁹. Thus selectively deuterating solvent or surfactant molecules, or even specific regions within surfactants, can be used to increase the scattering contribution from a component or allow multiple datasets to be collected from essentially identical systems. These datasets can then be used to co-refine a model, reducing the chance of a non-unique solution being found.

Contrast matching is a technique where a mixture of protonated and deuterated solvent molecules are selected with ratios such that the scattering length density of the solvent is equal to that of a specific component in the system, often the substrate or an adsorbate. As neutrons only scatter when travelling through an interface between regions of different scattering length densities, contrast matching can be used to negate scattering from particular interfaces.

Neutron wavevector interactions obey the same rules as regular optics. For reasons discussed in Section 2.1.2 it is convenient to combine the incident neutron angle and wavelength into a single parameter: the momentum transfer in the direction of the surface normal, Q_z .

This may be calculated from the difference between the reflected and incident wavevectors, k_f and k_i , to give Equation 2.4. For brevity Q_z is frequently abbreviated to simply Q or q , and this notation is used in the remainder of the thesis.

$$Q_z = \frac{4\pi \sin(\theta)}{\lambda} \quad (2.4)$$

A neutron refractive index may be defined for a given material in the same way as for electromagnetic radiation, by the ratio of the wavevector in a vacuum to the wavevector in the material. The equation for the refractive index is given in Equation 2.5, and as ρ is much less than one for most materials a truncated Taylor series may be used and the refractive index is well approximated by the form given in Equation 2.6⁵⁰. These equations neglect the absorption component, which will be imaginary and is only significant in the case of strongly adsorbing materials. Including this term gives Equation 2.7, where σ_a is the absorption cross section.

$$n^2 = 1 - \frac{\lambda^2 \rho}{\pi} \quad (2.5)$$

$$n \approx 1 - \frac{\lambda^2 \rho}{2\pi} \quad (2.6)$$

$$n \approx 1 - \frac{Nb}{2\pi} \lambda^2 + \frac{N\sigma_a}{4\pi} i\lambda \quad (2.7)$$

Snell's law dictates that in the case of a reduction in refractive index across the interface there will be an angle (for a given wavelength) below which there will be no transmitted wave. This is termed the critical angle, and gives a critical value of Q which is termed Q_c . From Snell's law it is clear that a critical angle will only be present for a decrease in refractive index, n , across the interface, which from Equation 2.6 corresponds to an increase in SLD. The formula for Q_c is given in Equation 2.8, where $\Delta\rho$ is the change in SLD across the interface. For $Q \leq Q_c$ there is total reflection.

$$Q_c = \sqrt{16\pi\Delta\rho} \quad (2.8)$$

Fresnel Coefficients

Reflectivity is defined as the ratio of the reflected intensity to the incident intensity. From considerations of the components of the wavevector parallel and perpendicular to the surface, and from the continuity of the wavefunction, the Fresnel coefficient for reflection may be derived. The equation for the Fresnel coefficient for an interface is given in Equation 2.9, in terms of the components of the wavevectors perpendicular to the surface. Taking the square of the modulus of the amplitude, $r_{j,j+1}$, gives the intensity, $R_{j,j+1}$. This is given in Equation 2.10.

Reflectivity for a single interface modelled using this equation is shown in Figure 2.2, for various changes in SLD across the interface. The position of Q_c increases for larger SLD differences.

$$r_{j,j+1} = \frac{k_{j\perp} - k_{(j+1)\perp}}{k_{j\perp} + k_{(j+1)\perp}} \quad (2.9)$$

$$R_{j,j+1} = |r_{j,j+1}|^2 \quad (2.10)$$

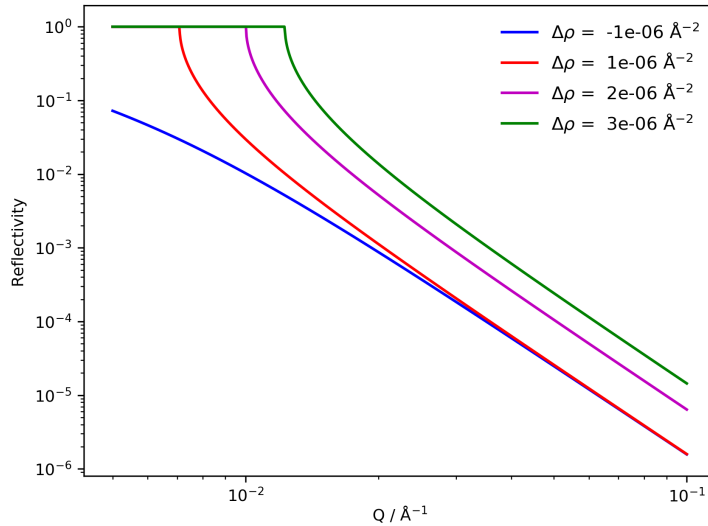


Fig. 2.2 Modelled reflectivity for a single interface between two bulk phases, for a range of SLD differences. Reflectivity is calculated from Equations 2.9 and 2.10. Total internal reflection and a critical edge is only seen for an increase in SLD across the interface.

Born Approximation

Applying perturbation theory to the Schrödinger equation yields the Born approximation⁵¹, which may be used to calculate the reflectivity for $Q \gg Q_c$, far from the critical edge and is useful for rudimentary fitting. Here the reflectivity has a Q^{-4} dependence (in the absence of roughness, discussed in the following section). The specific relation is given in Equation 2.11, and a comparison of the reflectivity calculated from the Fresnel coefficient and Born approximation is shown in Figure 2.3, showing the validity at high Q only.

$$R = \frac{16\pi^2}{Q^4} \Delta\rho^2 \quad (2.11)$$

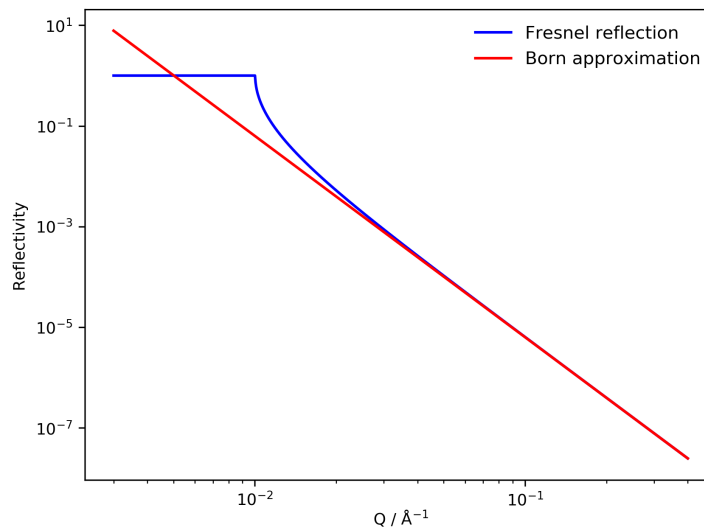


Fig. 2.3 Comparison of modelled reflectivity from the Fresnel coefficient (Equation 2.9), and from the Born approximation (Equation 2.11). Above $Q \approx 0.05 \text{ \AA}^{-1}$ the Born approximation agrees well with the Fresnel reflectivity, but for Q closer to Q_c it breaks down.

Roughness

Roughness at an interface will reduce the intensity of the specular reflected signal. This may be accounted for by applying a Nevot-Croce factor to the Fresnel reflectivity⁵². The modified Fresnel reflectivity with the included Nevot-Croce factor is given in Equation 2.12, where the roughness σ depends on the root-mean-square of the height variation h at the interface. The effect of increased surface roughness on a single interface is shown in Figure 2.4, illustrating

the dramatic effect of roughness on reflectivity. This can limit the use of neutron reflectivity to situations with surfaces of lower roughness than the layer thickness of interest. For molecular adsorbates roughnesses of lower than approximately 5 - 10 Å are therefore required.

$$r_{j,j+1} = r_{j,j+1} e^{-2k_j k_{j+1} \sigma^2} \quad \text{where } \sigma = \sqrt{\langle h^2 \rangle} \quad (2.12)$$

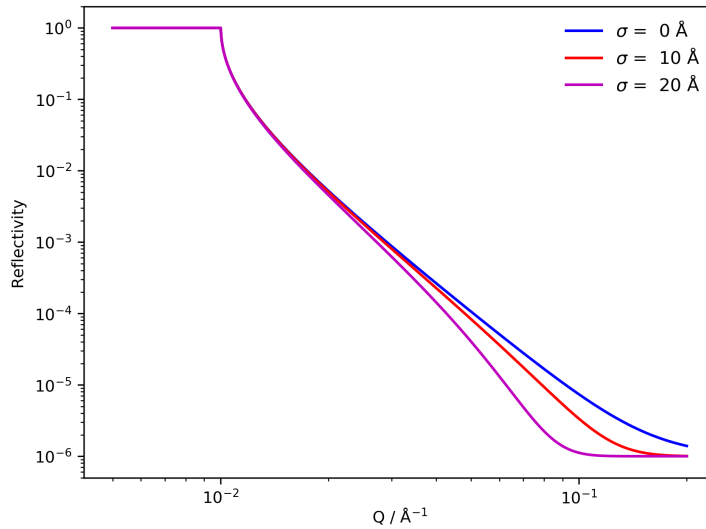


Fig. 2.4 Reflectivity from a single interface with varying roughness, as calculated from Equation 2.12. The reduction in intensity, particularly at higher Q , for increased roughness is clearly visible. An experimentally realistic background of 1×10^{-6} has been included.

Reflection by a Thin Layer

Figure 2.5 schematically illustrates the case of a thin layer at the interface between two bulk phases. The waves reflected from the lower interface will interfere with those reflected from the first interface, along with waves multiply reflected between the two. The interference can be constructive or destructive, depending on the relative phases of the waves. Calculating the reflectivity requires consideration of all of these waves, which can be solved by recognising that the amplitude of this series of waves reaching the detector forms a geometric progression. By taking the sum of this series, the reflectivity may be calculated, as given in Equation 2.13, where $r_{j,j+1}$ are the Fresnel coefficients given earlier, and d_1 the thickness of the layer at the interface. The intensity can then be calculated from $R = |r|^2$ as before.

The reflectivity modelled for a thin layer at an interface, from Equation 2.13 is shown in Figure 2.6 for two different layer thicknesses. For the thicker layer the fringe spacing, given by $2\pi/d$, is clearly reduced. The fringes are often referred to as Kiessig fringes.

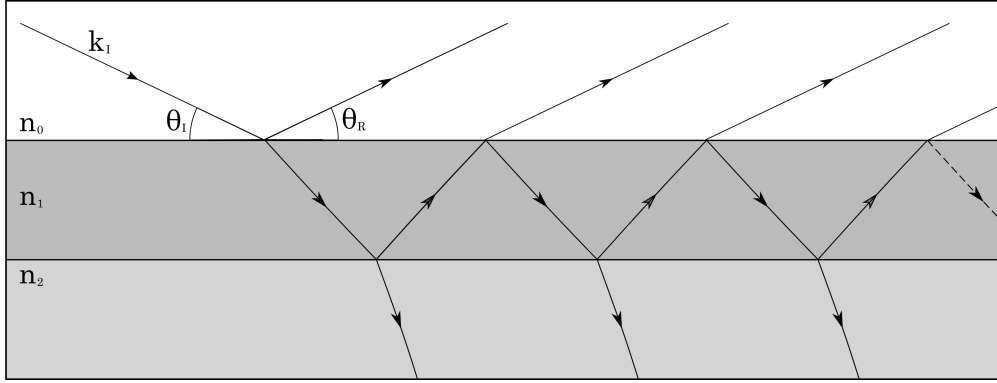


Fig. 2.5 A schematic representation of a wave being reflected at a thin layer between two bulk phase. Reflection and transmission occurs at both interfaces, and the resultant reflectivity is the result of interference between the waves, with the phase differences being dictated by the path length in the thin layer.

$$r_{012} = \frac{r_{01} + r_{12}e^{-i2\beta_1}}{1 + r_{01}r_{12}e^{-i2\beta_1}} \quad \text{where } \beta_1 = k_1d_1 \quad (2.13)$$

Matrix Method

For systems with more than two layers, summation of the beams arising becomes overly complex, and instead a different method of calculating reflectivity is used. This is the Abeles matrix method^{48,51,53}, or optical matrix method, and involves assigning an optical transfer matrix to each layer. The form of this matrix is given in Equation 2.14.

$$c_j = \begin{bmatrix} e^{\beta_j} & r_j e^{\beta_j} \\ r_j e^{-\beta_j} & e^{-\beta_j} \end{bmatrix} \quad (2.14)$$

The matrices for all the layers in the system are multiplied together to give a resultant matrix, as in Equation 2.15. From this the reflectivity is calculated from Equation 2.16.

$$M = \prod_{j=0}^j c_j \quad (2.15)$$

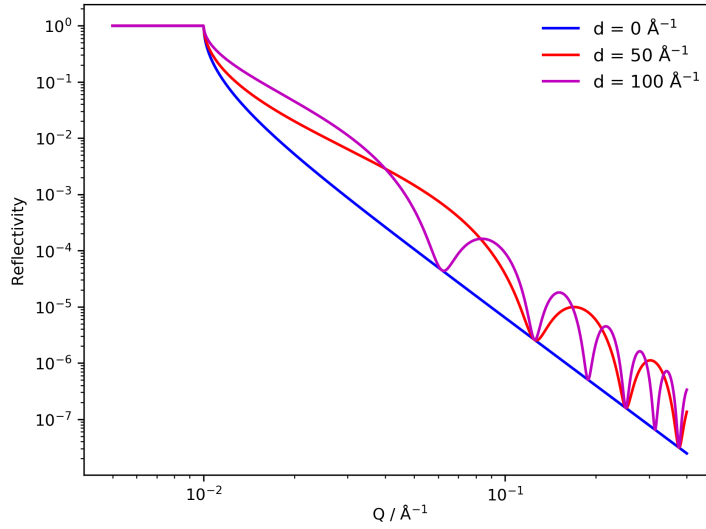


Fig. 2.6 Modelled reflectivity for a single layer with different thicknesses, as calculated from Equation 2.13. The SLDs of the substrate, layer, and subphase are 1, -2, and $3 \times 10^{-6} \text{ \AA}^{-2}$. When the SLD of the thin layer is between that of the substrate and bulk then the fringes in the reflectivity profile appear below the profile for the single interface. The fringe spacing is related to the thickness of the layer, with the periodicity given by $2\pi/d$.

$$R = \left| \frac{M_{11}}{M_{21}} \right| \quad (2.16)$$

Coherence and ‘Thick’ Layers

The discussion above holds for ‘thin’ layers where the waves reflected at the first and second interface can interfere. In this context, ‘thin’ refers to layers with thickness less than the coherence length of the neutron radiation. The coherence length is the distance over which the information about the phase of the radiation is lost¹⁹. For ‘thick’ layers, where the thickness is greater than the coherence length, a different treatment is required. In this case the intensities of the reflected waves must be summed, rather than the amplitudes⁵⁴.

Here the reflectivity may be calculated from Equation 2.17, where L is the path length in the layer, N the number density of atoms, and σ_{tot} the absorption cross section^{55,56}. As described in Section 2.1.3, a combination of thick and thin layers is required in this work.

$$R_{tot} = R_{01} + \frac{(1 - R_{01})^2 e^{-2LN\sigma_{tot}}}{1 - R_{12}R_{01}e^{-2LN\sigma_{tot}}} \quad (2.17)$$

Model Fitting

Because of the ‘phase problem’, where only the intensity and not the phase of the incident waves is measured, analysis of neutron reflectivity data is conducted through model-fitting. The model consists of a stack of layers, from which the reflectivity is calculated. The thicknesses, roughnesses and SLDs of the layers are then refined to minimise the difference between the calculated and measured reflectivity. The background signal may also be included, as well as the resolution although this can generally be determined by the experimental arrangement and not fitted. As much constraint as possible is applied to the fitting, with as few independent parameters as are required and a physically reasonable model. The result of the fitting is an SLD profile normal to the surface, representing the structure and composition of the interfacial region.

In this work, the simplest possible model with physical grounding was attempted at all stages. If the simplest model was not able to fit the data adequately then the next most simple model was attempted.

2.1.2 Instrumentation

Two types of research neutron source exist: spallation sources, such as the ISIS Neutron and Muon Source, and reactor sources, such as the Institut Laue Langevin. Spallation sources work by accelerating pulses of protons to high speed in a particle accelerator, then impacting them onto a target which ejects neutrons. These neutrons pass through moderators which control the speed and therefore wavelengths produced for particular experiments. For the work here where low Q is generally of interest, long wavelengths are preferred and so a ‘cold’ source might be used. Reactor sources use highly enriched uranium fuel and produce neutrons through nuclear fission, which are then moderated in the same way.

Neutrons are delivered from the moderator to the instrument by neutron guides, which are made from surfaces highly reflective to neutrons such as nickel-coated glass. Guides allow high flux at the instrument. Slight curvature of the guides also allows reduction of background gamma signal which would otherwise arrive at the instrument directly from the source.

Measurements of neutron reflectivity are typically made with two methods. Time-of-flight (TOF) measurements calculate the wavelengths of packets of incident neutrons by measuring the speed of the neutrons from the time taken to travel a well defined path length, usually from the source to the detector. The wavelength is calculated from the de Broglie equation $\lambda = h/mv$. Spallation sources are particularly suited to TOF measurements as the neutrons are produced in pulses by the target. At reactor sources, choppers may be used to define pulses. All data described in this thesis were collected using TOF measurements. An alternative to TOF is monochromated mode, where a fixed wavelength of neutrons is used and the angle to the sample is continuously varied to build up the reflectivity profile. The sources produce a wide spectrum of wavelengths and monochromation is therefore generally inefficient.

In a single TOF pulse, a limited wavelength range is available, depending on the specifics of the target, moderators, and other factors. A number of incident angles are therefore used to cover the desired range in momentum transfer. The angles are chosen that the reflectivity profiles produced from each angle overlap in Q and these are then ‘stitched’ together using the overlapping regions. This can be convenient where the absolute intensity is not known. For example, at low Q there may be a critical scattering region where the reflectivity must be unity. Any experimental data can be scaled to ensure unity of reflection in this region and any other data collected at higher reflection angles correctly scaled.

The footprint of the neutron beam on the sample is controlled by a series of adjustable slits along the incident beam. These slits also serve to collimate the beam. As the incident angle is varied the slits are controlled to maintain the same footprint on the sample. The footprint was set as 75 mm along the beam direction and 30 mm across it, slightly smaller than the size of the substrate trough described in Section 2.1.2, to ensure no edges were clipped by the beam.

To correct for inefficiencies in the detector and for absorption in the substrate, data is reduced against data collected with a ‘straight-through’ beam (incident angle of 0° , and beam offset to pass through the entire silicon wafer without reflection), with the same slit settings as the angles used for reflectivity measurements. The resolution, defined as $\Delta Q/Q$, was set at 3% for measurements at ISIS. At the ILL the resolution varied slightly over the Q range, but was approximately 4%.

ISIS: Inter and Offspec Reflectometers

The majority of the neutron experiments contained in this thesis were performed at the ISIS Pulsed Neutron Facility, Oxfordshire, on the Inter⁵⁷ and Offspec⁵⁸ reflectometers. These have vertical scattering geometry (horizontal surface of interest) and operate in time of flight.

On Inter incident angles of 0.4°, 0.9°, and 2.3° were used, and on Offspec 0.3°, 0.9°, and 2.3° prior to a slit alteration and 0.4°, 0.9°, and 2.0° in later experiments after this change had been made to the instrument.

ILL: D17 Reflectometer

Work was also carried out at the Institut Laue Langevin, Grenoble, on the D17 reflectometer⁵⁹. This instrument has horizontal scattering geometry (vertical surface of interest). D17 can be operated in either TOF mode, as with the reflectometers at ISIS, or in monochromatic mode which was not used in this work.

The broader nature of the wavelength packet on D17 compared to the reflectometers at ISIS required the use of only two incident angles to cover the required range in momentum transfer with sufficient overlap for stitching; angles of 0.8°, and 3.2° were used.

Alignment Procedure

For a reflectivity experiment to be successful, it is necessary to know the position and angle of the surface of interest to an extremely high degree of accuracy. A high contrast between the substrate and cell solution is advantageous in the alignment procedure, so before alignment cells were filled with D₂O to give a large Q -range with total reflection and therefore high overall reflectivity. Initially the approximate horizontal and vertical position of the sample were ascertained using a laser. The beamline experimental chamber, 'blockhouse', was then locked for safety reasons and the neutron beam used for the remainder of the alignment procedure.

Initial 'coarse' alignment takes place with measurements of intensity with the incident beam, sample, and detector aligned; the 'straight through' beam is measured. A height scan was performed around the approximate interface position; the intensity of signal dropping as the beam moves from silicon wafer substrate to solution reservoir which attenuates more strongly. An error function may be fitted to this profile and the centre of the drop taken as

the height of the interface. A rocking curve was then measured, varying the substrate angle between the beam and scattering direction. A peak results from occlusion of the beam by the sample when not parallel, and a Gaussian fit may be used to find the peak centre. These scans are iterated until self-consistent.

After this step, the detector and sample angle are altered to move the geometry into reflection. Similar height scans and angle scans are then performed with a peak generated in each case when the reflected signal is on the detector position, and the scans are iterated. A final horizontal translation scan, and cross beam angle (ψ) scan may be conducted if deemed necessary. All angle and translation positions are controlled by high precision motors.

Mica Substrates

Substrates for neutron reflectivity measurements were prepared using the method of Browning et al.⁵⁵, with the modification of Griffin et al.⁵⁶ to access a larger substrate size. Silicon wafers of dimensions $100 \times 50 \times 10$ mm and polished to a roughness of $< 5 \text{ \AA}$ on the (111) face were obtained from either PI-KEM Ltd or Sil'tronix. n-type doped (P) wafers were used to avoid any inclusion of boron, which is strongly attenuating. The wafers were cleaned by immersing in concentrated nitric acid for 5 h using a custom teflon holder, followed by soaking in ultra pure water overnight and repeated rinsing. Loctite® 3301 (approximately 2 ml), a low viscosity UV-curable glue, was passed through a syringe filter (5 \mu m , nylon membrane) then spin coated onto the dried wafers at 5000 rpm for 5 min to yield a thin layer.

A mica sheet ($10 \text{ cm} \times 5 \text{ cm} \times 25 \text{ \mu m}$, Attwater & Sons Ltd) was cleaved by laying adhesive tape onto both sides, and gently peeling the sides apart. As the mica was cleaved a small volume of water was dropped into the freshly forming surface to lower the free energy, and facilitate the cleaving. Generally the cleaving procedure resulted in a visibly thicker and thinner side, and the thicker side was retained. The freshly cleaved face was carefully laid down onto the glue layer on the silicon wafer. A stiff card was swiped across the top of the mica as it was deposited to aid the prevention of trapped bubbles between the silicon and mica. A small overlap over the edge of the silicon block of a few millimetres was left, to aid the second cleaving as discussed later. The mica was then clamped against the glue layer using a highly polished Pyrex block (OptoSigma). The glue was cured with a UV lamp (UVP CL-1000, λ 254 nm) for 30 min.

The overlapping end of the mica was gently scored on the back face with a scalpel, and the mica was finally cleaved once again by peeling back the adhesive tape to yield a fresh

top surface of mica for investigation. As before, a small volume of ultrapure water was introduced during cleaving. The fresh mica surface was then blown dry with a jet of clean N_2 . In almost all cases, and where not specifically mentioned in the text, the mica surface was UV- O_3 cleaned (BioForce Nano) for 20 min. The silicon block with mica surface was clamped against a teflon trough to form the solid - liquid reflectivity cell.

A schematic of the neutron path through the multilayered substrate is shown in Figure 2.7, with the thicknesses of the layers not to scale. Example values of fitted layer thicknesses are given in Table 2.1.

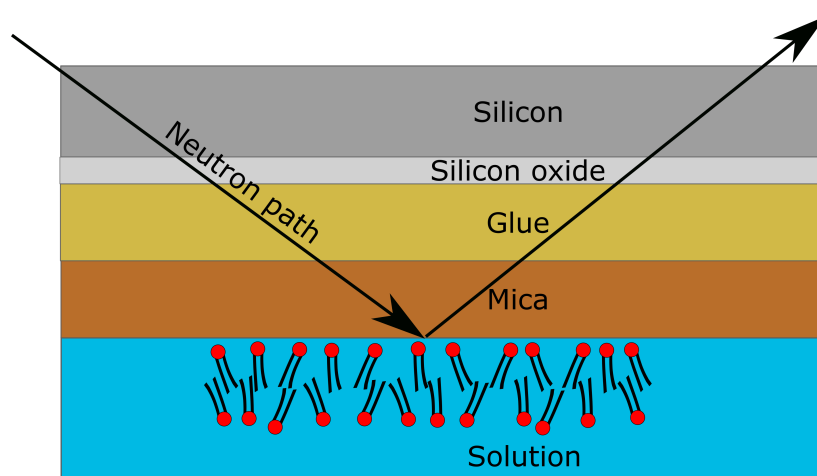


Fig. 2.7 Schematic of the multiple layers of the supported mica substrates used for neutron reflectivity experiments, with the path of the neutron beam shown and an example surfactant layer on the mica surface. Layer thicknesses are not to relative scale.

Solid - Liquid Cells

Reflectivity measurements were carried out using custom machined teflon troughs, clamped against the substrate of interest to create a reservoir for solutions and a solid - liquid interface. An example of the troughs used is shown in Figure 2.8. The dimensions of the trough are 85 mm along the beam direction and 40 mm across it, and the seal with the surface of interest is made by a machined lip approximately 0.5 mm in height. The deformation of this lip provides the liquid-tight seal. The volume of the reservoir was determined as approximately 2 ml through controlled filling experiments.

HPLC fittings and pump connected to the trough were used to fill and exchange the cells, in situ on the neutron instruments. This is significant as it means that different solution contrasts can be used without removal, emptying, refilling and re-aligning of the sample

cells, which is very time consuming and can be very challenging with weakly scattering contrasts. The assembly was held together by aluminium plates on each side, with a rubber mat between the bottom plate and silicon wafer to evenly distribute the clamping load.

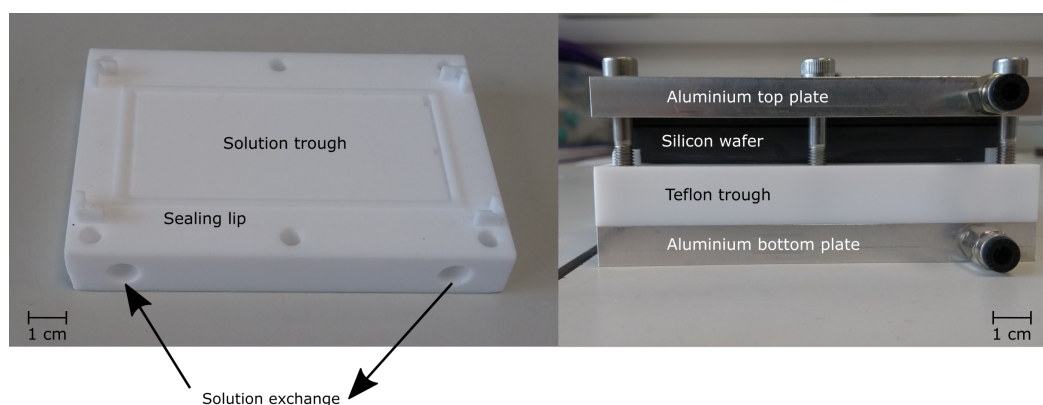


Fig. 2.8 The sample cells used to conduct reflectivity experiments. Left is the teftlon trough which seals against the surface of interest. HPLC fittings thread into the solution ports labelled. Right is the full assembled cell; the rubber mat between the silicon wafer and top plate is not visible, nor are the glue and mica layers on the face of the silicon wafer contacting the teftlon trough. The ports visible on the top and bottom plates are for connection to the recirculating glycol bath for temperature regulation.

The top and bottom plates of the cells are drilled with channels and have fittings to allow connection to a recirculating glycol or water bath for control of temperature. This was utilised in some experiments where temperature control was of importance, but where not stated in the text the cells were run without specific temperature control and at the ambient conditions of the instrument blockhouse, approximately room temperature. When temperature control was employed, the temperature of the silicon wafer was monitored by a thermocouple taped directly to the side of the wafer, and the recirculating glycol bath was adjusted until the measured temperature stabilised at the desired value. The glycol bath had to be set a few degrees higher than the desired value due to losses between the heated plates and the sample itself.

The cells were assembled by clamping the components together evenly across the cell and to the minimum torque at which the cell was found to seal during pump driven exchange at a flow rate of 2 ml/min. This was achieved using a torque screwdriver, and typically required torques were 0.4 - 0.6 N m⁻¹. The minimum torque was used so as to minimise the pressure applied to the mica surface, and the chance of inducing curvature or fracturing. Due to the creep of teftlon under load, the cells were re-tightened to the initial sealing torque after a 12 h delay.

Each cell was initially filled with care by hand using a syringe while oriented vertically, to avoid trapping bubbles. After the cells were connected to the HPLC pump they were gently rocked and tapped during flow to attempt to remove any further bubbles. Subsequent solution exchanges were carried out with an HPLC pump using a volume of 30 ml and a flow rate of 2 ml/min. Previous work has shown this to be more than sufficient for complete exchange of the cell solution. HPLC lines were flushed between different solutions to avoid contamination across cells.

The HPLC pumps used can take up to four input solutions, and are capable of mixing given ratios of these inputs to dilute the stock solutions as appropriate. This allows accurate and automated sweeping of concentrations. Testing revealed that at very low percentage selections the mixing ratios pulled by the pump were not accurate, and so a minimum of 10% of any single feed solution was used. In some experiments, specifically those described in Chapter 4, it was important that the solution entering the experimental cell was very thoroughly mixed prior to moving into the cell and no variation in concentration of species was translated to the cell. The HPLC pump incorporates a mixing chamber, but for added certainty an additional external mixing chamber was added before the lines to the cells.

In cases where there was any possibility of precipitation of additives occurring on mixing of solutions, the desired final solution was tested 'offline' prior to the experiment. Examples of such situations were mixing of two oppositely charged surfactants, and mixing surfactant solution with salt solution. In these cases the desired solutions were prepared in the same manner that would occur in the pump (by mixing more concentrated solutions of the components), and observed for any turbidity or precipitation.

With such a small surface area under investigation, cleanliness is of great importance and enhanced cleaning methods were used to avoid contamination. The teflon troughs were cleaned with nitric acid in the same manner as the silicon wafers, as were any glass bottles used for making up solutions. All items not compatible with acid cleaning, such as HPLC fittings, were cleaned by soaking overnight in Decon 90, rinsing 10 times with water, further soaking overnight in water, then rinsing 10 times and drying. HPLC tubing was flushed with a large volume of 1:1 ethanol:water, then a large volume of water.

The major complications associated with the neutron reflectivity samples were found to be trapped bubbles and leaking. Air bubbles were evidenced by lower than expected reflectivity, and enhanced off-specular scattering. Bubbles trapped during cell filling were generally hard to remove, and in some cases only disassembly and refilling of the cell was successful.

Sample Mounting

For all experiments, samples were mounted to an automated sample changer in the beamline. These are motor-controlled to a very high degree of accuracy and operated remotely, which allows alignment of a number of samples (in general either three or four samples were mounted adjacent to each other) and measurement of different samples without the need to open the blockhouse or remove and realign samples. This ability, when combined with the automated solution exchanges provided by the HPLC pump, is extremely valuable in the intensive experimental environment of a neutron experiment. Removal of any single sample from the sample stage has the potential to change the balance of the table, so whenever a sample was removed the alignment of the other samples on the table was checked and corrected if necessary.

For experiments at ISIS the reflectivity cells were attached to the sample changer table by magnetic kinematic mounts provided by the facility. This was not possible at the ILL due to the space constraint and vertical sample geometry on D17. The purpose of the kinematic mounts is both to allow easy removal and replacement of samples, as unbolting is not required with the magnetic fixings, but primarily to allow near exact replacement of the samples in the same location back onto the stage. This dramatically speeds up the alignment procedure as the coarse horizontal alignment procedure was not required and in nearly every case it was possible to go straight to fine alignment in reflection mode without any straight-through alignment.

2.1.3 Neutron Reflectivity Data Analysis

As mentioned in Section 2.1.2, measured reflectivity data is divided by the measured intensity for a straight through beam, and converted from wavelength and angle into Q in a process termed data reduction. The ‘coherent summation’ method of Cubitt et al.⁶⁰, implemented in the data reduction software COSMOS⁶¹, was utilised on the data from D17 to account for a small degree of curvature of the mica surface. This method involves binning the data in ‘constant Q ’, rather than the conventional method of summing over constant wavelength then converting the data to Q and re-binning. A full explanation of the analysis, and the appropriate treatment of the resolution is described further by Cubitt et al.⁶⁰. For the reflectometers at ISIS, data was reduced in Mantid⁶² in the usual manner by converting TOF to wavelength, then normalising by monitor counts and transmission measurement. For D17 a region of the multi-detector outside the specular condition was used to subtract the background from

the data. Any remaining background was accounted for during data fitting, as was the background in data collected from ISIS.

Due to the complex nature of the substrates used, comprised of layers both thicker and thinner than the coherence length, a specialised fitting routine must be used to fit a model to the reflectivity data. I-CALC, a custom program properly taking into account this analysis has been developed by prior members of the group, and was used and modified through the course of this work. The routine properly accounts for the ‘thin’ and ‘thick’ layers, for which the amplitude and intensity must be respectively considered. The attenuation of neutrons, in the mica and more significantly the glue layer, is also accounted for. This attenuation is wavelength dependent, and to account for this the attenuation has been directly measured using a thin section of each material, and a polynomial fitted to the wavelength dependence. Resolution is dealt with by convolution of a Gaussian, of width selected appropriate to the resolution, with the calculated reflectivity.

The attenuation will also vary with the path length of the neutrons in each medium, and this is also calculated and accounted for. The details of I-CALC are further described in the work of Browning et al.⁵⁵ and Griffin et al.⁵⁶, including the parameters fitted for the polynomials to the wavelength dependent attenuation of both mica and the glue. Validation of I-CALC has been performed against a well established neutron fitting routine⁵⁵, MOTOFIT^{53,63}.

Due to slight imperfections away from the idealised crystal structure of the natural mica mineral the classically forbidden Bragg peak at 0.32 \AA^{-1} is visible for some substrates. In these cases the data was truncated at 0.24 \AA^{-1} , just below the onset of the peak, for the purposes of fitting to avoid contribution from the Bragg peak to the fitting routine. The full reflectivity profiles are still displayed in figures.

Development of Fitting Algorithm

As discussed above, a specialised fitting routine must be utilised to fit a structural model to the neutron reflectivity data generated from the multilayered supported mica substrates. During initial use of the fitting program, it was observed that the fit produced by the script occasionally varied depending on the dataset being fitted; even with the same input parameters a small shift in q was observed in the simulated reflectivity in some cases. After significant investigation it was found that the effect depended on the number of datapoints in the dataset being fitted.

In the routine the ‘smearing out’ of reflectivity data caused by instrumental resolution and sample effects is included in the calculation by convolution of the calculated reflectivity with a Gaussian, with a width chosen to reflect the broadening for a given experimental set-up. The Gaussian used for convolution is not a true continuous function but discrete, and in the original program composed of the same number of data points as the measured reflectivity. It was found that in the implementation when the Gaussian was formed from an even number of points convolution resulted in an offsetting of the calculated reflectivity. This behaviour was verified using a step function, as shown in Figure 2.9. The fitting routine was therefore modified to ensure the Gaussian profile was always composed of an odd number of points to prevent this issue.

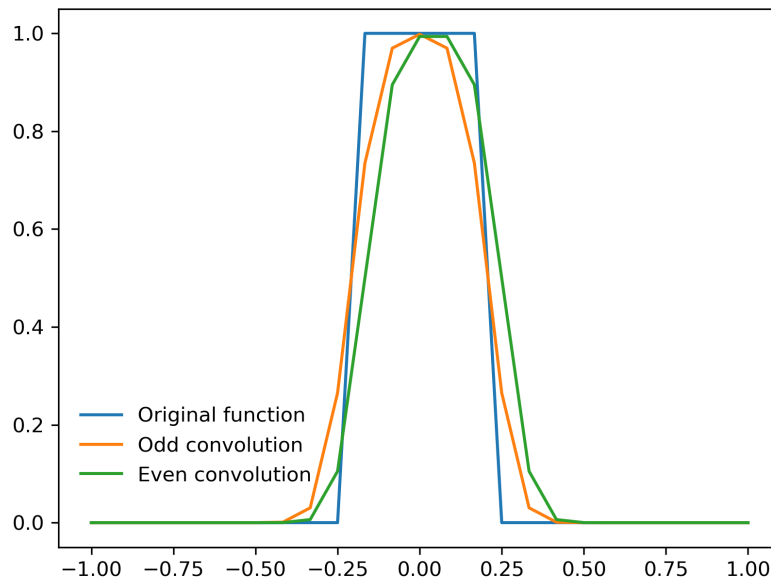


Fig. 2.9 Convolution of a step function (blue) with a Gaussian constructed from either an odd (orange) or even (green) number of points.

This correction was verified by confirming that the critical edges fall at the positions calculated from the SLDs of the relevant phases when using the new implementation of the fitting algorithm.

Substrate Characterisation

A large number of mica substrates were used in the experiments described in this thesis. Each substrate was initially characterised in three water contrasts prior to addition of any salts or surfactants; H₂O, D₂O and either a mixture contrast matched to the silicon substrate (CMSi) or to the mica layer (CMMi). The three datasets were then co-refined using the procedures described in Section 2.1.3 to give the thickness and roughness for each of the silicon, silicon oxide, glue, and mica layers.

An example of reflectivity data collected from the bare mica - water interface is shown in Figure 2.10 with fits superimposed, and the associated fitted parameters are given in Table 2.1. The SLD value for the glue is based on measurements of glue composition and density carried out by prior group members, and the SLD for the mica is calculated from the idealised formula and crystal structure. Both of these parameters were allowed to vary within tight bounds. As Figure 2.10 indicates, the agreement between the experimental data and the model described above is very good indeed, particularly given the complexity of the experimental system and highly constrained nature of the fitting.

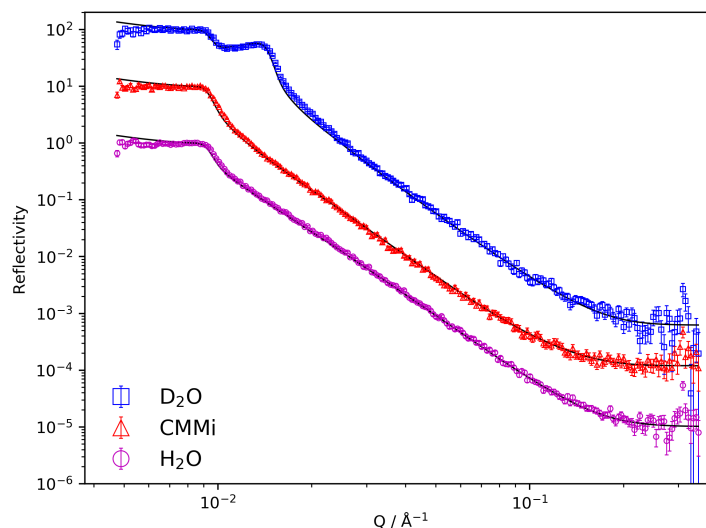


Fig. 2.10 Reflectivity profiles collected from the bare mica surface exposed to H₂O, water contrast matched to mica (CMMi), and D₂O. Profiles offset for clarity.

The fitted parameters for the glue layer are found to depend largely on the adsorption correction and attenuation of the glue. They were found to have significant uncertainty and hence a reasonably wide range of values are consistent with the data. A reasonable value

Table 2.1 Fitted parameters for bare mica surface from KAOT adsorption.

| Material | SLD / $\times 10^{-6} \text{ \AA}^{-2}$ | Thickness | Roughness / \AA |
|---------------|---|------------------|--------------------------|
| Silicon | 2.07 | - | 6 |
| Silicon oxide | 3.49 | 15 \AA | 6 |
| Glue | 1.08 | 9 μm | 14 |
| Mica | 3.79 | 12 μm | 3 |

is included in the fitting. Importantly this parameter makes essentially no difference to the fitting of layers on the surface of the mica, which are of central interest in this work.

Parameters for all the substrates used in this thesis were found to be consistent within reasonable bounds, and reflectivity profiles and parameters from every bare surface are not shown for brevity.

2.2 X-Ray Reflectivity

2.2.1 X-Ray Reflectivity Theory

X-ray reflectivity (XRR) is a complementary technique to neutron reflectivity; it can give information about the composition and structure of layers in a sample. The principles of optics described in Section 2.1.1 with reference to neutron reflectivity still hold for X-ray reflectivity and govern the behaviour observed. Whereas neutrons interact with the nuclei of atoms, X-rays interact with the electron density surrounding the nuclei so a different contrast is seen and this technique is more suitable to observing species with significant atomic mass.

The issue of beam attenuation is a more constraining factor for XRR when compared to neutrons. Passage through even thin (centimetres path-length) layers of solvent will attenuate the X-ray beam significantly, leading to reduced intensity and higher background signal.

For X-rays, the refractive index includes components for dispersion and absorption. The full refractive index is given in Equation 2.18:

$$n = 1 - \delta - i\beta \quad (2.18)$$

where the dispersive component, δ is given in Equation 2.19 and the absorption component, β is as defined in Equation 2.20.

$$\delta = \frac{\lambda^2}{2\pi} r_e \rho \quad (2.19)$$

$$\beta = \frac{\lambda}{4\pi} \mu \quad (2.20)$$

λ is the wavelength, r_e the electron radius, ρ the electron density of the material, and μ is the absorption length.

More details of the background theory may be found elsewhere^{64,65}.

2.2.2 Instrumentation

X-ray measurements were carried out using a monochromated beam with the incident and reflected angles continually varied to build up the reflectivity profile. Measurements were performed on the I07 beamline at the Diamond Light Source⁶⁶, using a beam monochromated at 0.7251 Å with a width of 300 μm.

The high intensity of the X-ray beam from the synchrotron, even the reflected signal, can be sufficient to damage the detector. To avoid this, attenuating filters are generally used to reduce the intensity of the beam incident on the sample. As the incident angle is increased and the intensity of the measured signal reduces, less attenuating filter-sets are utilised to allow greater measured intensity and a higher signal to noise ratio. The much greater intensity of the mica Bragg peak also required additional filters to be in place. The result is that the reflectivity profile is constructed in a series of discrete sections, much like during neutron reflectivity. These were stitched together using a script provided by Diamond, which also accounted for any over-illumination of the sample area at low angles, which would lead to lower than expected reflected intensity.

The high intensity of the source can be sufficient to cause changes or damage to the surface and structures of interest. This is frequently referred to as ‘beam damage’, and may be mitigated by horizontal translation of the sample during measurement. In this way a fresh unaltered region of the sample can be probed. The system under study in this work was of a layer under aqueous solution, which will help dissipate any heat build up and make beam damage less likely. Mitigation through horizontal translation was planned, but not conducted due to other experimental issues.

Custom reflectivity cells were used, the design of which is discussed further in Section 3.3. PEEK components were cleaned by sonication in ethanol, then soaking and sonicating in water. Substrates were prepared in the same manner as for neutron reflectivity, as described in Section 2.1.2, but with two different wafer sizes for the appropriate cells. $50 \times 50 \times 10$ mm wafers, and $10 \times 10 \times 3$ mm wafers were used, all polished to a roughness of $< 5 \text{ \AA}$.

2.2.3 X-Ray Data Analysis

X-ray data was fitted using the fitting routine GenX⁶⁷ (Version 2.4.9). In this routine scattering lengths are calculated by inputting layers as formula units per \AA^3 . As in neutron data fitting each layer in the model is described by composition, roughness, thickness, and hydration. The model is refined to minimise the difference between the calculated reflectivity and experimental data.

2.3 Powder X-Ray Diffraction

2.3.1 Theory

Diffraction of X-rays from a powder allows identification of the crystalline minerals present in the sample. The diffraction pattern generated by a crystal is the 3D Fourier transform of the real space structure, though a more physical interpretation may be reached by considering electrons scattering from planes of atoms in the sample.

Depending on their relative phases, the beams scattered by different atoms in the crystal may interfere constructively leading to a peak in the diffraction pattern, or they may interfere destructively resulting in no peak. A simple schematic of the situation is given in Figure 2.11. The condition for constructive interference can be derived geometrically and is given by Bragg's Law (Equation 2.21).

$$n\lambda = 2d \sin(\theta) \quad (2.21)$$

In Equation 2.21, n is an integer, λ the wavelength of the X-rays, θ the angle of incidence and d is related to the unit cell dimensions and angles. Due to the random orientations of

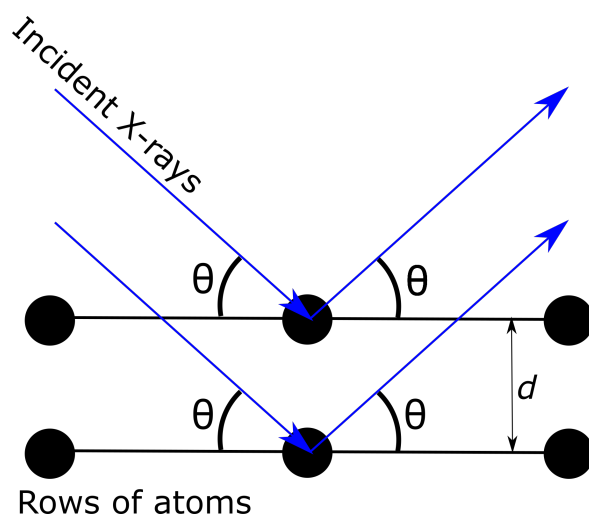


Fig. 2.11 X-ray diffraction from adjacent planes in a crystal, of layer spacing d in PXRD.

crystals in a powder, all lattice planes are represented and should be evident in the pattern as the incident angle is scanned.

2.3.2 Experimental

Powder X-ray diffraction measurements were conducted using a Bruker D8 Advance diffractometer, with Cu $K\alpha$ radiation ($\lambda = 1.541 \text{ \AA}$). Due to the large d -spacings under investigation, an instrument capable of low angle measurements with low background was required.

Samples for XRD analysis are often prepared by dispersing and grinding the powder of interest in a small volume of acetone, spreading this across an amorphous glass slide, then allowing the solvent to evaporate to yield a relatively flat and well dispersed sample. The specific nature of the organically modified clays under study with this technique, described in more detail in Section 4.2.5, is such that organic solvents can swell the interlayer spacing. There was therefore concern that this acetone preparation method might alter the parameter under investigation.

To test this effect, measurements from a sample prepared through the described acetone method were compared with a sample prepared through an alternative method; organically modified clay sprinkled 'dry' through a fine copper mesh onto a small amount of vacuum grease on a glass slide. This method was less convenient and difficult to produce a well dispersed and even sample from. Preparation of samples was conducted by Holly Smith, a

Masters student under my supervision. The results of X-ray diffraction measurements from each of the two preparation methods are shown in Figure 2.12.

The signal from the acetone preparation is much less noisy, with a sharper peak at $2\theta \approx 4.25^\circ$, and a second order peak visible at $2\theta \approx 8.5^\circ$. An increase in layer spacing would result in a shifting of the peak to smaller angle. Whilst it is difficult to locate the exact centre of the broad peak in the mesh-prepared sample it is clear that the peak position of the acetone-prepared sample is essentially the same as for the mesh-prepared, or if anything at marginally higher angle/lower spacing. Therefore it was concluded that the acetone preparation of samples did not lead to significant swelling, and this preparation method was used for all subsequent experiments.

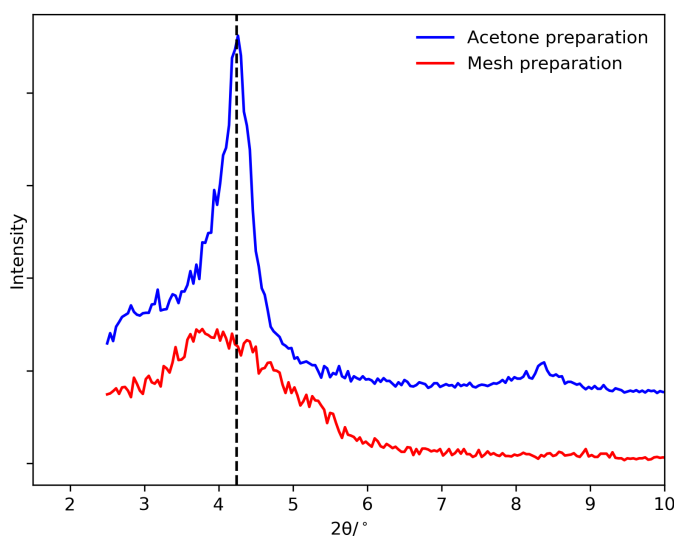


Fig. 2.12 X-ray diffraction data from the same organically modified clay, with diffraction samples prepared either by dispersion in acetone or ‘dry’ dispersed through a fine mesh. Data are offset but are the same scale. The position of the peak for the acetone prepared sample is shown for comparison.

Preferential alignment of sample with the support can be an issue for X-ray diffraction, in particular for ‘platey’ layered samples such as the clays used here. As diffraction was only conducted to measure the basal spacing of the clays, and preferential alignment of the flakes would orient these planes parallel to the substrate and enhance the contribution of this scattering, this alignment was not of concern in this work.

2.4 Zeta Potential Measurements

2.4.1 Zeta Potential Theory

The motion of colloidal particles in an applied electric field gives information about the potential at the plane of shear in the electrical double layer, termed the zeta potential. Light scattering may be utilised to measure the mobility of these colloids; if a laser is incident on a colloidal sample then the frequency of any scattered light will be shifted relative to the incident frequency by an amount proportional to the velocity of the particle scattering the light. The Doppler shift of this light will be very small relative to the incident laser frequency, but through optical heterodyning becomes detectable. A reference beam is split from the main beam before interaction with the sample, and the reference is recombined with the scattered light after modulation to a lower frequency. The frequency shift on scattering is now detectable relative to this lower frequency.

The relation between mobility (which is the velocity per electric field, $(\text{m s}^{-1})/(\text{V m}^{-1})$) and zeta potential is not straightforward. Two limiting cases are commonly applied depending on the ionic strength and particle size (a), where $\kappa a \ll 1$ and where $\kappa a \gg 1$, though a more detailed analysis is possible⁶⁸. For the former case, where the Debye length (κ^{-1}) is much larger than the species radius, the Hückel limit applies as given in Equation 2.22 where μ_e is the electrophoretic mobility, η the viscosity of the fluid, ζ the zeta potential, and the other symbols have their usual meanings.

$$\mu_e = \frac{2\varepsilon\varepsilon_0\zeta}{3\eta} \quad (2.22)$$

Whilst this limit might be valid for atomic ions or in non-aqueous systems, it is not well met for aqueous colloidal systems where Debye lengths are generally much smaller and radii are larger. In the limit of $\kappa a \gg 1$, the Smoluchowski equation given in Equation 2.23 applies⁶⁹.

$$\mu_e = \frac{\varepsilon\varepsilon_0\zeta}{\eta} \quad (2.23)$$

In this work the Smoluchowski model was utilised in all cases, though in the case of colloidal silica in 1 mM KCl the limit is not well met. In this electrolyte concentration and if the silica is unaggregated then $\kappa a \approx 1$, but conditions were chosen such that some

aggregation is likely and ‘a’ will be increased. Despite this, the calculated zeta potential values will show some deviation from the true values, and no major conclusions were drawn from exact magnitudes of zeta potential data.

2.4.2 Experimental

Ludox™ colloidal silica stock was sonicated for 15 min, then samples were diluted to 10 wt%, and made to 1 mM KCl. pH was adjusted with addition of 0.1 M HCl or NaOH. After equilibration approximately 2 ml of the sample was removed, passed through a 0.2 μm nylon syringe filter, and used for zeta potential analysis. The pH of the remainder of the sample was measured.

Zeta potential measurements were carried out using a Brookhaven ZetaPlus instrument. The laser was allowed to stabilise for at least an hour before measurements, and the electrodes were cleaned between samples. Measured mobility was converted to zeta potential values using the Smoluchowski equation in the integrated software.

2.5 Streaming Potential Measurements

2.5.1 Theory

For large flat surfaces, rather than colloidal systems, determining the zeta potential is experimentally more challenging. Clearly moving the solid is not possible, but by moving the electrolyte over the surface and measuring the potential or current, the zeta potential may still be determined. When an electrolyte flows under some applied pressure through a plug or through a narrow channel composed of a charged material, the displacement of ions from the electrical double layer creates a potential difference across the plug or channel, termed the ‘streaming potential’.

$$\zeta = \frac{dU}{dp} \frac{\eta}{\epsilon \epsilon_0} \frac{L}{A} \frac{1}{R} \quad (2.24)$$

$$\zeta = \frac{dI}{dp} \frac{\eta}{\epsilon \epsilon_0} \frac{L}{A} \quad (2.25)$$

For a narrow channel cell this potential difference is related to the zeta potential by the Helmholtz - Smoluchowski equation⁷⁰ as given in Equation 2.24, where $\frac{dU}{dp}$ is the streaming potential per unit pressure, L is the length of the channel, A the cross-sectional area, and R the resistance across the cell. All other symbols have their usual meanings. The component $\frac{L}{A} \frac{1}{R}$ is equivalent to the electrical conductivity. The current causing this potential is related to zeta potential by the related Equation 2.25.

2.5.2 Experimental

Instrumentation

A SurPASS electrokinetic analyser by Anton Paar, equipped with integrated titration unit, was used for measurements of streaming potential⁷¹. All measurements were conducted in a background electrolyte of 1 mM KCl, and pH was controlled by addition of 0.1 M HCl or NaOH as with zeta potential measurements. The electrolyte reservoir was continuously purged with nitrogen during operation to reduce pH changes due to CO₂ dissolution. The essence of the measuring device is straightforward; two gas-tight syringes driven by syringe pumps control flow across the sample and can generate a pressure gradient, and two electrodes mounted each side of the sample measure potential difference and current flow.

Various mounting cells exist for different substrate types, and for the flat surfaces of interest a 'clamping cell' arrangement was selected. This utilises a polypropylene spacer to create a narrow channel, which can be bounded above and below either by the surface of interest on both sides, or by the surface of interest on one side and a reference surface on the other. A schematic of the clamping cell set up is reproduced in Figure 2.13. For the mica and silica surfaces being measured it was not possible to easily introduce holes for electrolyte flow, so a reference surface provided by Anton Paar was used to make up the top side of the channel.

This was a polypropylene film, and the relation of the zeta potential of the surface of interest is given by $\zeta_{\text{surf}} = 2\zeta_{\text{tot}} - \zeta_{\text{ref}}$ where ζ_{surf} is for the surface of interest, ζ_{tot} is the measured zeta potential, and ζ_{ref} is for the reference surface. Any contribution to the measured zeta potential from the spacer used to separate the surfaces was not included in the calculation, but as the material is polypropylene and will not have a significant surface charge, and the surface area is approximately 9% of the total channel⁷¹, this is likely to be a reasonable approximation.

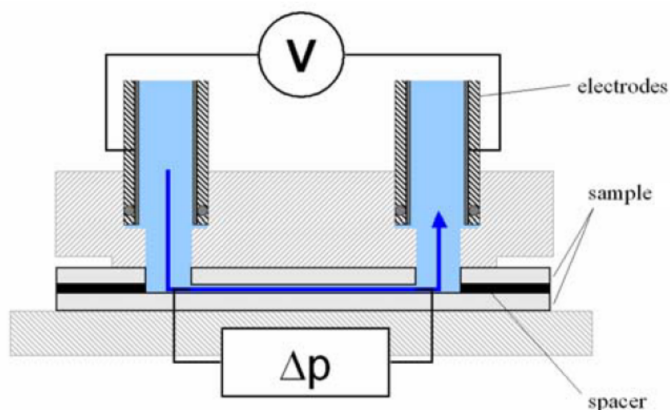


Fig. 2.13 Schematic of the clamping cell for the SurPASS device, reproduced from Bukšek et al.⁷¹

The instrument operates by linearly increasing the pressure across the cell and measuring the response of the current and potential, then repeating this process in the converse direction. This is repeated a number of times for each new electrolyte pH value. Standard operating procedures for the SurPASS were followed for all measurements⁷², and flow checks were conducted before zeta potential determination. Zeta potentials were calculated from the pressure ramps automatically using Equation 2.25.

Operation of the instrument was not without complication, with numerous faults arising over the course of the experimental period. Gas-tight syringes were found to develop leaks after some period and required maintenance and finally replacement. The motors driving the syringe pumps for electrolyte transport were also prone to unexplained errors and stalling with no obvious cause. Great care was also required to prevent bubbles in the electrolyte transport hoses and measurement cell.

Validation

pH and conductivity electrodes were calibrated prior to each use and maintained such that the cell parameters fell within the acceptable limits. For validation of the electrodes, Anton Paar provide both a 'single point' validation sample of viscose fibres, which should produce a specified zeta potential at a given pH, and a reference foil with a supposedly known IEP. This same surface is also the foil used as a reference surface in the clamping cell, as the opposing surface to a surface of interest.

The viscose fibres validation limits are a zeta potential of -9 ± 3 mV in 1 mM KCl at pH 6. Measurement of the validation material resulted in an experimentally determined zeta potential of -11 ± 3 mV in 1 mM KCl at pH 6.2, so within the accepted limits. This gave some confidence that the instrument was operating correctly and electrodes were in acceptable condition.

For the validation reference foil a number of measurements over a broad pH range were made over several different days to assess variability. The results of these measurements are shown in Figure 2.14, and it can be seen that there is reasonable consistency at near-neutral pH values but the zeta potential showed significant deviation between measurements at lower pH; whether this is variation in the true zeta potential of the polypropylene film or in the measurement is unclear. The stated IEP of the reference⁷² was $\text{pH } 4 \pm 0.2$, whereas the measurements show no IEP within the tested range and by extrapolation an IEP of $\text{pH } 2 - 3$ can be estimated.

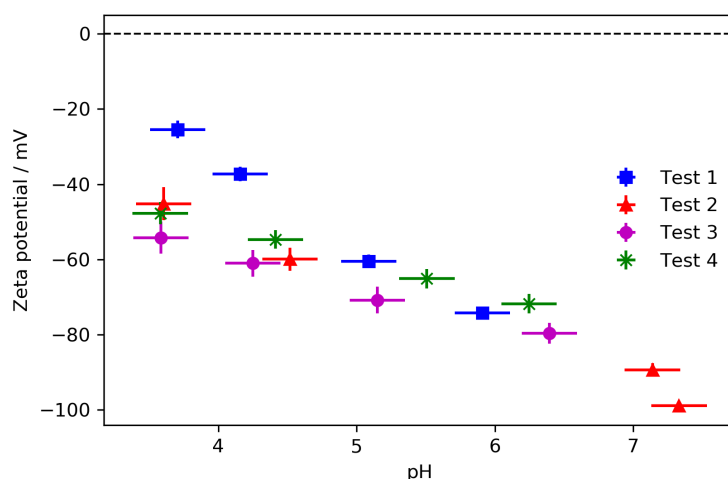


Fig. 2.14 Experimentally measured zeta potentials for the polypropylene reference foil, conducted over a range of pH values. Four separate tests are shown, which were different samples of foil and with extensive cleaning and flushing of all equipment between measurements.

Despite a number of enhanced cleaning cycles and re-calibrations of pH and conductivity electrodes, no difference to the measured zeta potential profile was found. After a maintenance visit by Anton Paar and discussion with technicians it was suggested by them that the literature value of the supplied reference foil might be incorrect, and given that the single point calibration measurement was successful that the machine was functioning as intended. Despite this unsatisfactory conclusion, the relative consistency of measurements

at near-neutral pH was deemed sufficient to cautiously proceed with measurements, even if results may only be analysed comparatively.

Substrate Preparation

Substrates were prepared as per the standard operating procedures for the clamping cell; a section of reference foil was cut to shape and had two holes punched using the supplied apparatus, to allow electrolyte flow. A spacer was then applied and the surface of interest clamped against the reference to create the channel for electrolyte flow.

Mica substrates for zeta potential analysis were prepared in an analogous way to those for neutron reflectivity studies, as described in Section 2.1.2. The same cleaving and cleaning procedure was applied but there was no requirement to glue the mica sheets to a support so they were clamped against the reference surface using a polished glass block. Silicon wafers (roughness < 10 μm) were nitric acid cleaned then rinsed with copious ultrapure water, as with the preparation for neutron experiments. Oxidisation of the surface of the silicon wafer results in the measured surface being silica, and so is comparable to the Ludox colloidal silica particles. Some wafers were also UV-O₃ cleaned prior to measurement as discussed in Section 5.3.

Data Analysis

As previously mentioned, calculation of the zeta potential for a measured surface requires knowledge of the zeta potential of the reference surface at the same pH values. To collect this data, a measurement/titration programme was performed on a cell consisting of two opposing reference foils. The lower surface was swapped to the surface of interest and the same measurement/titration programme was repeated with a new electrolyte. This generated zeta potential measurements at essentially identical pH values for the reference and investigated cell. Calculation of zeta potential from reference and investigated surface was calculated by a custom program which accounted for slight variations in pH between the two measurements by linear interpolation between points, and discarded data outside of an acceptable range.

2.6 Surface Charge Calculations

The Poisson Boltzmann equation may be solved in the case of a planar interface and a symmetric electrolyte to give the potential at a particular distance, x , away from the surface relative to the potential at the surface, Ψ_0 . Equation 2.26 gives this form, where the specific distance x is the plane of shear and the potential here is the zeta potential ζ . All symbols have the meanings defined in Section 1.2.2.

$$\frac{\tanh\left(\frac{z_i e}{4kT} \zeta\right)}{\tanh\left(\frac{z_i e}{4kT} \Psi_0\right)} = \exp(-\kappa x) \quad (2.26)$$

The concentration of ions and counter-ions integrated to an infinite distance from the flat surface into solution must exactly balance the surface charge density. By assuming only a diffuse layer, and integrating the exponential decay of the potential away from the surface, the Grahame equation may be derived as given in Equation 2.27. This relates the surface potential to the surface charge density. c is in the non-standard concentration units of ‘mol m⁻³’, which is equivalent to ‘mM’.

$$\sigma_0 = (8RT c \epsilon_r \epsilon_0)^{1/2} \sinh\left(\frac{e}{2kT} \Psi_0\right) \quad (2.27)$$

An empirical modification to this formula for spherical surfaces is given in Equation 2.28⁷³.

$$\sigma_0 = (8RT c \epsilon_r \epsilon_0)^{1/2} \left[\sinh\left(\frac{e \Psi_0}{2kT}\right) + \frac{2}{\kappa a} \tanh\left(\frac{e \Psi_0}{4kT}\right) \right] \quad (2.28)$$

Where appropriate, surface charge densities were estimated from zeta potential data using Equations 2.26, 2.27 and 2.28. These neglect the presence of any Stern layer and are based purely on the Guoy-Chapman model of the EDL; the calculated surface potentials and surface charge densities are likely under-estimates, and are intended only as very approximate values. The functionality of the equations used was verified against examples in the literature where similar conversions have been performed^{74,75}.

2.7 Inductively Coupled Plasma - Atomic Emission Spectroscopy

Inductively coupled plasma (ICP) is an elemental analysis technique used for the detection of trace metals and other elements. A nebuliser converts the liquid sample to a fine mist, and high temperature plasma is generated and used to ionise the sample. The ions then emit radiation at wavelengths characteristic of the element as they recombine repeatedly with electrons. Recent advances in ICP have been reviewed by Donati et al.⁷⁶

Samples were prepared by dissolving a known mass of species in 1 wt% nitric acid and diluting with more acid of equal concentration until the sample was dilute enough to be within the detection limits for the element of interest without saturating the detector.

ICP measurements were conducted in the Department of Geography, University of Cambridge, by Laura Healy. Samples were diluted to the measurable range, which varied depending on the ion being measured. Concentrations were calculated by comparing measurements with those of calibration solutions (TraceCERT®).

2.8 AOT Counter-Ion Exchange

As discussed in Section 3.1, the role of different inorganic counter ions in clay and organic binding is under study in this work. To aid this, it was useful to prepare salts of the anion dioctyl sodium sulfosuccinate (AOT) with different cationic counterions. AOT is most commonly available as the sodium salt, here referred to as NaAOT.

2.8.1 Salt Metathesis

A method based on that of Eastoe et al.⁷⁷ was used to exchange counter ions. A saturated aqueous solution of the metal chloride salt (50 ml) was added to a solution of NaAOT in ethanol (1 M, 25 ml) and shaken vigorously. Diethyl ether (10 ml) was added and the organic phase extracted and washed repeatedly with water until no chloride was present as indicated by silver nitrate. The organic phase was evaporated with a rotary evaporator and the product dried in a vacuum oven at 40°C under vacuum for 48 h.

2.8.2 Ion Exchange Column

An alternative method for exchange which is more appropriate for ions with a lower affinity for the AOT anion was employed, also based on a method by Eastoe et al.⁷⁸ A solution of NaAOT (10 g, 0.022 M) in 1:1 water:ethanol (20 ml) was eluted through a column of Amberlite IR-120 ion exchange resin in its H-form (height 20 cm, diameter 2 cm) at a rate of 2 drops/s. The acid form of AOT generated was neutralised to pH 7 by a dilute solution of the hydroxide of the relevant counterion (e.g. tetramethylammonium hydroxide) as measured with a Metrohm pH probe. The solution was carefully evaporated in a rotary evaporator and the product dried in a vacuum oven at 40°C under vacuum for 48 h.

2.8.3 AOT Exchange Results

The method described in Section 2.8.1 was attempted using KCl as the counter salt with the aim of synthesising KAOT, but upon the addition of ether to the salt mix, precipitation occurred. This prevented the extraction of the desired AOT salt, and it has been subsequently noted that others have seen a similar effect specifically with the potassium salt⁷⁹. The method detailed in Section 2.8.2 was therefore used to synthesise KAOT and also tetraethylammonium-AOT by the use of KOH and tetraethylammonium-OH respectively to neutralise the acid AOT. In both cases the initial product was a translucent jelly like substance, as shown in Figure 2.15a, which after drying in a vacuum oven at 40°C for 48 h dried further to a white waxy solid as shown in Figure 2.15b.



(a) KAOT after rotary evaporation of the neutralised acid AOT solution.



(b) KAOT after further drying in vacuum oven, yielding a white waxy solid which could not be dried further.

Fig. 2.15 Drying stages of KAOT after synthesis.

ICP analysis of highly diluted samples of the KAOT was performed, with a range of dilutions of Na and K ICP standards run concurrently as calibration. This analysis revealed a final molar proportion of K in KAOT as $84 \pm 4\%$ as calculated from the relative concentrations of Na and K determined and assuming no other cations were present. This incomplete exchange is most likely due to the ion exchange column not being fully converted to the acid form prior to exchange, or elution occurring too rapidly, or through a column of insufficient length.

The tetraethylammonium-AOT salt was synthesised in an identical manner and was therefore assumed to have a similar percentage exchange. ICP cannot easily detect nitrogen, making direct measurement of exchange difficult for this salt. Despite prior observations that NaAOT does not bind to mica, this level of exchange was not deemed to be sufficient for the use of the synthesised AOT salts in further experimentation. Repeated exchanges through the column of the produced species should increase the percentage exchange, and this could be used in future experiments, but would increase the risk of introducing hydrolysis products with further exposure to a low pH environment and so this was not conducted.

2.9 UV-O₃ Cleaning

In various cases a UV-O₃ treatment was used to clean substrates prior to experiments. In the cleaning process, UV radiation causes atmospheric O₂ to decompose into O(³P), which can combine with other O₂ molecules to generate ozone, O₃. UV radiation then causes dissociation of the O₃ into molecular oxygen and the reactive species O(¹D). It is this O(¹D) which causes the oxidative cleaning process, removing organic contaminants by oxidising them into volatile species which will leave the surface. This treatment is an effective cleaning method for a variety of contaminants⁸⁰.

UV-O₃ treatment was conducted using a BioForce Nano UV Ozone Cleaner.

2.10 Cation Exchange Capacity Measurements

As discussed in Section 1.1, knowledge of the CEC of a clay mineral is a proxy for direct measurement of the surface charge density, assuming the surface area is known. Two methods were considered for the determination of the CEC, both involving depletion of a cationic species from solution. The standard units of CEC are eq/100g, where an *equivalent* (eq) is

the number of moles of an ion multiplied by its valence, and so is interchangeable with a mole of monovalent cations. The unit is therefore identical to moles of charge sites per 100 g.

2.10.1 CEC - Methylene Blue Method

Adsorption of the cationic dye methylene blue to clays is a commonly used test due to its simplicity and convenience. A standard test method exists to calculate the Methylene Blue Index of a clay⁸¹, and this protocol was used essentially unchanged. A known mass of clay (approximately 2 g), which had been previously dried in an oven at 100°C for 5 h to ensure removal of water and hence an accurate mass, was stirred into a slurry with 300 ml of ultrapure water. Sufficient sulfuric acid was added to bring the pH to 2.5 - 3.8 as determined with pH indicator paper. A solution of 0.01 M methylene blue was titrated slowly into the slurry with stirring until the end point was reached as determined by a 'blue halo' persisting around the drop when a droplet of the slurry was placed onto filter paper. The end point determination for a standard kaolinite KGa-2 sample is shown in Figure 2.16 as an illustration of the technique.

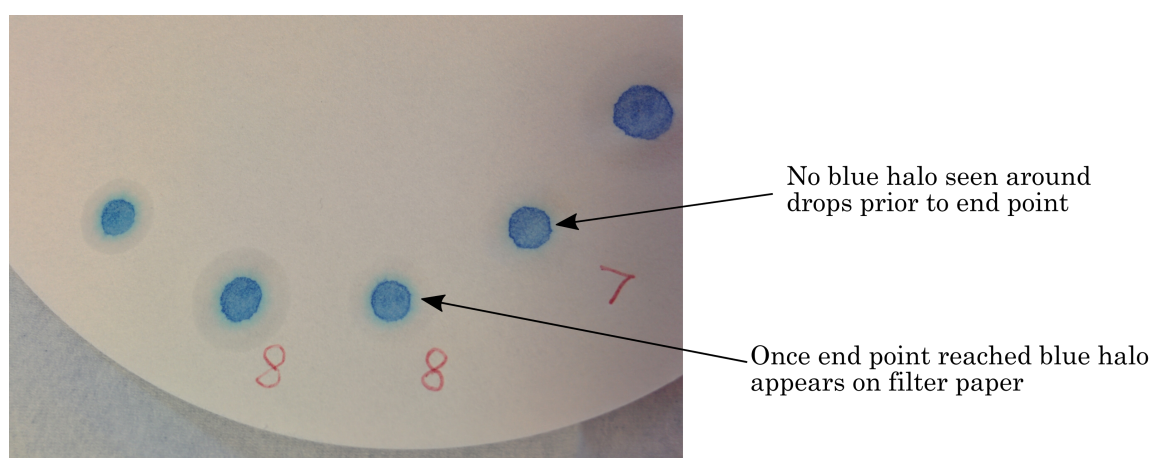


Fig. 2.16 End point determination with the "blue halo" test for determination of CEC by Methylene Blue. The example shown is for Kaolinite KGa-2.

To test the methodology of the methylene blue method outlined in Section 2.10.1 a validation measurement was conducted with the source clays Kaolinite KGa-2, a low CEC non-swelling clay, and Montmorillonite SWy-2, a high CEC swelling clay. The determined end points gave CEC values of 4 meq/100g and 25 meq/100g respectively, compared to literature values⁸² of 3.3 meq/100g and 76.4 meq/100g.

Whilst the value determined for the kaolinite is close to the literature value, that determined for montmorillonite is significantly below the expected range. This is likely to be due to the saturation of the surface with methylene blue molecules before all the exchangeable cations have been exchanged due to the large area occupied (130 Å) by the molecule⁸³. As montmorillonite is more highly charged than kaolinite, this issue arises. Mica is expected to have a much lower CEC (in per mass units) than montmorillonite due to its non-expanding nature resulting in the interlayer cations being fixed and not exchanged. The surface charge density is higher however, with an area per charge site of 47 Å² which is significantly less than the area of methylene blue⁵⁵. Another issue with the methylene blue method is the difficulty of increasing the accuracy of the method by determining the concentration photometrically, as methylene blue partially aggregates in solution, changing the adsorption properties⁸⁴. The methylene blue method was demonstrated to be a reasonable approach in some cases but was not utilised further here because of these issues.

2.10.2 CEC - Cu^{II} Method

An advancement on the Methylene Blue Index method for CEC determination has been proposed and developed in the literature^{85–87}. This involves the use of a copper complex, specifically Cu(trien)²⁺ where ‘trien’ refers to triethylenetetramine. The concentration of the copper complex in solution can be determined photometrically at 577 nm making this technique experimentally straightforward⁸⁸. The Cu(trien) method has been shown to be consistent with other methods and reliable within certain constraints, being robust to pH except in the case of strongly acidic samples, and exchange occurring quickly with no over-adsorption artificially inflating the measured CEC (a common problem associated with the methylene blue method)^{86,87}. This method has been previously applied to mica powder which had been partially delaminated with a treatment by hot lithium nitrate to give a larger surface area, and found to be a valid method for CEC determination⁸⁹.

A stock solution of 10 mM Cu^{II}(trien) was made up by mixing 500 ml of 10 mM triethylenetetramine (Sigma, ≥ 97%) and 500 ml of 10 mM CuSO₄. Approximately 2 g of clay powder (less for the montmorillonite validation measurement due to the high CEC) was weighed into a centrifuge tube with 10 ml of either 5 mM or 10 mM Cu^{II}(trien). The mixture was tumbled for 1 h then centrifuged at 15000 g for 30 min. The supernatant was extracted and passed through a syringe filter (pore size 0.2 μm) into cuvettes, and the absorption determined at the extinction maximum of 577 nm. The syringe filter was found

to be necessary as particles could still be seen in suspension in the supernatant and gave absorbances higher than the stock solution. Calibration of the stock solution with and without syringe filtering showed no absorbance of the copper complex to the filter membrane. A series of calibration samples were used to convert the absorbance into concentration, and the calibration was retaken for each round of CEC measurements.

CEC values for the samples clays KGa-2 and SWy-2 were measured with the Cu complex depletion method described in Section 2.10.2 and calculated as 2.1 ± 0.6 meq/100g and 70 ± 1 meq/100g. The errors estimates are based on repeat readings. These are in good agreement with the literature values⁸² of 3.3 meq/100g and 76.4 meq/100g. and this method of CEC determination was used for further measurements.

2.11 Mica Powder Modification

As detailed in Section 1.1.4, there is significant literature evidence that exchanging the surface cations of clays, including mica, for relatively small cations such as Li^+ or Mg^{2+} and then calcining the clay (heating at high temperature) can lead to a reduction in surface charge.

A method was developed to investigate these effects on both samples of mica powder or mica sheets. Mica powder (20 g) was first suspended in ultrapure water (150 ml) then filtered under vacuum. The mica was split evenly into three vessels and equilibrated by tumbling in a 1 M solution (20 ml) of the chloride salt of the desired metal ion (e.g. MgCl_2), or in ultrapure water as a control, overnight. The mica was removed from the solution by vacuum filtration, and placed into silica crucibles and calcined at 300°C for 7 h in air. Studies have shown that changes to the mica crystal structure do not occur at temperatures below 800°C so destruction or alteration to the crystal structure is not expected⁹⁰, and powder X-ray diffraction data of mica powders post-treatment were identical to those of the untreated powder, confirming this hypothesis. Silica crucibles were used to avoid leaching of sodium into the clay slurry from glassware as has been noted in the literature⁹¹. After calcination the mica was allowed to cool, re-suspended in water (150 ml) to remove excess salt, filtered, and dried in a vacuum oven under reduced pressure for 5 h.

2.12 Mica Ion-Exchange Isotherms

2.12.1 Initial Potassium Saturation

The hypothetical mica structure has each isomorphous substitution site compensated for by a potassium sitting between the layers or on the surface. In the natural mineral a small number of these potassium ions may be replaced by alternative inorganic cations in small quantities; EDX analysis of the mica powder revealed trace impurities of sodium. To increase the accuracy of mica cation exchange isotherms, initial potassium saturation of the mica powder was carried out to ensure that all the surface cations of the sample were potassium.

Mica powder (6.0 ± 0.1 g) was weighed into 50 ml centrifuge tubes, and 0.1 M KCl solution (20 ml) was added. Samples were equilibrated for 24 h, then filtered under vacuum using Whatman™ filter paper, and washed on the filter with water (2×40 ml). Samples were re-suspended in water (30 ml) and further equilibrated, filtered under vacuum and washed on the filter (20 ml), then re-suspended as before and re-filtered and washed. The powder was then dried under vacuum at 60°C for two days.

2.12.2 Exchange Isotherm Protocol

K-saturated mica (2.00 ± 0.02 g, accurate masses used for analysis) was weighed into 50 ml centrifuge tubes. Solutions of the desired concentration of magnesium or lithium were introduced by adding the appropriate volume of 10 mM stock solution and water to make up 10 ml. The exact concentration of stock solutions was determined with ICP analysis. Samples were equilibrated for 24 h, then centrifuged at 15000 g for 30 min. The supernatant was carefully extracted, and as there was some mica powder still visible the supernatant was syringe filtered using a nylon membrane, and the first 2 ml of filtrate discarded. 5 ml of filtrate was measured out for ICP analysis, and acidified with 52 μ l of 10 wt% concentrated nitric acid. This volume change was accounted for in concentration calculations.

The remaining filtrate was retained for pH measurement; the pH of each sample was measured and though a slight decrease in pH was found as equilibrium salt concentration increased, all samples were between pH 7.9 and 6.5 so action of protons as alternate cations was neglected in the analysis.

With mica, and clay minerals in general, comparison between the use of powders and behaviour on the basal surface is complicated by the marked difference in behaviour between

the basal surfaces and edge sites. For this reason no organic adsorption work on powders is included in this thesis, as adsorption on edges could make a significant difference to the bulk measurement. As the ion exchange isotherms discussed in this section focus solely on the exchange of cations, which ideally are present only on the basal surfaces, it is expected that the use of a powder will not lead to significant edge contributions in the results. The edge sites are likely to be dangling aluminol bonds, which will carry a positive charge at neutral pH and not interact with the cations being measured.

2.13 Fluorescence Microscopy

2.13.1 Background

Certain molecules or atoms may absorb a photon of a specific incident wavelength and be promoted to a higher energy level. The species may then relax to the ground state some time later, in part by emission of another photon. Generally the emitted photon is of a lower energy and correspondingly longer wavelength than the absorbed photon, because of energy transfer from the excited species to the surroundings. The delay from excitation to emission is typically a few nanoseconds¹⁹.

This phenomenon of fluorescence is used for a large number of techniques, and is so effective as through fluorescence a signal is measured against an effectively blank background. Applications range from selective imaging to more complex techniques such as fluorescence resonance energy transfer (FRET) and fluorescence lifetime imaging (FLI)⁹². Fluorescence techniques have historically been used in the most part for biological imaging, though more recently also for physical chemistry and engineering applications. In the biological studies, one or more fluorescent probes are typically introduced to bind selectively to desired species or environments. How much the introduction of probes perturbs the system under study is an open question.

Recent developments in imaging have allowed increases in spatial resolution, to what has been termed ‘super-resolution’ microscopy⁹³. Through the use of stochastic emission, and localisation of the point spread function of the emitted photons, resolution to single molecule levels may be achieved down to 10 - 20 nm. It is noted that while this is extremely impressive, and ideal for imaging of the large molecules typical of biological systems, this is still some way above the molecular area occupied by surfactants in an adsorbed layer, which is ultimately the focus of this work.

Exposure to high intensity of light may have the effect of ‘photobleaching’ the fluorophore, destroying the fluorescence. This can also occur at lower intensities, including those used for normal imaging, over longer time-scales which can cause problems with imaging. In contrast, the effect can be exploited by monitoring recovery of fluorescence after bleaching, to give information about mobility of fluorophores in the sample.

The spectral properties of some dyes, specifically the emission wavelength, can vary depending on the local environment. In this way properties such as pH, hydrophobicity, or local viscosity may be mapped with high spatial precision⁹⁴.

2.13.2 Imaging Methods

A number of methods of fluorescence based imaging are possible, and are widely used both for study of biological and other systems⁹⁵. The use of the technique for adsorption studies of the type described here is a novel development. In this work two distinct imaging regimes were employed: epifluorescence (EPI) and total internal reflection fluorescence (TIRF) imaging. Schematics of the two imaging orientations used are shown in Figure 2.17. In EPI, the laser is introduced normal to the substrate, and all dye molecules above the surface in the path of the laser are excited and emit. In this way the bulk solution is imaged.

In TIRF the laser is inclined at a sharp angle to the substrate. This angle must be below the critical angle, where the critical angle is defined between the surface and the laser, using the convention described earlier, rather than the more common optics convention of the angle between the surface normal and incident light. The laser therefore undergoes total internal reflection at the interface, but an evanescent wave propagates into the sample. The intensity of this evanescent wave decays exponentially, and so only fluorophores within approximately 100 - 200 nm of the surface will be excited⁹⁶. TIRF is analogous to attenuated total reflection - IR in principle, where an IR spectrum is recorded by an evanescent wave propagating into the sample from a high refractive index crystal. Two configurations of TIRF imaging are possible, where the objective lens is on the opposite side of the sample to the substrate in which the laser reflects, termed *trans*, or where the objective and laser are on the same side, termed *cis*. TIRF was operated in *cis* configuration in experiments described in this work.

A further possible imaging configuration is HILO where the laser is inclined at a sharp angle but above the critical angle, and passes refracted into the medium above the substrate. The imaging height is increased relative to TIRF and varies depending on the angle, but background noise is reduced compared to EPI. In the work in this thesis the maximum amount

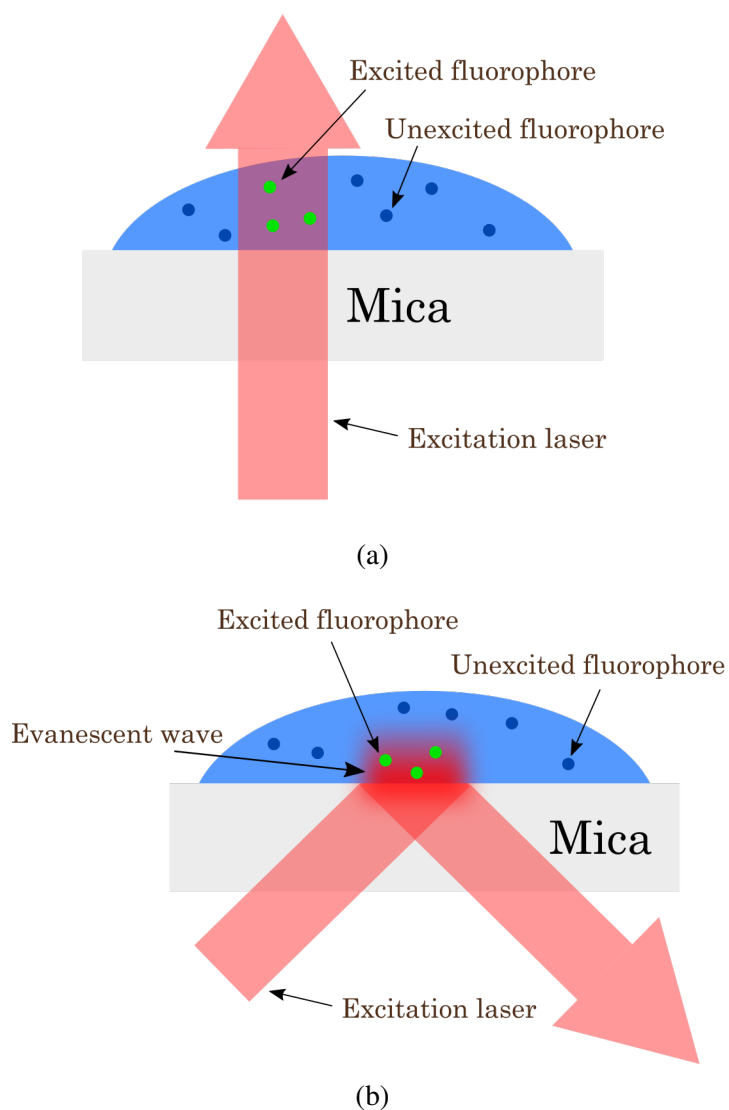


Fig. 2.17 Schematic of (a) epifluorescent and (b) TIRF microscopy set-ups. The green dots represent fluorophores in solution which are excited by the laser, and the dark blue dots fluorophores in their unexcited state.

of surface selectivity was desirable, so TIRF was used rather than HILO imaging. During imaging of all types, a bandpass emission filter may be used to remove any Rayleigh scattered light from the incident laser; as this filtering causes only light of the emitted wavelength to be recorded, a very high signal-to-noise ratio may be achieved.

2.13.3 Instrumentation

The experiments were performed on a bespoke instrument with Dr. Aleks Ponjavic in the group of Dr. Steve Lee, Department of Chemistry, University of Cambridge. A 100X, 1.49 numerical aperture oil immersion objective lens (Nikon, MRD01991) housed in the microscope (Eclipse Ti-U, Nikon) was used for excitation and acquisition. For TIRF imaging the laser was focused on the back focal plane of the objective off axis at an angle greater than the critical angle, by reflecting the laser off a dichroic mirror (Di01-R405/488/532/635-25x36, Semrock). Epifluorescence images were taken by focusing the laser on axis. The fluorescence emission was filtered by a bandpass emission filter (#67-031, Edmund Optics), and focused onto an EMCCD camera (Evolve 512 Delta, Photometrics).

Bleach recovery measurements were conducted by continuously recording images while reducing the laser filters for a short period of time to bleach a region of the dye smaller than the imaged area, then reducing the intensity back to normal imaging intensity and recording the recovery of the bleached region. Image processing was conducted in ImageJ^{97,98}.

2.13.4 Substrates

High quality mica discs (Attwater & Sons Ltd) of dimensions 100 μm thickness and 25 mm diameter were used for fluorescence microscopy. Initial work used thinner substrates but these were found to be overly flexible and experimentally hard to handle. The mica discs were cleaved using a scalpel, by lightly scoring the face of the disk then gently flexing it to remove a sheet from the top face. The freshly exposed surface was then UV-O₃ cleaned for 20 min as in the neutron substrate preparation.

During preliminary experiments, a glass slide was used to support a thin mica sheet. For the evanescent wave to propagate through to the mica - solution interface of interest from the glass interface a very thin layer of mica is required. This was experimentally challenging to support. Subsequent experiments then utilised a mica disc as the complete substrate, with the objective lens directly in contact (via immersion oil) with the bottom of the mica. The specific set up of the substrates used for imaging was altered as work progressed, and is explained in more detail in Section 6.3.

Chapter 3

Surfactant Adsorption at the Mica - Aqueous Solution Interface

This chapter presents a body of experimental data and analysis of the adsorption and desorption of surfactants at the mica - aqueous solution interface.

3.1 Adsorption of Anionics to Mica

3.1.1 Background

Electrostatic interactions frequently play a key role in determining adsorption behaviour, and studies into adsorption of charged surfactants onto oppositely charged surfaces are prevalent in the literature⁹⁹. It is perhaps expected that charged molecules adhere strongly to an oppositely charged substrate.

It has been found that adsorption of some anionic surfactants on surfaces of the same charge can in fact occur when certain cations are present, described as cation ‘bridging’. It was assumed that only divalent (or higher valency) ions could lead to this ‘bridging’ and that monovalent ions would not cause binding. Numerous examples of divalent ions bridging have now been reported, including on silica¹⁰⁰, mica¹⁰¹ and montmorillonite¹⁰². This form of binding has been suggested as an important mechanism of crude oil adsorption onto mineral surfaces¹⁰³.

Using neutron reflectivity measurements Griffin et al.¹⁰¹ found that the anionic surfactant bis(2-ethylhexyl) sulfosuccinate (AOT) did not adsorb to mica when present as the sodium salt even above the CMC. The calcium salt was however seen to adsorb at the CMC, forming a multilayered structure.

Mica is also commonly used to image DNA, typically using AFM, bound to the mica by added cations. A wide variety of multivalent cations have been used to enhance the mica - DNA binding^{104,105}. Redeker and Briscoe¹⁰⁶ also reported that calcium ions stabilised bacterial lipopolysaccharide layers on mica.

3.1.2 CsAOT on Mica

Experimental data in this section was collected by Dr. Lucy Griffin, Dr. Seung Yeon Lee, and Prof. Stuart Clarke prior to my joining the group, using the same methods described in this thesis. Analysis of the reflectivity data was my own work.

Results

In this work the surfactant AOT has been used to investigate selective ion binding behaviour. The structure of AOT is given in Figure 3.1; the key group involved in the bridging interaction is the sulfonate anion. This surfactant has been studied extensively in the literature¹⁰⁷, including for prior work into cation binding^{100,101,108}, in part because the counterion may be exchanged using the methods of Eastoe et al.⁷⁷

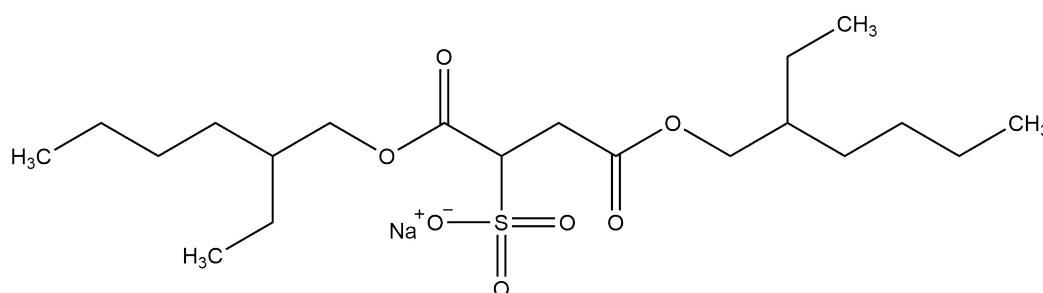


Fig. 3.1 Structure of NaAOT

Caesium exchanged AOT was prepared from sodium AOT according to the method of Eastoe et al.⁷⁷ and dried in a vacuum oven. Elemental analysis indicated greater than 99% ion exchange. Surface tension measurements were performed to confirm there was no evidence of a minimum, which would have suggested a surface-active impurity, and gave the

CMC as 2.8 mM. The caesium salt has been observed to form disc-like micelles at 1 wt% compared to oblate micelles for the sodium salt¹⁰⁹.

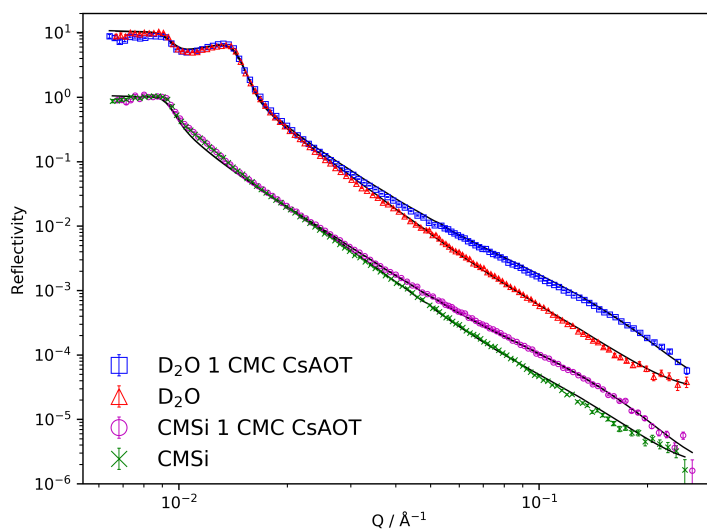
A range of values for the bulk density of NaAOT are reported^{78,110–112} between 1.14 and 1.16 g cm⁻³. The molecular weight of NaAOT (444 g mol⁻¹) and the density give a molecular volume of 636 - 648 Å³. Assuming a density of 1.15 g cm⁻³ the molecular volume of the NaAOT was calculated as 641 Å³. The volume of the Na and Cs ions are a very small fraction of the volumes of the overall species, and hence to a reasonable approximation the molecular volume of the CsAOT may be taken as 641 Å³. Using this molecular volume the SLD of the whole CsAOT group is $0.68 \times 10^{-6} \text{ \AA}^{-2}$.

It is also possible to attribute volumes to the head and tails separately, but the apportionment between the head and the tail is more subjective. By comparing volumes of simple hydrocarbons, molecular volumes may be roughly estimated for hydrocarbon 'building blocks'. In this way volumes of 56.2, 26.5, and 0 Å³ were calculated for CH₃, CH₂, and CH respectively¹¹³. Whilst a volume of 0 Å³ for CH is clearly non-physical, this is a reflection of a minimal increase in volume from an additional CH group. It is noted that these estimations will be affected by molecular packing in the compounds they are calculated from.

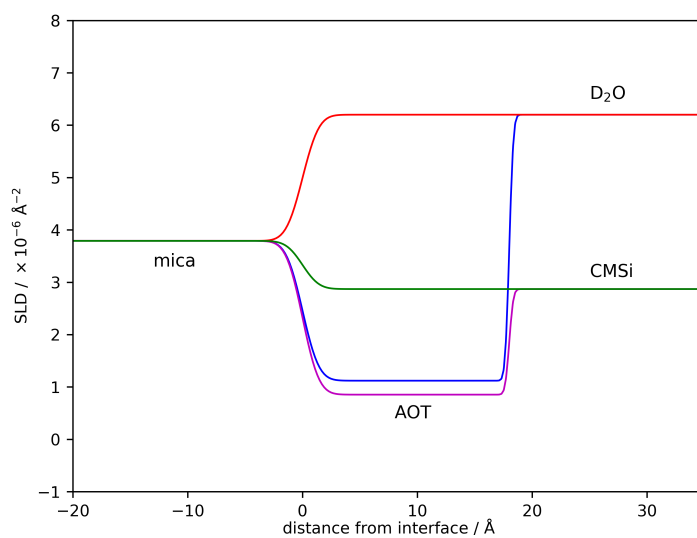
The AOT hydrocarbon tails consist of 10 CH₂, 4 CH₃, and 2 CH groups giving a total volume of 490 Å³ and hence an SLD of $-0.42 \times 10^{-6} \text{ \AA}^{-2}$. The headgroup can therefore be attributed a volume of 151 Å³ (641 less 490 Å³) yielding an SLD of $4.25 \times 10^{-6} \text{ \AA}^{-2}$. Others have made similar but slightly different apportionments¹¹². Different fitting models were applied to the experimental data, with both a single layer of uniform SLD and a three layer model of heads and tail regions being considered.

Figure 3.2 presents neutron reflection data from the mica substrate exposed to 1 CMC of CsAOT in two different water contrasts. It is evident from this figure that there are significant changes in reflection and hence it was concluded that there was significant adsorption of CsAOT at 1 CMC. This adsorption is somewhat surprising given that both the mica and the AOT molecule will be significantly negatively charged at this pH. This contrasts with previous neutron reflectometry measurements, carried out in the same way, of AOT in the presence of the monovalent ion sodium, where no adsorption was observed¹⁰¹.

Similar data collected at the higher concentration of 2 CMC gave an identical reflectivity profile. Neutron reflection data taken after washing the surface with copious amounts of water indicated that the AOT layer was lost and the scattering returned to that of the bare mica. On re-exposure to the 1 CMC CsAOT the reflectivity returned to that of the initial layer.



(a)



(b)

Fig. 3.2 (a) Reflectivity profiles for the mica surface in D_2O (red), water contrast matched to silicon (CMSi)(green), and with 1 CMC CsAOT in each of these contrasts (blue and magenta). D_2O contrasts are offset by a factor of 10. (b) SLD profiles of the fitted layer structure.

This reversibility is in marked contrast to the adsorption of a cationic surfactant reported previously⁵⁵.

Two related samples were also considered: a freshly cleaved substrate and the same substrate after it was dismantled, UV-O₃ cleaned for a period of 20 min, and then returned to the cell. The reflectivity profile of the subsequently adsorbed CsAOT layer was the same on the cleaned substrate as for the layer adsorbed to the freshly cleaved mica. This suggests that here the UV-O₃ treatment did not alter the surface in any way that affected adsorption behaviour. For the verification experiment, described later and referred to as ‘Experiment 2’, the mica substrate used had been UV-O₃ cleaned as in the normal case.

The reflectivity profile of an alternative mica surface, which had been UV-O₃ cleaned for 20 min, exposed to 1 CMC CsAOT was recorded at pH 4, pH 7 and pH 9. The same reflectivity profile was observed in each of these cases, as illustrated in Figure 3.3, indicating that the adsorbed layer structure is independent of pH over this pH range. This is in good agreement with the structural charge of mica where isomorphic substitution leads to the negative surface charge and pH dependence is not expected, in contrast to silanol groups on silica where protonation and deprotonation lead to surface charge. The anionic headgroup of the AOT is the conjugate base of a strong acid, and is therefore also not expected to show pH dependence over this range.

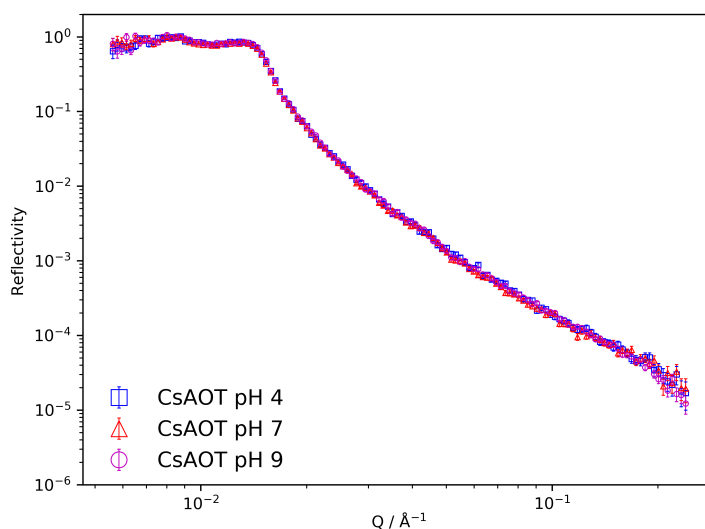


Fig. 3.3 Reflectivity profiles of mica exposed to 1 CMC CsAOT in D₂O at pH 4 (blue), pH 7 (red), and pH 9 (magenta).

The structural parameters of the CsAOT layer deduced from fitting the NR data are given in Table 3.2 below. In this model, the AOT is represented by a single layer with uniform scattering length density, as the most simple model consistent with the experimental data.

The extended chain length of a monolayer of AOT is reported to be $\sim 18 \text{ \AA}$ ^{110,114}, which is approximately the thickness of the single block fit to the data. The mica surface is highly charged and hydrophilic and so the AOT might be expected to adsorb 'head down'. This would leave a surface covered by hydrophobic tails which is unfavourable. Hence a second layer of AOT may adsorb to make the external surface hydrophilic however the overall layer thickness is significantly less than the 36 \AA expected for two AOT molecules end to end. The AOT molecules must therefore be significantly interdigitated and/or tilted at the surface and the layer might be described as a bilayer-like monolayer. The scattering length density indicates that there is little solvent in the layer and hence the layer is essentially all CsAOT. A schematic of the structure is shown in Figure 3.4.

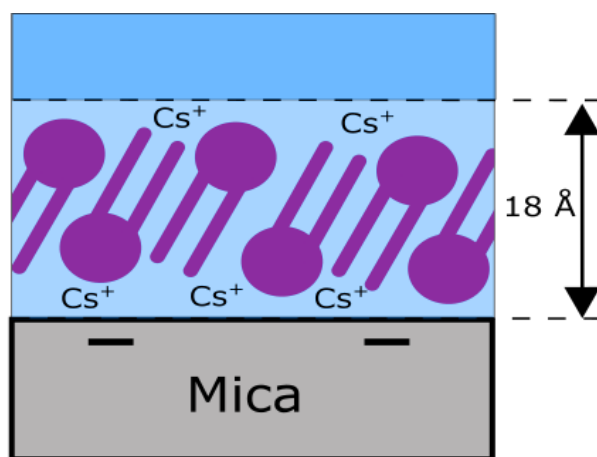


Fig. 3.4 Schematic of the fitted structure of CsAOT adsorbed to the mica surface from aqueous solution. A dense and interdigitated structure is shown, with a layer thickness approximately equal to the extended chain length.

More complex models, such as a three-layer model where the head and hydrocarbon tail regions are treated separately, were also considered but when the SLDs of the layers were fixed at the values calculated in Table 3.1 for the heads and tail layers (without mixing) no reasonable fit of the data could be achieved. This was true over the parameter space spanned by physically reasonable layer thickness, roughness, and hydration values, and was attributed to the enhanced contrast that arises when the heads and tails are separated. When the SLD of the head layer region was allowed to decrease with some alkane penetration into this region, the fits improved. It was concluded that there is significant mixing of head and tail components in the head group region, either from interdigitation or undulation in the adsorbed layer, consistent with the fitted layer thickness of close to the extended chain length. The head group layer thickness has been estimated as approximately 7.1 \AA .¹¹⁵ It was therefore concluded that some of the tails must overlap the opposite head group regions.

Table 3.1 Calculated SLDs for the CsAOT molecule.

| Component | Formula | Volume / \AA^3 | SLD / $\times 10^{-6} \text{\AA}^{-2}$ |
|-----------------|--|-------------------------|--|
| CsAOT | $\text{C}_{20}\text{H}_{37}\text{CsO}_7\text{S}$ | 641 | 0.68 |
| CsAOT headgroup | $\text{C}_4\text{H}_3\text{CsO}_7\text{S}$ | 151 | 4.25 |
| CsAOT tailgroup | $\text{C}_{16}\text{H}_{34}$ | 490 | -0.42 |

Table 3.2 Fitted parameters to CsAOT layer.

| Experiment | Thickness / \AA | Roughness \AA | SLD / $\times 10^{-6} \text{\AA}^{-2}$ | Hydration / % |
|------------|--------------------------|------------------------|--|---------------|
| 1 | 18 ± 2 | 1 ± 1 | 0.68 | 8 ± 2 |
| 2 | 18 ± 2 | 3 ± 2 | 0.68 | 10 ± 5 |

To verify the unexpected observation that CsAOT did adsorb to mica, in a separate later experiment with an alternate sample of CsAOT the adsorption was repeated. The reflectivity profile of the mica surface when exposed to 1 CMC CsAOT in this second experiment is shown in Figure 3.5, and the fitted parameters are included in Table 3.2. This data shows clear adsorption as with the previous experiment, and the layer structures are consistent within error margins, giving confidence that the CsAOT does indeed adsorb into a dense layer.

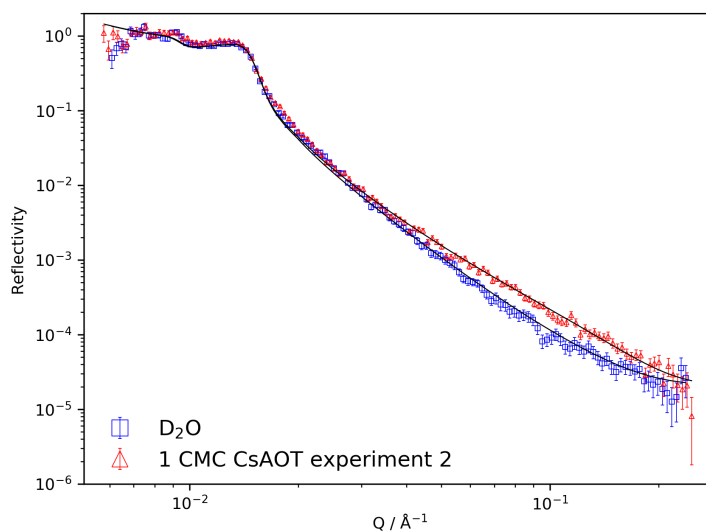


Fig. 3.5 Reflectivity profiles for bare mica in D_2O (red), and 1 CMC CsAOT in D_2O (blue) from Experiment 2.

Discussion

The area per surfactant molecule may be calculated from the thickness and volume fraction hydration of the fitted structures, and the molecular volume as calculated from the bulk density, by Equation 3.1.

$$APM = \frac{V_{molec}}{thickness \times (1 - hyd)} \quad (3.1)$$

From the fitted parameters, the area per molecule is calculated as approximately $40 \pm 7 \text{ \AA}^2$. A fully close packed alkyl chain has an area of approximately 19 \AA^2 ¹¹⁶, so two alkyl chains should take up at least 38 \AA^2 . AOT has branched alkyl chains so an even larger area might be expected. The calculated area per molecule is consistent with this estimate, suggesting close-packing of the tails in the layer. If a bilayer-like arrangement is assumed, the area per pair of molecules is calculated as $80 \pm 14 \text{ \AA}^2$. This is consistent with values found by others for AOT salts; Stocker et al.¹⁰⁸ found an area of $86 \pm 27 \text{ \AA}^2$ for NaAOT and $61 \pm 14 \text{ \AA}^2$ at the calcite - water interface, and Wang et al.¹⁰⁰ found an area of $70 \pm 5 \text{ \AA}^2$ for NaAOT at the water - silica interface.

It is not considered that many water molecules will be in the headgroup region, and this is supported by the low hydration determined experimentally by the fit to the data, on the order of one per headgroup. This is attributed to the low energies of hydration of the Cs^+ and the RSO_3^- head groups, meaning they can more easily lose water molecules and prefer to bind directly without intervening water, forming an inner sphere complex. Similar behaviour is expected for the Cs^+ ion on the mica. The hydration of Cs^+ is reported to be much lower than that of the other group IA elements, particularly Li^+ and Na^+ ¹¹⁷. The lack of hydration is also consistent with the results of Li et al.¹¹⁸, who found that caesium dodecyl sulfate adsorbed to the (positively charged) sapphire - aqueous solution interface with essentially no hydration.

Importantly, the adsorption of the anionic surfactant on the anionic surface in the presence of the monovalent Cs^+ cation cannot arise from the usual explanation of divalent (or multivalent) ion ‘bridging’ where the divalent ions form a bridge between the two negatively charged species, a concept found in several related areas from DNA binding^{119–122} to oil recovery^{36,37}. This is especially evident as previous work indicated that the monovalent sodium salt of AOT did not show any adsorption on mica or silica^{100,101}. The interesting

behaviour of the monovalent caesium ion reported here shows that it is not simply the valency of the ion that is significant.

The charge density of these ions seems to form part of the explanation; this also characterizes several aspects of solution behaviour, such as the Hofmeister series and the swelling or non-swelling nature of smectite clays. In outline, the interaction of these ions with water is strongly dependent on the charge density. If the ions are small and highly charged, water molecules are strongly bound to the ion and the complex is reluctant to bind to the mineral surface or the surfactant headgroup. However, if the ion has a lower charge density (such as Cs^+ compared to Na^+) then the interaction strength with water is significantly reduced. Hence, the loss of water is relatively easy, and the bare ion can bind more effectively to the mineral surface and to the AOT anionic groups. This hypothesis is consistent with the observation that for divalent ions the larger ions bind DNA less tightly to mica than smaller ions, making it harder to image with AFM¹⁰⁵. Through simulations Boek et al.⁶ found that potassium ions were much less able to hydrate fully in smectite interlayers compared to the more charge dense sodium and lithium cations.

As discussed previously, the divalent Ca^{2+} ion, which is strongly hydrated, was also found to mediate adsorption of AOT to mica¹⁰¹. The hydration effect might not fully explain which cations will cause bridging but may be an important consideration when comparing cations of the same valency.

3.1.3 AOT Adsorption from Mixed Salt Solutions

As reviewed in Section 3.1.2, the counterion to the AOT anion may be exchanged using the methods of Eastoe et al.⁷⁷ Previous studies into cation binding have utilised the pure AOT salt of the cation under investigation. In commercially relevant systems however, there will often be multiple cations competing for the surface and organic species. Ion exchange of AOT is also a non-trivial process and adds complexity, as well as the possibility of introducing surface active hydrolysis products of the AOT. In this section the readily available sodium AOT salt was utilised at a fixed concentration and other cations of interest were added into solution. In this way sodium, potassium, calcium, and magnesium were studied.

For fitting of the neutron reflectivity data the SLDs of the different AOT salts were calculated based on bulk densities. These are given in Table 3.3. It is noted that the structures fitted to adsorbed layers in this section are based on fitting of only one contrast in each case,

Table 3.3 Scattering Length Densities of AOT salts.

| Material | SLD / $\times 10^{-6} \text{ \AA}^{-2}$ |
|----------------------|---|
| KAOT | 0.65 [†] |
| Ca(AOT) ₂ | 0.63 [†] |
| Mg(AOT) ₂ | 0.64 [†] |

[†] The SLD values for the respective AOT salts are computed based on a molecular volume of 641 \AA^3 for NaAOT¹²³, as calculated from the bulk density, and the assumption that the metal cation takes up a small enough volume that cation exchange does not change the overall volume. This assumption was extended to divalent ions where there are two AOT anions per cation.

Table 3.4 CMCs of relevant AOT salts.

| AOT salt | CMC / mM |
|----------------------|---------------------|
| NaAOT | 2.5 ¹²⁴ |
| KAOT | 2.8 ¹²⁵ |
| Ca(AOT) ₂ | 0.5 ¹¹⁴ |
| Mg(AOT) ₂ | 1.25 ¹²⁶ |

and are not necessarily a unique fit to the data. However, the primary conclusions here do not depend on the specifics of the layer structures.

For adsorption measurements the concentration of AOT⁻ was fixed at the critical micelle concentration (CMC) of the sodium salt of AOT, 2.5 mM¹²⁴. To allow a comparison between added cations, the initial concentrations of non-sodium inorganic salts added to the AOT solution was matched to the CMC of the pure AOT salt of that cation. For example the added [Ca²⁺] was 0.5 mM as the CMC of Ca(AOT)₂ is 0.5 mM. The CMCs of the different AOT salts of the cations used are given in Table 3.4.

Ionic strength, as defined by $I = \frac{1}{2} \sum_i c_i z_i^2$ where c_i and z_i are the concentration and charge of ion i respectively, can affect adsorption characteristics, particularly for ionic surfactants. It was therefore desirable to maintain a consistent ionic strength throughout, to give certainty that any effects shown were due to the nature of the cations present and not an ionic strength change. Using NaAOT at 2.5 mM and adding MgCl₂ up to the CMC of Mg(AOT)₂ resulted in an ionic strength of 6.25 mM, so this ionic strength was used consistently. Ionic strength was controlled where required with the addition of NaCl.

Table 3.5 Effective concentrations of salts used in the resulting solutions.

| Ion under examination | NaAOT / mM | Chloride salt of ion [†] / mM | NaCl / mM |
|-------------------------|------------|--|-----------|
| Na | 2.5 | N/A | 3.75 |
| K | 2.5 | 2.8 | 0.95 |
| Ca | 2.5 | 0.5 | 2.25 |
| Mg | 2.5 | 1.25 | 0 |
| reduced Ca [‡] | 2.5 | 0.05 | 3.6 |

[†] The relevant chloride salt, so KCl for K under investigation, and MgCl₂ for Mg under investigation. For Na this is neglected as NaCl is already present. [‡] ‘Reduced Ca’ refers to the experiment described in Section 3.1.3, where the concentration of Ca²⁺ was reduced below the level of the CMC of Ca(AOT)₂ but ionic strength was maintained at 6.25 mM.

Table 3.6 Resultant concentrations of the ions present.

| Ion under examination | Ion of interest / mM | Na ⁺ / mM | Cl ⁻ / mM | AOT ⁻ / mM |
|-------------------------|----------------------|----------------------|----------------------|-----------------------|
| Na | 6.25 | N/A | 3.75 | 2.5 |
| K | 2.8 | 3.45 | 3.75 | 2.5 |
| Ca | 0.5 | 4.75 | 3.25 | 2.5 |
| Mg | 1.25 | 2.5 | 2.5 | 2.5 |
| reduced Ca [‡] | 0.05 | 6.1 | 3.7 | 2.5 |

[‡] Defined as in Table 3.5

Solutions of reagents were prepared at higher concentrations, but all well below the respective solubility limits, and mixed or diluted using an HPLC pump to give the desired concentrations in the cell. Solubilities of all resultant solutions were checked prior to the experiment, and no precipitation or turbidity was visible in any case. All mica substrates were characterised in three water contrasts prior to surfactant exposure. Table 3.5 gives the effective concentrations of the various salts in the solutions tested after stock solutions were diluted together, and Table 3.6 gives the concentrations of the ions in solution.

NaAOT and NaAOT with Elevated Ionic Strength

NaAOT at the CMC (2.5 mM) was introduced to the mica surface and the sample remeasured. No change in reflectivity was observed compared to the bare surface in D₂O indicating no adsorption, which is consistent with prior observations¹⁰¹. NaAOT with added NaCl, to raise

the ionic strength to 6.25 mM, was then introduced and again no adsorption was observed. These results are shown in Figure 3.6.

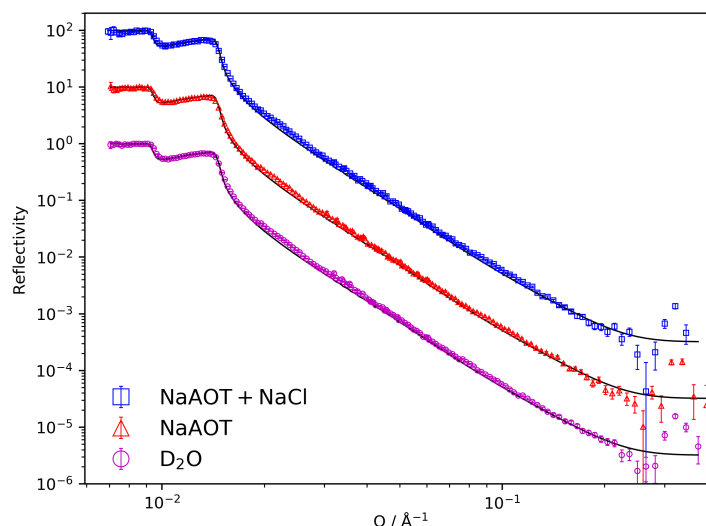


Fig. 3.6 Reflectivity profiles of mica exposed to NaAOT with ionic strength raised to 6.25 mM by NaCl addition (blue, offset by factor of 100), NaAOT (red, offset by factor 10), and D₂O (magenta). The shown fit is identical in all cases, and fitted to the bare mica surface in D₂O.

In certain later experiments when the mica surface was exposed to NaAOT a small change in reflectivity profile was observed. From prior fitting experience this change corresponds to some diffuse hydrated layer, and it was found that when the cell solution was exchanged back to pure water the profile returned to that of the bare surface. These changes are shown in Figure 3.7. It was established that only older batches of NaAOT showed this behaviour, leading to the conclusion that the adsorption was due to a contaminant, most likely a hydrolysis or break down product. Purification protocols for AOT have been developed in the literature¹²⁴. Here fresh batches of AOT were used for each experiment, and for each NaAOT solution it was verified that no adsorption of any species occurred.

Different mica samples were used for each of the three additional cations investigated to prevent any uncontrolled effects of salt history on the surface behaviour. The lack of any adsorption of NaAOT at raised ionic strength was verified on every mica crystal used, partly to check for consistency between mica samples, and also to check the AOT solutions for surface active impurities as discussed above.

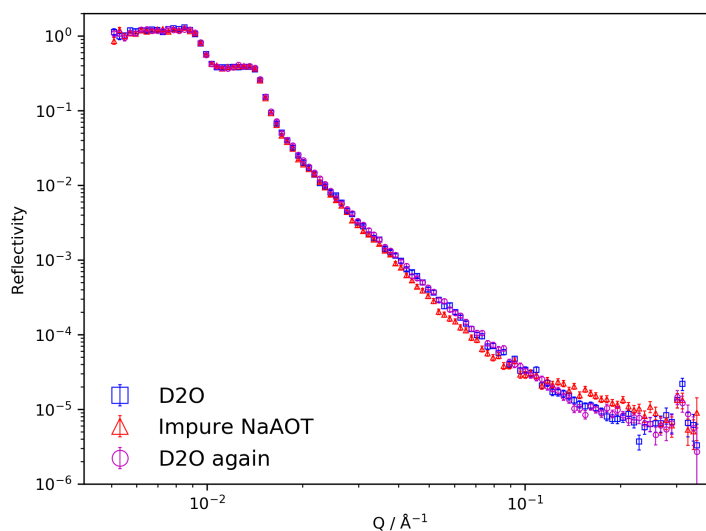


Fig. 3.7 Reflectivity profiles from a bare mica surface in D_2O , when exposed to an impure batch of NaAOT, and when the solution was exchanged back to D_2O .

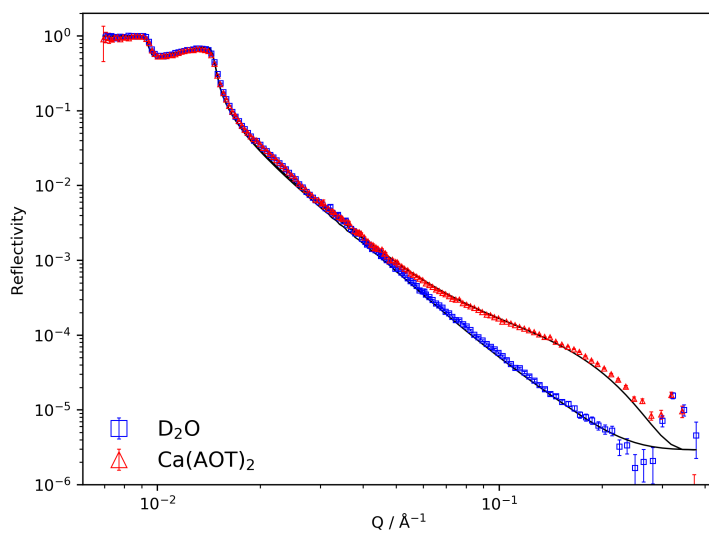
Table 3.7 Fitted parameters for Ca^{2+} bound structure.

| Layer | SLD / $\times 10^{-6} \text{ \AA}^{-2}$ | Thickness / \AA | Roughness / \AA | Hydration / % |
|-------------|---|--------------------------|--------------------------|---------------|
| Water | 6.30 | 8 ± 2 | 1 ± 1 | - |
| $Ca(AOT)_2$ | 0.63 | 18 ± 1 | 1 ± 1 | 0 ± 3 |

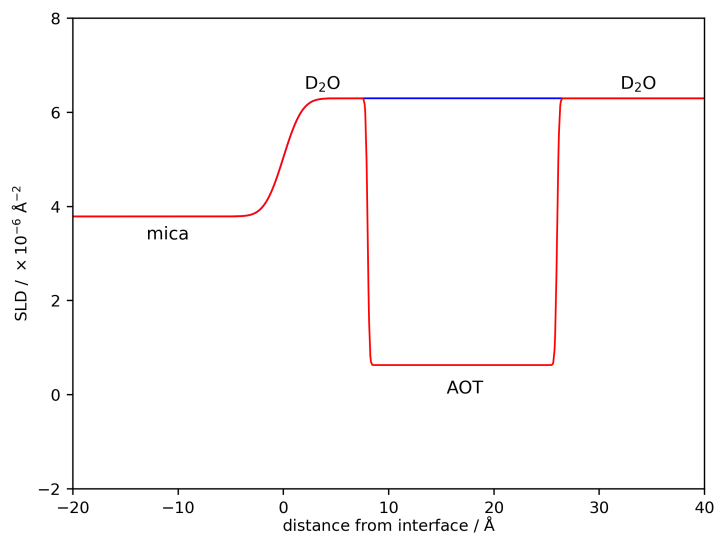
Calcium Bridging

When a solution of NaAOT at 2.5 mM with added $CaCl_2$ at 0.5 mM and NaCl at 2.25 mM (to fix the ionic strength at 6.25 mM) was introduced to the mica surface a clear change in reflectivity profile was observed, as given in Figure 3.8, indicating adsorption of some material. A single layer model could not adequately fit the data, but it was found that a structure consisting of a water layer between the mica surface and an unhydrated surfactant layer closely reproduced the observed data. Reflectivity data with calculated fits and the associated SLD profile are shown in Figure 3.8, and the fitted parameters are given in Table 3.7.

As it has been shown that the Na^+ counter ion of the AOT^- does not lead to a bridging interaction, adsorbed species have been referred to as the AOT salt of the bridging counterion in question. For example the adsorbed species from a solution of NaAOT with added $CaCl_2$ is referred to as $Ca(AOT)_2$.



(a)



(b)

Fig. 3.8 (a) Reflectivity profiles for the mica surface in D_2O (blue) and when $\text{Ca}(\text{AOT})_2$ had adsorbed (red). (b) SLD profile of the fitted layer structure.

Table 3.8 Fitted parameters for the Mg^{2+} bound structure.

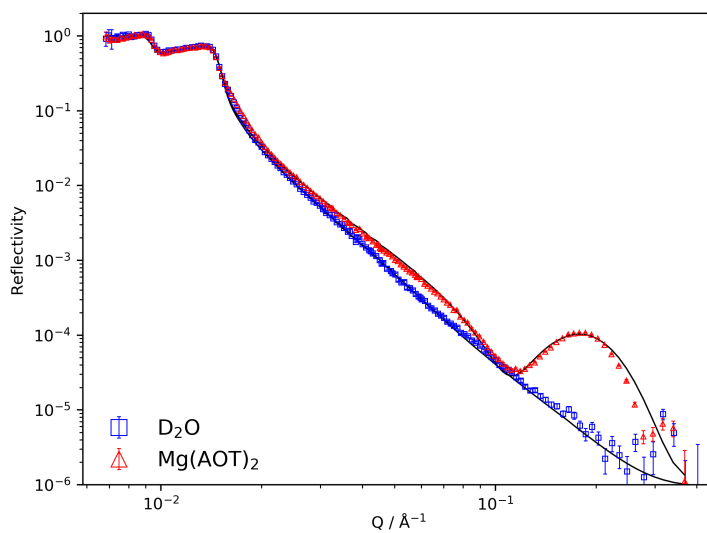
| Layer | SLD / $\times 10^{-6} \text{ \AA}^{-2}$ | Thickness / \AA | Roughness / \AA | Hydration / % |
|---------------------------|---|---------------------------|---------------------------|---------------|
| Water | 6.30 | 6 ± 1 | 1 ± 1 | - |
| $\text{Mg}(\text{AOT})_2$ | 0.64 | 16 ± 1 | 1 ± 1 | 0 ± 5 |
| Water | 6.30 | 13 ± 1 | 1 ± 1 | - |
| $\text{Mg}(\text{AOT})_2$ | 0.64 | 16 ± 1 | 1 ± 1 | 0 ± 5 |

Magnesium Bridging

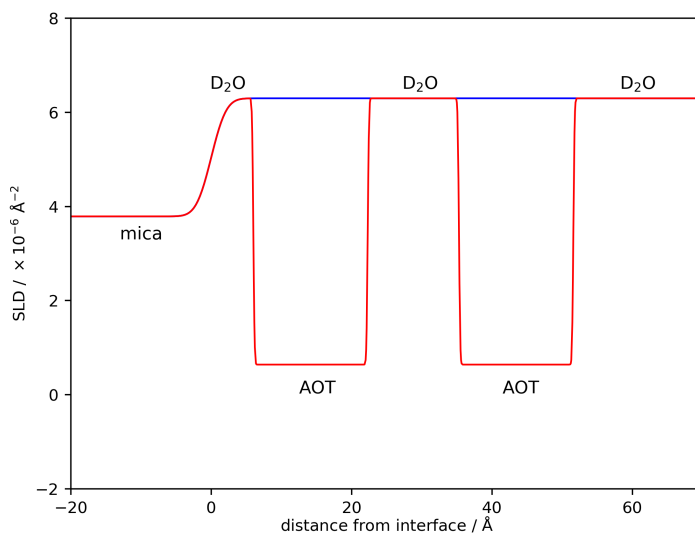
A fresh mica surface was characterised as before in three water contrasts. NaAOT at 2.5 mM with MgCl_2 at 1.25 mM was introduced to the cell and the reflectivity profile measured. Again a large change was visible, indicating adsorption of an organic layer as shown in Figure 3.9a.

Various models were considered during data fitting, and the least complex model which could replicate the experimental results satisfactorily was found to be a four layer fit consisting of a water layer adjacent to the mica, followed by two surfactant layers with an intervening water layer. In this fit the thicknesses of the two surfactant layers were constrained to be the same. Parameters fitted to the data are given in Table 3.8.

After layer removal, discussed in more detail later, introducing the same solution back to the cell resulted in a very similar reflectivity profile to the initial layer, showing repeatability and reversibility of this adsorption process. The reflectivity profiles from the initially formed layer and after desorption then re-adsorption are shown in Figure 3.10.



(a)



(b)

Fig. 3.9 (a) Reflectivity profiles for the mica surface in D_2O (blue) and when $\text{Mg}(\text{AOT})_2$ had adsorbed (red). (b) SLD profile of the fitted layer structure.

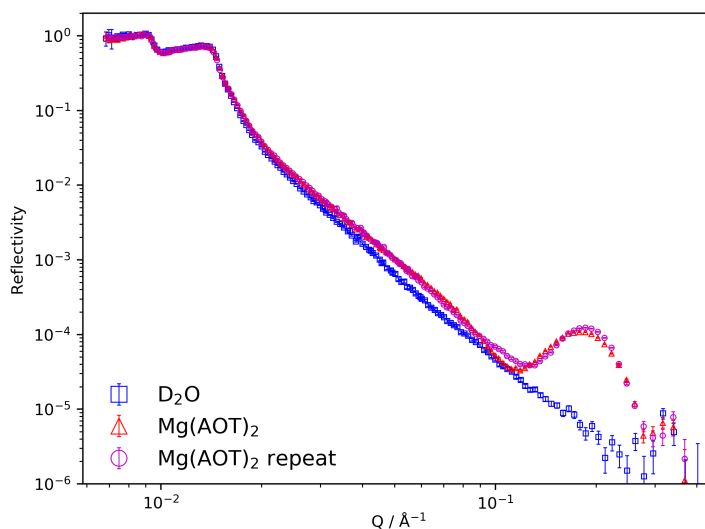


Fig. 3.10 Reflectivity data of the initial $\text{Mg}(\text{AOT})_2$ layer (red) and after re-adsorption (magenta), revealing a very similar profile. Bare mica in D_2O is shown for comparison (blue).

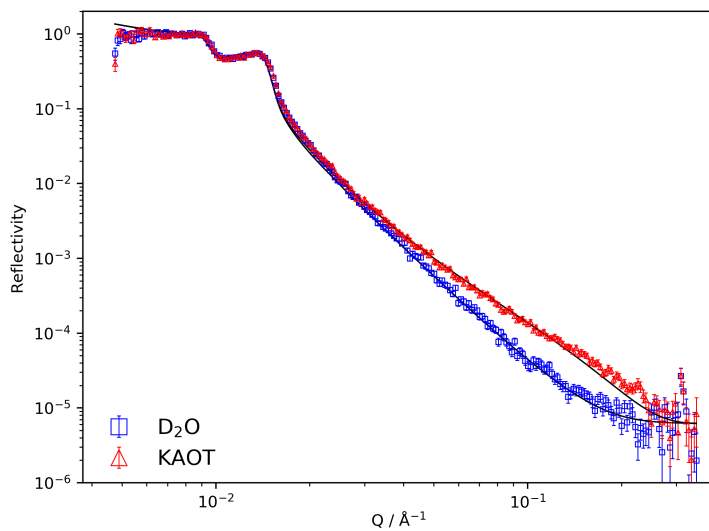
Table 3.9 Fitted parameters for the K^+ bound structure.

| Layer | SLD / $\times 10^{-6} \text{ \AA}^{-2}$ | Thickness / \AA | Roughness / \AA | Hydration / % |
|-------|---|--------------------------|--------------------------|---------------|
| KAOT | 0.65 | 18 ± 2 | 1 ± 1 | 0 ± 3 |

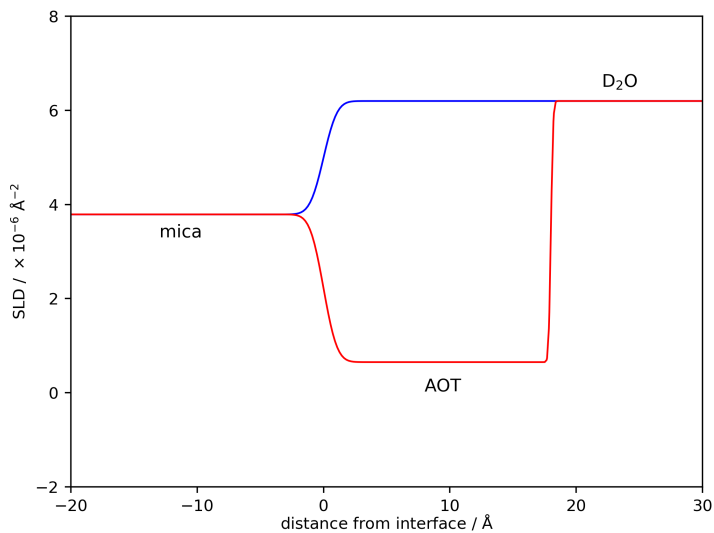
Potassium Bridging

A further new mica surface was again fully characterised. NaAOT at 2.5 mM, with KCl at 2.8 mM and NaCl at 0.95 mM was introduced to the cell. The measured reflectivity is shown in Figure 3.11a and again layer formation was seen, though a different adsorbate structure is evident from the reflectivity profile when compared to the other cations.

The parameters fitted to the layer are given in Table 3.9. The fit could be improved moderately by adding a water layer between the mica and AOT with a thickness of 2-3 \AA , although this is less than the roughness associated with the mica surface and so it was not deemed a reasonable parameter to include.



(a)



(b)

Fig. 3.11 (a) Reflectivity profiles for the mica surface in D_2O (blue) and when KAOT had adsorbed (red). (b) SLD profile of the fitted layer structure.

Concentration Dependence of Calcium Bridging

The concentration range over which bridging occurred in the calcium system was probed. The same mica crystal which had been used for $\text{Ca}(\text{AOT})_2$ adsorption was utilised, after layer desorption and exchange of the cell into D_2O . Using a concentration of Ca^{2+} reduced to 0.05 mM, 10% of the initial value used, while maintaining the same ionic strength and concentration of AOT^- ($[\text{CaCl}_2] = 0.05$ mM, $[\text{NaAOT}] = 2.5$ mM, $[\text{NaCl}] = 3.6$ mM) resulted in an essentially identical reflectivity profile as at the initial calcium concentration for layer adsorption. The reflectivity profiles from the initial calcium bridged layer, and the structure with reduced calcium concentration, are shown in Figure 3.12. This shows that the same structure adsorbs even at this much reduced concentration of the bridging ion. Concentrations of Ca^{2+} below 0.05 mM were not tested.

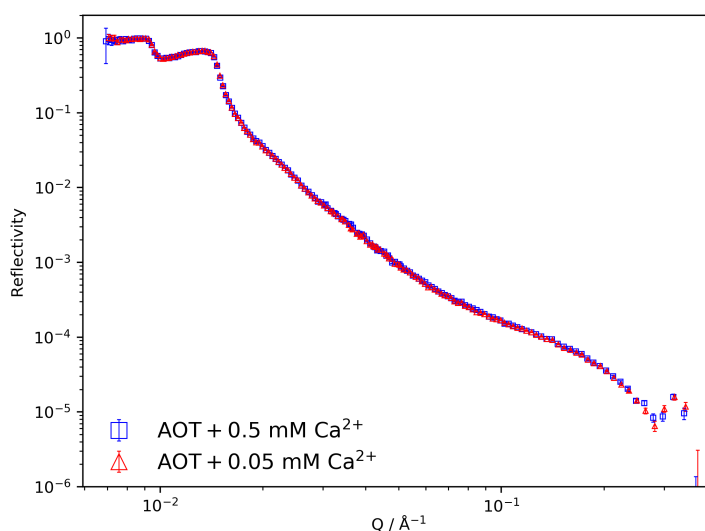


Fig. 3.12 Reflectivity profiles from the mica exposed to the initial solution concentration of Ca^{2+} (blue) and identical profile produced when $[\text{Ca}^{2+}]$ was reduced to 0.05 mM, 10% of the initial value (red). The same structure is clearly present in both cases.

Layer Removal

To probe the stability and strength of binding of the adsorbed layers, the desorption behaviour of both the calcium and magnesium bridged structures was studied. In both cases the cell solution from which bridging was observed was directly exchanged to a solution of the same ionic strength (controlled with NaCl) and same concentration of calcium or magnesium

respectively, but without any AOT. In both cases the reflectivity profile returned to that of the bare mica substrate, as shown in Figure 3.13, revealing complete desorption of any organic from the surface.

For the potassium bridged structure the equivalent test was not conducted, but the solution of AOT with KCl was exchanged directly into D₂O. This also resulted in complete desorption of the organic layer, with the reflectivity profile returning exactly to that of the bare surface in D₂O.

Re-Adsorption Behaviour of Potassium Bridged Layer

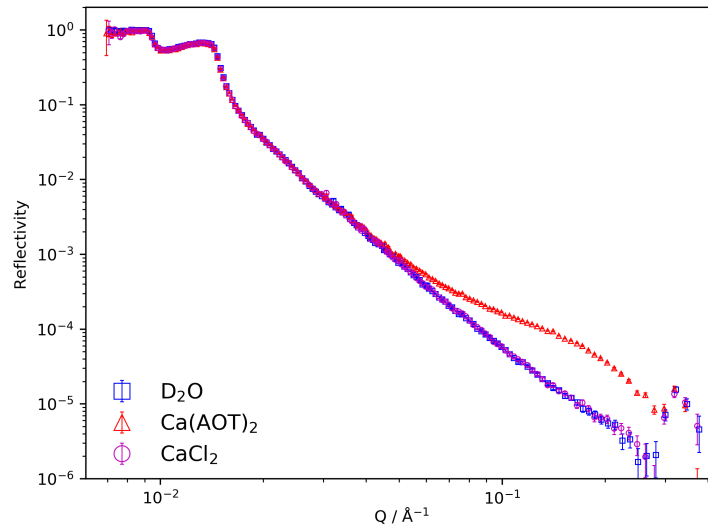
As previously mentioned, the potassium bridged layer was seen to desorb completely from the surface when the bulk solution was exchanged into D₂O. The solution was further exchanged into a solution of NaAOT at the CMC (2.5 mM), with no added potassium. From this solution no adsorption was seen. This was despite adsorption being observed on the same mica surface previously when AOT and K were both present in solution, and there having been no alternate cations present between these conditions.

Discussion

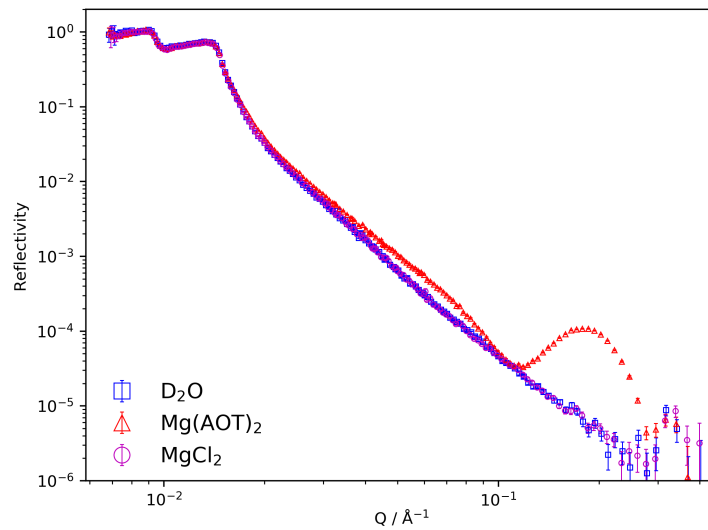
A summary of the adsorption results with different added cations is shown in Figure 3.14.

This study builds on previous investigations into the question of which cations are capable of binding anionic molecules to an anionic surface. It was postulated that as Group 1 is ascended and the charge density increases, there will be some break point at which ions no longer cause binding. This was attributed to the greater enthalpy cost of strongly hydrated ions losing solvating water molecules, in order for the ions to bind to the substrate. By showing that K⁺ also causes cation mediated binding whereas Na⁺ does not, even with increased [Na⁺] relative to the pure NaAOT salt, the limiting point in Group 1 at which this bridging occurs has been localised to between K⁺ and Na⁺ for this organic - mineral system.

In all the fitted structures the surfactant layer thickness is of the order of the measured monolayer thickness of $\sim 18 \text{ \AA}$ ^{110,124}. As discussed in Section 3.1.2, the mica surface is hydrophilic, and it would be energetically unfavourable for the surfactant molecules to order such that the hydrophobic tails are all oriented towards either the mica or to water. It is therefore suggested that while the structures are essentially monolayers based on the thickness parameters, there will be significant disorder and different orientation of the molecules to



(a)



(b)

Fig. 3.13 Data showing the complete desorption of bound layer structures when the solution was exchanged to a solution of the same ionic strength and binding ion concentration but with no AOT. In (a) calcium binding is shown and (b) magnesium binding.

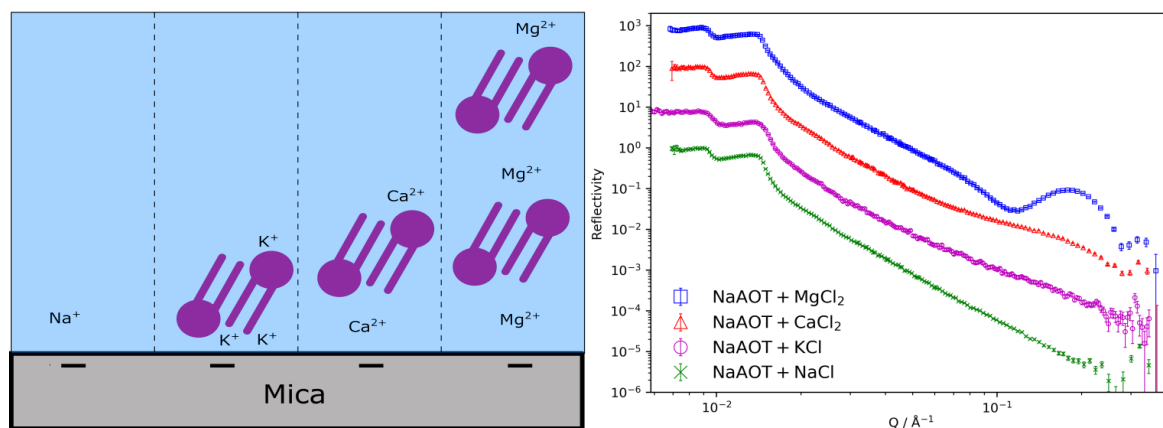


Fig. 3.14 Graphical summary of the adsorption behaviour and structures of AOT with different added cations. A summary of the reflectivity data is shown to the right.

allow head groups to be present on both sides of each unhydrated surfactant layer. More complex fitting models consisting of separated surfactant head and tail regions could present slightly thicker adsorbed layers, with solvated head groups more closely matching the solvent SLD, but the simplest model consistent with the experimental data was adopted. The added ionic strength will lead to a reduced Debye length from greater screening between charged species, and could therefore influence closer packing than has been seen in some pure salt solutions, where bilayer thicknesses have been observed in the range 31 - 38 Å for the calcium system^{100,101}. Dense packing is also consistent with the unhydrated nature of the layer from the fits to the data.

In the studied regime multilayering was seen only from Mg^{2+} , and not from Ca^{2+} or K^+ . The phenomenon of multilayering at the air - solution interface has been extensively reviewed by Thomas and Penfold¹²⁷, and using their nomenclature the structure formed in the added magnesium case may be referred to as an S_2 structure. For the mica - solution interface the hydrophilic nature of the surface will favour a more bilayer-like first adsorbed structure in contrast to the air - water interface, but behaviour of subsequent layers might be expected to be similar in the two cases. It has been shown previously that $\text{Ca}(\text{AOT})_2$ can form multilayered structures on mica at the CMC (0.5 mM) with up to four bilayers and intervening water, and significantly more layers at twice the CMC¹⁰¹. In the system studied here the Ca^{2+} concentration is the same as in that work, but the $[\text{AOT}^-]$ is higher in this case, at 2.5 mM.

The presence of additional adsorbed layers for magnesium addition may be due to the ratio between cation: $[\text{AOT}^-]$ being approximately that required for charge neutrality at 1.25

mM:2.5 mM (as would be present in the pure $\text{Mg}(\text{AOT})_2$ salt), when compared to 0.5 mM:2.5 mM for the added calcium case in this work. If this ratio is key in determining multilayer formation then it might be expected that further increasing the calcium concentration to 1.25 mM might induce this behaviour, subject to the constraints of solubility. No multilayering is observed in the added potassium case despite the relative concentrations of potassium and $[\text{AOT}^-]$ being close to charge neutrality (2.8 mM : 2.5 mM), but it may be the case that multivalent ions are a necessary condition for multilayer formation, as suggested by others^{128,129}. Multilayering is clearly a process sensitive to multiple factors, and the conclusions here are focussed on the presence or absence of adsorption rather than the specifics of the structures.

Molecular dynamics simulations by Kobayashi et al.¹³⁰ suggested that Na^+ and Mg^{2+} would bind organic acids to mica via a water mediated interaction, whereas K^+ and Ca^{2+} would bridge directly. These results are not fully consistent with the findings of this work in that a water layer was required to satisfactorily fit the structure of the Ca^{2+} bound layer, and even at elevated concentrations Na^+ was never found to bridge. The simulations did however propose that the Na^+ binding strength was the weakest of the ions investigated.

The sulfonate head group of AOT is also likely to differ in behaviour to a carboxylate anionic head group, as discussed in more detail later. Consistent with the simulation, it was seen that the K^+ layer appeared to have little, if any, of a water layer between the mica and surfactant. A suggestion for the mechanism of cation bridging is one in which the surface charge sites, cations, and anionic head group must all lose some degree of hydration to come together and bridge. The multivalent cations will be more strongly solvated by the water molecules, and if only partial loss of hydration of the cation occurs on bridging then a water/ion layer would be expected. The thicknesses fitted to the water layers for the added magnesium and calcium case are of the order of a few water molecules, which is consistent with this model.

At the lowest Ca^{2+} concentration experimentally tested (0.05 mM) the ratio of $\text{Na}^+:\text{Ca}^{2+}$ is greater than 100:1 and yet binding of a layer to the mica is still observed. Clearly the relative affinity of the Ca^{2+} for both the mica and the AOT^- ion is so great that it can successfully out-compete the Na^+ . There have been suggestions that multivalent ions can adsorb to mica in sufficient quantities to over-compensate the surface charge and lead to a charge inversion¹³¹, however de Poel et al.¹³² showed that exchange of mica with CaCl_2 followed by pure water did not lead to over-exchange of Ca^{2+} onto the surface. Without over-exchange it seems unlikely that AOT^- would adsorb in the absence of additional bridging ions in solution, even after exposure of the mica surface to Ca^{2+} .

This hypothesis is consistent with the observations for potassium ions, as described in Section 3.1.3. The data shows that NaAOT will not adsorb even to a mica surface which had previously had a potassium bridged structure, unless there are potassium ions also in solution.

At the concentrations tested, sodium ions were never seen to out-compete the calcium ions and prevent bridging of AOT. At some relative concentrations of sodium and calcium set by the binding constants, solubility constraints aside, the sodium must out-compete the calcium. A three dimensional phase space consisting of sodium, calcium, and AOT concentrations can be visualised, with a region where bridging will occur. Collated results of the work described here and the results of Griffin et al.¹⁰¹ are shown in Figure 3.15. A dividing plane between the bridging and non-bridging points may be visualised. The position of this division may also be influenced by the CMC of the compositions, as adsorption of anionics to mica below the CMC has not been observed.

It was earlier shown that the proffered explanation of oil release by exchange of divalent 'bridging' ions for monovalent ions incapable of bridging is not a full description, with the observation of monovalent Cs^+ binding organic anions to mica. Here it was shown that Cs^+ is not unique in this ability as a monovalent ion but in fact the K^+ ion shows the same effect. This is industrially important as it provides further evidence that the specific cations present, rather than the total salinity or monovalent and divalent concentrations, are important for water flooding.

Secondary water-flooding generally occurs using either sea-water or water from aquifers; in both cases potassium can be present in concentrations at least equivalent to the calcium concentration¹³³. If efforts are made to remove only the divalent ions before enhanced recovery then cations which can still cause organic-mineral binding will remain present. It was also shown in this work that even at cation ratios heavily biased to the non-binding Na^+ cation, small concentrations of binding ion may dominate and facilitate adsorption. This could further inform the design of controlled salinity water for flooding. This is consistent with molecular dynamics simulations which suggested that cation bridging to montmorillonite would occur independent of salt concentration due to unhydrated cations in the Stern layer¹³⁴.

Two of the mechanisms commonly offered to explain low salinity enhanced oil recovery are multivalent ion exchange and double layer expansion. This study has shown that for the system of the AOT anion bridged to mica by either calcium or magnesium ions, neither of these mechanisms is required for organic release. Layers bridged by either of these ions showed complete desorption when both the ionic strength and bridging ion concentration

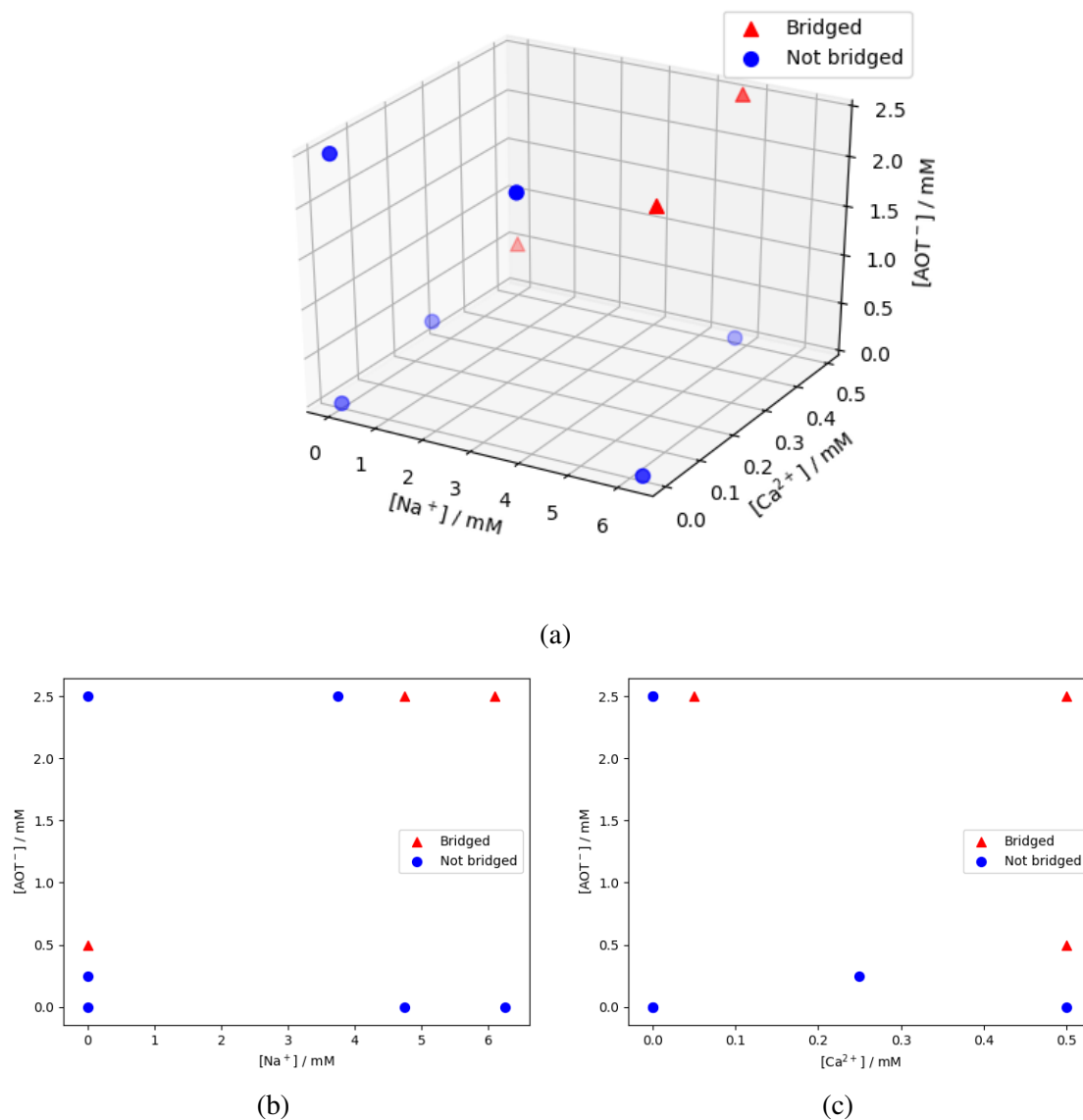


Fig. 3.15 (a) 3D phase plot showing concentrations of sodium, potassium, and AOT which have been tested on mica. Sets of conditions which were observed to lead to adsorption are shown as red triangles, and non-adsorbing as blue circles. For clarity, projections onto the 'x-z' and 'y-z' planes are shown in (b) and (c) respectively.

were maintained at a constant level but the organic component was removed from solution, suggesting that the bridged organic is only weakly bound and in rapid equilibrium with the species in the bulk. It is sufficient to simply remove this free organic to facilitate layer desorption. As the calcium to sodium ratio is well above the lowest ratio at which binding was still observed, it is not the case that the increased sodium concentration out-competes the calcium for either the AOT^- or the mica surface.

3.1.4 Carboxylate Adsorption

The sulfonate head group of the AOT^- anion investigated earlier is very strongly acidic; the pK_a of the structurally similar methanesulfonic acid is approximately -1.9 ¹³⁵. The pK_a can be related to the strength of binding between the anion and an associated cation. As the AOT^- anion shows such stability, the binding to any cation (and therefore the cation mediated binding to the surface) may be weaker than for an anion with a more positive pK_a . Organic carboxylic acids, which are commonly present in crude oils¹³⁶, have significantly higher pK_a values (e.g. for acetic acid $\text{pK}_a = 4.8$ ¹³⁵). It may be the case that if these higher pK_a groups adsorb in a cation mediated fashion to the anionic surface, they will adsorb in a less reversible fashion due to the stronger binding between anionic head group and cation. This would be more comparable to the observed adsorption behaviour of cationic molecules to mica⁵⁵, which were seen to persist even when the bulk organic was removed.

Protonated acids have very low solubilities in water, particularly for longer alkyl chain lengths¹³⁷. The sodium salts show greatly increased solubilities. For this study the 'medium' chain length sodium octanoate and sodium decanoate were chosen. These were selected for the balance of a sufficiently long alkyl chain which should be easily resolvable in neutron reflectivity, and give accessible CMC values, but not so long as to result in sparing solubility. The structures are given in Figure 3.16. The CMCs are 300 mM for sodium octanoate and 86 mM for sodium decanoate¹³⁸.

Literature bulk densities for these sodium carboxylates could not be found, but values for the bulk density of both the corresponding acids are available. Exchange of the proton for the sodium cation might have a small effect on the molecular volume which can be accounted for. For sodium hexanoate a density of 0.97 g cm^{-3} has been reported¹³⁹, and 0.93 g cm^{-3} for hexanoic acid (manufacturer). Based on these values the change in molecular volume on exchange from the protonated acid to the sodium salt was calculated as 28 \AA^3 . Using this value and bulk densities of 0.91 g cm^{-3} and 0.89 g cm^{-3} for octanoic acid and decanoic acid

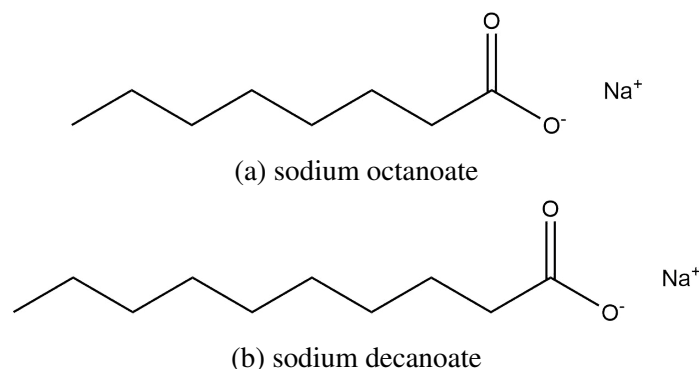


Fig. 3.16 Structures of the sodium acid salts used in this adsorption study.

respectively the SLDs of sodium octanoate and sodium decanoate were calculated as 0.42×10^{-6} and $0.65 \times 10^{-6} \text{ \AA}^{-2}$ approximately.

The pKa value for the two acids is approximately 4.8¹³⁷. The pH of the solutions used during the experiment were in the range 7.2 - 7.8, indicating that essentially all of the dissolved species will be present as the carboxylate anions. From the definitions of pH and pKa for an acid AH and its conjugate base A^- , the relative concentrations are related by $\log_{10} \frac{[A^-]}{[AH]} = \text{pH} - \text{pKa}$. Assuming a pH of 7.5 then from this relation it can be calculated that approximately 99.8% of the species will be present as the carboxylate ion.

Sodium Carboxylate Adsorption

For both acids, after characterisation of the bare mica surface, the concentration was increased through the series 0.1, 0.5, and 1 CMC (for the CMC of each acid respectively). In both cases no change in reflectivity profile was seen for concentrations below the CMC but at the CMC adsorption was seen, with slightly different structures evident. On exchange of the bulk solution back to pure water, the reflectivity profile returned to that of the bare mica, showing reversibility of binding as was seen for all the anionic surfactants which have been found to adsorb. Reintroducing the sodium carboxylate solution resulted in identical profiles to those of the initial adsorbed layers.

From these unexpected observations it was concluded that the sodium salts of the carboxylate ions do adsorb to mica, possibly through a bridging interaction of the sodium ion.

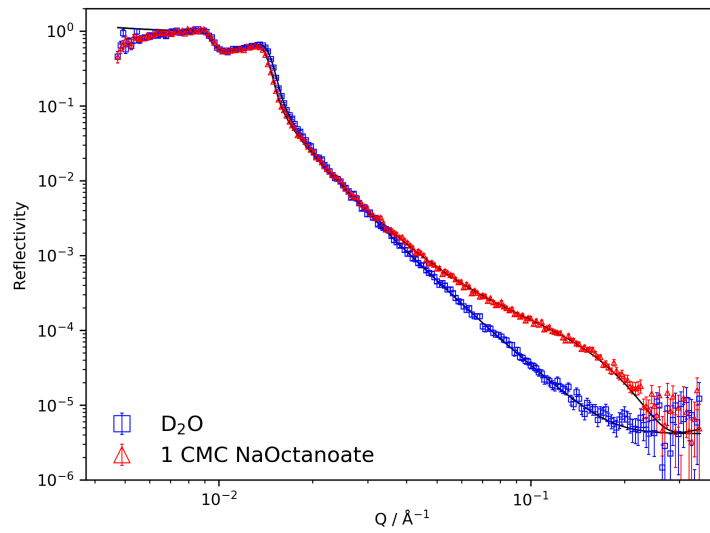
Table 3.10 Fitted parameters for the adsorbed sodium carboxylate structures.

| Layer | SLD / $\times 10^{-6} \text{ \AA}^{-2}$ | Thickness / \AA | Roughness / \AA | Hydration / % |
|--------------------|---|--------------------------|--------------------------|---------------|
| NaOctanoate | | | | |
| Water | 6.05 | 10 ± 2 | 1 ± 2 | - |
| Acid | 0.42 | 21 ± 1 | 1 ± 2 | 0 ± 5 |
| NaDecanoate | | | | |
| Water | 6.15 | 11 ± 2 | 1 ± 3 | - |
| Acid | 0.31 | 21 ± 1 | 1 ± 2 | 20 ± 5 |

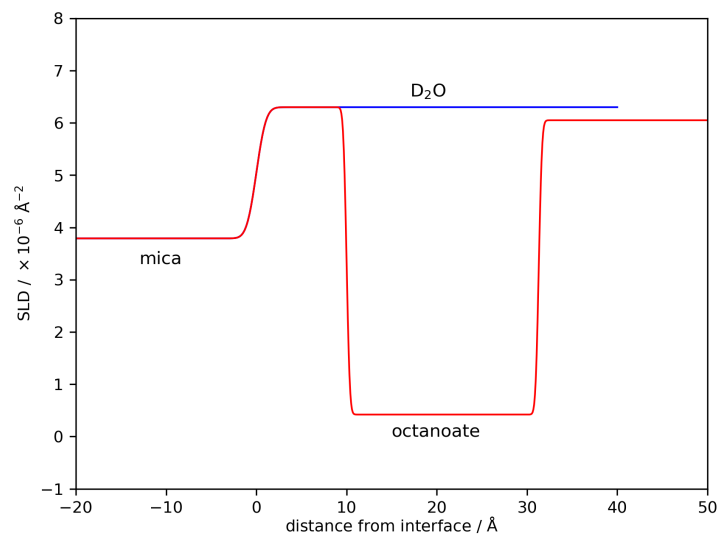
Structural Characterisation of Sodium Carboxylate Layers

The very high CMC values for the carboxylates compared to the surfactants previously studied results in a visible change in the position of the critical edge, due to a change in the SLD of the bulk solution with these high surfactant concentrations. This was accounted for during analysis, with the bulk solution SLD fitted to the position of the critical edge. Single block models were trialled but could not adequately reproduce the form of the experimental data. A model consisting of a water layer adjacent to the mica and a single uniform surfactant layer was considered as the next most simple, and was found to fit the data well. The reflectivity data from sodium octanoate at 1 CMC, and the SLD profile to the fit are shown in Figure 3.17 and those for sodium decanoate at 1 CMC in Figure 3.18. The parameters fitted to each of the two datasets are given in Table 3.10.

The structures formed by the two acids are similar, as would be expected for compounds differing only by two extra carbon atoms in the tailgroup. Using Tanford's formula¹⁴⁰, the extended chain lengths for sodium octanoate and decanoate are calculated as 11.6 \AA and 14 \AA respectively. The fitted organic layer is thicker than these distances in both cases so the structures are concluded to be bilayers, as might be expected, with hydrophilic headgroups on each side exposed to water. As the fitted layer is slightly thinner than twice the extended chain length, some degree of interdigitation or tilting may be present. The fits suggest that the acid layers are of approximately the same thickness, but with slightly greater hydration for the decanoate than for octanoate. This is slightly unexpected given that the longer chain acid might be expected to pack more densely and into a thicker layer. The difference in hydration could in part be due to an underestimation of the SLD of sodium decanoate, which was only calculated approximately from consideration of bulk physical parameters. This would lead to an overestimate of the hydration of the layer, as including D_2O raises the effective SLD.

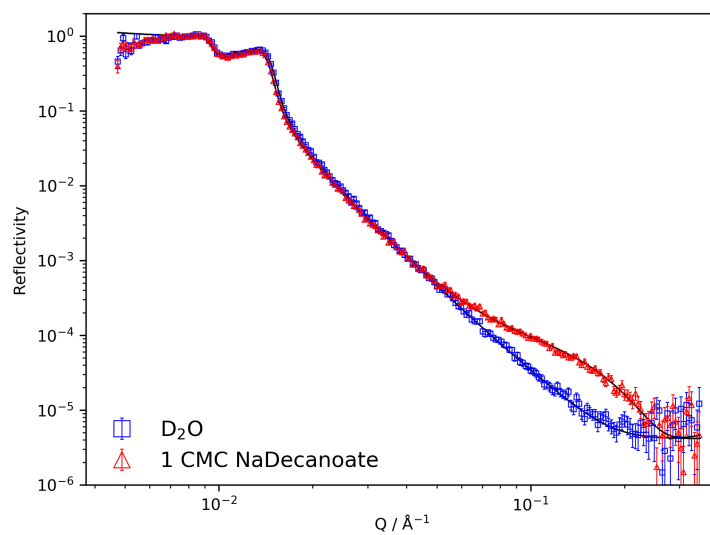


(a)

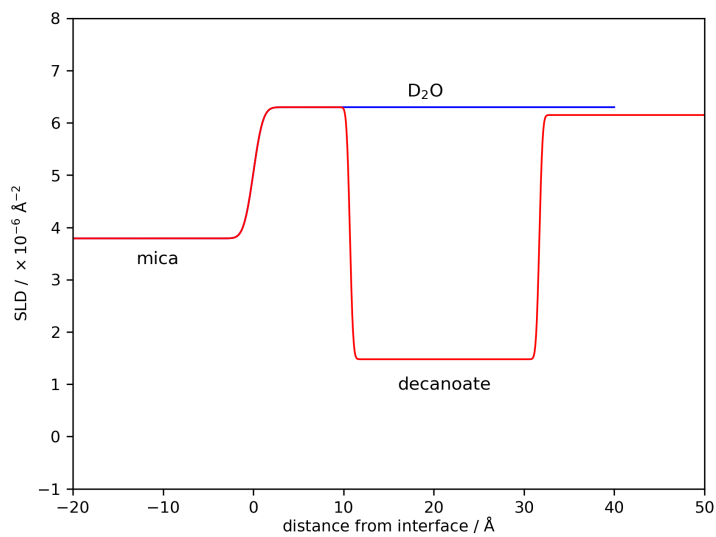


(b)

Fig. 3.17 (a) Reflectivity data for 1 CMC NaOctanoate adsorbing to the mica surface with (b) fitted SLD profile.



(a)



(b)

Fig. 3.18 (a) Reflectivity data for 1 CMC NaDecanoate adsorbing to the mica surface with (b) fitted SLD profile.

Ruling Out the Role of Cations Impurities

As it was found in Section 3.1.3 that very low concentrations of calcium could facilitate bridging even in the presence of an excess of sodium ions, the presence of trace impurities of metal ions was considered. ICP analysis of both stock solutions of sodium octanoate and decanoate was conducted and compared to reference solutions. These showed no trace impurities of calcium or magnesium. Finite potassium concentrations were detected, but at levels of $0.2\% \pm 0.02\%$ for octanoate and $0.13\% \pm 0.06\%$ for decanoate as percentage by concentration (1% being 1 potassium ion for every 100 sodium decanoate moieties), which were considered as very unlikely to be contributing to adsorption behaviour.

Sodium Carboxylate Summary

Clear evidence for two different sodium carboxylates adsorbing to mica has been shown, in contrast with the behaviour of the sulfonate head grouped AOT surfactant.

Through molecular dynamics simulations with decanoic acid on muscovite mica Kobayashi et al.¹³⁰ suggested that sodium ions would act to facilitate adsorption, but do so through a mechanism mediated by water molecules which they termed ‘water-bridging’; this is consistent with the experimental findings presented here. The simulations gave a distance between the carboxylate carbon and the sodium ion of 5 Å, with a further distance between the sodium and the mica surface. This greater distance than the hydrated radius of sodium is also consistent with the measurements.

In the case of the AOT anion the action of cations was clear in causing binding, as the sodium salt did not adsorb but other metal ions caused bridging (as long as the system was at or above the CMC). In the carboxylate systems no null case was observed, so it is not possible to conclude unambiguously that cations are responsible for the adsorption, though adsorption of the anionic headgroup without cation mediation does not seem physically reasonable. 3.6 Å has been measured as the hydrated radius of a sodium ion¹⁴¹, which is a little smaller than the fitted water layers between the surface and surfactant, supporting the idea of cation bridging here.

Calcium Carboxylates

Whilst the adsorption of the sodium carboxylates was found to be entirely reversible, calcium might be expected to bind more strongly between the carboxylate and the anionic mica

surface. It was of interest as to whether this could lead to less reversible binding, more closely resembling binding of cationic species to mica.

The strength of interaction between carboxylate anions and calcium ions is such that carboxylates show very low solubilities in the presence of even low concentrations of calcium ions. This is particularly true for saturated, and longer chain acids¹⁴². Pereira et al.¹⁴³ found that in the presence of 1 mM CaCl₂, sodium decanoate showed precipitation even at 1 mM, whereas sodium octanoate was soluble at concentrations of 10 mM, though this is still well below the CMC of sodium octanoate at 300 mM. In Section 3.1.3 it was found that AOT adsorbed to mica in the presence of 0.1 mM Ca²⁺, therefore solubility tests were carried out for both sodium carboxylates at this calcium concentration.

It was found that in 0.1 mM CaCl₂, sodium decanoate was soluble at 1 mM but at 4 mM precipitation was visible. For sodium octanoate the solubility was much higher; at 150 mM octanoate some precipitation was visible but none was seen at 90 mM even after a day. Due to the much higher tolerance for calcium in solution, octanoate rather than decanoate was used while attempting to study a calcium bridged layer. A concentration of 50 mM sodium octanoate was decided upon to ensure that the solution was away from the solubility limit.

A 50 mM sodium octanoate solution with 0.1 mM CaCl₂ was exposed to a mica surface, but no adsorption was seen in the neutron reflectivity data, as shown in Figure 3.19. The CMC of sodium octanoate in 0.1 mM CaCl₂ was not tested, and whilst the presence of calcium will lead to a CMC reduction, the lack of adsorption suggests that 50 mM is still below the CMC for this calcium concentration. As noted earlier, higher carboxylate concentrations could not be tested, and the difficulty in forming a calcium bridged structure is ascribed to the solubility limit being met before the CMC is reached.

Pre-exchanging the surface cations of the mica surface for calcium ions was also trialled in an attempt to form a calcium bridged structure. A fresh mica surface which had not been exposed to any surfactant or salt solutions was exchanged into 10 mM CaCl₂ and then back into D₂O before introduction of sodium decanoate at the CMC. The exchange back into D₂O was necessary to remove any calcium from the cell solution, as any contact between calcium and carboxylate solution would lead to instant precipitation. Adsorption of the acid was seen, with an identical profile to that measured when sodium decanoate had adsorbed to an untreated mica surface, and as in that case this layer was also seen to desorb completely on removal of bulk acid.

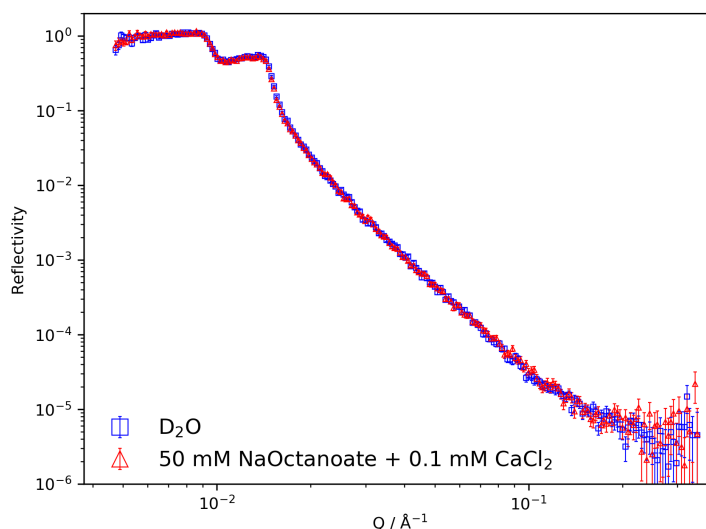


Fig. 3.19 Reflectivity profiles from bare mica in D_2O and on exposure to 50 mM NaOctanoate in 0.1 mM CaCl_2 , showing no adsorption from this solution.

Whilst it is not possible from these measurements to know if the calcium exchanged on to the mica did remain when the acid structure adsorbed, the identical reflectivity profiles formed from the untreated and pre-calcium exchanged mica surfaces suggests that the calcium did not play a role. Given that the sodium concentration in the decanoate solution is 86 mM, and 30 ml of solution was passed through the cell to ensure complete exchange, the sodium ions may have re-exchanged the mica surface cations and replaced any calcium, despite the divalent ions higher affinity for the surface.

3.1.5 Discussion

In this section the role of cation bridging of anionic organics onto mica has been addressed in detail. Understanding which cations will lead to bridging interactions is clearly important for many commercial systems, both for predicting what adsorption behaviour is occurring in pre-existing systems and for designing solutions and additives tailored to desired adsorption characteristics. The observation that monovalent ions can bridge as well as higher valency ones is an important one, and a step forward in furthering this understanding.

Evidence that the specifics of the cations which cause adsorption varies down the IA group and between IA and group IIA is very interesting. However, it is clear that the overall

combination of the substrate, cation and the nature of the anionic group present may all play a role.

The finding that even the sodium salt of carboxylic acids adsorbs to the clay mineral surface has implications for the understanding of the mechanism of reduced salinity water flooding. If carboxylate adsorption may occur even in the absence of the ions which were found to be required for AOT adsorption to mica, then this suggests that none of the proffered mechanisms for enhanced recovery are sufficient to explain release of oil on reduced salinity flooding in this model.

An alternative or contributory mechanism might simply be the solubilisation of carboxylic acids precipitated onto the clay surfaces. Given that the sodium acid salts adsorb and that acids show only sparing solubility in the presence of calcium ions, as the divalent ion concentration is reduced then slight re-solubilisation of acid components might allow the alteration of some regions from 'oil - wet' to 'water - wet', and the liberation of incremental oil.

In a series of papers using contact angle techniques, Mugele et al.¹⁴⁴ have investigated the relative wettability of oil and water on mica substrates in a range of conditions¹⁴⁵⁻¹⁴⁷. They observed that the water contact angle in ambient decane reduced dramatically on removal of divalent ions from the water phase. This effect was enhanced by addition of stearic acid into the oil, which they attributed to formation of calcium stearate at the three phase contact line leading to a more oil - wet surface. This effect is clearly related to the results described here, and is consistent with the theory that precipitation of acid groups could have a role in the controlled salinity water flooding effect.

As the hypothesised mechanism of cation bridging involves partial dehydration of the cations and anionic organic groups, which involve significant partial molar volume changes, it might be expected that pressure could influence these interactions. Similar experiments to those described in this section but conducted under reservoir pressures would be of interest, and work by others has shown that these pressure conditions can influence clay hydration behaviour¹⁴⁸.

3.2 Adsorption of Non-Ionic Surfactants to Mica

3.2.1 Background

Non-ionic surfactants are popular in many applications; the absence of charge makes them compatible with other classes of surfactant, and they show good resistance to precipitation in hard water¹⁴⁹ which presents a particular problem for anionic surfactants. A common class of non-ionic surfactants are polyoxyethylene (POE) based compounds. These may be denoted as 'C_nE_m' where 'n' refers to the length of hydrophobic tail, and 'm' the number of oxyethylene units in the headgroup. The properties of such molecules may be adjusted by the relative lengths of the alkyl chain and POE head group, and by the terminal functionality¹⁵⁰.

The literature on adsorption of non-ionic surfactants to mica is not entirely consistent, but most studies conclude little or no adsorption of non-ionics to mica. Blom et al.¹⁵¹ reported that a diblock copolymer of the POE type showed no adsorption to the bare mica surface. Using AFM Dong and Mao¹⁵² reported that C₁₂E₅ did adsorb into a continuous layer of approximately 40 Å thickness but only at temperatures above 21°C, and below this temperature patches or islands were seen with combinations of closely and more weakly adsorbed species extending further into the solution. Using the surface force apparatus, Rutland and Christenson¹⁵³ found that in a background electrolyte of sodium sulfate the C₁₂E₅ surfactant adsorbed only weakly to a mica surface at concentrations below 100 times the CMC. The weakly adsorbed layers were found to be easily pushed off the surface.

3.2.2 C₁₂E₅ Adsorption to Mica

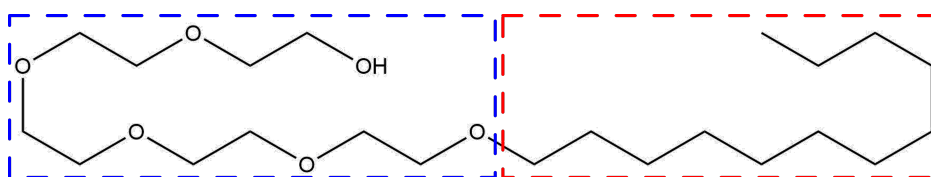


Fig. 3.20 Structure of the nonionic surfactant pentaethylene glycol monododecyl ether (C₁₂E₅). The region considered the hydrophilic 'head' is shown in a blue dashed box, and the hydrophobic 'tail' in red.

For this study the surfactant C₁₂E₅ was chosen, as it has been well characterised in the literature^{151,153,154} and its adsorption to mica has already been studied through alternate

methods¹⁵² as discussed earlier. It has previously been shown that in some systems the use of invasive probes, such as in AFM, can alter the structure under investigation⁵⁶.

For POE non-ionic surfactants, the CMC has a marked temperature dependence; as the temperature increases from room temperature the POE head group becomes less soluble and the CMC decreases initially¹⁵⁵. Because of this the reflectivity cells were temperature controlled at 25°C using a Julabo recirculating glycol bath and a temperature probe connected directly to the silicon wafer. Stock solutions for exchange of the cell solution were also maintained at this temperature by means of an additional water bath. The CMC of C₁₂E₅ has been reported as 0.064-0.065 mM^{149,156} at 25°C, and unaltered by a background electrolyte of even 0.1 M NaCl. In this work the CMC was taken as 0.064 mM. From a density of 0.963 g/ml (Sigma) the molecular volume may be estimated as 701 Å³, giving an SLD of $0.13 \times 10^{-6} \text{ \AA}^{-2}$.

Results

When the cell solution was exchanged from D₂O to 0.2 then 0.5 CMC C₁₂E₅ in D₂O little change in reflectivity profile from the bare mica surface was recorded, showing no appreciable adsorption. When the concentration was further increased to 1 CMC a clear difference in reflectivity was observed. These reflectivity profiles are shown in Figure 3.21. After 5 h of equilibration the profile of the 1 CMC solution was remeasured and had not changed. On increasing the concentration to 2 CMC no further change in reflectivity was seen. The adsorption was found to be reversible; on exchanging the solution back to D₂O the profile reverted to that of the bare mica surface, and on reintroduction of 1 CMC C₁₂E₅ the same structure occurred as initially formed.

Fitting Models

Initially fitting of the structure formed at 1 CMC was attempted with a single uniform layer with the SLD calculated for the surfactant molecule, and variable hydration. It was found that no satisfactory fit to the data could be achieved within this parameter space, and so more complex models were considered.

As C₁₂E₅ has a large hydrophilic head group and hydrophobic tail region, a bilayer might be expected to form on the hydrophilic mica. The most simple structure was considered to be a symmetrical bilayer arrangement. When fitting structures such as this it is important

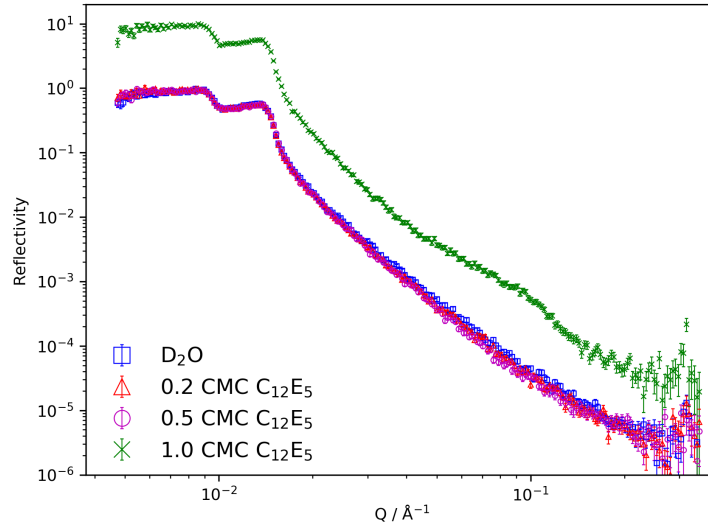


Fig. 3.21 Reflectivity profiles from a mica surface exposed to increasing concentrations of $C_{12}E_5$ in D_2O . Data for 1 CMC $C_{12}E_5$ is offset by a factor of 10.

that the resultant structure is physically possible, which can have important constraints on the fitting. For example, the number of headgroups of the surfactant must equal the number of tails. For a bilayer consisting of two headgroup layers with equal thickness and hydration with an intervening unhydrated tail group layer, with parameters as shown in Figure 3.22, in a unit area the total number of head and tail groups respectively are given by:

$$\#_{heads} = \frac{2d_1(1 - hyd_1)}{V_{head}}$$

$$\#_{tails} = \frac{d_2}{V_{tail}} \quad (\text{for unhydrated tails layer}) \quad (3.2)$$

$$\#_{tails} = \frac{d_2(1 - hyd_2)}{V_{tail}} \quad (\text{for hydrated tails layer})$$

where V_{head} and V_{tail} are the molecular volumes of the surfactant regions ascribed to the head and the tail, hyd_1 is the volume fraction hydration of the head layers, and hyd_2 the same for the tails layer.

Table 3.11 Fitted parameters for the $C_{12}E_5$ structure.

| Layer | SLD / $\times 10^{-6} \text{ \AA}^{-2}$ | Thickness / \AA | Roughness / \AA | Hydration / % |
|------------|---|--------------------------|--------------------------|---------------|
| Headgroups | 0.64 | 27 ± 4 | 3 ± 3 | 87 ± 5 |
| Tailgroups | -0.39 | 28 ± 5 | 3 ± 3 | 76 ± 5 |
| Headgroups | 0.64 | 27 ± 4 | 3 ± 3 | 87 ± 5 |

On the basis of the approximations for hydrocarbon components made in Section 3.1.2, the volume of the $C_{12}E_5$ tail region of $C_{12}E_5$, consisting of $(CH_2)_{11}CH_3$, can be estimated as 348 \AA^3 giving a volume of 353 \AA^3 for the head region. These values give SLDs of 0.64 and $-0.39 \times 10^{-6} \text{ \AA}^{-2}$ for the head and tail groups respectively. During fitting the thicknesses and hydration of the layers were coupled and constrained during optimisation such that the number of heads and tails were equal, as calculated by Equations 3.2.

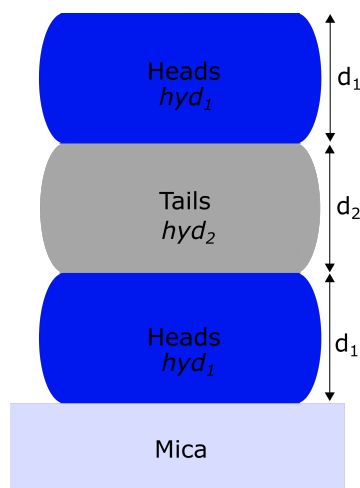
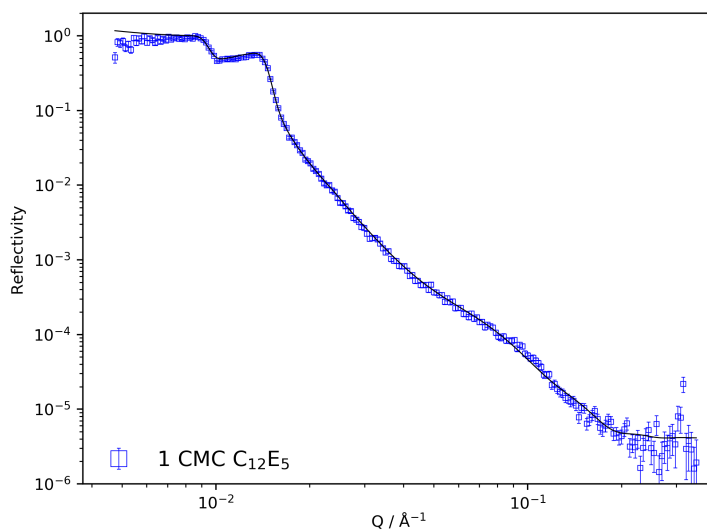


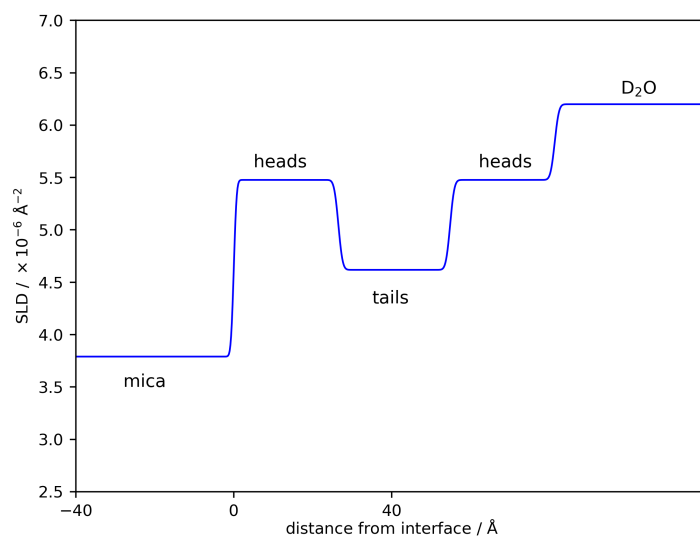
Fig. 3.22 Schematic of a symmetrical bilayer structure, with head group layer thicknesses d_1 , and tail layer thickness d_2 . Associated hydrations are hyd_1 for headgroups, hyd_2 for tails.

The tail region is expected to be strongly hydrophobic, so the hydration of this layer was constrained to be less than 20% in initial fitting using the bilayer model. As with the single layer model, this resulted in greater than observed change in reflectivity from the bare surface, from too high a change in contrast in the SLD profile. When the hydration of the tails layer was allowed to vary to higher values, a reasonable fit to the data could be achieved. The fit to the reflectivity data and SLD profile are shown in Figure 3.23, and parameters are given in Table 3.11.

The high degree of hydration of the tail group layer is perhaps surprising. However, this can be rationalised by recognising that the SLD is an average over a layer across the surface.



(a)



(b)

Fig. 3.23 (a) Reflectivity data with fitted profile to the adsorbed structure from 1 CMC C₁₂E₅ on to mica, and (b) the corresponding SLD profile.

The layer may have in plane heterogeneity; there may be regions of tails and regions of water, typical of an adsorbed micelle or other self associated aggregate, though it is not possible to distinguish between this case and a homogeneous layer in specular reflectivity data. Patchy coverage of a more uniform layer is also possible, as seen by others¹⁵².

If it is assumed that the structure is a patchy bilayer with no hydration of the inner tail region then the surface coverage may be calculated as 24%, with 46% hydration of the head layers in these patches. The tail region thickness of 28 Å is more than the 16.7 Å extended chain length of the 12 carbon tail as calculated from Tanford's formula¹⁴⁰, but less than twice this value, so consistent with a bilayer with some interdigitation or tilting.

The fitting here is based on just one contrast, and a relatively small variation in reflectivity profile from the bare surface, so there is significant uncertainty in the fitted structure. As the parameters are coupled the true uncertainties may be larger than those calculated from the manual method used to estimate them. It is possible that other structures, such as low surface coverage micelles rather than bilayers, might equally reproduce the measured data. The primary conclusion here is that adsorption occurs as a very diffuse or hydrated structure, with a small change in reflectivity compared to the bare surface.

Discussion

The adsorption behaviour of the non-ionic surfactant on the surface of mica observed here is consistent with the previously mentioned studies which find very little adsorption of non-ionic surfactants. Qualitatively the small change in reflectivity profile from that of the bare surface, and quantitatively the very large hydration values fitted to the layer, show very little surfactant adsorption occurs. The lack of detectable adsorption at 0.2 and 0.5 CMC and the further lack of change between 1 and 2 CMC $C_{12}E_5$ suggest the adsorption roughly follows an S-shaped type isotherm, as discussed in Section 1.4, which is as might be expected for a surfactant.

The thickness of the determined layer at 82 ± 13 Å is thicker than the 49 ± 4 Å bilayer thickness determined for $C_{12}E_6$ on silica in previous neutron studies¹⁵⁷, with coverage varying between 40 - 60%. The significant hydration of the layer makes an accurate estimate of the complete thickness difficult, and may partially explain this difference. The longer hydrophilic headgroup in $C_{12}E_6$ might also associate more closely with the hydrophilic surface, in what is not a dense packed layer, and lead to a thinner layer. Another alternative is the presence of vesicle structures rather than more micellar aggregates.

The complete desorption of the layer seen on removal of bulk surfactant and exchange back to pure water, is consistent with the observation of weak binding by Rutland and Christenson¹⁵³. It is also consistent with the expected behaviour for a very hydrated or

diffuse layer, and that seen for anionic surfactants bridged to the mica surface as discussed in Section 3.1.

This preliminary study into the role of non-ionics on mica has indicated that rather little adsorbs, in marked contrast to the cationic surfactants or anionic surfactants with bridging cations.

3.3 X-Ray Reflectivity from Mica

3.3.1 Cell Design and Experimental Setup

Whilst X-ray reflectivity measurements do not offer the contrast variation possibilities or the contrast between hydrocarbon and solvent of neutron scattering studies, they have successfully been applied to the study of surfactant adsorption from aqueous solution. Briscoe et al.¹⁵⁸ have succeeded in measuring adsorption on mica using their novel ‘bending-mica’ technique, both at the mica - air¹⁵⁸ and mica - water¹⁵⁹ interface. This mounting configuration overcomes the issues of crystal waviness and flexibility which have historically prevented reflectivity studies being applied to the mica surface, but adds significant experimental difficulty and mathematical complication to the data analysis.

As the mica/glue/silicon substrates used for neutron reflectivity studies have been shown to produce a mica surface of sufficient flatness for reflectivity studies, this preparation method was considered as an alternative to the ‘bending-mica’ in use for X-ray reflectivity. In neutron reflectivity the incident beam is introduced through the silicon wafer, but this is not a possibility with X-rays due to complete attenuation by the silicon. Instead the beam must be introduced through the solution above the mica, and must therefore pass through the cell which forms the solution trough. The cells for neutron studies are machined from PTFE which is strongly attenuating to X-rays as it is a fluoropolymer, so new cells were designed from PEEK. PEEK is a more rigid polymer than PTFE so cannot provide a seal against the mica surface in the manner of the neutron cells.

The vertical collimation of the beam and the very small experimental angles made it impossible to avoid clipping whatever sealing device was employed, however minimising the size of the seal would allow the smallest correction. A knife edge seal was initially favoured but machining constraints prevented this from being a viable option. Two methods were then considered for sealing the cells: a gasket cut from 0.5 mm rubber and a 1 mm rubber

O-ring sitting in a machined groove in the cell. The trough of the O-ring cell is shown in Figure 3.24a, the gasket cell is identical but with a flat lip on the raised edge of the trough rather than the machined O-ring groove. These cells were also designed to accommodate a 50×50 mm square wafer rather than the rectangular blocks used for neutron studies.

Deep walls of the trough allow the path length of the beam through the PEEK to be constant over the range of angles covered, and avoid interaction with the solution channels in the top of the cell at larger angles. As the volume of liquid is significantly greater than the neutron cells, a larger volume is required to exchange the solution. To test the exchange characteristics of the design a clear glass block was clamped against the trough, which was filled with dye and displaced using a LKB Bromma HPLC pump flowing at 4 ml/min. The results of this test are shown in Figure 3.25, and indicate that even after 56 ml of solution was pumped through, complete exchange was not achieved, with some stagnation points evident. During beamtime solution exchanges were carried out with 80 ml.

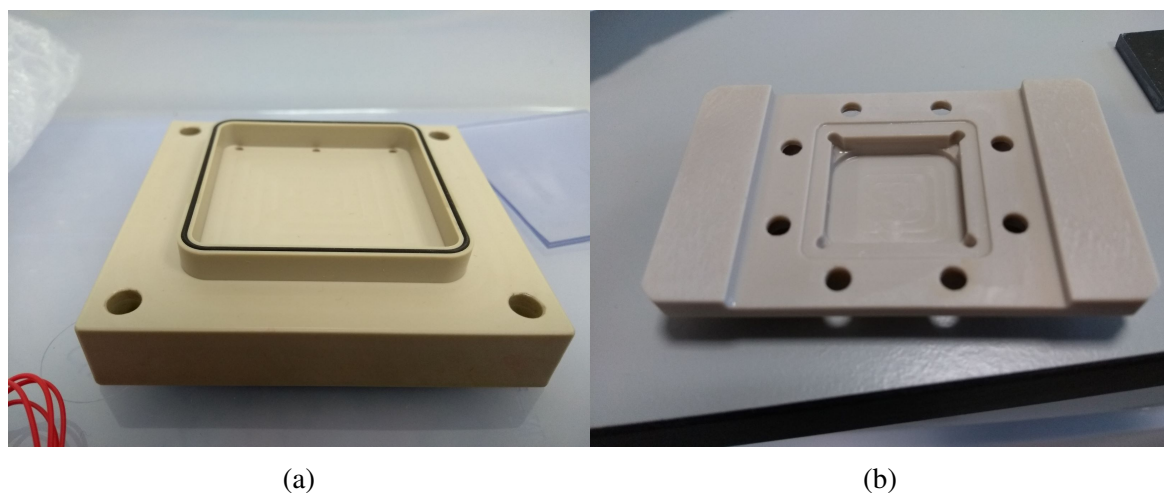


Fig. 3.24 Two X-ray reflectivity cells designs trialled; (a) a large cell design with O-ring, (b) a smaller cell which seals behind the inserted silicon wafer using a rubber mat.

An additional cell provided by Dr. Tom Arnold, the previous beamline scientist at I07, was also tested, which incorporated a smaller mica sample (20×20 mm). This cell was designed for surface diffraction studies, and seals on the back face of the inserted silicon wafer using a rubber mat, which would allow undesirable exposure of the solution to the side of the mica and glue layers in the supported mica samples, giving possible purity concerns. There is also the possibility of increased pressure on the mica surface leading to bending or buckling, as the top of the cell contacts the substrate surface at the corners. The trough of this cell design is shown in Figure 3.24b.

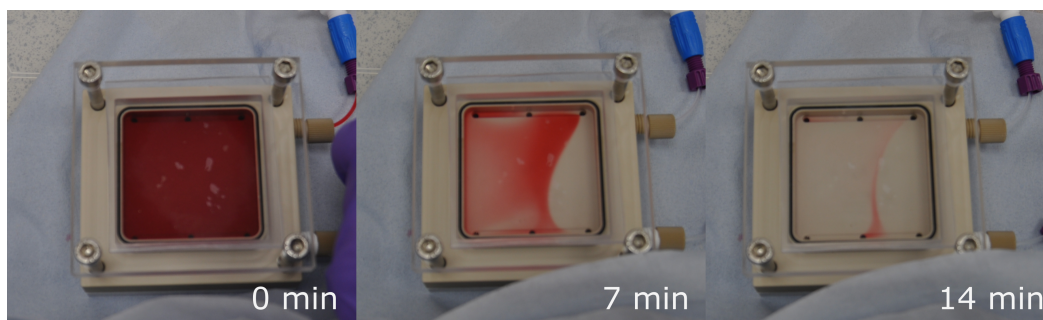


Fig. 3.25 Dye displacement test showing slow exchange of the larger XRR cell design.

During alignment on the beamline an initial height scan is performed with the substrate approximately parallel to the incident beam, to find the height of the surface of interest relative to the sample table. Height scans for each of the three cells are shown in Figure 3.26. Locating the position of the mica surface in these scans was not as trivial as in the case of the neutron reflectivity cells. Much larger than expected attenuation from both the O-ring and gasket was observed, as illustrated by the large drop in intensity. The transmission scan revealed that the height of the gasket was less than that of the O-ring, at ~ 0.4 mm compared to ~ 0.8 mm, but the greater depth parallel to the substrate led to such a large drop in intensity for the gasket cell that alignment was not possible. The other two cells were therefore used for the remainder of the experiment.

3.3.2 Results

Initially the large mica substrate was characterised by X-ray reflectivity in air (not in the cell). Figure 3.27a shows the reflectivity data recorded; a relatively sharp critical edge is visible indicating that the substrate preparation has been successful in generating a surface flat enough for X-ray reflectivity measurements. Measurements were taken out to a high enough angle of reflection to observe the Bragg peak of the mica, the presence of which confirms the presence of the mineral on the substrate as desired. From the position of the peak the d-spacing of the mica can be calculated using Bragg's law; the peak centre is at $q = 0.62 \text{ \AA}^{-1}$ which gives a d-spacing of 20 \AA . This agrees with both the literature and the structure of a mica sample determined by single crystal X-ray diffraction.

For fitting the data was truncated at $q = 0.4 \text{ \AA}^{-1}$, prior to the influence of the Bragg peak, and it was assumed that only the interface at the top of the mica crystal contributed to the reflected intensity. As shown in Figure 3.27b, the data could be adequately fitted using

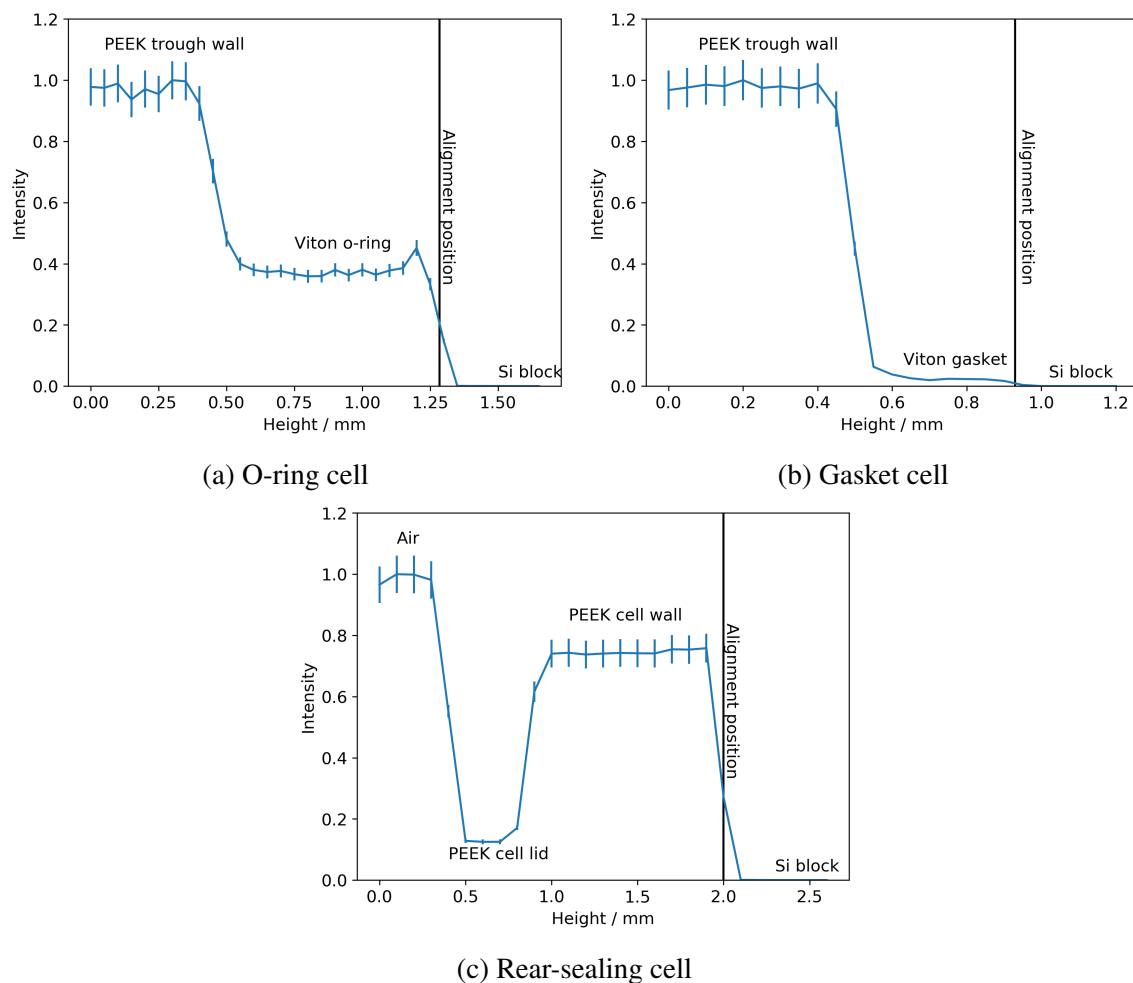
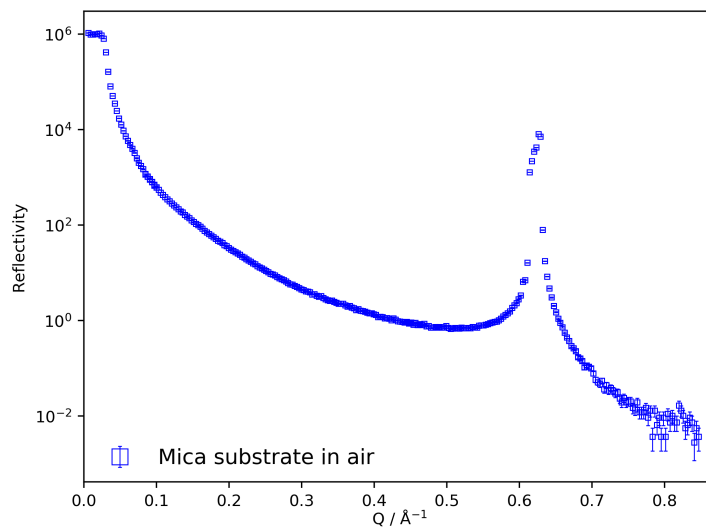


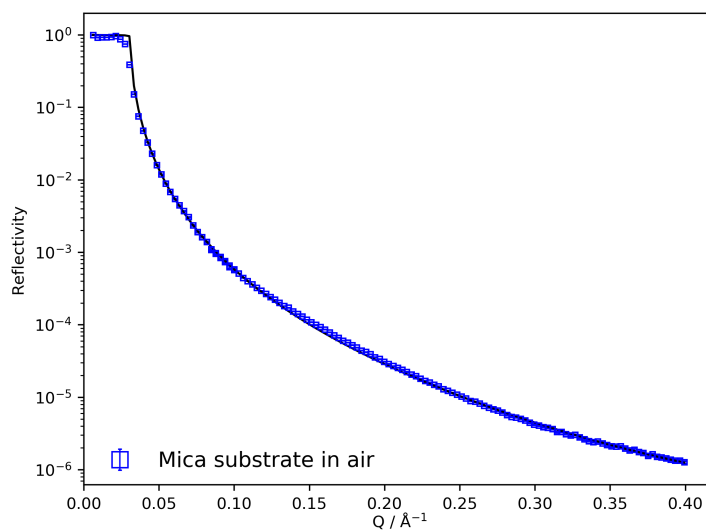
Fig. 3.26 Transmission height scans for the three designs of cell trialled for the X-ray reflectivity study. Reflectivity data is normalised to unity by the most intense recorded signal within the range of the height scan.

the idealised mica formula ($\text{KA}_3\text{Si}_3\text{O}_{12}\text{H}_2$) and allowing a density slightly lower than the literature value, and a roughness of 2.5 \AA . The reduced density would be equivalent to some substitution of lighter elements in the naturally occurring crystal, such as Na for K or Mg for Al, reducing the electron density in the crystal.

For the case of the small cell design shown in Figure 3.24b, on clamping the mica substrate into the cell and filling it with water, there were clear artefacts visible in the reflectivity profile. These could be due in part to geometric factors as the X-ray beam passes through different cell components as the angle is varied, which could in principle be corrected for, or some deformation of the mica surface caused by the cell.



(a)



(b)

Fig. 3.27 (a) Un-normalised X-ray reflectivity from the mica - air interface, with substrate not clamped into the cell, and (b) the same profile normalised and truncated prior to the Bragg peak with superimposed fit.

As the larger mica substrate was transferred into the cell, then as the cell was filled with H_2O , the background relative to the intensity before the critical edge was observed to increase, as expected with the presence of additional sources of scattering. These reflectivity

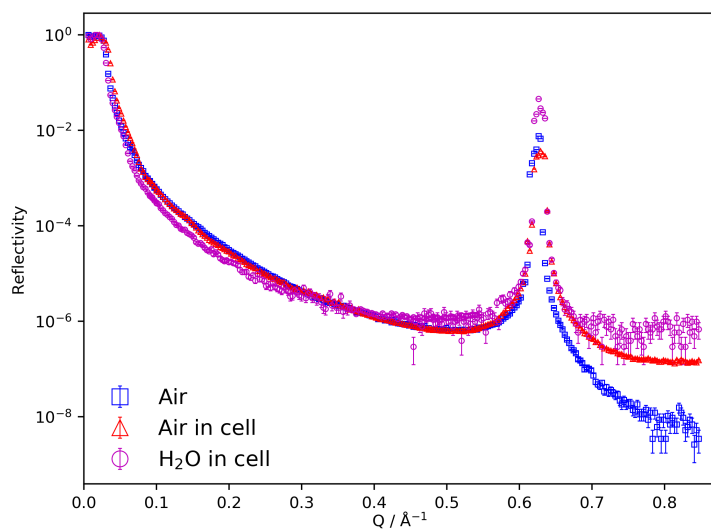
profiles are shown in Figure 3.28a. Datasets were then collected for the mica surface exposed to water, and to 1 CMC CsAOT and 2 CMC DDAB, both of which have been shown to adsorb in ordered layers^{55,123}. Whilst changes in profile were recorded, as shown in Figure 3.28b, these changes on exposure to either of the surfactants were not greater than the changes in profile between equivalent H₂O contrasts, and so fitting of the data was not further pursued.

The magnitude of the expected changes from adsorption, based on the work of Briscoe et al.¹⁵⁹, would be within this variation so adsorption cannot be confirmed or precluded. In this study no attempt was made to avoid beam damage, which can be caused to adsorbed structures or even the substrate by the high illumination of synchrotron X-ray sources. The high degree of variation in the data was at least in part attributed to technical complications with the instrument at the time of the experiment. Further attempts to apply this substrate preparation technique to X-ray reflectivity measurements are planned.

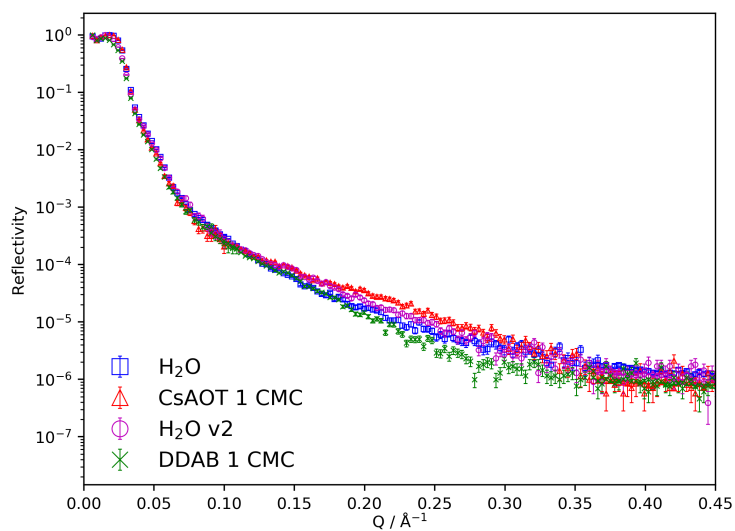
3.4 Adsorption Comparison with Simulations

In an ongoing collaboration, the results of molecular dynamic simulations carried out by Georgia Tsagkaropoulou, in the group of Professor Philip Camp, from the University of Edinburgh have been compared to experimentally recorded neutron reflectivity data. Simulations were conducted by Georgia who provided both the snapshots, and the atomic density profiles which I have analysed. Significant contribution was made to advise on conditions and iteration of simulations to achieve better consistency with experimental data.

Comparison between molecular dynamics (MD) simulations with neutron reflectometry experiments of surfactant systems on mica was carried out, for the dual purpose of aiding and verifying simulations through comparison to experimental data, with the hope of then being able to use the robustly developed simulation techniques to screen further surfactant systems and gain higher resolution insight into the structures formed. Detail of the methodology of the MD calculations is not included, but is discussed in Tsagkaropoulou et al.¹⁶⁰ Comparisons were conducted by calculating an atomic density profile for each type of atom in the simulation, discretised into 1 Å slices parallel to the surface, starting in the mica crystal and continuing through the interface and until bulk solution was reached. The density profile was taken from an average of the final 1500 frames in each simulation, to allow the system to equilibrate as far as possible prior to sampling. The data was then included into the I-CALC routine as a series of layers with SLDs calculated from the neutron scattering lengths of the



(a)



(b)

Fig. 3.28 Reflectivity data recorded from the larger mica substrate free in air, (a) in air in the cell and under H₂O, and (b) profiles recorded in various surfactant contrasts.

atoms in each 1 \AA bin. To match with experimental data, the solvent in the simulations was calculated as if D₂O, though H atoms were simulated.

Experimental data of different surfactant systems has been collected on numerous neutron reflectivity substrates over a large number of beamtime experiments. Direct comparison

of the results of MD simulations with different experiments would therefore require using fitted parameters for different substrates each time. To facilitate clearer comparison between simulations, it was decided that a more convenient choice would be to use the same mica substrate parameters in all cases, and instead compare reflectivity calculated from the SLD profile from MD simulations with reflectivity calculated from the SLD profile fitted to the experimental data for the relevant system. As the structure of the mica substrate has been seen to make little difference to parameters fitted to the adsorbed structure, this should still be a robust comparison. The substrate parameters used were those fitted to a mica substrate from a previous experiment¹⁶¹.

3.4.1 The Mica - Water Interface

The simulated mica surface is ideal, in the sense that it is atomically flat and ordered, which will never be perfectly reproduced experimentally where natural mineral samples are employed. This ideal structure produces sharp high-frequency oscillations in the SLD profile from the crystal, which when included into the calculated reflectivity lead to very broad oscillations which are of very low intensity. Due to 'smearing out' of the sharp spikes in SLD because of roughness, imperfect alignment, and paracrystalline disorder these have not been witnessed experimentally, and the magnitude of the effect is also close to being within the experimental error in measured reflectivity.

A snapshot of a simulation of the bare mica surface with potassium counter ions, as will be the case in the initial water characterisation of the neutron reflectivity substrates, is shown in Figure 3.29. The SLD profile calculated from the MD simulation is shown in Figure 3.30b, with sharp oscillations from the mica as outlined above. Further oscillations in SLD are visible just beyond the mica interface which are due to some degree of ordering of the first few layers of water. As shown in Figure 3.30a, there is excellent agreement between the reflectivity profile calculated from MD and that from experimental data.

The ordering of water molecules seen in the simulation is consistent with the results of high resolution crystal truncation rod experiments¹⁶². These experiments suggested a periodicity of approximately 2.5 - 2.7 Å and ordering extending to around 10 Å from the surface, both of which are remarkably consistent with the simulation result.

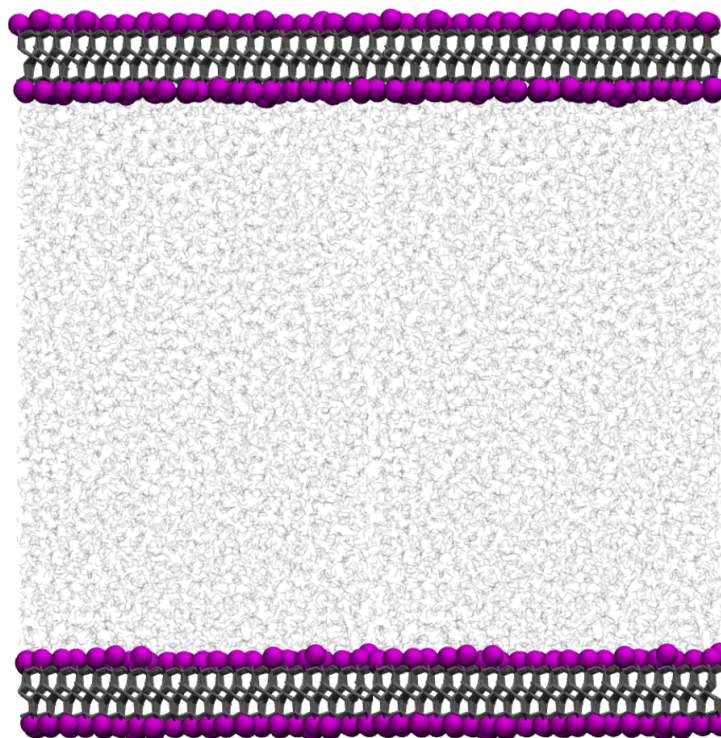
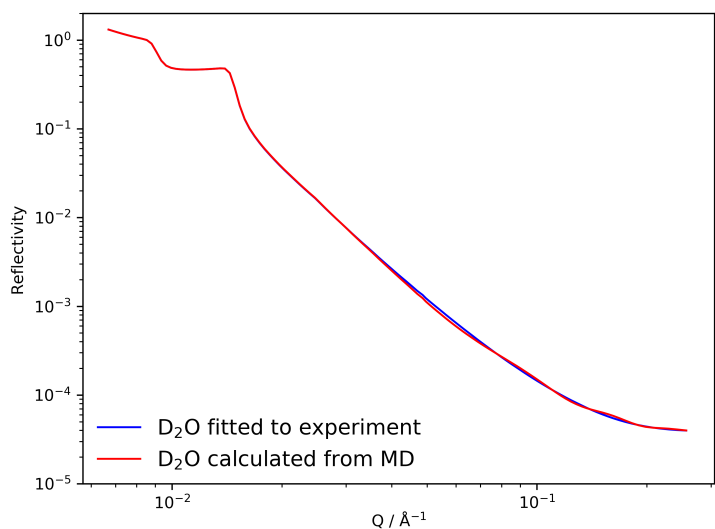


Fig. 3.29 Snapshot of an MD simulation of the bare mica surface, showing both boundaries. Potassium ions are shown in purple.

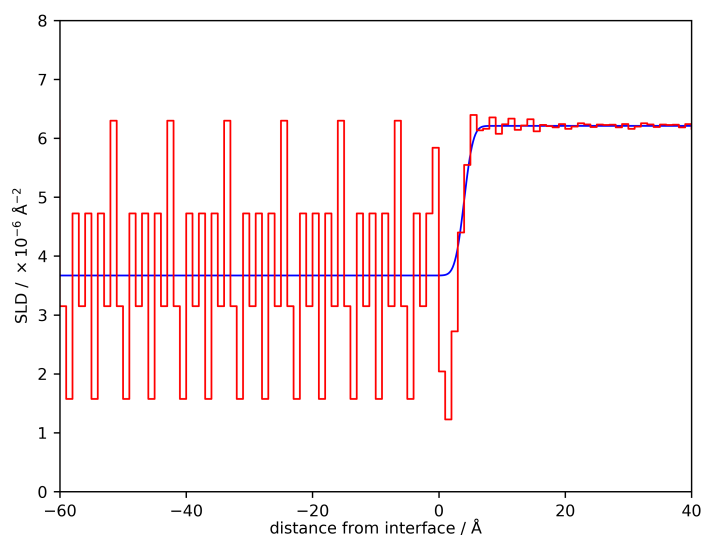
3.4.2 CTAB Adsorption

The exact parameter space being probed in the MD simulations is complex to relate exactly to experiment, due to the ill-defined concentration of surfactant present in the simulating routine. Simulations consist of a fixed volume box, and as a large number of surfactant molecules adsorb the solution concentration is depleted. The limited size of box and small volume of remaining ‘bulk’ solution does not allow easy determination of the bulk chemical potential. In the cases described here bulk aggregation was visible between the mica boundaries and so it is assumed that the concentration is above the CMC.

One of the two cationic surfactants simulated was cetyltrimethylammonium bromide (CTAB), the structure of which is given in Figure 3.31. This has been shown by Griffin et al.⁵⁶ to adsorb onto the mica surface at the CMC, and detailed analysis of the SLD profile revealed the structure to be bilayer like, rather than adsorbed micelles which have been reported in some prior studies^{163,164}. The parameters used for simulating the fit to the experimental data in the CTAB system were those in the same work, and were an SLD of $-0.26 \times 10^{-6} \text{ \AA}^{-2}$, thickness of 31 \AA , roughness of 3 \AA , and hydration of 6%.



(a)



(b)

Fig. 3.30 (a) Simulated reflectivity curves based on a fit to experimental data (blue) and to a calculated SLD profile from the MD simulation (red), and (b) associated SLD profiles.

The snapshots from the MD simulations shown in Figure 3.32 reveal that including the K^+ ions, which compensate the surface charge in the native mica, in the simulation has a dramatic impact on the adsorption behaviour. When present these ions can compete for the anionic surface and result in a clear reduction in adsorption and ordering of organic

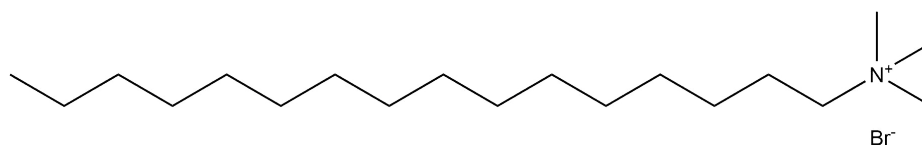


Fig. 3.31 Structure of the cationic surfactant cetyltrimethylammonium bromide (CTAB).

onto the mica. If the potassium ions desorb, the small simulation box size results in an artificially very high concentration of K^+ in the volume simulated which will not be the case in experiments. The specific nature of the neutron experiments to which these simulations are being compared, where solutions are flowed through the cell with large volumes to ensure complete exchange, means that any potassium ions will likely have been exchanged for organic cations and removed from the cell. They will therefore have no effect on the system, and the simulations without potassium ions present should be the more relevant case for comparison. This key difference and development to potassium free simulations was steered by the comparisons between simulation and experimental data.

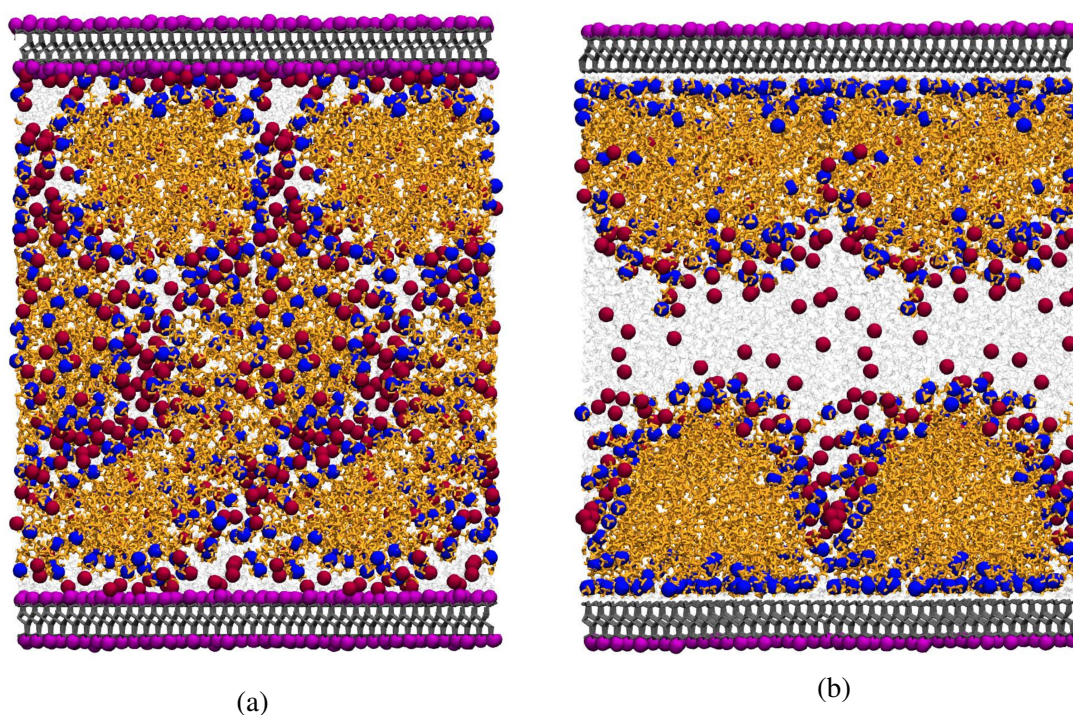


Fig. 3.32 Snapshots from MD simulations of CTAB on mica, both with (Figure 3.32a) and without K^+ ions present (Figure 3.32b). Nitrogen atoms are shown in blue, and bromine are red.

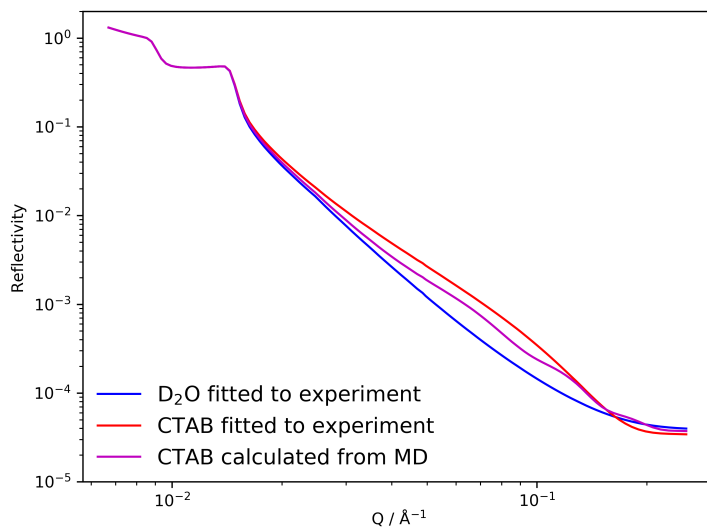
The images in Figure 3.32 clearly show that the simulated CTAB adsorbs in a more micellar structure than a true bilayer. The water present between adsorbed aggregates results in a smaller difference in SLD between the adsorbed structure and either the bulk mica or bulk solution, and a smaller change in reflectivity profile, than the experimentally fitted structure. Both cylindrical and spherical micelles have been observed for CTAB adsorption on mica, and there have been reports that cylindrical micelles can rearrange over a period of 6-24 h to form a bilayer¹⁶³⁻¹⁶⁵, although neutron reflectivity data showed a bilayer in the first one to two hours⁵⁶. The length of time covered by the MD simulations is of the order of nanoseconds, so it may be the case that if this rearrangement were to occur in the simulations it is beyond the timescale which can be computed. Increasing the separation of the mica walls to ensure no cross-bulk interaction of adsorbate structures was trialed, but made no discernible difference to the results.

Closer agreement between simulated surfactant structure and experimentally determined reflectivity was not achieved, though much better agreement was seen than with preliminary simulations and those conducted with potassium ions present.

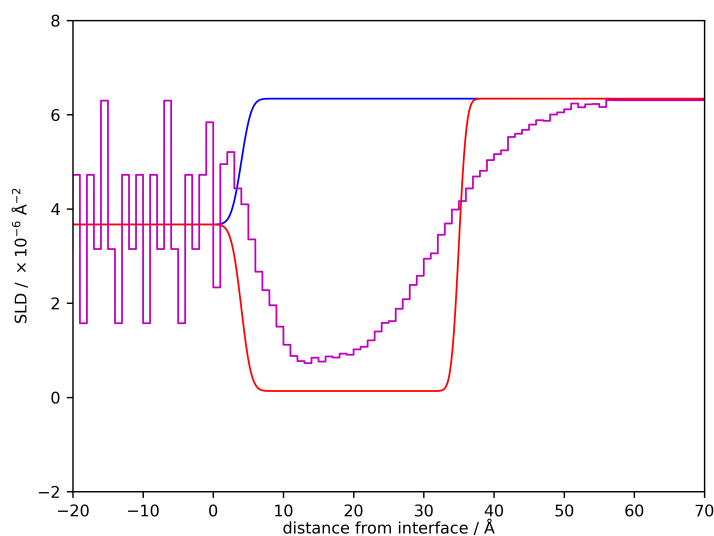
3.4.3 DDAB Adsorption

The other cationic surfactant simulated was didodecyldimethylammonium bromide (DDAB), the structure of which is given in Figure 3.34. This di-chain surfactant has also been shown to adsorb strongly to mica⁵⁵. The parameters used for simulating the fit to the experimental data were those from a specific earlier experiment¹⁶¹, and were an SLD of $-0.25 \times 10^{-6} \text{ \AA}^{-2}$, thickness of 22 Å, roughness of 1 Å, and hydration of 0%. These parameters are specifically for the DDAB layer adsorbed from a solution of DDAB at 1 CMC (though the same profile was recorded at the higher concentration of 2 CMC), not for the slightly altered layer retained when the solution was exchanged to pure water. Snapshots of the simulations are shown in Figure 3.35, and again if K^+ is included then adsorption of the organic molecule is essentially precluded as it is out-competed. When these ions are removed then ordered bilayers are observed, in agreement with experiments.

The SLD profile calculated from the simulation is shown in Figure 3.36b. When compared to the SLD profile fitted to experimental data of the system, both the thickness and density of the adsorbed layer are very similar and the resulting reflectivity profile shown in Figure 3.36a is a close match to the fit to experiment. As the thickness of the adsorbed layer is less than twice the extended chain length (17 Å by Tanford's formula¹⁴⁰) it was assumed that



(a)



(b)

Fig. 3.33 (a) Calculated reflectivity profiles from experimental fits to a bare mica surface in D₂O (blue), with an adsorbed CTAB layer (red), and calculated from MD (magenta), with (b) associated SLD profiles.

the bilayer was either interdigitated or that there was significant tilting of the surfactant molecules⁵⁵. The bilayer formed in the MD simulation is neither of these; an ordered monolayer is visible with essentially vertical surfactant tails, and a further layer adsorbed on

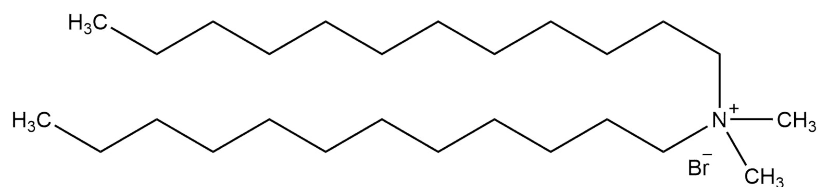


Fig. 3.34 Structure of the cationic surfactant didodecyldimethylammonium bromide (DDAB).

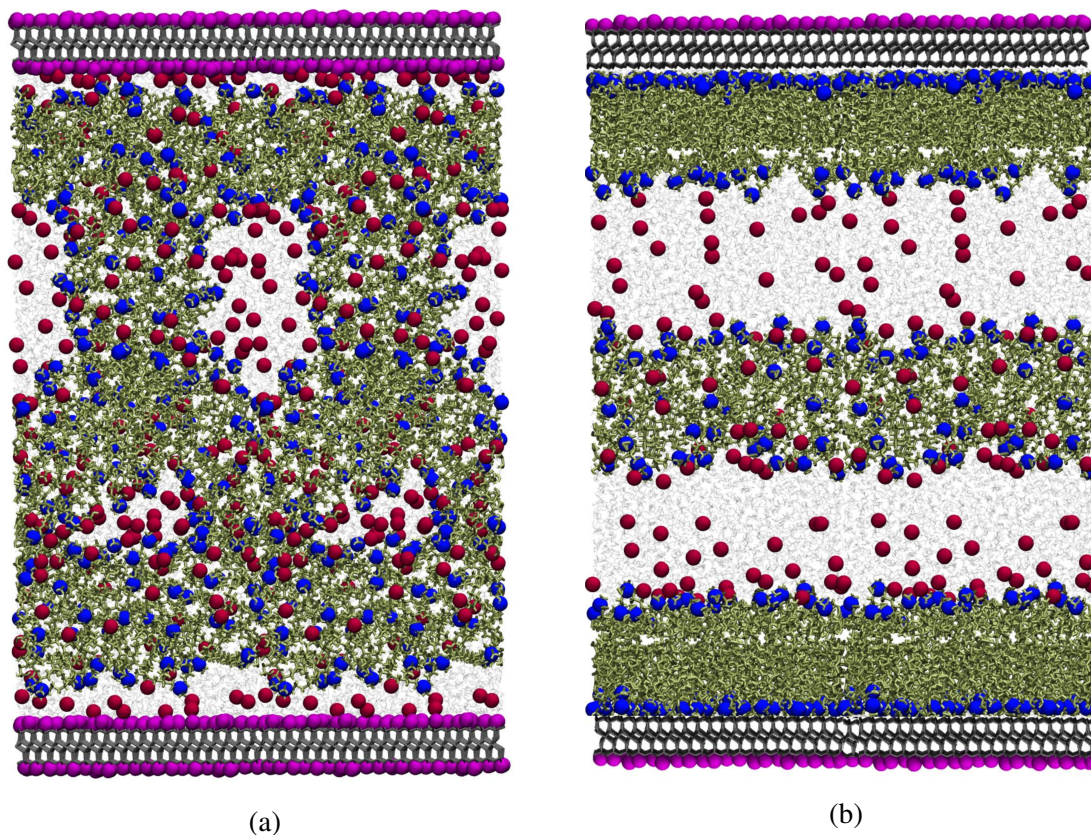
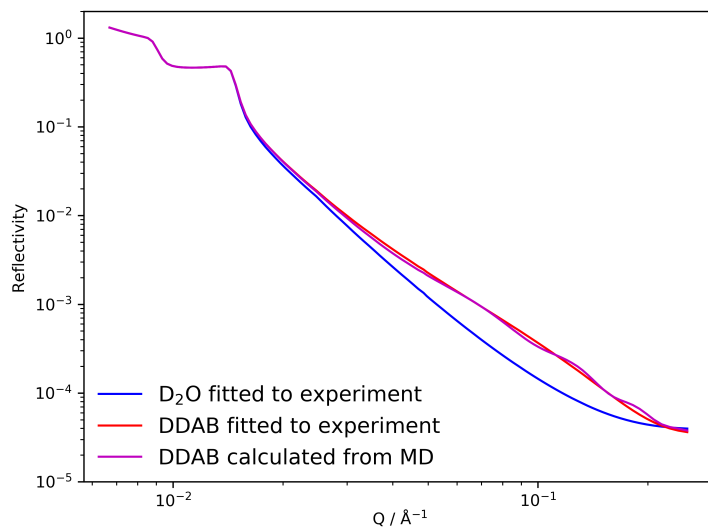
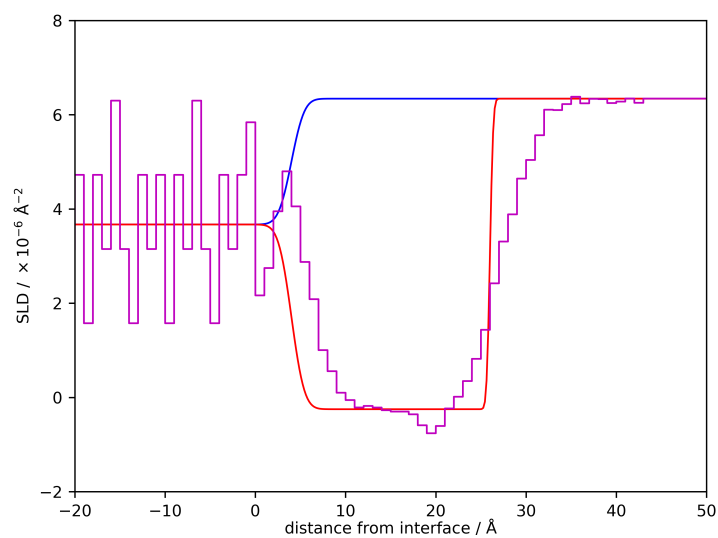


Fig. 3.35 Snapshots from MD simulations of CTAB on mica, both with (Figure 3.35a) and without K^+ ions present (Figure 3.35b). Nitrogen atoms are shown in blue, and bromine are red.

top of this with a much more inclined angle relative to the mica surface. If this is the case then some differences in behaviour might be expected compared to the interdigitated bilayer which had been presumed, for example ease of exchange of the outer leaflet.



(a)



(b)

Fig. 3.36 (a) Calculated reflectivity profiles from experimental fits to a bare mica surface in D_2O (blue), with an adsorbed DDAB layer (red), and calculated from MD (magenta), with (b) associated SLD profiles.

3.4.4 Summary

The combination of MD simulations with experimental data from neutron reflectivity has proved to be very beneficial to both sides. By comparing the output of MD simulations to the collected data, the simulation method and parameters have been refined within physical constraints until the resulting structure from the simulations reproduced the observed data as closely as possible. This provides an opportunity for otherwise difficult verification of simulation output. The final refined simulations then allow added insight into the molecular structures present, and inform further experiments.

In particular there is very good agreement of MD and NR for the DDAB adsorption on mica, that broadly support the ‘coarse’ grained view accessible from data inversion of the NR data. However, the MD reveals a much more subtle molecular distribution with one leaflet of the adsorbed bilayer essentially complete and with upright molecules, while the other leaflet is very disordered. This high resolution insight is only accessible in this combined approach. Similarly, the NR clearly indicated that the initial MD simulation models were completely incorrect and only this disagreement led to the final structural solution with increased confidence.

3.5 The Influence of Surface Treatment on Adsorption Behaviour

Surface treatments and cleaning procedures can have various intended and unintended effects on the nature of the resultant surface, ranging from altered hydrophobicity to oxide growths¹⁶⁶.

3.5.1 Experimental Evidence

In one experiment, a mica surface was used which had not been UV-O₃ treated prior to adsorption studies. Apart from this step, the substrate had been prepared identically to the other substrates described in this thesis, and as detailed in Section 2.1.2.

A solution of 1 CMC DDAB was introduced to the surface, and as expected adsorption of a layer was seen. The experimental data recorded from the bare mica in D₂O, the same substrate on exposure to 1 CMC DDAB in D₂O, and after subsequent exchange back into

D₂O are shown in Figure 3.37. The parameters fitted to the adsorbed layer are given in the first line of Table 3.12, and show a much thinner layer than expected from prior results.

On exchange of the bulk solution to pure D₂O with no surfactant present, the reflectivity profile returned to close to that recorded for the original mica surface. This indicates that nearly all of the surfactant had been desorbed from the surface, again in contrast with prior results.

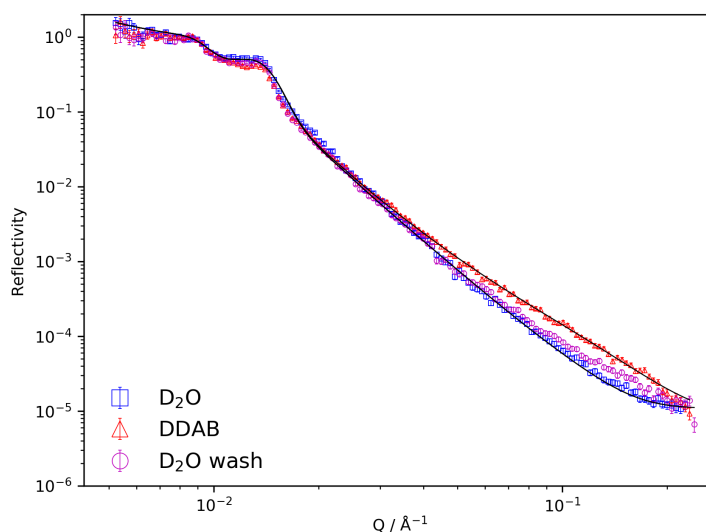


Fig. 3.37 Reflectivity profiles collected for a bare mica substrate (blue) which had not been treated with UV-O₃, after introduction of DDAB at 1 CMC (red), and after subsequent reintroduction of pure D₂O (magenta). Fits are shown to all three profiles.

After these results, the cell was disassembled and the substrate removed. The mica surface was blown dry with a jet of dry N₂, then UV-O₃ cleaned for 20 min. The cell was carefully reassembled, and filled in the usual manner. The surface was re-characterised in water contrasts, and the profiles were essentially identical to those recorded of the mica surface in the first instance. The second critical edge appeared slightly sharper after reassembly, which was attributed to better alignment, or possibly less curvature of the surface after reassembly.

The same 1 CMC DDAB in D₂O solution as before was reintroduced to the cell, and this time adsorption of a much thicker layer was seen. The reflectivity profile of this layer is shown in Figure 3.38, with the data from the initial DDAB layer before UV-O₃ treatment for comparison. The fit to the newly formed layer is shown, and parameters given in Table 3.12. The fitted layer thickness had nearly doubled, from 11 Å before treatment to 20 Å after.

Table 3.12 Fitted parameters for the Mg^{2+} bound structure.

| Layer | SLD / $\times 10^{-6} \text{ \AA}^{-2}$ | Thickness / \AA | Roughness / \AA | Hydration / % |
|----------------------------------|---|---------------------------|---------------------------|---------------|
| Initial DDAB layer | -0.25 | 11 ± 2 | 3 ± 2 | 0 ± 10 |
| Post-UVO ₃ DDAB layer | -0.25 | 20 ± 2 | 2 ± 2 | 0 ± 5 |

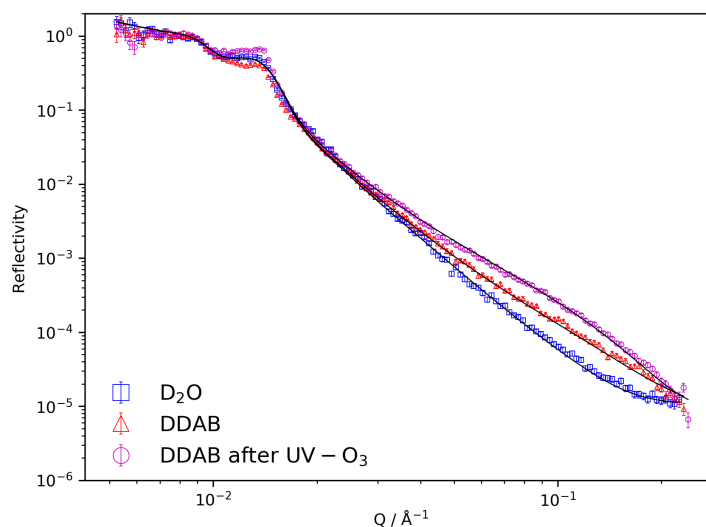


Fig. 3.38 Reflectivity profiles of the bare mica surface (blue), the DDAB layer formed from 1 CMC before UV-O₃ treatment (red), and the DDAB layer formed from the same solution on the surface after UV-O₃ treatment and reassembly of the cell (magenta). Slight differences in intensity for the reflected signal above the second critical edge are visible between runs; this was attributed to slight differences in alignment before and after reassembly of the cell.

The cell solution was then exchanged to pure D₂O as before, and this time there was little change in measured reflectivity (not shown), indicating little change to the adsorbed structure.

3.5.2 Discussion

There are clear differences in the observed behaviour at the surface before and after the UV-O₃ treatment in this case. The fitted thickness of the layer on the mica prior to UV-O₃ of 11 \AA is much less than values found by others for DDAB on mica; Browning et al.⁵⁵ found a layer thickness of $24 \pm 2 \text{ \AA}$, and Griffin et al.¹⁶⁷ found a layer thickness of $23 \pm 2 \text{ \AA}$, both on mica surfaces which had been UV-O₃ cleaned for 15 min. In both cases fitting suggested

no hydration of the layers. The DDAB layer on the mica was almost completely removed by exchange into pure water in the first instance, but showed very little change in the second. The almost complete retention of the layer on this surface in the second case is consistent with the observations of others⁵⁵.

One possible explanation for this change in behaviour on treatment is that some contaminant on the surface, either pre-existing in the natural mica crystal or in some way introduced after cleaving, was affecting the binding behaviour of the DDAB either through exclusion or repulsion. No clear layer of adventitious carbon or other material is evident from the neutron fitting of the bare surface characterisation before treatment, and little change in the bare surface contrasts before and after UV-O₃, which might suggest that this is not the case. A molecularly thin layer of the order of a few Angstroms thickness would likely make little alteration to the data compared to a bare surface, so the possibility of contaminant removal being responsible for the change is not precluded by the measurements.

The nature of the final cleave of the mica crystal to produce the surface of interest is described in detail in Section 2.1.2, but is initiated by scoring with a scalpel. Whilst the depth of this score will approximately set the position of the cleave within the crystal, there will still be a large number of layers along which the cleaving may occur. If in this subset there is an interlayer with some organic or other material impurity between the layers then it might be likely that the reduced interlayer adhesion on this plane will lead to selective cleaving in this location.

A second possible explanation is that the action of UV-O₃ cleaning is altering the mica surface in some way. Ozone is known to lead to oxidation of the surface of silicon¹⁶⁸. Plasma treatment of mica has been shown to be able to produce surface silanol groups (Si-OH) on mica¹⁶⁹, though these are considered to be unstable in water^{169,170}. UV-O₃ is however a less aggressive treatment than plasma cleaning¹⁷¹.

In Section 3.1.2, the adsorption of the anionic surfactant CsAOT was seen to be identical on an 'untreated' mica surface and on the same surface after a 20 minute UV-O₃ treatment. That system is slightly different however, as cation-mediated adsorption of an anionic surfactant, rather than the cationic adsorption described in this section.

This behaviour warrants some further investigation, both as to whether the surface is simply being cleaned of contaminant or in fact being altered by the treatment, and the nature of this alteration if present.

Chapter 4

Induced Desorption of Surfactants at the Mica - Aqueous Solution Interface

4.1 Background

4.1.1 Cationic Adsorption

Prior work in the literature on adsorption of cationic species to mica from aqueous solution was summarised briefly in Sections 3.4 and 3.5, but is discussed in more depth here.

Neutron reflectivity has previously been used to study adsorption of the cationic surfactant DDAB (structure shown in Figure 3.34) to the mica basal plane^{55,167}. The molecule was observed to adsorb as a bilayer of thickness $24 \pm 2 \text{ \AA}$ and roughness $2 \pm 1 \text{ \AA}$ in one case, and $23 \pm 2 \text{ \AA}$ and roughness $2 \pm 1 \text{ \AA}$ in the other, with effectively no water inclusion in the layer in both cases. These numbers are in good agreement with other measurements of DDAB bilayers on mica¹⁷² and on quartz¹⁷³, and indicate an interdigitated or tilted bilayer. It was observed that exchange into D₂O caused the bilayer thickness to decrease to $20 \pm 1 \text{ \AA}$. However, subsequent washes with 10 mM KCl or CaCl₂ did not alter the layer structure further. A UV-O₃ treatment was required to remove the surfactant from the mica surface. Hence it was concluded that the adsorption of the DDAB cation on the anionic mica is very tenacious. In this present work the behaviour of sequential surfactant solutions at the mica surface is probed, an advance from the single, one-component solution as previously investigated.

4.1.2 Mixed Surfactant Adsorption

Adsorption of surfactant mixtures has been the subject of many studies in the literature. In commercial and industrial applications, surfactants are very rarely employed as a single component as the enhanced performance of mixtures is desirable. The nature of the interactions between surfactants is discussed at length by Rosen and Kunjappu¹⁴⁹; interactions between surfactants may be either *synergistic*, where combining them enhances the properties of interest relative to the pure components, or *antagonistic*, where the converse is true. Usually in commercial applications synergism is sought.

The interaction of cationic and anionic surfactants in solution has been the subject of considerable research, and mixed micelles termed catanionic micelles are known to form in solution¹⁷⁴. Due to the favourable interactions, the CMC of a cationic - anionic mixture would be expected to show a minimum at some composition ratio with a surface tension below that of the CMC surface tension of either pure surfactant. This behaviour has been observed experimentally¹⁷⁵. Mixtures of cationic and anionic surfactants frequently show precipitation at certain mole fractions and above a minimum concentration, limiting the application of this type of mixture.

The alteration of properties on mixing of surfactants is of course not limited to bulk properties, and adsorption of mixtures of surfactants is a much studied field, reviewed by Zhang and Somasundaran¹⁷⁶ and others. A surfactant which does not adsorb on a specific surface may be influenced to do so by a second surfactant which does adsorb. This has been shown to be the case for non-adsorbing anionic surfactants SDBS and SDS on silica, where mixed adsorption was seen when cationic surfactants were present¹⁷⁷. An analogous effect has been observed for non-ionic C₁₂E₈ on alumina, where the single component non-ionic did not adsorb but mixed adsorption was seen in the presence of anionic sodium *p*-octylbenzene sulfonate¹⁷⁶.

4.1.3 Surfactant Influence on Pre-Adsorbed Layers

Whilst experiments examining adsorption from mixed solutions of surfactants are common, the interactions of pre-present layers with surfactants in solution are much less well studied. A simple example of the effect of subsequent surfactant exposure is a pre-existing layer precluding adsorption of a second species. This has been observed for an adsorbed non-ionic surfactant reducing adsorption of an ionic surfactant at the oil - water interface¹⁷⁸.

Sequential adsorption may lead to structurally or constitutionally different layers when compared to adsorption from mixed solution; this has been shown to be the case at both the oil - water and air - water interfaces for a protein and surfactant combination comparing 'simultaneous' and 'subsequent' adsorption¹⁷⁹.

Fröberg et al.¹⁸⁰ used the surface force apparatus to study lysozyme protein layers adsorbed on mica on exposure to increasing SDS concentrations. They found that the layer structure was modified by the SDS below the CMC, partial desorption was seen at concentrations close to the CMC, and at many times the CMC rapid removal was detected. Postulated mechanisms for these observations were a combination of charge inversion of the bound layer by SDS association into the protein, through both electrostatic and hydrophobic interactions, and denaturing of the protein by SDS leading to a break down in layer structure.

4.2 Induced Desorption of DDAB by SDS

4.2.1 Background

There have been studies of the DDAB - SDS mixed system in the bulk; Marques *et al.* showed the pseudo-ternary phase diagram to be complex, containing regions of lamellar liquid crystalline phases, and regions of vesicles rich in the cationic or anionic surfactant depending on the molar ratio¹⁸¹. The anionic rich region of the phase diagram has been studied further and for SDS solutions at the CMC of 0.24 wt%, which is the concentration used in this work, it was observed that the solution was stable on addition of DDAB up to a mole fraction of 0.06¹⁸². Above this mole fraction precipitation occurred. This is in agreement with work by Bai et al.¹⁸³ who identified this region as consisting of SDS-rich micelles¹⁸⁴. It is noted that these works were carried out in H₂O, and the use of D₂O, as in this study, has been seen to lead to small shifts in phase boundaries in similar systems¹⁸⁵.

4.2.2 SDS at the CMC

As discussed previously, an adsorbed layer of DDAB on mica has been shown to be very tenacious even with respect to competitive removal by other cations. In this section the behaviour of such a layer was investigated when exposed to anionic surfactants.

The first anionic surfactant investigated was sodium dodecyl sulfate (SDS), which is a well characterised compound with a CMC of 8.2 mM¹⁸⁶. SDS has been used as part of surfactant packages for EOR¹⁸⁷ and many other domestic and commercial products. The structure of SDS is shown in Figure 4.1, and the scattering length density was calculated as $0.34 \times 10^{-6} \text{ \AA}^{-2}$ from the bulk density of 1.01 g/cm³¹¹⁸.

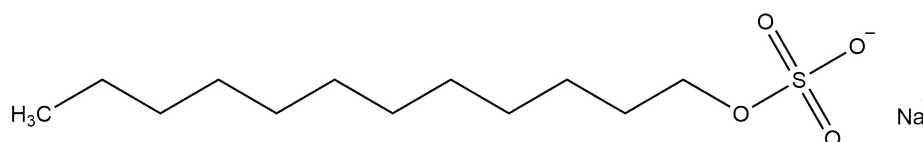
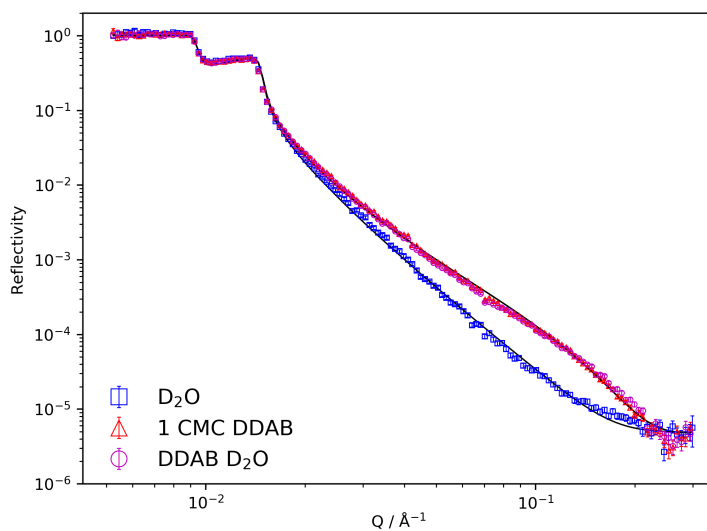


Fig. 4.1 Structure of sodium dodecyl sulfate, SDS.

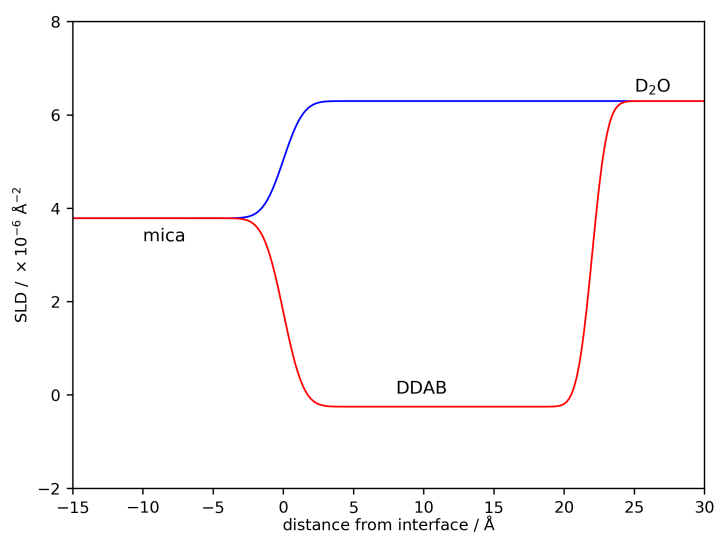
The CMC of DDAB has been determined as 0.08 mM.⁵⁵ The SLD was calculated as $-0.25 \times 10^{-6} \text{ \AA}^{-2}$ based on a bulk density of 0.946 g/cm³ from literature¹⁸⁸. A clean mica surface was characterised in three water contrasts, and then 1 CMC DDAB solution was introduced in D₂O; reflectivity data is shown in Figure 4.2a. Adsorption of an organic layer is evident in the data, and exchange of the solution to pure D₂O led to only a small change in reflectivity profile, indicating a moderate thinning or rearrangement of the layer but retention of the majority of the DDAB on the surface. The reflectivity profiles of this sequence are shown in Figure 4.2, with the fit to the structure of the initial DDAB layer and corresponding SLD profile.

The fitted parameters are shown in Table 4.1, along with the parameters fitted to the DDAB layer after the D₂O exchange (fit shown in Figure 4.3a) and fit to the mixed layer discussed later. The initial thickness of 22 Å and lack of hydration are consistent with previous observations of a DDAB bilayer on mica where the layer thicknesses were $24 \pm 2 \text{ \AA}$ and $23 \pm 2 \text{ \AA}$, both with no hydration^{55,167}. The thickness of a floating DDAB bilayer has been measured as 24 Å¹⁷². The slight reduction in thickness on exchange to D₂O is consistent with previous observations which found the DDAB layer decreased in thickness to $20 \pm 1 \text{ \AA}$ after a water/D₂O wash or after washing with 10 mM KCl or CaCl₂¹⁶⁷. At this stage it was concluded that the adsorbed DDAB layer reported in previous literature had been successfully replicated, and demonstrated to have the same high tenacity for mica.

The anionic surfactant SDS was then introduced to the adsorbed DDAB layer at a concentration of 1 CMC, and the surface re-characterised. The NR data returned exactly to that of the bare mica surface, as shown in Figure 4.3a, indicating complete removal of the bound organic layer from the mica. This observation was unexpected given the previously demonstrated tenacity of the adsorbed layer. As the DDAB has evidently desorbed from the



(a)



(b)

Fig. 4.2 (a) Reflectivity data showing the bare mica surface in D_2O (blue), then after exposure to 1 CMC DDAB (red), and further exchange of the bulk solution to pure D_2O (magenta). The shown fit is to the initially formed layer, and (b) shows the corresponding SLD profile.

surface, the nature of the solution exchange will result in the final cell solution being only SDS at the CMC. The bare mica surface measured in this solution also clearly shows that SDS does not adsorb.

Table 4.1 Fitted parameters for the DDAB structures.

| Structure | SLD / $\times 10^{-6} \text{ \AA}^{-2}$ | Thickness / \AA | Roughness / \AA | Hydration / % |
|-----------------------------|---|--------------------------|--------------------------|---------------|
| initial DDAB | -0.25 | 22 ± 2 | 3 ± 2 | 0 ± 5 |
| DDAB after D ₂ O | -0.25 | 20 ± 2 | 2 ± 2 | 0 ± 5 |
| DDAB 0.5 CMC SDS | -0.25 | 28 ± 3 | 2 ± 2 | 0 ± 5 |

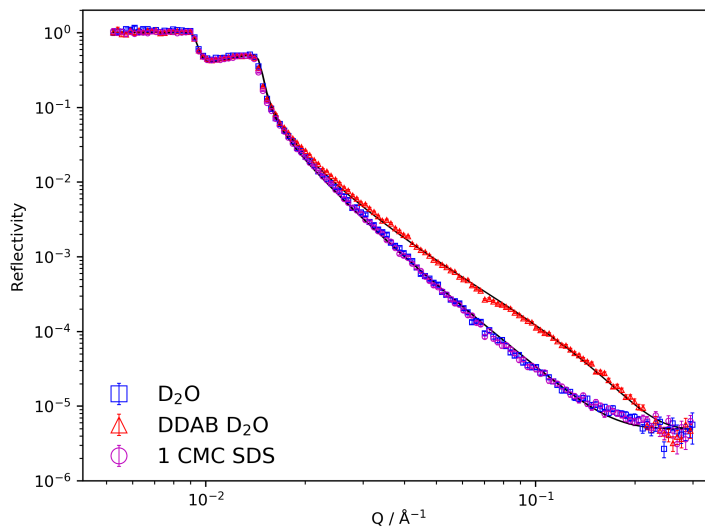
On re-exposure to DDAB at the CMC the same layer re-formed, and as before was persistent to exchange of the bulk solution to pure water; this is shown in Figure 4.3b. This data demonstrates that the mica surface has not been altered in any way by the surfactant adsorption and subsequent desorption. To verify and further understand this behaviour a later experiment investigated the interactions that occurred at a range of SDS concentrations.

The key result described in this section is significant and somewhat unexpected. The conventional logic is that to remove a cationic surfactant from an anionic substrate, a more strongly bound cationic is used to out-compete the initial compound. Here it has been clearly observed that an anionic surfactant completely removes the initially adsorbed cationic.

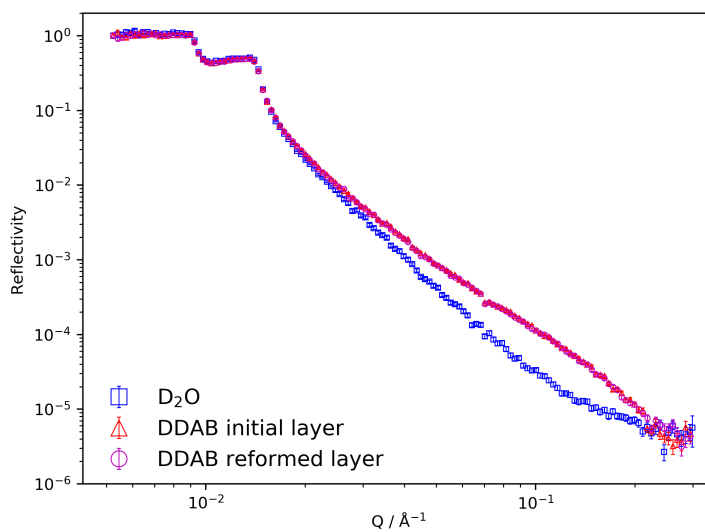
4.2.3 SDS Below the CMC

In contrast to the complete removal of DDAB present above, when the pre-adsorbed DDAB layer was exposed to an SDS concentration of 0.01 CMC SDS no desorption was observed; instead the narrowing of the Kiessig fringes in the data indicates a thickening of the adsorbed layer. NR data was collected with increasing SDS concentrations of 0.01, 0.1, 0.25, 0.5 and 0.75 CMC, which resulted in a slight further thickening of the adsorbed layer; selected profiles are shown in Figure 4.4. When the SDS concentration was increased from 0.75 to 1 CMC SDS the reflectivity profile returned to that of the bare mica as before.

Progressing directly from a DDAB layer in pure D₂O to 0.75 CMC SDS was also tested to investigate whether the stepwise concentration increase was affecting the behaviour, but the same structure as with stepwise concentration increase was recovered. The nature of exchange of the neutron cells means that the bulk solution will still have increased up to the final concentration over a finite time period, but much more quickly than in the stepwise experiment. The mixed layer formed from 0.75 CMC SDS was re-characterised after a 12 h wait and not found to have changed, suggesting the adsorbed structure is a stable one.



(a)



(b)

Fig. 4.3 (a) Reflectivity data from the bare mica surface in D_2O (blue), the DDAB layer after removal of surfactant from the bulk (red), and the same surface after further exposure to SDS at 1 CMC (magenta) showing complete layer removal. (b) Reflectivity data from the bare surface in D_2O (blue), after initial exposure to 1 CMC DDAB (red), and following layer removal and reintroduction of DDAB (magenta).

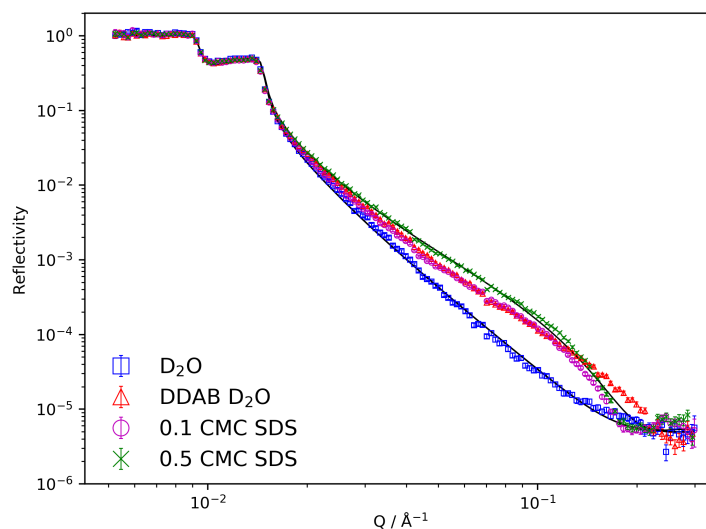


Fig. 4.4 Profiles from the pre-adsorbed DDAB layer when exposed to increasing SDS concentrations. Fit shown is to the 0.5 CMC SDS profile.

Mixed Layer Composition

The reflectivity profile recorded from the DDAB layer when exposed to 0.5 CMC SDS can be fitted to a reasonable degree with the parameters given in Table 4.1, as shown in Figure 4.4, which indicates a thickening of the adsorbed layer. This uniform block fitting of what is a mixture of two protonated surfactants gives no information about the internal structure of the layer. Whilst the protonated surfactants have similar scattering length densities, neutron reflectivity provides an opportunity to elucidate the intermediate structure formed from sub-CMC SDS by using selective deuteration to enhance the scattering from specific components within the layer. The SDS may adsorb in a layer on top of the pre-present DDAB structure, completely or partially replace the top layer, or intercalate the entire layer. A fully intercalated structure would result in anionic headgroups in close proximity to the anionic mica surface which is likely to be energetically unfavourable.

For further investigation d50-DDAB (referred to as dDDAB) was supplied by the ISIS Deuteration Facility. A characterised mica surface was exposed to 1 CMC dDDAB, then D₂O, then 0.5 CMC hSDS, to replicate the sequence described earlier which used fully protonated surfactants. The SLD of dDDAB was calculated as $6.16 \times 10^{-6} \text{ \AA}^{-2}$ by assuming the same molecular volume for dDDAB as that calculated for hDDAB. This SLD very closely matches that of D₂O. The surface was characterised after exposure to dDDAB then D₂O and

Table 4.2 Fitted parameters for the dDDAB - 0.5 CMC hSDS structure.

| Layer | SLD / $\times 10^{-6} \text{ \AA}^{-2}$ | Thickness / \AA | Roughness / \AA | % DDAB | % SDS |
|-------|---|--------------------------|--------------------------|-----------------|-----------------|
| Inner | 5.1 ± 0.5 | 16 ± 3 | 2 ± 1 | 0.7 ± 0.1 | 0.3 ± 0.1 |
| Outer | 2.9 ± 0.2 | 25 ± 3 | 2 ± 1 | 0.31 ± 0.03 | 0.69 ± 0.03 |

no change from the initial bare surface D_2O contrast was seen, but this was not unexpected and did not give an indication of lack of adsorption of dDDAB. After exposure to 0.5 CMC hSDS a change in reflectivity was observed, and as SDS has been found not to adsorb to the bare mica surface even at the CMC this gives confidence that some structure was present prior to SDS introduction.

The reflectivity profile recorded from dDDAB exposed to 0.5 CMC hSDS is shown in Figure 4.5a. A single uniform layer could not fit the data. When the model was increased to two layers with variable thicknesses and SLDs constrained between the calculated SLD of dDDAB and hSDS a good fit to the data was achieved. The SLD profile to the fitted model is shown in Figure 4.5b, and the parameters are given in Table 4.2.

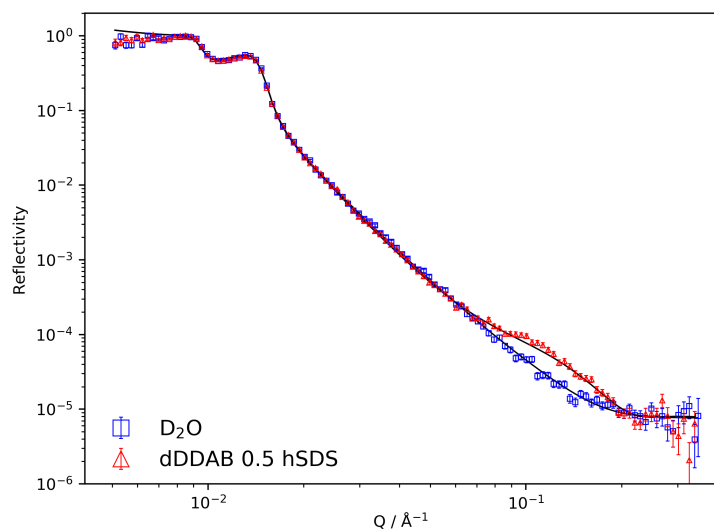
The overall thickness of the layer is approximately 41 \AA , which is thicker than the fit to the mixed layer formed from the two protonated surfactants (28 \AA) though the uncertainties in both thicknesses are large. Some variability between samples is also not unexpected given that mica is a natural mineral and tests with both protonated surfactants on different crystals did give slight variations in profile. From the fitted SLD of a layer and the calculated SLDs of the two components, A and B, it is possible to estimate the volume fraction, ϕ , of each species in that layer if it is assumed there is no hydration:

$$\phi_A = \frac{SLD_{tot} - SLD_B}{SLD_A - SLD_B} \quad (4.1)$$

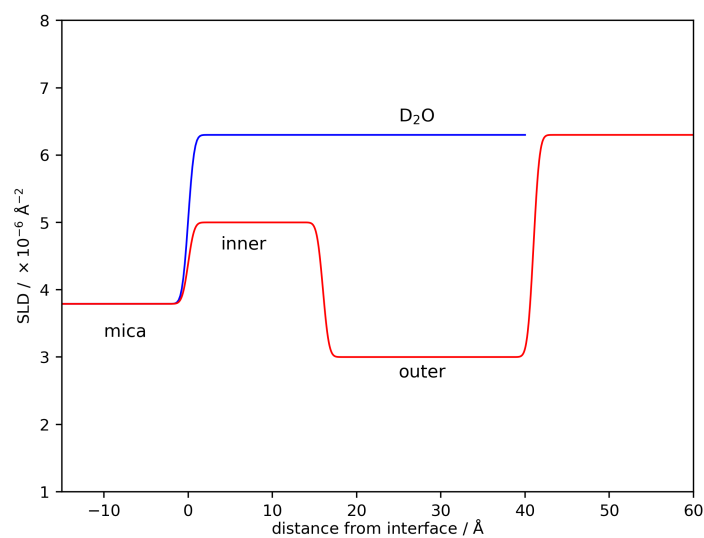
From further knowledge of the molecular volumes, V_A and V_B , which may be calculated from bulk densities, the mole fraction of each component, X , in a layer may be determined.

$$X_A = \frac{\phi_A}{\phi_A + (V_A/V_B)(1 - \phi_A)} \quad (4.2)$$

From bulk densities the molecular volumes of DDAB and SDS have been calculated as 812 and 474 \AA^3 respectively. The molar fractions of the components for each of the two layers in the fit have been calculated and these are shown in Table 4.2 with uncertainties propagated from the uncertainty in SLD. The assumption of no hydration in these calculations



(a)



(b)

Fig. 4.5 (a) Reflectivity profile of a pre-adsorbed dDDAB when exposed to 0.5 CMC hSDS. (b) SLD profile of the fitted model which consists of two layers.

was considered relatively robust given the lack of fitted hydration to the pure DDAB layer, but may add further uncertainty to the resulting values. Additional bulk water contrasts would allow the hydrations of the layers to be measured more accurately.

The compositions of the two fitted layers are logically consistent; the inner layer is predominantly DDAB as might be expected close to the anionic mica surface which will have a repulsive interaction with any SDS. The outer layer is mostly SDS, which is the only species present in the bulk solution and will have a large driving force to include into the layer, as discussed in more detail later. Whilst the fitting model considered consists of just two layers, the true structure could have a more continuous change in composition.

On increasing the SDS concentration to the CMC, the profile returned to that of the bare surface. After this, when hDDAB was reintroduced in D₂O no adsorbed layer was observed. This is in contrast to a large number of previous results where DDAB has been seen to adsorb, and it was postulated that a dDDAB layer may still have been present on the surface and precluding adsorption of hDDAB. The bulk solution was exchanged to H₂O which would show the presence of a deuterated adsorbed layer but none could be observed, and the reflectivity profile was the same as the bare surface contrasts. Further attempts to adsorb either hDDAB or dDDAB were also unsuccessful leading to the conclusion that some alternative species was occluding the surface in a layer too thin to be observed in either the H₂O or D₂O contrast; possibilities for this are NH₃ or N(CH₃)₃ impurities from the dDDAB, which was not used further. As the presence of an impurity may have altered the structure formed from dDDAB and hSDS which was described earlier, this specific dataset was treated with caution.

4.2.4 Discussion

The adsorbed layer of DDAB is significantly thicker at 22 Å than the molecular length, which has been calculated as 16.7 Å⁵⁵, but less than twice this value. The layer has hence been characterised as an interdigitated and/or tilted bilayer. The structure of the bilayer has been analysed in more detail by others⁵⁵, and is not the focus of this work. The slight decrease in layer thickness after washing without any increase in hydration is ascribed to a slight reordering of the layer and perhaps removal of a small proportion of the surfactant molecules, but there is only a very minor change in the layer.

With the cationic DDAB molecules liberated from the mica surface, charge compensation of the anionic mica surface is still required. The potassium cations initially bound to the freshly cleaved mica surface were replaced by the DDAB layer and will no longer be present in the sample cell after the DDAB, D₂O, and SDS washes through the cell. It is therefore considered that the only available cations will be the Na⁺ counter-ions from the SDS solution.

Na^+ is a strongly hydrated ion which has been observed to bind as an outer sphere complex on mica¹⁸⁹ compared to inner sphere adsorption of the native K^+ . It is not expected to bind as strongly to mica, or other clay minerals, as the native K^+ ¹⁹⁰ or the quaternary ammonium ions which formed the bilayer. This was confirmed experimentally in the mica ion-exchange isotherms described in Section 5.1.3.

The DDAB bilayer formed on mica has shown to be persistent to washes with a solution of the divalent Ca^{2+} salt at 10 mM, which might suggest that the DDAB has a more favourable interaction with the mica than the Ca^{2+} ion. The observation that DDAB is removed from mica by SDS micelles at the lower concentration of 8.2 mM, when the only ion available to compensate the surface charge is Na^+ , suggests that the favourable energetic interaction of incorporating the DDAB molecules into the anionic SDS micelles is greater than the difference in strength of interaction between the mica - DDAB and mica - Na^+ . The inclusion of cationic surfactant molecules into anionic micelles is expected to be significantly favourable, as there is both an attractive interaction between the oppositely charged head groups and a reduced repulsion between the like-charged head groups now separated by the included cationic surfactant and we conclude that this driving force is sufficient to result in DDAB removal.

Using the area per molecule of DDAB in the adsorbed layer (32 \AA^2 as calculated from the molecular volume and layer thickness), the dimensions of the mica - liquid interface in the cell ($40 \text{ mm} \times 85 \text{ mm}$), and the cell volume (2 ml) which was the volume of SDS solution in 'initial' contact with the DDAB layer, a very rough estimate of the concentration ratio of DDAB to SDS can be calculated when the SDS was introduced to the cell. The concentration of DDAB in this solution was calculated as $9 \times 10^{-3} \text{ mM}$, three orders of magnitude lower than the SDS in solution (8.2 mM). The molar ratio is then 1×10^{-3} , well below the minimum value for precipitation of 0.06 proposed by Marques et al.¹⁸² The estimate of the concentration ratio is very approximate and the local ratio at the DDAB layer surface will be higher before the layer de-adsorbs, but no precipitation was observed either in the solution leaving the cell or inside the cell after disassembly.

The observation that DDAB desorption occurred only at the CMC, and not below, indicates that the desorption is specifically induced by micelles and not by the free anionic surfactant. The driving forces for desorption will be both enthalpic and entropic. On inclusion of the DDAB molecules into SDS micelles there will be an attractive interaction between the oppositely charged headgroups, as well as reduced repulsion from separation of adjacent DDAB and SDS headgroups in the adsorbed layer and micelles respectively. These enthalpic

effects will be much larger when micelles are present than when only free SDS molecules are in solution. On the DDAB rich side of the phase diagram, Bai et al.¹⁸³ have reported an exothermic process on uptake of SDS into DDAB micelles with an enthalpy of -29.5 kJ/mol, which is consistent with these favourable interactions. The entropy of mixing when DDAB molecules leave the ordered surface layer and include into micelles will also favour this process.

Below the CMC of SDS, inclusion and partial replacement of the pre-adsorbed DDAB layer is observed. Again there will be both enthalpic and entropic driving forces. The deuteration study described in Section 4.2.3 suggests that there is little SDS in close proximity to the mica surface, which would repel the anionic headgroups. The structure of a DDAB bilayer suggested by MD simulations, as in Section 3.4.3, was a dense layer adjacent to the mica and a more flattened and less packed layer on top of this. The SDS might interact more strongly with this less well-ordered layer and result in a smaller tilt angle layer forming after SDS inclusion. This would result in a thickening of the total organic layer, as experimentally determined. The structure and relative composition of the mixed layer formed here could differ from an equilibrium structure, due to the two step formation and non-equilibrium bound DDAB.

A schematic of the differing behaviour of a DDAB layer on mica exposed to SDS below and above the CMC is shown in Figure 4.6.

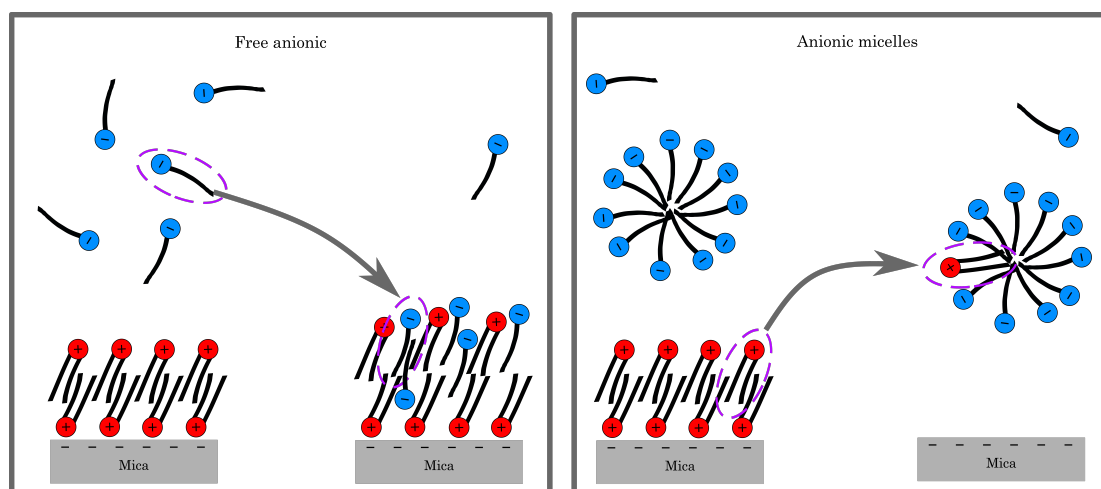


Fig. 4.6 A schematic of the differing behaviour of an adsorbed DDAB layer (shown in red) when exposed to the anionic surfactant SDS (shown in blue) below (left) and above (right) the CMC.

4.2.5 Surfactant Interaction in Organoclays

As part of a larger investigation into the structures and behaviour of organically modified clays (organoclays), which is not discussed in this thesis, a study was also conducted to see if the interaction described between DDAB and SDS on mica also occurred in the interlayer spaces in swelling clay minerals. Part of the aim of this was to look for a convenient offline measurement technique to expand on the neutron measurements.

Organoclays are formed from intercalation of organic molecules into the interlayer spacing of swelling clay minerals^{191–193}, such as the mineral montmorillonite which is discussed in Section 1.1.3. Generally the organic species are cationic, to exchange for the inorganic cations in the native clay mineral, and quaternary ammonium ions are frequently used. The applications of organoclays are varied, ranging from viscosity modifiers to pollutant removal tools^{194,195}.

Organoclays can be synthesised via an ion exchange process in solution¹⁹⁶, or by a mechanochemical process¹⁹⁷. Whilst the amount of intercalated organic does depend on the CEC of the clay, different amounts can intercalate both up to and over the CEC¹⁹⁸. The basal spacing, which can be monitored by XRD, is increased upon intercalation and varies with the quantity and orientation of organic between the clay layers.

The organoclay used in this study was synthesised from SWy-2, a sodium montmorillonite from the Source Clays project which is a collection of well classified clays. The CEC of SWy-2 has been reported as 76.4 meq/100g in the literature⁸². 1 CEC of DDAB was chosen for the organoclay. The synthesis method was adapted from Singla et al.¹⁹⁹, and in brief involved mixing a solution of DDAB into a slurry of clay, allowing the mixture to equilibrate, then filtering, washing excess surfactant out, then drying the organoclay formed. The resultant organoclay was characterised with XRD and TGA (not shown), to confirm essentially all the organic had intercalated into the clay. The XRD patterns from the raw and modified clay are shown in Figure 4.7, showing the increase in layer spacing on organic modification from approximately 14.5 Å to 21.5 Å. This increased value is consistent with that found by others for 1 CEC of DDAB intercalated into a montmorillonite²⁰⁰.

In Section 4.2.4 it was discussed how in the neutron reflectivity experiments into induced desorption, the anionic SDS was in vast excess of the cationic DDAB. In the case of the organoclay there is a large quantity of DDAB in a small mass of clay, and to attempt to ensure some parity in the experiments it was necessary to estimate the ratio of cationic to anionic surfactant. From a given mass of montmorillonite, M_g , modified with 1 CEC of DDAB, the

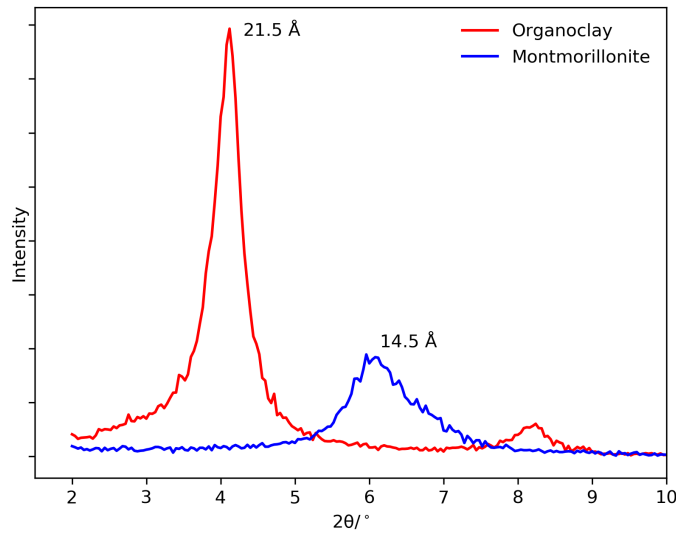


Fig. 4.7 XRD patterns from the raw montmorillonite, and synthesised organoclay. The peak shifting to lower angle shows an increase in layer spacing. The values of the d-spacing calculated from the peak heights are annotated. The peak at $2\theta = 8.2^\circ$ in the XRD for the organoclay is the second order peak.

resultant mass of organoclay, OM_g , is given by Equation 4.3. ‘CEC’ is in units of meq/100g by convention, and ‘diff’ is the difference in mass per mole of DDAB which is intercalated into the clay. It can be assumed that for each mole of DDAB that intercalates into the clay, the change in mass is $359.7 \text{ g} = MW_{DDAB} - (MW_{Br^-} + MW_{Na^+}) = 462.6 - (79.9 + 23.0)$. This is based on the assumption that only the ammonium cation intercalates, without the bromide counter-ion, and the sodium cations in the clay are completely replaced as might be expected for 1 CEC of surfactant addition.

$$OM_g = M_g + M_g \left(\frac{CEC}{10^5} \times diff \right) \quad (4.3)$$

By recognising that in Equation 4.3 the mass of DDA^+ (the didodecyldimethylammonium cation) is equal to $(M_g(CEC \times diff \times 10^{-5}))$, the mass of DDA^+ , DDA_g , in a given mass of organoclay, OM_g , can be calculated from Equation 4.4.

$$DDA_g = \frac{OM_g}{1 + (10^5 / (CEC \times diff))} \quad (4.4)$$

The mass of DDA^+ can then be converted into number of moles by dividing by the molecular weight of DDA^+ , as normal. $\text{MW}_{\text{DDA}^+} = 382.7 \text{ g/mol}$ ($\text{MW}_{\text{DDAB}} - \text{MW}_{\text{Br}}$).

From these calculations, and the CEC of 76.4 meq/100g, 0.2 g of 1 CEC organoclay contains approximately 0.11 mmoles of DDA^+ . 0.2 g of organoclay was the smallest amount that could be treated and recovered in sufficient quantity to provide an X-ray diffraction sample. The organoclay samples were exposed to 45 ml of 0.1 CMC and 1 CMC SDS solution. The amount of SDS in these solutions was 0.037 and 0.37 mmoles respectively. Even at these very low masses of organoclay and relatively large volumes of solution, the total amounts of the cationic and anionic surfactant present in the system are comparable, and it is experimentally difficult to bias the ratio further in favour of the anionic.

The testing was conducted by immersing 0.2 g of organoclay in different solutions, sonication for 20 min to aid dispersal of the clay, then equilibration by tumbling for 24 h. The samples were then centrifuged at 15000 g for 30 min, the supernatant carefully removed and the solid extracted. The solid was then dried *in vacuo* at 80°C for 6 h then ground as much as possible in an agate pestle and mortar. During sonication it was evident that the organoclay did not disperse well in aqueous media; the hydrophobicity of the layers resulted in the particles visibly re-aggregating almost instantly when broken apart by the sonication. An additional re-dispersion step to remove any surfactant deposited on the clay during drying was considered, but even after one dispersal and recovery the quantity of clay was only just sufficient to recover enough for XRD analysis.

For the organoclay in 1 CMC SDS a visible change in the clay was observed; some of the sample clumped together in a gel-like state. This was not seen for the organoclay in 0.1 CMC SDS or in pure water, but was more similar to the behaviour of unmodified montmorillonite in water. This suggests there may be some conversion of organoclay back to raw montmorillonite occurring, presumably facilitated by removal of DDAB from the clay by the SDS present at the CMC.

The XRD data collected from the resultant samples is shown in Figure 4.8, along with diffraction from the untreated clay and organically modified clay. From treatment by 0.1 CMC SDS little change is visible in the main diffraction peak, with a small degree of broadening. For the organoclay treated with 1 CMC SDS a clear change is seen. The sharp peak is strongly broadened, suggesting a range of different d-spacings present in the sample. Finite-size broadening might also cause this effect, but was considered less likely in this case. The peak is skewed to the low angle/larger spacing side. It is assumed that this is caused by SDS including into the hydrophobic interlayers and further increasing the layer spacing.

There also some additional sharp peaks evident in the data, most noticeably at $2\theta = 2.6^\circ$, which corresponds to a spacing of approximately 33 \AA . This is close to the lattice parameters for the crystalline structures of the monohydrate and hemihydrate of SDS, which are 29 \AA and 31 \AA respectively^{201,202}, and is likely due to crystallisation of a bulk structure of SDS, or liberated DDAB. As noted earlier, washing of the treated clays to remove bulk solution was not carried out so during drying any solutes in free solution may have precipitated.

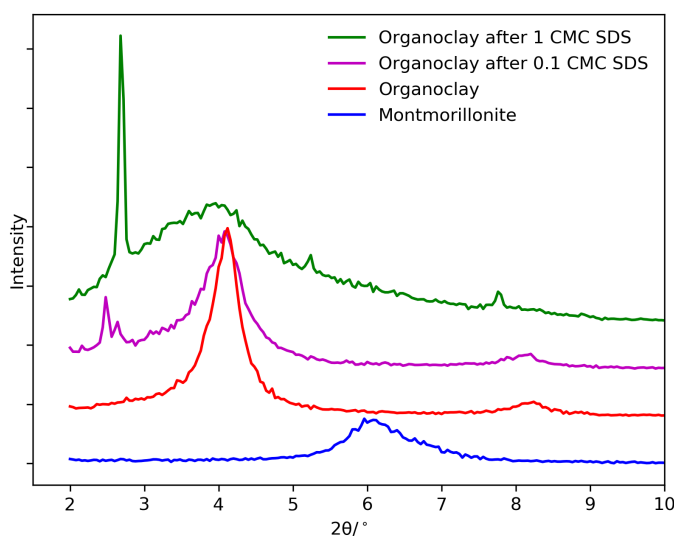


Fig. 4.8 XRD data from the untreated montmorillonite, synthesised organoclay, and organoclay after exposure to different concentrations of SDS. Profiles are offset for clarity.

It is evident that the SDS in solution is having some effect on the structure of the organoclay, and that this effect is significantly more pronounced for the 1 CMC SDS than for 0.1 CMC. A major issue in the experimental realisation of the interaction between the surfactants is the inaccessibility of the hydrophobic interlayer space to the surfactant in solution. Extended sonication may improve this. Exchange of the bulk solution, perhaps in a continuous nature, might also help bias the ratio in favour of the anionic in solution to ensure the equilibrium reached is that with the known concentration of SDS and negligible DDAB in solution.

In summary, these results present an interesting variety of behaviour much in accord with literature and expectations, and several new findings. However, the data is insufficient to conclude whether the mixed cationic/anionic surfactant behaviour observed on the basal plane of mica by NR is mirrored in the system of organically modified swelling clay minerals.

4.3 Diacid Effect on Pre-Adsorbed DDAB

In Section 4.2 it was shown that the induced desorption behaviour of the cationic DDAB from mica was a function of the presence of micelles of SDS. It is important to consider that this DDAB removal was not simply caused by the concentration of negatively charged species in solution. To verify this, a related series of measurements as were performed with SDS (which micellises) were repeated with a non-micellising species. Disodium succinate was used, the structure of which is given in Figure 4.9, as the short chain diacid is unlikely to show any aggregation behaviour due to the short chain length and distributed charge in solution. Based on a bulk density of 1.56 g/cm^3 for succinic acid²⁰³, and the assumption that replacement of the protons for sodium ions does not significantly alter the molecular volume, the SLD was estimated as $2.4 \times 10^{-6} \text{ \AA}^{-2}$.

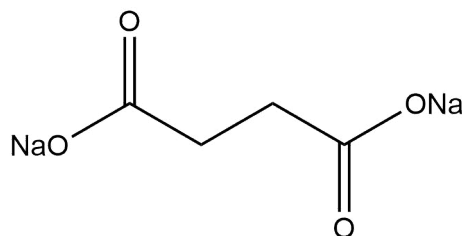
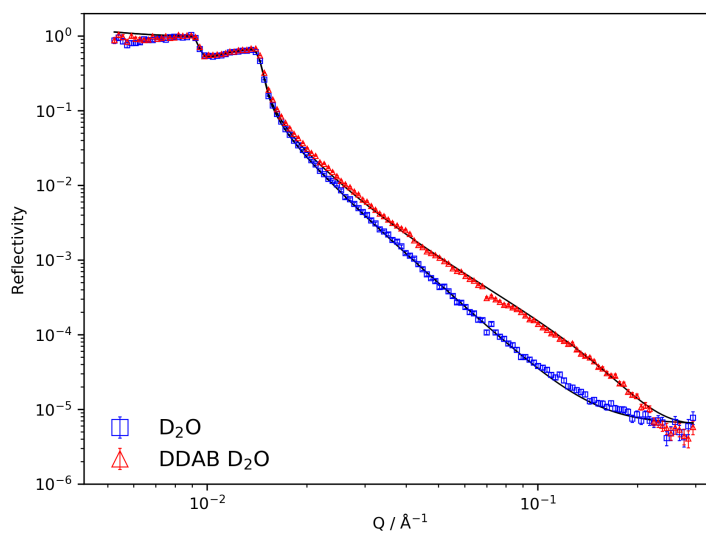


Fig. 4.9 Structure of disodium succinate.

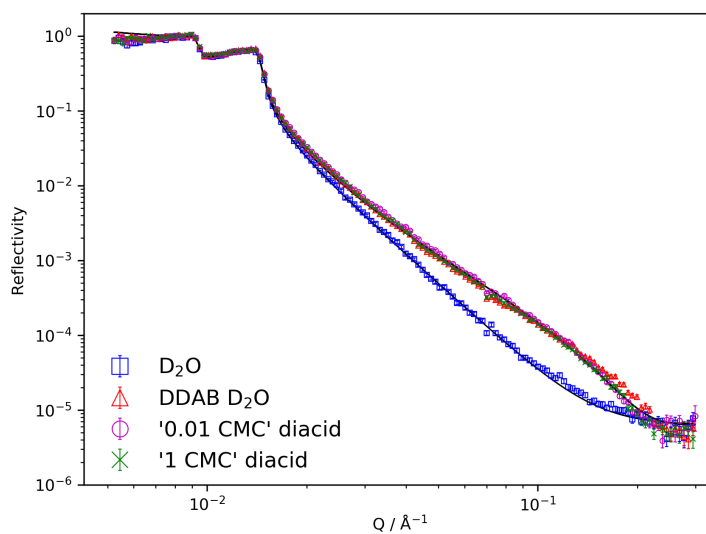
A new mica substrate was characterised by NR in three water contrasts, then a DDAB layer was adsorbed from 1 CMC solution. On exchange of the bulk to pure D_2O little change in reflectivity was observed and the structure of the layer after this exchange is shown in Figure 4.10a. This is consistent with the strong adsorption of DDAB demonstrated in prior sections.

This DDAB layer was then exposed to four increasing concentrations of succinate. These concentrations are expressed relative to the CMC of SDS (8.2 mM) for comparison to the results discussed in Section 4.2, and were 0.01, 0.1, 0.5, and 1 'CMC'. The reflectivity profiles from these systems are shown in Figure 4.10b. A small thickening in the hydrocarbon layer on the surface is visible on the addition of diacid, and essentially no further change as the diacid concentration was increased up to the CMC of SDS.

The NR profile for the formed layer may be fitted with a layer of uniform SLD with parameters given in Table 4.3. The fitted SLD is slightly higher than that of pure DDAB which is consistent with some inclusion of the higher SLD diacid into the layer. With a single contrast and both protonated surfactants it is not possible to distinguish between inclusion of



(a)



(b)

Fig. 4.10 (a) Reflectivity data showing the persistence of a DDAB layer adsorbed to the surface when the bulk solution was exchanged to water, (b) and the effect of adding increasing concentrations of disodium succinate. Concentrations are relative to the CMC of SDS, 8.2mM.

the diacid into the layer, and adsorption in a separate layer on top of the pre-adsorbed DDAB. The thickening of the layer by approximately 4 \AA could also be consistent with either model.

Table 4.3 Fitted parameters for the DDAB structures on exposure to diacid.

| Structure | SLD / $\times 10^{-6} \text{ \AA}^{-2}$ | Thickness / \AA | Roughness / \AA | Hydration / % |
|-----------------------------------|---|--------------------------|--------------------------|---------------|
| DDAB after D ₂ O | -0.25 | 19 ± 2 | 4 ± 3 | 0 ± 10 |
| DDAB exposed to 1 'CMC' diacid | 0.4 ± 0.3 | 23 ± 2 | 4 ± 2 | - |

As the SLD was allowed to vary to include penetration of the diacid into the DDAB layer and only one bulk water contrast was recorded, it was not possible to determine the extent of hydration of the layer, but the low SLD shows there is no significant hydration. At no concentration of disodium succinate was desorption observed, reinforcing the conclusion that the desorption seen for the DDAB/SDS system was indeed facilitated by the anionic micelles.

4.4 Induced Desorption of DDAB by AOT

4.4.1 Induced Desorption

It was of interest to investigate whether the characteristic behaviour of the DDAB/SDS system was generalisable to other surfactants.

The behaviour of a pre-adsorbed layer of DDAB on mica was further investigated when exposed to NaAOT, an alternative anionic surfactant, the structure of which is shown in Figure 4.11. The CMC of NaAOT is 2.5 mM¹²⁴, and as described in Section 3.1.2 the SLD was calculated as $0.65 \times 10^{-6} \text{ \AA}^{-2}$.

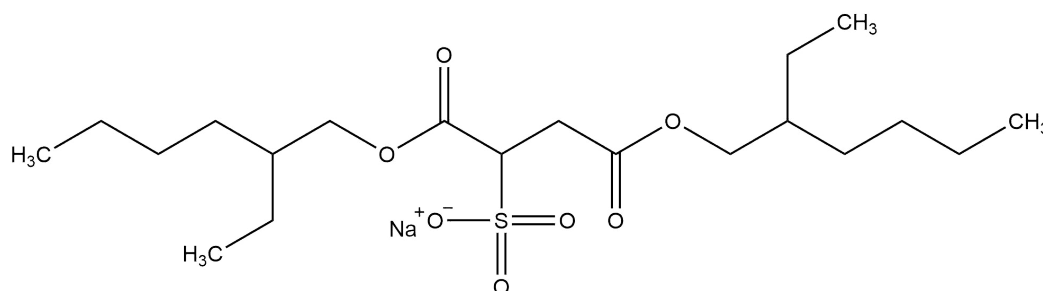


Fig. 4.11 Structure of NaAOT

As before, a DDAB layer was adsorbed onto a mica substrate and characterised before and after exchange of the bulk from DDAB solution to pure D₂O. The fitted parameters are given in Table 4.4, and are consistent with the previous fits to adsorbed DDAB.

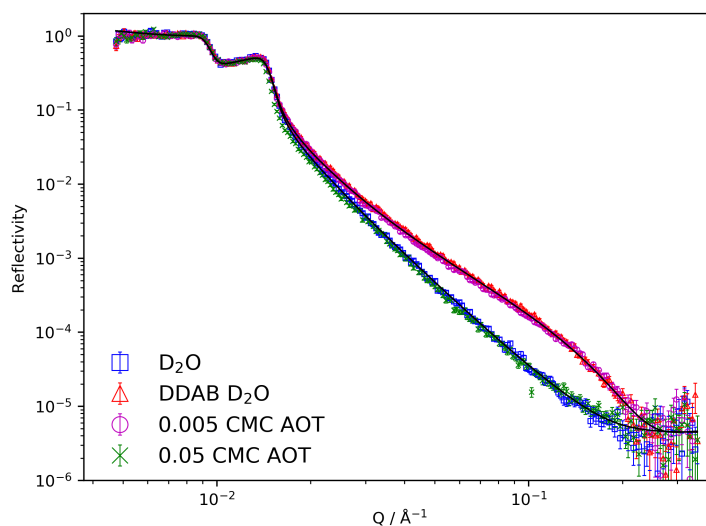


Fig. 4.12 Reflectivity data from a bare mica surface in D₂O (blue), after DDAB adsorption and subsequent exchange back into D₂O (red), and after exposure of such a layer to NaAOT at 0.005 CMC (magenta) or 0.005 CMC (green).

Table 4.4 Fitted parameters for the DDAB layer.

| Structure | SLD / $\times 10^{-6} \text{ \AA}^{-2}$ | Thickness / \AA | Roughness / \AA | Hydration / % |
|-----------------------------|---|--------------------------|--------------------------|---------------|
| DDAB after D ₂ O | -0.25 | 22 | 1 | 0 |

The solution was then exchanged to 0.05 CMC AOT and the reflectivity profile measured. Figure 4.12 presents the recorded data; even at this low AOT concentration the reflectivity profile returned exactly to that of the bare mica surface indicating complete desorption of the DDAB layer. The DDAB layer was re-adsorbed as before, and seen to form the same structure as the initial layer.

4.4.2 Concentration Dependence

On the same crystal after re-adsorption of the DDAB layer and exchange into D₂O, the even lower concentration of 0.005 CMC (0.125 mM) was introduced into the cell. At this lowered

concentration desorption did not now occur; instead there was no discernible change in the recorded data from that of the DDAB layer. This dataset is also presented in Figure 4.12.

Despite the enhanced mixing chamber used for HPLC solution input and minimum 10% per input protocol, it was considered that the removal effect seen for 0.05 CMC AOT could potentially be an artefact due to the mixing process of HPLC inputs resulting in pulses of higher concentration AOT coming into contact with the substrate. To verify that this was not the case a further experiment was performed utilising a stock solution of 0.05 CMC AOT and no mixing. A pre-adsorbed DDAB layer was seen to be removed by this concentration, just as when the concentration was generated by mixing in the pump.

4.4.3 Discussion

No inclusion of the AOT into the DDAB layer is resolved at the concentrations tested. At 0.005 CMC AOT where DDAB desorption was not observed, no change in reflectivity profile was seen. Whilst the SLDs of the AOT and DDAB are quite similar the fact that no change from the initial DDAB layer was seen strongly suggests that the AOT has not included into or partially replaced the DDAB layer.

Clearly, despite the evident similarities between them, the anionic surfactants SDS and AOT result in very different behaviour when a pre-adsorbed DDAB layer is exposed to a surfactant solution. These differences, and possible explanations for them, are discussed further in Section 4.6.

4.5 Interaction of Adsorbed DDAB with $C_{12}E_5$

4.5.1 Mixed Layer Formation and Partial Desorption

To observe the relative importance of enthalpic effects, driven by surfactant charge, and entropic effects from mixing into micelles during induced desorption, analogous experiments to those described earlier were conducted using a non-ionic surfactant in solution rather than an anionic. The non-ionic surfactant $C_{12}E_5$ was used for this investigation. The structure of the surfactant, and adsorption behaviour of $C_{12}E_5$ on mica are discussed in Section 3.2, and it was found that the surfactant adsorbed as only a very diffuse or hydrated layer with low surface coverage. As described there, experiments using $C_{12}E_5$ were conducted with

Table 4.5 Fitted parameters for the structures for DDAB and after exposure to C₁₂E₅.

| Structure | SLD / $\times 10^{-6} \text{ \AA}^{-2}$ | Thickness / \AA | Roughness / \AA | Hydration / % |
|--|---|--------------------------|--------------------------|---------------|
| DDAB after D ₂ O | -0.25 | 16 \pm 2 | 1 \pm 2 | 10 \pm 5 |
| DDAB then 1 CMC C ₁₂ E ₅ | -0.2 \pm 0.4 | 24 \pm 3 | 4 \pm 2 | - |

temperature control both of the experimental cells and stock solutions, all fixed at 25°C. The SLD was calculated as $0.13 \times 10^{-6} \text{ \AA}^{-2}$.

As in previous experiments a DDAB layer was adsorbed to the mica surface, and the bulk solution exchanged to pure water. In this case the adsorbed layer was slightly thinner than those previously observed, but still dense and unhydrated, with parameters given in Table 4.5. A solution of C₁₂E₅ at 0.2 CMC was exchanged into the cell. This resulted in a thickening of the hydrocarbon layer on the mica surface, as shown in Figure 4.14, which is comparable to the behaviour observed for DDAB exposed to the anionic SDS below the CMC. The concentration of C₁₂E₅ was further increased through the series 0.5, 1 and 2 CMC which resulted in only very slight further thickening of the layer, and no total desorption even at twice the CMC. Experimental data from the initially formed DDAB layer and the same layer upon exposure to increasing concentrations of C₁₂E₅ are shown in Figures 4.13 and 4.14 respectively with fits to the data. The reflectivity profile for the mixed layer could be fitted with a single layer of uniform SLD between the SLDs of pure DDAB and C₁₂E₅, which are both similar when compared to the bulk SLD of D₂O. It is not possible to gain information about the relative amounts of the two species using this contrast. Fitted parameters are given in Table 4.5.

The difference between the reflectivity profile from this DDAB layer exposed to C₁₂E₅ and the recorded data for a bare mica surface exposed to C₁₂E₅ (Figure 3.21) is large. The resultant structure is not therefore simply complete replacement of the DDAB by non-ionic surfactant.

4.5.2 Layer Re-Formation

In the case of the studied anionic molecules interacting with an adsorbed layer, sodium counter ions from the anionics were always present and assumed to compensate the anionic mica surface after desorption (where it was found to occur). In the case of the non-ionic surfactant no cations are present in the solution, and it was considered that this might be preventing desorption of the DDAB. To test this hypothesis the mixed layer formed from

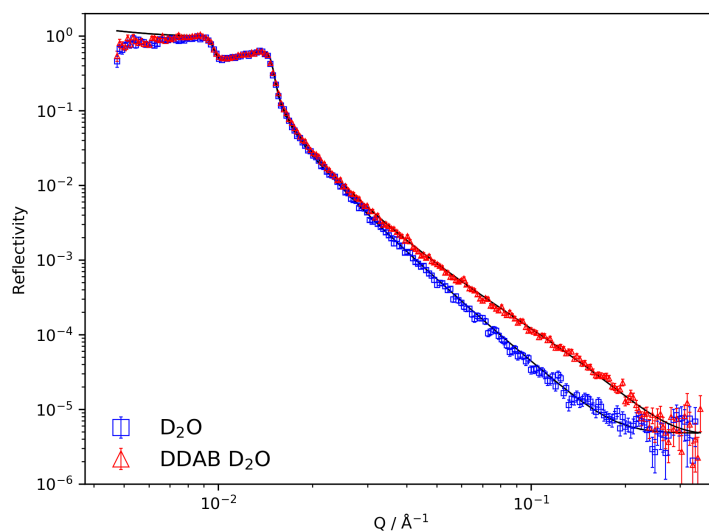


Fig. 4.13 Reflectivity profile from the adsorbed DDAB layer after exchange into pure D_2O .

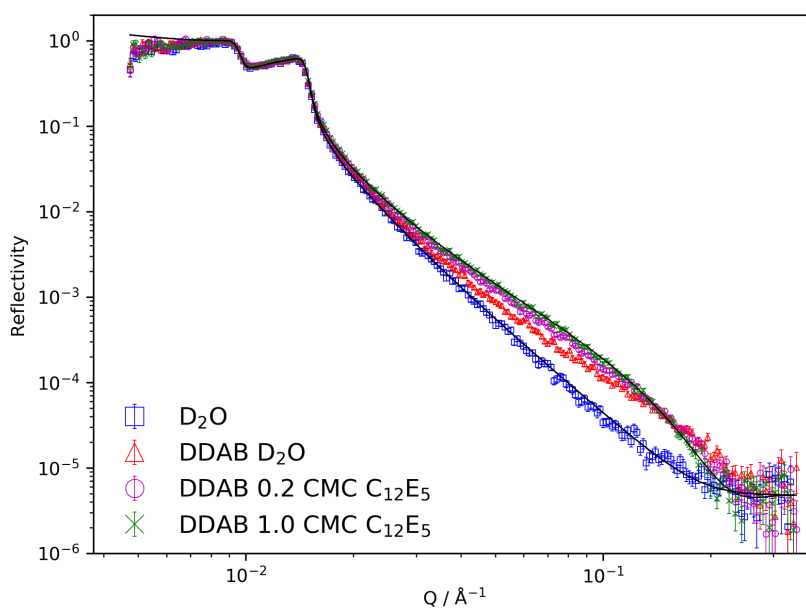


Fig. 4.14 Reflectivity profile from the DDAB layer on exposure to increasing concentrations of $C_{12}E_5$. Fit shown is to the mixed layer formed from $C_{12}E_5$ at 1 CMC.

DDAB and 2 CMC $C_{12}E_5$ was further exchanged into a solution of 10 mM NaCl. As 10 mM KCl or $CaCl_2$, both of which will show a greater affinity for the mica surface than sodium,

Table 4.6 Fitted structure to the DDAB layer after sequential exposure to 2 CMC C₁₂E₅ then 10 mM NaCl.

| Layer | SLD / $\times 10^{-6} \text{ \AA}^{-2}$ | Thickness / \AA | Roughness / \AA | Hydration / % |
|-------|---|--------------------------|--------------------------|---------------|
| Water | 6.3 | 5 ± 2 | 1 ± 3 | - |
| DDAB | -0.25 | 23 ± 3 | 1 ± 3 | 46 ± 3 |

have been shown not to remove DDAB from the surface¹⁶⁷, this salt solution would not be expected to remove an unaltered DDAB layer. The exchange did result in a change in profile, with the reflectivity shown in Figure 4.15, but the data does not return to that from the bare mica, indicating the persistence of some organic.

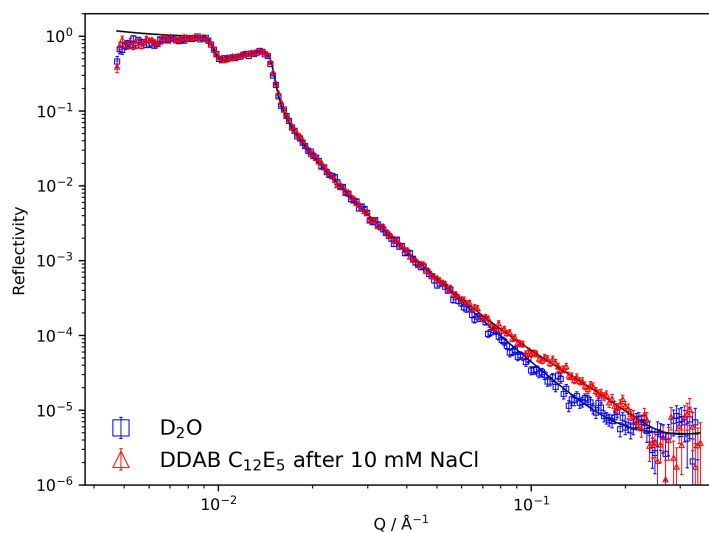
This new profile could not be fitted with a single layer of uniform SLD. As there was no strong interaction between the non-ionic surfactant and the mica surface, for the purpose of further fitting it was assumed that the remaining organic material was entirely DDAB. This makes little difference to the fitting as the SLDs of DDAB and C₁₂E₅ are similar (-0.25 and $0.13 \times 10^{-6} \text{ \AA}^{-2}$ respectively). The data could be fitted by a two layer model, with a water layer adjacent to the mica surface and a hydrated surfactant layer beyond this; fitted parameters are given in Table 4.6.

The non-ionic concentration was then brought back to 1 CMC in a solution of 10 mM NaCl, which as noted earlier has been shown not to influence the CMC. Unexpectedly this led to an adsorbed profile very close to that seen when the initially adsorbed DDAB layer was exposed to C₁₂E₅, as shown in Figure 4.16, in contrast with the very diffuse adsorption seen for C₁₂E₅ on bare mica. Increasing the concentration to 2 CMC, to ensure the system truly was above the CMC, did not cause further changes.

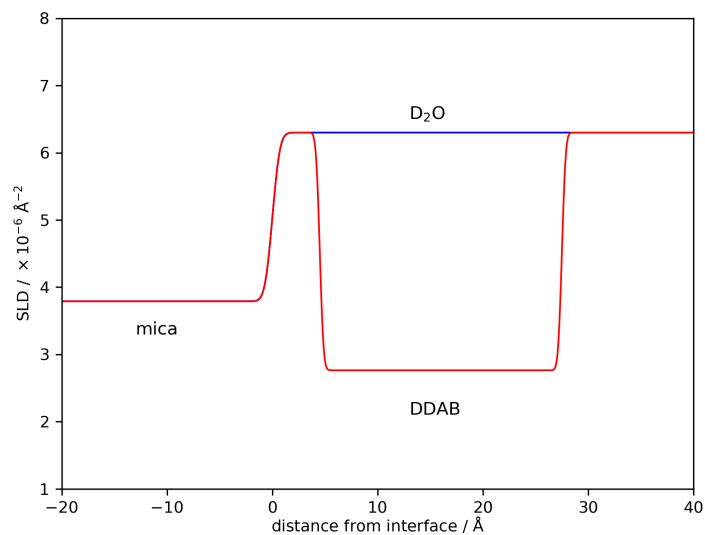
Further exchange into pure D₂O again resulted in near complete layer removal, but with definite evidence of some remaining surface organic, as was seen after exchange of the initial mixed layer into NaCl solution. Reintroduction of 1 CMC C₁₂E₅ led to a thicker organic layer forming, though the reduced amplitude of the fringe relative to the prior layer indicates a thinner structure. Profiles from this sequence are shown in Figure 4.17.

4.5.3 Discussion

This series of results shows that the behaviour of an adsorbed DDAB layer is very different on exposure to the non-ionic surfactant C₁₂E₅ compared to the behaviour seen in Sections 4.2 and 4.4 for exposure to the anionic surfactants tested previously; at no point did the non-ionic



(a)



(b)

Fig. 4.15 (a) Reflectivity profile of the mixed layer formed from DDAB exposed to $C_{12}E_5$ at 2 CMC, then exchanged into 10 mM NaCl. (b) SLD profile of the calculated fit.

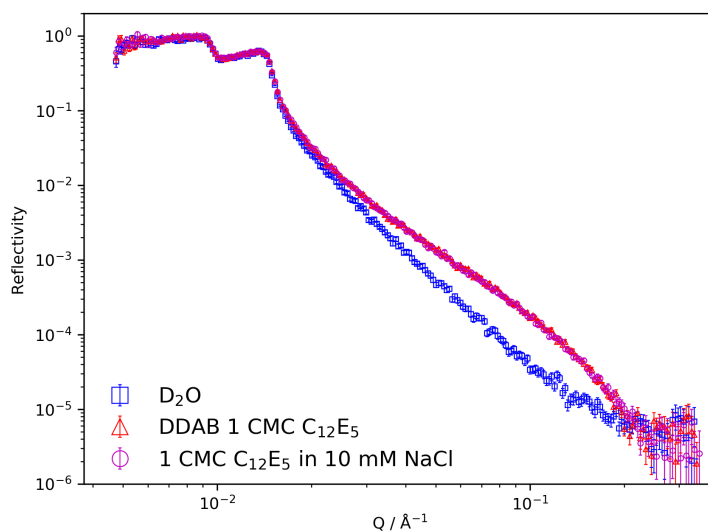


Fig. 4.16 Reflectivity profile of the mixed layer formed from DDAB exposed to C₁₂E₅, then after exchange into 10 mM NaCl and reintroduction of 1 CMC C₁₂E₅ in 10 mM NaCl.

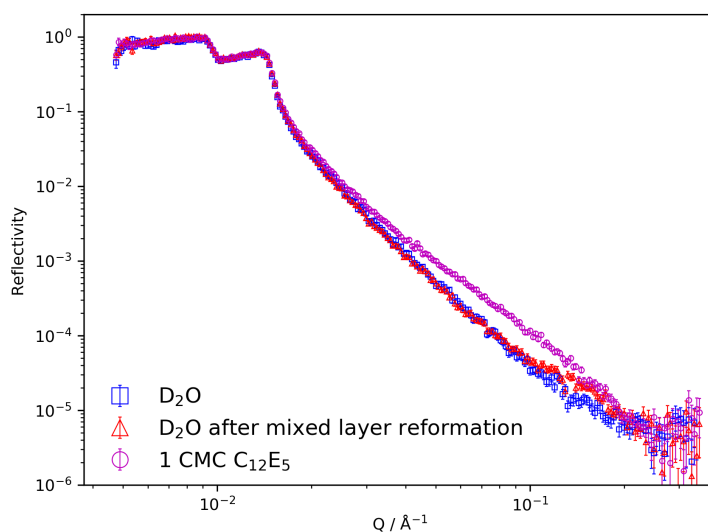


Fig. 4.17 Reflectivity profiles from the mica surface showing the initial bare characterisation in D₂O (blue), after partial desorption, reformation and further removal of the mixed layer (red), and after further re-exposure to 1 CMC C₁₂E₅ (magenta).

induce complete desorption of the surface bound layer. Unlike the anionic surfactants, C₁₂E₅ was found to adsorb to mica and would be expected to adsorb itself if desorption of the entirety of the DDAB layer did occur. This would then lead to an identical profile to that

seen in Figure 3.21, but the observed profiles are markedly different from this. A schematic of the effect of $C_{12}E_5$ on the adsorbed DDAB layer is shown in Figure 4.18.

For the combination of anionic SDS with non-ionic MEGA-10 or MEGA-12 surfactants, mixed micelles have been observed and particular synergism was seen in the non-ionic rich side of the phase diagram²⁰⁴. The system under study in this work is effectively in the very non-ionic rich side, but the driving force for mixed-micellisation and layer removal for DDAB and $C_{12}E_5$ is clearly not sufficient to clean the surface.

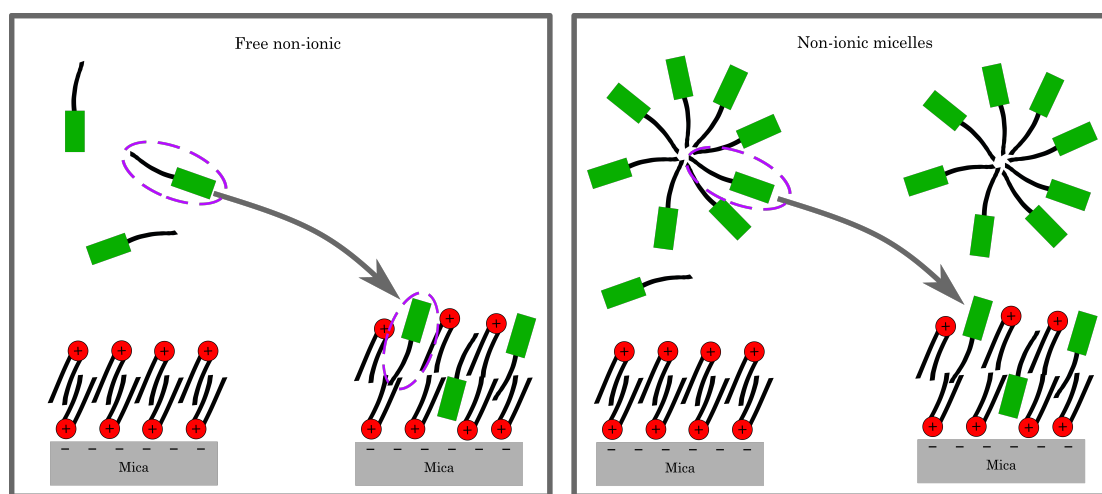


Fig. 4.18 A schematic of the behaviour of a DDAB layer (shown in red, round headgroups) on exposure to $C_{12}E_5$ (shown in green, rectangular headgroups) below and above the CMC, with little or no difference in resultant structure.

Mixed adsorption of DDAB and $C_{12}E_5$ has been reported in the literature; Bumajdad et al.²⁰⁵ found that $C_{12}E_5$ acted cooperatively with DDAB to stabilise an emulsion of water in heptane. The hydrophobic nature of the interface in that work and the simultaneous adsorption differ to the situation here, with a charged hydrophilic surface and sequential interactions.

As discussed earlier, it has been assumed that when the mixed layer of DDAB and $C_{12}E_5$ was exchanged into bulk water (or NaCl solution) that the non-ionic was reversibly removed from the layer and all remaining organic was DDAB. This assumption may not be entirely accurate but it is evident that at least some of the remaining material is DDAB from the effect of this remaining organic on subsequent $C_{12}E_5$ adsorption. The behaviour of the mixed layer formed from DDAB and SDS below the CMC was not investigated, and it is unknown how much of the layer would remain adsorbed if the bulk solution was exchanged to pure

water. The stronger interaction between the oppositely charged surfactants may cause greater retention of the anionic surfactant in the layer.

The area per DDAB molecule in the initial adsorbed layer, and after sequential exposure to C₁₂E₅ then 10 mM NaCl, may be calculated and compared. For the initial layer the area per molecule is approximately 56 Å², and if it is assumed that only DDAB remains after the series described then the area per molecule following layer alteration is approximately 65 Å². This is of the order of, but larger than, the idealised area per charge site of mica which is 47 Å², though some variation is expected in the natural mineral. It is possible that only the DDAB required for charge neutralisation remains after partial replacement by C₁₂E₅, but this DDAB is still tenaciously bound as it is not displaced by the 10 mM NaCl solution. On further exposure to C₁₂E₅ it appears even more of the DDAB is replaced and even less remains after subsequent exchange into pure water.

The fitted thickness to the DDAB layer is similar to the thicknesses previously observed for DDAB bilayers on mica. As a water layer now appears to be present between the DDAB and surface, the structure might be described as a surface-associated aggregate, rather than the closely adsorbed species initially formed.

The remaining DDAB on the surface has a profound effect on the re-adsorption of C₁₂E₅ compared to adsorption of the surfactant on the bare mica surface. Qualitatively the difference is evident from the reflectivity data; the changes seen in Figure 4.16 and 4.17 are much larger than the change on adsorption to the bare surface shown in Figure 3.21. The fits to the layers show that the presence of the cationic allows the C₁₂E₅ to form a dense, essentially unhydrated layer on the mica. This has implications for EOR and related fields, as it indicates that even a small quantity of remaining organic on the surface of the clay mineral can drastically alter the adsorption characteristics of other organic components. At least in this case, the transition from a nominally 'oil-wet' to 'water-wet' surface relies on complete removal of all surface organic material.

On cycling of the bulk solution between C₁₂E₅ and bulk water the profiles indicate a slight reduction in organic remaining on the surface after mixed layer formation and removal, and a thinner mixed layer formed when C₁₂E₅ was reintroduced. This can be seen from comparison of Figures 4.15 and 4.17. This may be explained by slight loss of DDAB from the surface on each partial desorption of the mixed layer, and the more diffuse remaining DDAB layer then being less able to template or influence C₁₂E₅ re-adsorption.

The series of experiments also further demonstrates the tenacity of binding of DDAB to the mica surface. After partial replacement of the DDAB layer by $C_{12}E_5$, then removal of this nonionic, the structure of the remaining DDAB is altered. Fitting suggests the new structure to be a more hydrated or diffuse layer, with an intervening water layer between the mica and DDAB. Even this new less dense structure was found to be persistent on the surface when exposed to bulk water or to 10 mM NaCl.

4.6 Comparison of Adsorbed Layer Behaviour

Evidently the adsorbed DDAB layer behaviour is markedly different in the case of each of the three surfactant systems studied. In the case of the non-ionic surfactant the cationic layer is never entirely removed from the mica surface, and the effect of the small remaining surface coverage of DDAB is drastic in the way that it allows and enhances the non-ionic surfactant adsorption. The lack of complete DDAB removal has been shown not to simply be a function of lack of alternative cationic species to compensate the surface charge.

The difference in behaviour arising from the two anionic surfactant molecules is also evident, with different removal mechanisms clearly occurring for the two cases. The structures of the surfactant molecules are reproduced in Figure 4.19 for comparison. The surfactant headgroups are similar; the pKaH of the sulfonate head group can be estimated from the pKa of methanesulfonic acid, which is approximately -1.9¹³⁵, and that of the sulfate head group may be estimated from the first pKa of sulfuric acid which is -3. Both anions will be very stable and essentially completely deprotonated under the conditions in this work.

The steric bulk of the surfactant tail region differs significantly between the single straight-chain of SDS and the branched di-chain tail of AOT. A suggested hypothesis for the observed behaviour is based on this steric difference, such that that the SDS tail group is sufficiently small to be able to fit into the adsorbed DDAB layer without significant disruption, whereas the AOT tail is too bulky to do this. At concentrations below the CMC, SDS can penetrate the DDAB layer and replace it to some extent, resulting in the thickening of organic layer seen. Even at the lowest SDS concentration tested a definite thickening of the bound organic layer was measured. The alkyl tail length of SDS matches the alkyl chainlengths of DDAB, which might also aid ordering on inclusion into a mixed layer. Once the SDS CMC is reached a sharp change in behaviour is observed as discussed in Section 4.2.4.

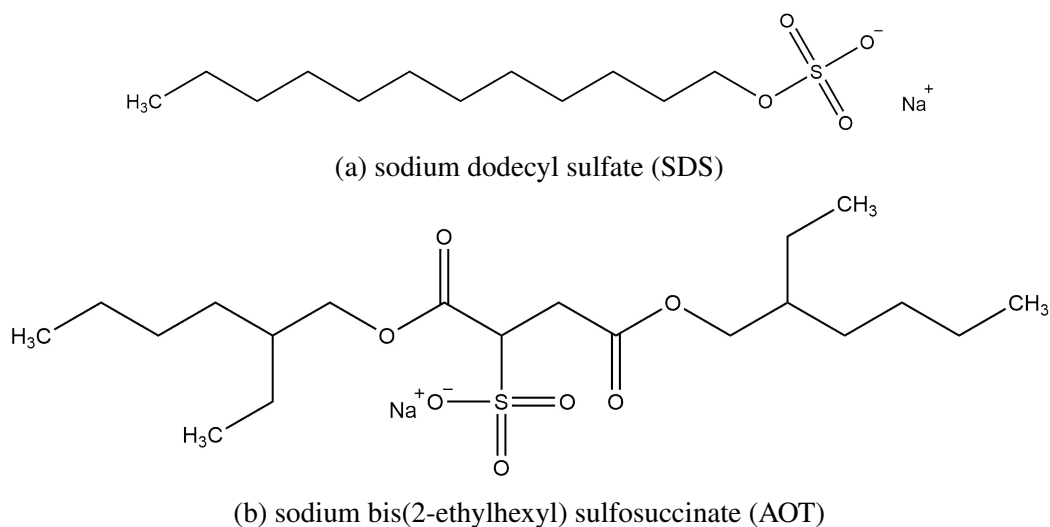


Fig. 4.19 Structures of the anionic surfactants used for the induced desorption study.

In the case of AOT at very low concentrations no thickening of the layer was seen. As the concentration was increased, though still below the CMC, the driving force for interaction between the hydrophobic tails in solution and the surfactant layer on the surface increases, and when sufficient the layer is broken down as the AOT cannot be included into the DDAB layer structure due to its steric bulk.

The strength of interaction between different surfactants in solution may be quantified by means of a molecular interaction parameter, or β parameter, as discussed by Rosen and Kunjappu¹⁴⁹. Based on non-ideal solution theory²⁰⁶, a β^σ parameter may similarly be calculated for the strength of interaction of two surfactants co-adsorbing in a monolayer at the air - water interface, and by extension β_{SL}^σ for adsorption at a hydrophobic surface. A β^M may also be defined for the interaction parameter for mixed micelle formation. These parameters may be calculated from measurements of the surface tension against concentration for the individual surfactants and the mixture, in an appropriate background electrolyte.

Whilst it would be interesting to determine and compare the molecular interaction parameters between the pairs of DDAB - SDS and DDAB - AOT, and this is an avenue for future study, the β^σ describes a situation quite different to the one experimentally probed in this chapter. Firstly the adsorption study here is at a hydrophilic surface, rather than hydrophobic, so may be more bilayer like than the monolayer described in the theory. The surface is also charged, resulting in additional interactions with the differently charged surfactants, and the layer formation is sequential rather than true mixed equilibrium adsorption.

Bumajdad et al.²⁰⁵ found that for surfactant mixtures stabilising water-in-heptane microemulsions, the effects of SDS and C₁₂E₅ on DDAB were very different; C₁₂E₅ aided the stabilisation whereas SDS reduced the ability to stabilise the emulsion. These results, though at an uncharged and hydrophobic interface, are consistent with our findings. If the SDS removes DDAB from the interface to preferentially form micelles, this will reduce the stabilisation, compared to C₁₂E₅ instead including into the layer without surfactant removal.

Chapter 5

Modification of Surface Charge

The roles of different cations and surfactants on adsorption to mica have been explored in the prior chapters. The nature of the surface, and in particular the surface charge density, will also play a key role in determining adsorption behaviour. It is much more complex to investigate the role of different surfaces, especially with techniques such as neutron reflectometry which rely on surfaces with a very low roughness over a macroscopically large area (of the order cm^2). This limits the substrates which can be used, and is particularly problematic in the study of behaviour at the clay mineral interfaces of interest in enhanced oil recovery, as typically clay minerals are of micrometre particle size or smaller. If flat surfaces could be generated with well defined but selected surface charge densities then this would provide the opportunity to determine how interfacial interactions vary with surface charge, and specifically to investigate behaviour at analogues of the basal surfaces of various clay minerals by using selected charge densities. The important role of the surface in determining the behaviour presented in the earlier chapters could then be examined.

Two commonly used substrates for the aforementioned techniques are muscovite mica sheets, which have been used for the majority of the work described in this thesis, and silicon wafers, which can be polished to very high levels of flatness. As discussed in Chapter 1, surface charge can come from either permanent structural charge or from pH dependent groups. Mica has one of the highest charge densities among clay minerals, but is expected to have few silanol groups so little pH dependent charge behaviour. Silica has no structural charge, as there is no isomorphic substitution, but will have a pH dependent component from numerous silanol groups²⁰⁷. The number of SiOH groups per unit area depends on the substrate preparation and extent of de-hydroxylation.

It was decided to attempt to generate controlled charged surfaces by both reducing the structurally highly charged mica, and by introducing structural charge in silicon wafers.

5.1 Modification of Mica

5.1.1 Powder Characterisation

Whilst the aim of this section was to develop substrates with well defined surface charge over a large area of a single flat surface, attempting to measure the charge on substrates of this type is experimentally challenging. This is because these single surfaces still have a very small total surface area, making measurement difficult for standard laboratory techniques. In contrast, powdered substrates allow access to much larger surface areas, and for this reason powdered materials are generally used in batch adsorption isotherms. On many substrates this presents little issue but for the layered mineral mica, generating a powder exposes large areas of edge sites which have markedly different behaviour to the basal planes of interest. Hence rather than investigating adsorption on to the basal plane of interest, a combination of basal planes and edge sites would be experimentally accessed. Data resulting from any experiments utilising powdered mica as a substrate must therefore be carefully considered and interpreted.

Two samples of muscovite mica powder were procured: Imercare 3000M donated by Aston Chemicals Ltd., and a sample of dry-ground mica provided by MicaMills (Mahlwerk Neubauer-Friedrich Geffers GmbH). The MicaMills powder was described as 50% passing through a 45 μm mesh. Powder X-ray diffraction of both powders was conducted, the results of which are shown in Figure 5.1. By comparison with literature data taken from the RRUFF database²⁰⁸ it is clear that both samples are predominantly mica.

The MicaMills powder contains only peaks present in the literature spectrum, indicating that there are no crystalline impurities. The Imercare sample however does show additional peaks, most notably at $2\theta = 12.4^\circ$ and 24.9° . Comparison with the kaolinite spectrum reveals this to most likely be a kaolinite impurity in the Imercare powder. Due to this the MicaMills muscovite sample was utilised for powder experiments. Optical microscopy of the powder, shown in Figure 5.2, confirmed that the particles were present as high aspect ratio ‘flakes’, as would be expected for a ground sample of a layered mineral.

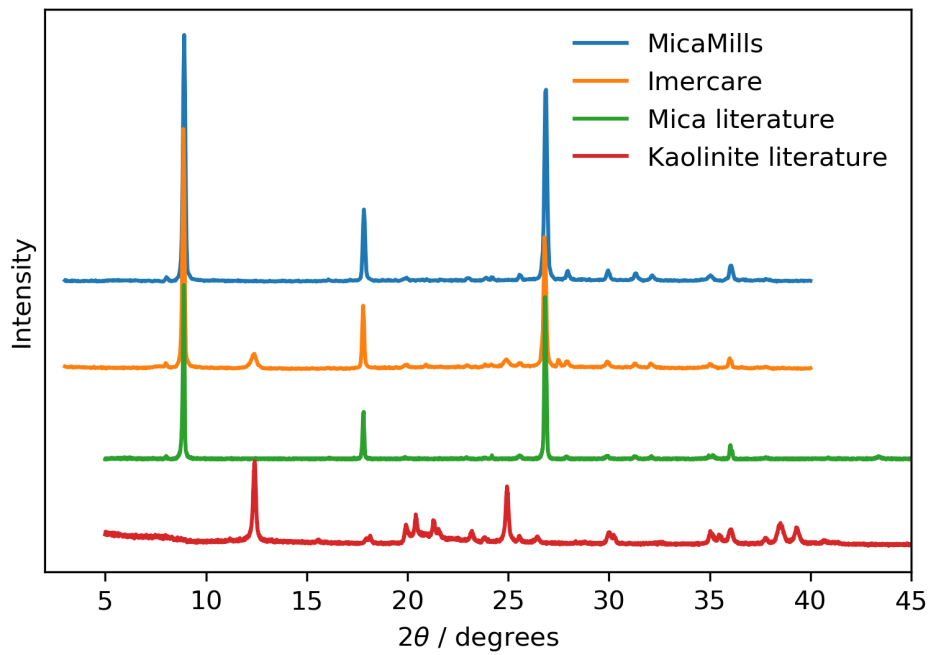


Fig. 5.1 Powder X-ray diffraction data collected from samples of the two types of mica powder obtained, Imercare and MicaMills. Repository diffraction data for muscovite mica and kaolinite, taken from the RRUFF project²⁰⁸ is also plotted. Data are offset for clarity.

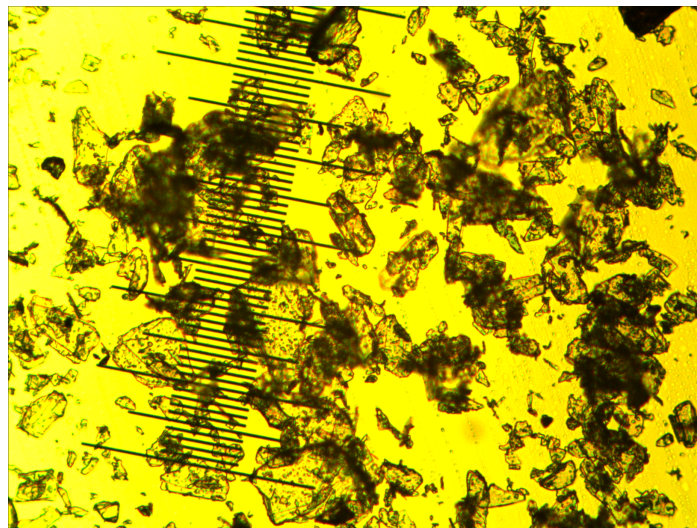


Fig. 5.2 Optical microscopy of MicaMills mica powder, showing that the powder is comprised of high aspect ratio platelets. Each division of the scale bar is 10 μm.

5.1.2 Powder Modification to Reduce the Surface Charge of Mica

The modification treatment detailed in Section 2.11 was applied to samples of both mica powders, to attempt to induce charge neutralisation by the Hofmann-Klemen effect discussed in Section 1.1.4. The solutions in which the powder was immersed before calcination were 1 M MgCl_2 , 1 M LiCl , and H_2O as a control. After the modified powders were dried, the CEC of each was measured as described in Section 2.10.2, as well as the CEC of an untreated mica sample. pH of the Cu^{II} solution during the CEC determination was measured and did not vary significantly from neutral, all being in the range pH 6 - 7. Mica charge is also expected to be mostly pH independent in the range pH 6 - 10¹⁸⁴, so no effort was made to control the pH. The measured values are displayed in Figure 5.3.

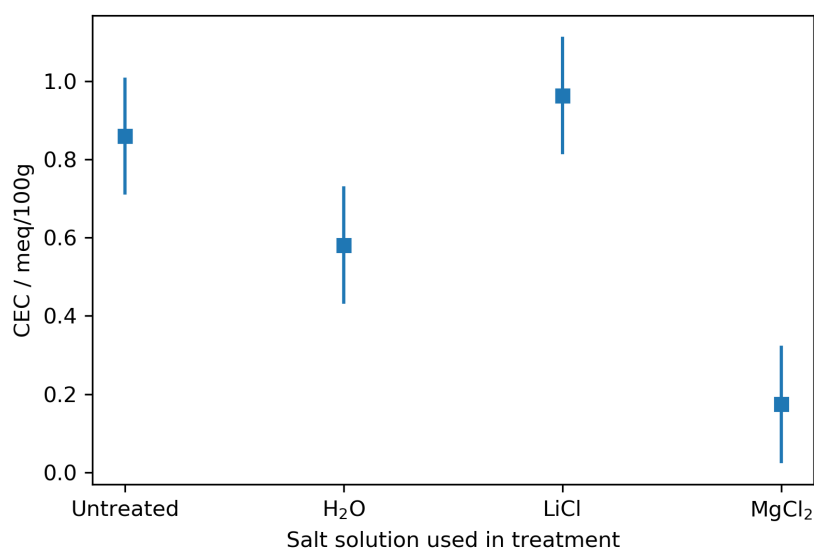


Fig. 5.3 Measured CEC values in meq/100g for mica powders treated with various cation solutions. Error estimates are based on experimental limitations.

A slight decrease in CEC is seen for the treatment with water, and potentially a slight increase in CEC for LiCl , which is unexpected though is comparable to the experimental error. Significantly, a large and statistically significant decrease is observed when the treatment was carried out with MgCl_2 .

The standard unit of CEC as per mass of clay is shown, which is the directly measured quantity, when in fact the surface charge density is ideally expressed in per unit area. Hence the interpretation of the raw CEC values in the desired context requires further clarification. As the treatment process involves washing and filtering it is possible that the smallest fraction

Table 5.1 BET area values for clay samples

| Sample | BET area / m ² /g |
|---------------------------|------------------------------|
| Untreated MM | 2.3 ± 0.1 |
| H ₂ O treated | 1.9 ± 0.1 |
| LiCl treated | 2.1 ± 0.1 |
| MgCl ₂ treated | 1.9 ± 0.1 |

of particles have been removed in this process, and these will have a specific surface area higher than the sample average. This could be the reason for the lower CEC measured for the water treated mica compared to the untreated sample. To convert the CEC values to surface charge density, the specific surface area of the samples must be known. This was measured for the untreated and treated MicaMills powders using BET area measurements; the values are shown in Table 5.1.

It is seen that the specific surface area does decrease as a result of the treatment for all samples, most likely through fractioning out of the smallest particles during the treatment as discussed. Interestingly the decrease is less for the LiCl treated powder than the other cases. An explanation for this could be partial delamination of the mica by lithium exchange and heat treatment, exposing new areas. This would occur by exchange at the edges of the mica plates, and a subsequent ‘opening’ of the booklet like structures. There is literature evidence for this process occurring²⁰⁹.

With the specific surface area values in Table 5.1, the CEC can be converted to units of meq/area, and these results are shown in Figure 5.4. These CEC values are easier to interpret, and the value for the water treated powder is now more consistent with the untreated sample as expected. Significantly the data does clearly indicate that MgCl₂ treated mica shows a marked decrease in surface charge density as desired. The calculated CEC is 1.2 ± 0.6 eq/m² which is similar to the values for kaolinite as calculated both from measured CEC and BET values (0.9 eq/m²) and calculated using literature values for the source clay⁸² (1.4 eq/m²). It was therefore concluded that the surface charge of mica had been reduced, as intended.

The increase in CEC after LiCl treatment is unexplained, although a rather small increment, and contrary to the Hofmann-Klemen effect reported previously. If partial delamination has occurred on the edges of plates then it is possible that interlayer areas have been exposed which are accessible to cations in solution but not to the nitrogen gas during BET measurements, and hence a larger area is being sampled by the CEC measurement than the BET area. This would essentially correspond to a partial conversion from mica to vermiculite, a

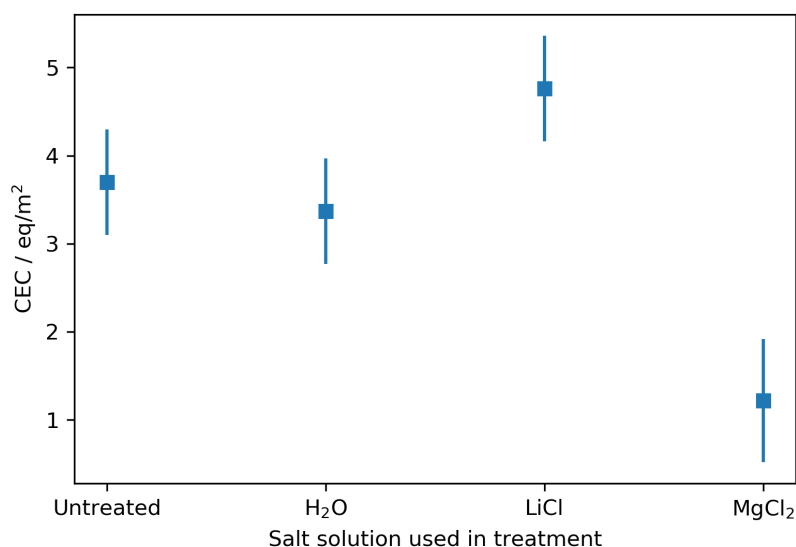


Fig. 5.4 Measured CEC values in eq/m^2 for MicaMills powder, calculated from BET areas. Errors are based on experimental factors.

swelling Li^+ analogue of muscovite, and is consistent with the enhanced hydration of lithium relative to potassium allowing some swelling in solution.

It is also interesting to note that the CEC calculated from the ideal mica structure of 1 charge site per 47 \AA is 3.5 eq/m^2 , within the error of the measured value of $3.7 \pm 0.6 \text{ eq/m}^2$. This is reassuring and suggests that the mica powder edges contribute negligibly to the behaviour, at this pH.

5.1.3 Mica Ion Exchange Isotherms

In the previous section it was demonstrated that the surface charge of mica may be dramatically reduced by ion implantation. In the case above this was from a very high charge to very low.

One strategy for producing different surfaces with an intermediate range of controlled surface charges from ion implantation into mica would be to exchange the mica surface cations for a mixture of ions that can and cannot be included into the crystal structure, then to induce implantation. Assuming spatially uniform distribution of the included and non-included ions, this process would only neutralise a chosen proportion of the pre-existing

mica surface charge, as selected by the ratios of ions. The other sites would not be expected to be changed in their structural charge.

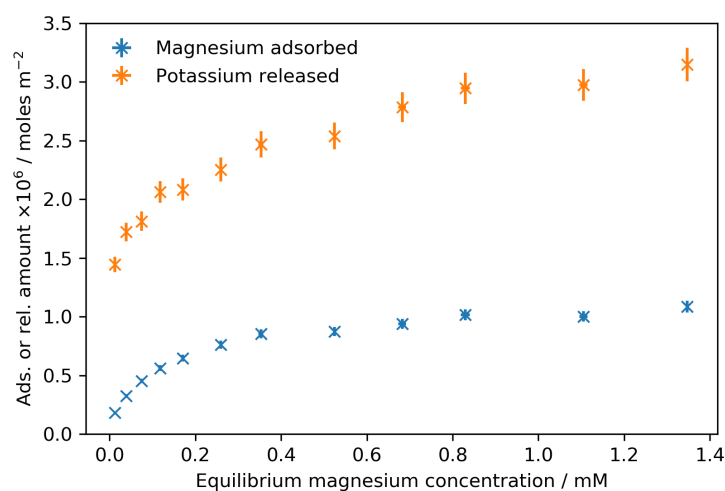
To control the ratio of surface cations, the equilibrium constants between different surface bound ions are required. With knowledge of these constants, it should be possible to generate the desired ratio of surface cations by immersing a mica surface in a solution with specified concentrations of the two relevant cations. To measure exchange constants, isotherms were carried out with potassium saturated mica exchanging with either magnesium or lithium ions in solution. Experiments were conducted as described in Section 2.12.

Adsorption Analysis

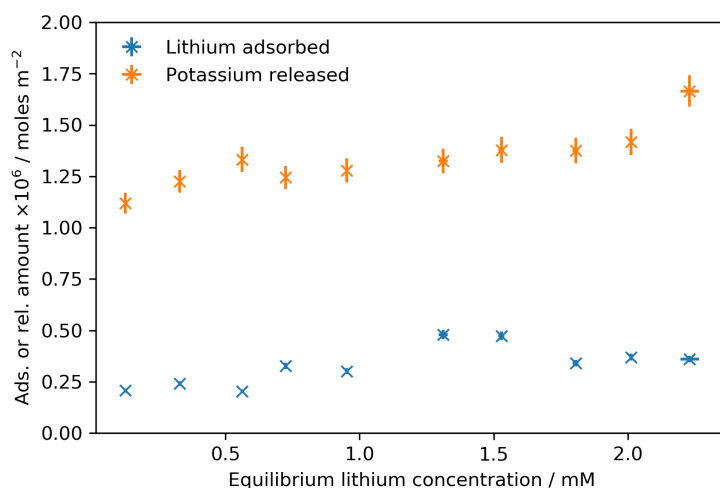
Traditional analysis of adsorption isotherms involves plotting the adsorbed amount per unit area against the equilibrium adsorbate concentration, and fitting the data with a Langmuir fit or another model. This gives a binding constant between the surface and adsorbate. In the case of the mica exchange isotherms conducted here this analysis is not possible, as it is an exchange process rather than simple adsorption taking place. As more of an added ion 'A' displaces a pre-present ion 'B', the concentration of 'B' in solution will increase and inhibit further exchange by driving the equilibrium towards adsorption of 'B' to the surface. It is however instructive to present the data as adsorption and release per unit area.

In these experiments it is also possible to measure the amount of pre-present potassium ion released from the surface per area, as ICP analysis can measure concentration of numerous analytes simultaneously. Figure 5.5a shows the results from potassium mica exchanging with magnesium ions in solution, and Figure 5.5b for potassium mica exchanging with lithium ions. The adsorbed amount is calculated from the difference between the initial and equilibrium concentration of adsorbate, and based on the surface area of solid present as determined from BET specific surface area and mass.

It is evident from the results that as the magnesium ion concentration in the bulk increases, adsorption of magnesium ions to the surface increases with a Langmuir like form. The potassium per unit area released also increases with increasing bulk magnesium as would be expected. Interestingly, this value of released potassium continues to increase even after the magnesium ion adsorption has plateaued. The other observation which indicates effects beyond simple stoichiometric exchange is that more than twice as much potassium is released as magnesium is adsorbed for each sample. The initial expectation might have been that one divalent Mg^{2+} can replace two monovalent K^+ ions.



(a)



(b)

Fig. 5.5 Salt exchange isotherm results of potassium saturated mica, exchanging with (a) magnesium and (b) lithium. Error bars are estimated from error analysis from experimental parameters, with the majority of the error in adsorbed amount originating from uncertainty in the measured BET area. Note the difference in y-axis scales between the two plots.

An explanation for this behaviour is that in solution ions dissociate from the mica, leaving a net negatively charged surface, forming an electrical double layer and enter the bulk solution. The entropic driving force for ions to move from the surface layer to the bulk is large. Here there is a low ionic strength which means there is a comparatively large volume of solution involved in the double layer, relative to the surface area. It is noted that when

only a low concentration of Mg^{2+} has been added the ionic strength will be expected to be low. As more Mg^{2+} is added the ionic strength will increase and the Debye length shrink.

In the hypothetical situation of a charged surface, with counter ions only, in an infinite volume of pure aqueous solution, the entropic driving force would be such that all of the surface cations would dissociate fully into the bulk, leaving a charged surface uncompensated by cations. However, this is a particular case and usually experiments have some 'background' electrolyte or the auto-dissociation of water provides a non-zero ionic strength.

Figure 5.5b indicates that the more strongly hydrated lithium ion appears to be unable to displace the potassium ions as effectively from the mica, as might be expected when compared to the divalent magnesium ion. The adsorbed amount of lithium does not increase as the bulk concentration increases. The potassium released shows little to no increase either, and maintains an amount slightly below the minimum potassium released from the magnesium isotherm (approximately 1.5×10^{-6} moles m^{-2}).

From the raw data it is possible to estimate the approximate concentrations of magnesium and potassium ions in solution which would be required to result in a surface with mixed cations. This can be done by taking data points on the leading edge of the curve and comparing the magnesium adsorbed to the plateau value, to see what proportion of the surface sites will be occupied by the magnesium at each magnesium and potassium bulk concentration.

The value of the area per surface charge site may be estimated from the potassium - magnesium isotherm, where significant exchange has occurred, and compared to the idealised mica formula¹¹ which gives an area of 47 \AA^2 . Normally the plateau adsorbate value of an isotherm would be used to determine an area per molecule, but in this case additional effects are clearly present as more than twice the amount of potassium is released as magnesium is adsorbed. As no source of potassium is present other than the mica surface, the maximum released potassium amount is perhaps the best estimate, though a slight upward trend is still visible for increasing equilibrium magnesium concentrations.

From the data, the largest amount of potassium released is $3.2 \times 10^{-6} \pm 0.1 \times 10^{-6}$ moles/ m^2 . This gives an area per charge site on the mica of $52 \pm 2 \text{ \AA}^2$, which is reasonably close to that predicted from the idealised formula (47 \AA^2). The slight discrepancy could be explained by the continued upward trend in released potassium meaning the measured concentration is not all the potassium ions from the surface, and the fact that not all of the surface area present will be due to basal planes of the particles.

Equilibrium Analysis

As previously mentioned, traditional isotherm analysis is not appropriate for this exchange process. The most simple analysis would assume stoichiometric exchange and neglecting any net dissociation from the surface. This is equivalent to using the Helmholtz model of the electrical double layer²¹⁰. For a mica surface initially saturated with K^+ and exchanging partially with Mg^{2+} , the equilibrium equation is given in Equation 5.1 where ' $\vdash X$ ' is the species ' X ' adsorbed to a mica charge site ' \vdash '. It is more convenient for later calculations to consider each mica charge site in pairs.



The equilibrium constant for the exchange process, K_{eq} , is then given by Equation 5.2. These are now true concentrations of species in the sample, rather than per unit area, so the specific surface area does not come in to these calculations. The potassium - magnesium isotherm replotted in these units is shown in Figure 5.6.

$$K_{eq} = \frac{[\vdash_2Mg][K^+]^2}{[\vdash_2K_2][Mg^{2+}]} \quad (5.2)$$

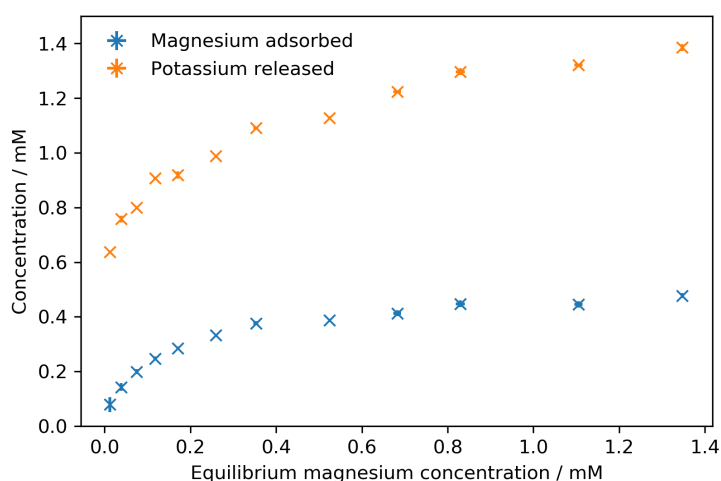


Fig. 5.6 Salt exchange isotherm of magnesium for potassium on mica, in units of bulk concentration. Error bars are calculated from error propagation from a single sample in each case.

The concentration of surface bound magnesium ions may be calculated directly through depletion of magnesium from solution, as given in Equation 5.3. If it is assumed that exchange is strictly stoichiometric and the initial condition is all mica charge sites are bound to a single potassium ion, at equilibrium it would be expected that $[\text{r}_2\text{Mg}] = 2[\text{K}^+]$. As discussed in the previous section, this is experimentally seen not to be the case.

The surface bound potassium concentration may be calculated similarly by taking the plateau concentration of magnesium depletion as a surface saturation to measure the total number of surface sites, and using the calculated bound magnesium concentration. This is shown in Equation 5.4, where $[\text{Mg}^{2+}]_0$ is the initial magnesium ion concentration before equilibration, and $[\text{r}_2\text{Mg}]_{\text{sat}}$ is the saturated concentration of magnesium ions on the surface, taken from the plateau in the isotherm.

$$[\text{r}_2\text{Mg}] = [\text{Mg}^{2+}]_0 - [\text{Mg}^{2+}] \quad (5.3)$$

$$[\text{r}_2\text{K}_2] = [\text{r}_2\text{Mg}]_{\text{sat}} - [\text{r}_2\text{Mg}] \quad (5.4)$$

An alternative calculation method to Equation 5.4 is to use the maximum concentration for released potassium ions. This alternative is shown in Equation 5.5. Given the ‘over-release’ of ions this calculation was considered the more appropriate approximation of the two.

$$[\text{r}_2\text{K}_2] = \frac{1}{2}([\text{K}^+]_{\text{sat}} - [\text{K}^+]) \quad (5.5)$$

The points at low equilibrium magnesium concentration in the isotherm, before the magnesium adsorption plateau is reached, will provide the most accurate estimate of the equilibrium constant. Equilibrium constants calculated in the described manner for the first five points in the isotherm are shown in Figure 5.7, plotted against equilibrium magnesium concentration as before. To calculate these values, $[\text{K}^+]_{\text{sat}}$ was taken as 1.4 ± 0.1 mM. The rough consistency between these calculated points gives some confidence that this method might be useful for estimating an approximate equilibrium constant for the exchange, despite the simplifications. These first five points give an average $K_{eq} = 6.4 \pm 0.6$.

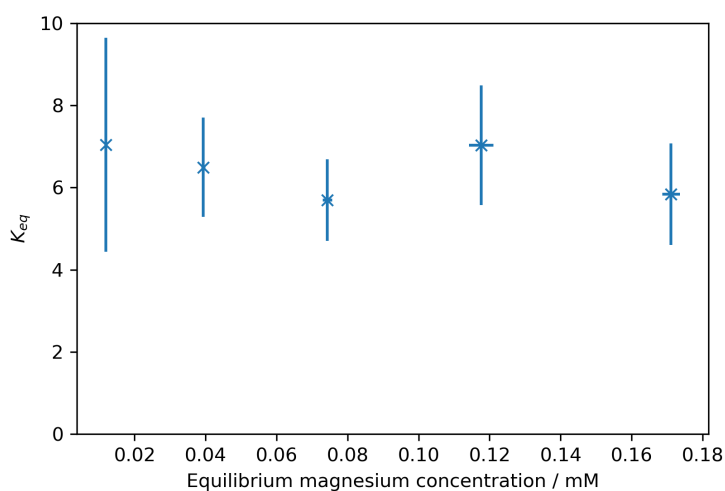


Fig. 5.7 Equilibrium constants calculated from Equation 5.2 using Equation 5.5 for concentration of adsorbed potassium ions.

If, for example, it is then desired to generate a surface which is 1/3rd exchanged with magnesium ions and 2/3rds with potassium ions, then $[{}_{-2}\text{K}_2] = 2[{}_{-2}\text{Mg}]$ and concentrations of K^+ and Mg^{2+} can be chosen such that $[\text{K}^+]^2/[\text{Mg}^{2+}] = K_{eq}[{}_{-2}\text{K}_2]/[{}_{-2}\text{Mg}] = 6.4/2$.

This calculation of equilibrium constant was intended as a very approximate tool to act as a starting point for using mixed salt solutions to part-exchange flat surfaces with negligible surface area. More accurate analysis of the data was considered by accounting for the variable ionic strength across the isotherm and assuming some structure of the EDL near the surface, which others have attempted for alternate systems⁷⁰, but this was not deemed necessary.

The error in CEC powder measurements were deemed to be too large to be able to clearly distinguish between differences in surface charge with partially exchanged substrates, so intermediate versions of the modification treatment described in Section 5.1.2 were not attempted on powders.

Future Work on Mica Exchange Isotherms

The initial preparation of the mica to ensure that all the exchangeable surface cations present were potassium ions is detailed in Section 2.12. Significant washing steps were taken to attempt to prevent any remaining over-exchange of potassium on the surface, but this was not experimentally verified. Various techniques could be applied to ascertain whether this was

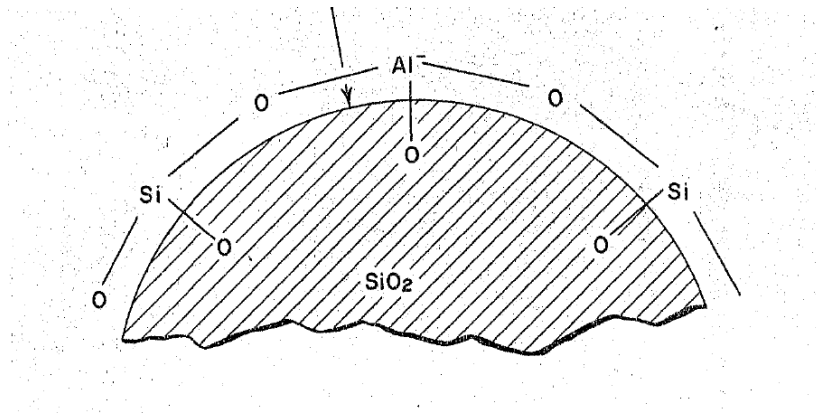


Fig. 5.8 Schematic of isomorphous substitution of silicon for aluminium in the outer layer of a silica sol. Reproduced from the 1959 DuPont patent²¹¹.

truly the case, including energy dispersive X-ray spectroscopy (EDX) or similar to check for the presence of chloride counterions which would indicate adsorption of excess K^+ .

Additional KCl on the mica surface prior to the isotherm would lead to errors in the calculation and could be an alternative explanation for the greater potassium release than magnesium adsorption. The calculation of area per charge site from the maximum potassium release being so consistent with the mica ideal structure does however suggest that this is not the case.

A further desirable test would be to measure the released potassium concentration from mica in the presence of differing volumes of pure water, and absence of other ions.

5.2 Isomorphous Substitution of Silica Surfaces

As silica has no structural charge, methods of introducing isomorphous substitution were considered. In a 1959 patent by DuPont²¹¹, a method which was believed to introduce isomorphous substitution of aluminium ions into the surface of silica sols is described. The replacement of the tetravalent silicon ions with trivalent aluminium ions introduces a structural negative charge, just as in muscovite mica. The described method involves a treatment of the silica with a sodium aluminate solution at high pH. A schematic of the claims from the patent is reproduced in Figure 5.8.

5.2.1 Colloidal Silica Characterisation

Various commercial colloidal silica grades are available from WR Grace, who purchased the patent from DuPont, and are collectively sold under the name Ludox™. These grades include Ludox LS, which is untreated colloidal silica, Ludox AM, which is described as silica with isomorphic substitution of aluminium, and Ludox CL, which is described as silica particles with complete replacement of the outer shell with aluminium ions and as such they are expected to exhibit the behaviour of colloidal alumina.

As the intention in this present work was to attempt to replicate these treatments on a flat surface, and investigate the effect on the zeta potential, initial zeta potential measurements were conducted on the commercially available colloidal equivalents to give an indication of the expected later results.

If a treatment were applied to substitute silicon atoms for aluminium, an initial fall in zeta potential (at neutral pH) would be expected as negative charge is imparted by isomorphic substitution. However, with increasing aluminium present at the surface ultimately the behaviour would be expected to change and become more alumina like. This would correspond to an increase in zeta potential reflecting the isoelectric point of alumina and the protonation of aluminol groups.

Zeta potential of Ludox LS, AM, and CL were all measured as described in Section 2.4, over a range of pH values in a background electrolyte of 1 mM KCl. The results of these measurements are shown in Figure 5.9. The observed trends in zeta potential are consistent with the expected nature of the specific surfaces; silica-like for Ludox LS, alumina-like for Ludox CL, and isomorphically-substituted-silica-like for Ludox AM. The determined isoelectric points of Ludox LS and CL are approximately 2 - 3 and 8 - 9 respectively, which are consistent with the literature values for silica and alumina⁹. Comparing the Ludox LS and AM, where AM is described as isomorphically substituted, it is clear that the AM grade does indeed shows a more negative zeta potential over the entire pH range, and does not show an isoelectric point. Both of these observations are consistent with the presence of structural negative charge in the silica surface.

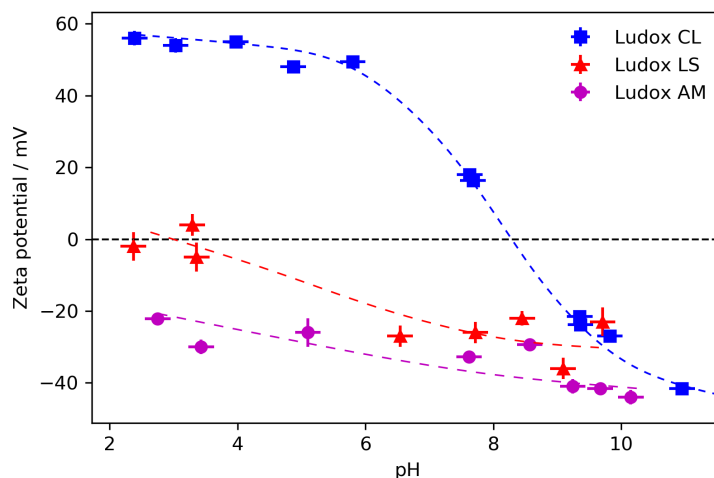


Fig. 5.9 Measured zeta potential values for Ludox colloidal silica; the three tested grades have significantly different magnitudes of zeta potential. Lines are intended only as a guide to the eye, and are not fits to the data or based on a physical model.

5.3 Flat-Surface Charge Measurements

Before attempting to apply any modifying treatments to macroscopically flat surfaces, the zeta potential of unmodified planar samples was characterised using a SurPASS electrokinetic analyser, as described in Section 2.5.

5.3.1 Silica Results

The zeta potential of a silicon wafer (Wafer 1) was measured as described in Section 2.5, in 1mM KCl over the pH range 7 - 3.5. As described in Section 3.5, certain other experiments had suggested the possibility that UV-O₃ treatment might alter the behaviour of some surfaces, so the same wafer was rinsed and remeasured after 20 min exposure then a further 20 min (40 min cumulative) of UV-O₃ treatment. A separate wafer (Wafer 2) from the same batch was also measured after 20 min of UV-O₃, which was the standard treatment for the mica neutron substrates. These results are displayed in Figure 5.10.

The trend in zeta potential of all samples is consistent with the Ludox LS data and the physical interpretation of increased protonation of Si-O⁻ groups. From extrapolation of the streaming potential data the IEP can be estimated at a pH of 1 - 2, which is close to but slightly lower than the expected 2 - 3 for silica. It appears that there is a change in zeta

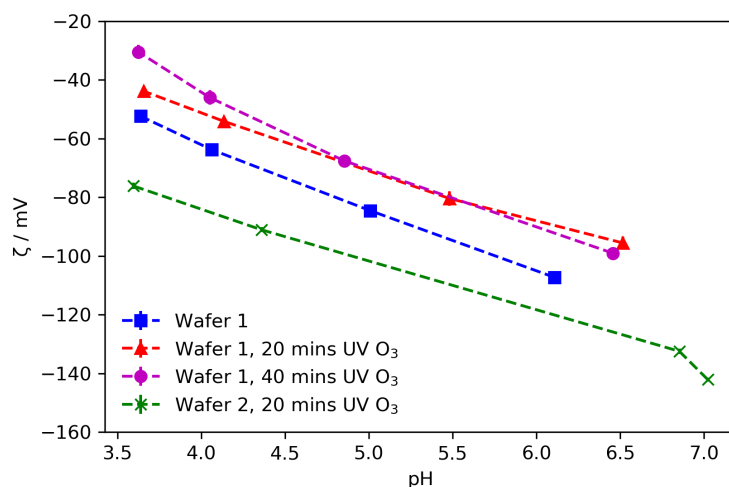


Fig. 5.10 Zeta potential values as a function of pH, after varying times of UV-O₃ treatment. Values measured with the SurPASS electrokinetic analyser.

potential upon UV-O₃ treatment, with a slight reduction in magnitude after 20 min, though little further change after an additional 20 min treatment. This change would appear to be contradictory with observations that UV-O₃ treatment can increase the hydroxylation of silica²¹², which might be expected to increase the magnitude of the zeta potential.

There is a large difference in zeta potential between data from Wafer 1 and Wafer 2, both after 20 min of UV-O₃. Whether this is variation between samples or measurement error is unknown, but the magnitude of the difference is approximately 40 mV which is a significant percentage of the total. Because of this inconsistency, smaller changes in zeta potential seen with Wafer 1 after different treatments were treated with caution. Hoggard et al.²¹³ measured a zeta potential of approximately -80 mV for silicon wafers in 1 mM KCl at neutral pH, using a custom rotating disc apparatus, which is broadly consistent with the data collected here.

In work related to an existing collaboration, Dr Becky Welbourn (ISIS, STFC) kindly offered to conduct some trial measurements on substrates prepared by me on a new model of the SurPASS, the SurPASS3 analyser also by Anton Paar. This device is identical in concept and differs only slightly in operation to the SurPASS, utilising a membrane pump and modified mounting stage. The data collected by Dr Welbourn with Anton Paar technicians on the SurPASS3 from a silicon wafer is shown in Figure 5.11a, labelled 'alternate measurement'. On the same plot is shown the data from one of the earlier measured wafers for comparison. A very significant difference in measured zeta potential is evident.

Figure 5.11b shows the new data plotted with the zeta potential measurements for Ludox LS which was discussed in Section 5.2.1. Although the surfaces of the silicon wafer and the colloidal silica are likely to have slightly different chemistry due to the specifics of preparation and very small radius of colloidal samples, it is still instructive to compare them and it is very clear that the newly collected flat surface data is more consistent with the colloidal measurements. This further supports the conclusion that the data collected on the SurPASS must be treated with extreme caution, and whilst the SurPASS data was consistent with the results of Hoggard et al.²¹³ the differences between the two instruments measuring a supposedly similar quantity reinforces the argument that zeta potentials of flat surfaces are very difficult to measure reliably.

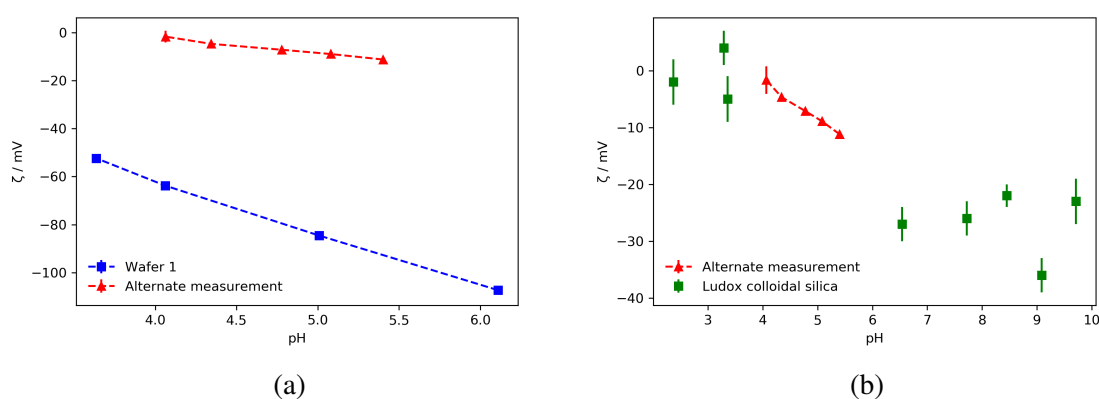


Fig. 5.11 Zeta potential data measured by Dr Becky Welbourn (STFC) for a silicon wafer on the SurPASS3 device, in an electrolyte of 1 mM KCl. (a) shows the new measurements plotted alongside my measurements on an equivalent sample measured on the SurPASS, and (b) shows the data plotted with the measured zeta potentials for Ludox LS colloidal silica also in 1 mM KCl.

5.3.2 Mica Results

A similar comparison of measurements was conducted for mica sheets prepared in an analogous way to those used in neutron experiments. The results of experimental data collected on our instrument, and data collected on the SurPASS3, are shown in Figure 5.12. Again a much smaller magnitude of measured zeta potentials for the SurPASS3 data is seen. The presence of some variation in zeta potential with pH is surprising given the ideal structure of mica where all charge is structural, but is attributed to the presence of a few surface silanol species.

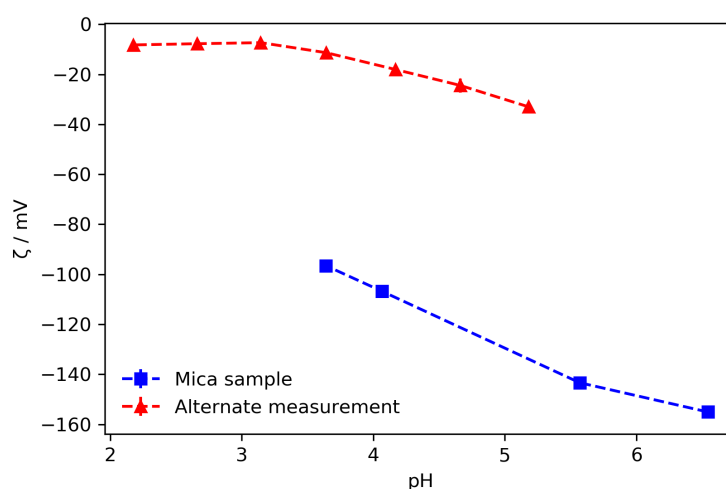


Fig. 5.12 Zeta potential values over a pH range for two mica sheets; measurements I conducted on the SurPASS instrument are labelled 'Mica sample', and measurements by Dr Becky Welbourn on the SurPASS3 are labelled 'Alternate Measurement'.

Whilst it is tempting to draw further conclusions from this data when compared to that of the silica surface, such as that the mica is more negative over the whole range (when the two measurement sets are compared independently), this does not seem reasonable given the unreliability of the data.

As discussed in Section 2.6, estimates can be made of the surface charge density from zeta potential measurements by assuming a slip-plane location and the Guoy-Chapman model of the electrical double layer. This may be done using Equations 2.26 and 2.27. Taking the data at a pH of approximately 5.5, the zeta potential determined by the SurPASS is -140 mV compared to -33 mV for the SurPASS3.

Work on liposomes has suggested a slip-plane location of 0.24 nm from the surface and little to no ionic strength dependence of this distance²¹⁴. Using this slip plane location, the zeta potentials of -140 mV and -33 mV give surface charge densities of -0.037 Cm^{-2} and -0.0027 Cm^{-2} respectively. Both of these are well below the ideal mica surface charge of -0.33 Cm^{-2} , but the data collected with the original instrument (SurPASS) is much closer to the literature value. At larger zeta potentials small changes in zeta potential propagate to large differences in calculated charge density. Back-calculating the supposed zeta potential for a surface charge density of -0.33 Cm^{-2} , using the same assumptions listed earlier, gives a zeta potential of -203 mV. This is not significantly above the initial measurements conducted with the SurPASS, further suggesting that these may be the more reliable of the two.

The estimation of slip plane location does influence the calculated charge density to a large degree. Using the same zeta potential values, the slip plane location which would give the correct surface charge density of -0.33 Cm^{-2} may be calculated; zeta potentials of -140 mV and -33 mV would give slip plane locations of 1.1 nm and 11 nm respectively. Estimations of the true slip plane locations in the literature vary over orders of magnitude; for liposomes the location has been proposed as 0.24 nm invariant of ionic strength, but other work with montmorillonite proposed a location 8 nm from the surface in 1 mM NaCl .

5.4 Future Work

To be able to apply the promising treatments for modifying the surface charge of silica, or partially neutralising the surface charge of mica, a more robust approach able to reliably and accurately measure the zeta potential or surface charge is required. This is particularly true if surfaces of well defined charge are desired over small increment in surface charge density, as is desirable to mimic the behaviour of the basal planes of the discrete clay mineral classes.

Use of X-ray photoelectron spectroscopy (XPS) to analyse the atomic constituents of the surface of either mica or silica could provide an alternative method for monitoring progress of surface treatments. Measuring the level of included magnesium into mica, or included aluminium into silica, would be valuable direct data on the treatment effect and calculation of surface charge density based on these could then be compared to further measurement. Angle resolved XPS can give information about the depth profile of atomic species²¹⁵, which is also of interest in predicting the extent of charge localisation on the surface of any sub-surface charge sites.

Once the surface can be characterised then application of the ion exchange and heat treatment described in Section 5.1.2, and the proposed basic sodium aluminate treatment, may be trialled on mica sheets and silicon wafers respectively.

Chapter 6

Fluorescence Study of Adsorption

During experiments described in this section, operation of the fluorescence microscope was carried out by Dr Aleks Ponjavic with my assistance. All experimental planning, preparation, and analysis was my own work.

6.1 Background

Neutron experiments, whilst very powerful in their capability to distinguish the structures of adsorbed layers in the out-of-plane direction, are limited in their capability for in-plane resolution. Specular reflection gives an in-plane averaged structure only. Neutron reflectivity also requires the use of a national or international facility which limits the frequency and duration of the experiments, subject to beamtime applications, and any time-resolved measurements are limited to timescales of minutes or less and generally require a compromise in spatial resolution or range of q -space accessed.

Alternative techniques were considered which might provide similar information to neutron reflectivity studies about adsorption onto the basal plane of mica, without the added complication of edge behaviour which arises from powder techniques. Additionally methods to measure surface charge density which did not rely on streaming potential measurement, as discussed in Chapter 5, were required.

Fluorescence microscopy has been employed widely in the field of biophysics, as it allows imaging of specific structures or functionalities⁹⁵. This has been extended to super-resolution

single molecule imaging²¹⁶. Fluorescence microscopy can also be used to spatially map other properties or environments, such as pH²¹⁷ or hydrophobicity⁹⁴.

A number of designs and configurations of fluorescence microscope exist, to serve a range of purposes. As described in Section 2.13, two configurations were employed in this work; total internal reflection fluorescence (TIRF) microscopy allows imaging of only the region within a few hundred nanometres of the surface, the ‘surface composition’, and epifluorescence imaging (EPI) visualises the bulk solution above the interface, the ‘bulk composition’.

By utilising the phenomenon of photobleaching, information about the in-plane mobility of an adsorbed layer may also be found. Fluorescence recovery after photobleaching (FRAP) measurements, where a region of space is bleached and the recovery monitored, are used for this purpose. By fitting the time dependence of the fluorescence intensity recovery profile after bleaching, it is possible to estimate the surface diffusion constants and any immobile fraction of bound species^{218,219}.

The specifics of the instrumentation used and the imaging set up are described in Section 2.13.

6.2 Dye Cation Exchange

A number of measurements were planned, to complement various investigations described earlier in this thesis. If the surface cations of mica can be exchanged entirely and in a stoichiometric manner for fluorophores, then observing fluorescent intensity should give a measure of cation exchange capacity and therefore surface charge density. The approximate area per charge site of 47 \AA^2 is however large compared to many commonly used fluorophores, which typically consist of a large aromatic structure, and this may result in incomplete exchange. A further complication is that the native potassium ions display a relatively strong affinity for the mica surface, and fully exchanging them for dye molecules is hampered by relatively low solubility limits of many dyes in aqueous solution. Adsorption independent of cation exchange, by effects such as hydrophobic association, must also be considered.

To attempt to overcome some of these issues, a selection of comparatively small dye molecules, with structures comprising as few functional groups as possible and reasonable water solubility, were selected. The cationic dyes rhodamine 6G and oxazine 725, as well as the fluorescein sodium salt, were utilised. The structures of these dyes are shown in

Figure 6.1. The anionic fluorescein salt was used as it is structurally similar to rhodamine 6G, but will carry a doubly negative charge in solution rather than a positive charge. Any adsorption of this dye may then likely be attributed to Van der Waals and other forces, which could indicate that adsorption of the rhodamine is not exclusively due to cation exchange.

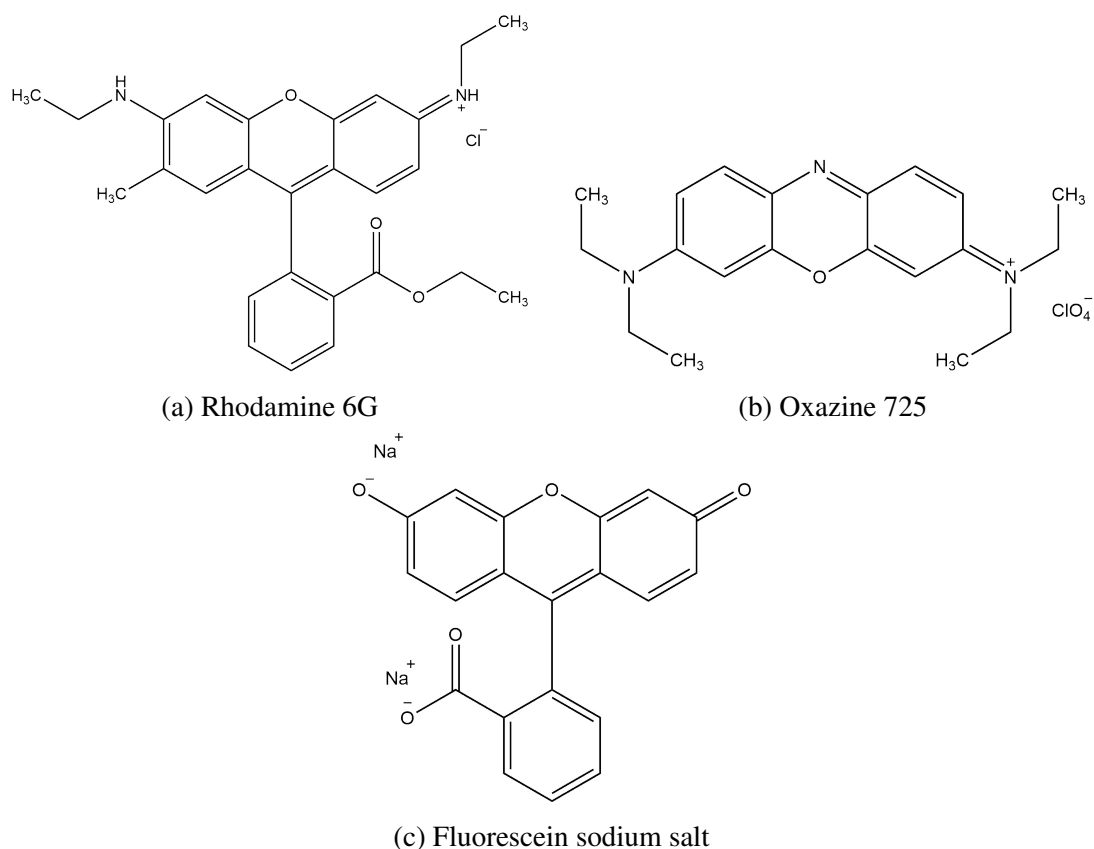


Fig. 6.1 Structures of fluorescent dyes used for adsorption to mica.

The preliminary experiments focussed on exchanging the mica surface cations with fluorophore molecules, then repeated exchange into bulk water to remove any free dye molecules from solution. The specifics of the method are described in the subsequent section.

6.2.1 Cation Exchange Process and Imaging

Imaging of a mica sample with no dye, and a droplet of pure water on the surface, showed a low level of autofluorescence of the mica itself which was sufficiently weak to present no problem in imaging of surface dye molecules.

Experiments were then conducted using a droplet of dye solution on the mica surface, which had to be contained using a hydrophobic barrier pen (Thermo Fisher Scientific) due to the low contact angles exhibited by water on the hydrophilic mica. The pen is designed for use with fluorescent dyes, so should have minimal interaction with the dye molecules. The area contained by the pen was approximately circular and 6 - 8 mm in diameter. The dye solution was allowed to 'incubate' on the surface, then exchanged using a pipette by near complete removal of the liquid droplet and deposition of a fresh droplet. For as much of the process as possible, dye solutions were covered to avoid any bleaching from ambient light sources.

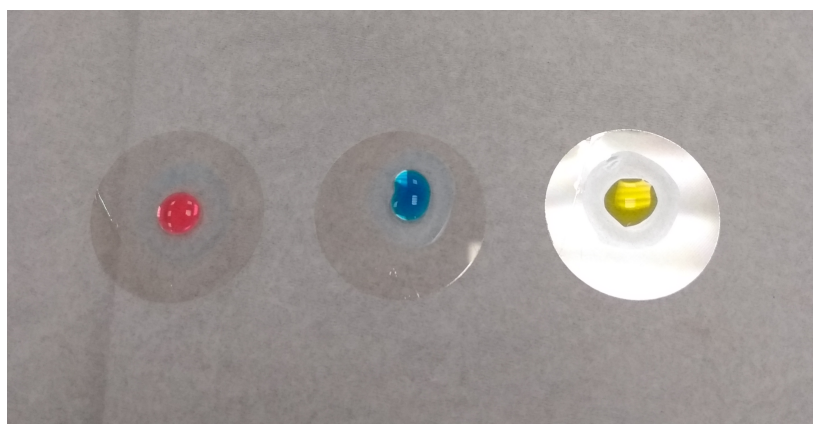


Fig. 6.2 Image of dye incubation step of exchange protocol. The dye solution droplets are contained on the freshly cleaved mica surface by a ring of hydrophobic barrier pen. From left to right, the shown dyes are rhodamine 6G, oxazine 725, and fluorescein sodium salt.

Liquid removal and reapplication were conducted on opposite sides of the sample region to attempt to exchange the solution as thoroughly as possible by inducing a cross-flow, and a number of exchanges were conducted with delays between to allow for any kinetically slow desorption of weakly bound species. Care was taken not to allow the solution to dry on the mica sample, which would change the effective concentration of any solute or precipitate it out onto the surface. Samples were then imaged with both TIRF and epifluorescence to excite dye in the near-surface region and the bulk droplet respectively.

For each of the dyes, a 15 μl volume of 1 mM solution was placed on each mica substrate. Although a higher concentration would have been desirable to drive cation exchange, the solubility limits of the dyes are close to 1 mM and any precipitation needed to be avoided. This situation was allowed to equilibrate for 20 min, before the dye solution was exchanged for fresh dye solution. The aim of this double exposure was to drive the equilibrium of cation exchange towards dye adsorption. After a further 20 min the surface was washed five times

with 15 μl of water then left in water for 20 min. The washing step was repeated four times before imaging, as preparatory work indicated that dye in solution was extremely difficult to reduce to concentrations which were no longer measurable. The TIRF images focussed on the mica surface, with the relevant laser used for excitation of each dye, are shown in Figure 6.3.

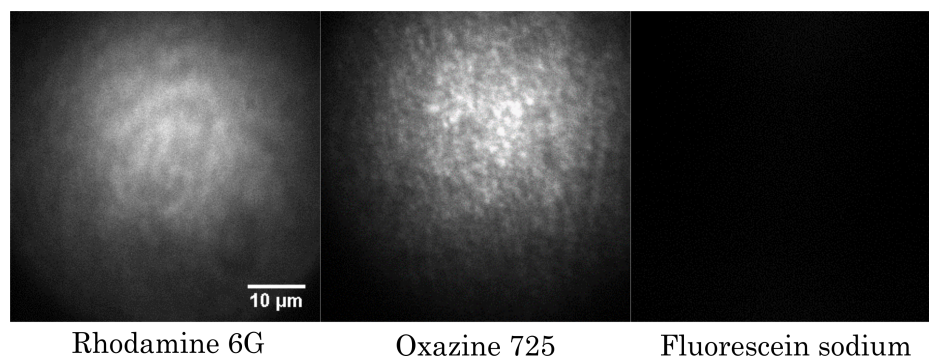


Fig. 6.3 TIRF microscope images of the mica surface, after exposure to three fluorescent dyes followed by repeated rinsing. Rhodamine 6G and oxazine 725 are cationic, whereas fluorescein sodium is doubly anionic in solution.

The TIRF images show significant fluorescence for the two cationic dyes, but essentially no measurable fluorescein adsorbed at the surface. This is as might be expected for adsorption of cationic species onto an anionic surface, and provides encouragement that this technique may be used to measure adsorption behaviour from solution onto mica. The imaging regime here, in which measures have been taken to remove bulk dye from solution, will only reveal ‘irreversible’ adsorption. Although the fluorescein has carboxylate functionality and work described earlier in this thesis revealed adsorption of carboxylates to mica in the presence of sodium ions, this was a reversible adsorption so would not be evident in these experiments.

The image of oxazine appears to show some granularity, compared to the more homogeneous fluorescence intensity of the rhodamine sample. The length scale of these structures is of the order of 1 μm , and could be due to aggregation of dye molecules. In the case of measurements of cation exchange capacity, intermolecular interactions are undesirable and so subsequent measurements focussed on the use of rhodamine 6G.

Imaging of the samples in epifluorescence was conducted after TIRF images, as shown in Figure 6.4, and revealed that there was still a measurable concentration of dye in solution, despite significant solution exchange. Conversion of fluorescence intensity to concentration is not trivial and would require careful calibration with the same setup and filters, but the

bulk solution above the mica clearly contains a non-negligible concentration well above single-molecule levels for all the tested dyes.

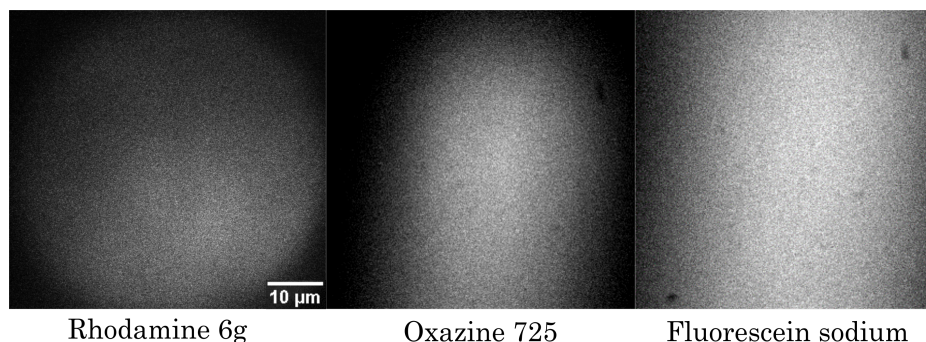


Fig. 6.4 EPI fluorescence images, showing the bulk solution above the mica surface for the three dyes after exchange then copious rinsing. Finite dye concentrations are visible in all cases.

Even after 20 exchanges using a pipette, imaging the bulk solution still revealed a finite fluorophore concentration. The high sensitivity of the technique to even nanomolar concentrations, when compared with the initial millimolar concentrations of compound present, as well as the manual difficulty in this exchange process may have contributed to the maintained presence of visible free dye. It is also possible that the initial exchange and adsorption at high concentration was reversible to some extent, and as the bulk solution was diluted there was a slow desorption of some of the excess in the bound layer into the bulk.

In order to ensure that any photobleach recovery measurements were truly a result of the in-plane mobility of adsorbed species, rather than the result of exchange between adsorbed species on the surface and free molecules in solution, it was desirable to remove all the unbound species from the bulk before carrying out these measurements.

6.2.2 Bleach Recovery

Despite the maintained presence of some low concentration of dye species in solution, an initial bleach recovery measurement was attempted for the rhodamine 6G on the surface, as this sample showed the greatest intensity and most uniform adsorption of surface species. The measurement was conducted as described in Section 2.13. Results of the measurement are shown in Figure 6.5. As the figure illustrates, after bleaching a clear darker region is visible on the sample where the dye molecules have been photobleached. Over time the dark region reverts back to the bulk fluorescence.

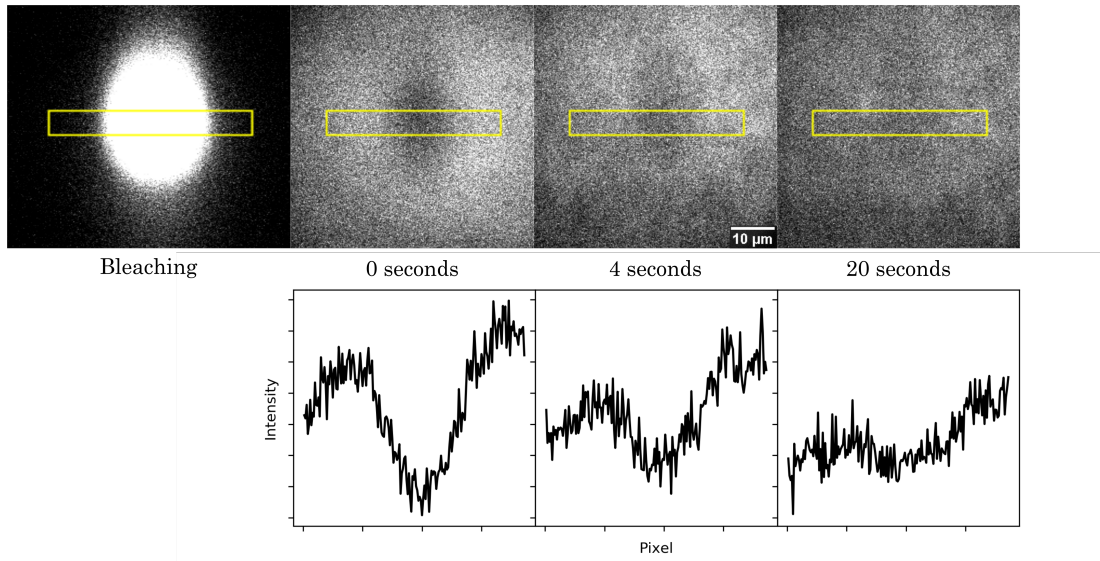


Fig. 6.5 Images captured during fluorescence recovery after photobleach measurements of rhodamine 6G exchanged onto mica. A small concentration of free dye remained in solution. From left to right the images recorded were: during bleaching with high laser intensity, and 0, 4, and 20 seconds after bleaching. Line profiles shown below are intensity across the central region shown on the images, integrated in the y-direction. Almost complete recovery is shown after approximately 20 seconds.

After approximately 20 seconds, nearly complete recovery is seen. This suggests that dye molecules are relatively mobile on the surface, though as previously mentioned the finite and undefined concentration of dye in solution makes this conclusion hard to draw with confidence. It is not possible from the images to clearly see whether the fluorescence recovery occurs uniformly across the bleached area, which would suggest exchange with solution species, or from the edges, which would suggest surface-diffusion.

Assuming only surface-diffusion, and neglecting diffusion occurring during bleaching, an order of magnitude estimate of the diffusion coefficient may be calculated from the data. From numerically solving the relevant diffusion equations, Soumpasis²²⁰ related the diffusion coefficient, D , to the radius of a uniform bleach laser, r_n , and the time for the bleached spot to recover halfway, $t_{1/2}$. The Soumpasis equation is given in Equation 6.1.

$$D = 0.224 \frac{r_n^2}{t_{1/2}} \quad (6.1)$$

From $r_n \approx 20 \mu\text{m}$, and $t_{1/2} \approx 10$ seconds, the diffusion coefficient for Rhodamine 6G adsorbed to the mica surface may be estimated as $9 \mu\text{m}^2/\text{s}$ ($9 \times 10^{-12} \text{m}^2/\text{s}$). Literature values

for diffusion coefficients of surfactants on surfaces are very scarce, and even more so for the solid - liquid interface.

Diffusion coefficients for rhodamine 6G in aqueous solution have been reported²²¹ in the range $3 - 4.5 \times 10^{-10} \text{ m}^2/\text{s}$. These are over an order of magnitude larger than the estimated surface diffusion coefficient, as might be expected for inhibited mobility of dye on the surface due to a strong electrostatic interaction between mica and dye.

6.2.3 Interaction with SDS

In Section 4.2 it was described how exposure to SDS at concentrations above the CMC induced complete desorption of an adsorbed layer of the cationic surfactant DDAB. Fluorescence microscopy could provide a useful tool for similar studies either as preliminary work for, or in addition to neutron studies. To this end, the mica substrate with adsorbed rhodamine 6G was exchanged directly into a solution of 2 CMC SDS, by pipette removal of water and replacement with SDS of the same volume. A different region of the mica was imaged to that used for the bleach recovery measurement described in the prior section.

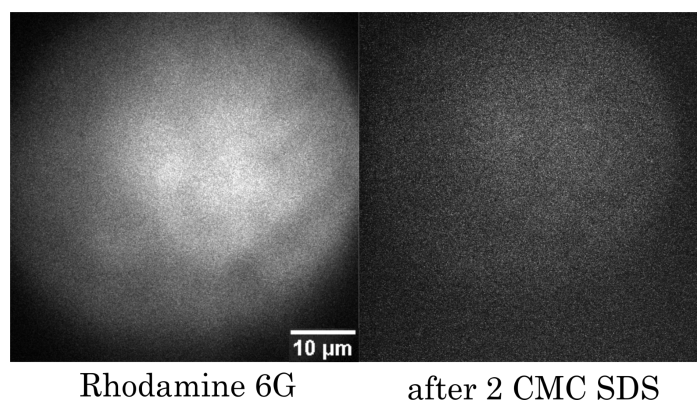


Fig. 6.6 TIRF images of the mica surface after exposure to rhodamine 6G and repeated rinsing (left), then after exchange into 2 CMC SDS. The reduction in intensity strongly suggests removal of much of the rhodamine from the mica surface.

As can be seen in Figure 6.6, a large reduction in fluorescence intensity was visible on exchange to 2 CMC SDS. The most likely explanation for this is removal of rhodamine from the surface by the anionic SDS. This is in agreement with the NR data discussed in Section 4.2, where cationic removal from the mica surface by uptake into anionic SDS micelles was seen for DDAB.

If all the dye was in a single layer on the surface and no other sources of fluorescence intensity were present, then the measured intensity could be directly related to the surface concentration of dye. The analysis is not this straightforward here, as some dye persists in solution which could give additional signal, although this is limited by the exponential decay of the TIRF excitation field. The autofluorescence of the mica may also preclude this analysis, though pre-bleaching of the mica will be considered as a solution.

The same near complete loss of intensity was seen when the cationic oxazine 725 exchanged mica was exposed to 2 CMC SDS. It was therefore concluded that fluorescence microscopy provides useful additional evidence that surface bound cationic species can be effectively removed by SDS micelles.

6.3 Method Development

To facilitate easy and complete exchange of the solution in contact with the mica, an alternative substrate set-up to the sessile droplet of solution was sought. Custom microfluidic devices were considered but for convenience and reproducibility a commercially available system was chosen. Adhesive chambers (Grace Bio-Labs HybriWell™ sealing system, SecureSeal™) were utilised, with a circular chamber of 13 mm diameter and thickness 0.15 mm. The design of the cell is shown in Figure 6.7. The quoted volume was 18 μl , and the chamber may be connected to standard microfluidic or HPLC tubing using press fit tubing connectors.

The small volume was chosen to allow easy and rapid solution exchange, and the chamber could be connected to an HPLC or syringe pump for controlled flow rates and volumes. The chamber is manufactured from polycarbonate, which is preferable to the PDMS which many microfluidic devices are fabricated from as PDMS been shown to retain small hydrophobic molecules²²², possibly affecting imaging. The thickness of the well is 0.15 mm. This is well beyond the evanescent decay length of the TIRF excitation field, so any adsorption to the top surface of the well will not be observed.

The speed and completeness of filling and exchange were investigated in the same manner described in Section 3.3. A cell was prepared consisting of the described adhesive cells adhered to a glass slide. The cell was filled with water, then exchanged into a red dye solution, then back into water. Snapshots of this process are shown in Figure 6.8. It was observed that the cell exchanged almost instantly, due to the very small internal volume. On initial filling

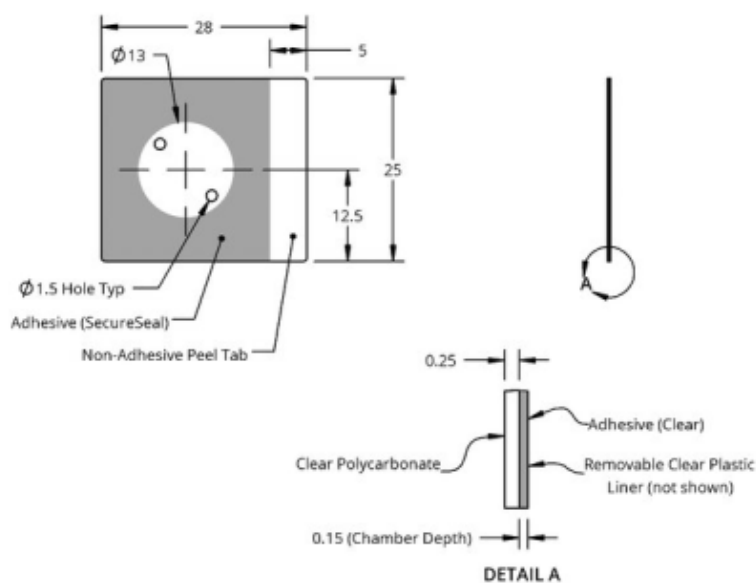


Fig. 6.7 Details of the Grace Bio-Labs hybridisation wells used for fluorescence microscopy measurements. Reproduced from Grace Bio-Labs technical information.

a small air bubble was trapped which persisted throughout. As the imaging area is much smaller than the area of the cell, this would not be an issue in practice as the area could be avoided and the bubble appeared stable, but in most cases complete filling occurred.



Fig. 6.8 Images of the cell used for fluorescence measurements, adhered to a glass slide rather than mica. The images from left to right show the cell filled with water, after injection of approximately 1 ml of red dye, and after subsequent injection of approximately 1 ml of water. Exchange was found to be very fast and complete. On initial filling a small air bubble was trapped, visible in the central picture to the lower left of the reservoir.

On attempting to use the adhesive hybridisation wells on mica discs, it was discovered that there was leaking between the cell and the mica surface. Even at very low flow rates of less than 0.1 ml/min (controlled by a syringe pump) leaking of fluid was seen. Spreading

of cell solution into the gap between the mica and adhesive cell top will be problematic as this solution will exchange very slowly, if at all. A more serious issue is the possibility of concentrated dye solution escaping and contacting microscope components, and in particular the objective lens which sits directly below the cell during imaging. The fluorescence microscope used is capable of measuring concentrations down to single molecule levels, and so contamination by a high (millimolar) concentration is very serious.

The cell sealing was rechecked on glass slides and it was found that the cell sealed effectively on glass, being able to tolerate flows of greater than 1 ml/min with no leaks even after flow of significant volume. There are a number of possible reasons for the cells sealing better to a glass slide than freshly cleaved mica; the adhesive used on the flow cells might adhere better to the surface chemistry of glass than of mica, the extremely flat nature of the cleaved mica might prevent strong adhesion, or partial delamination of the mica surface might allow leaking through the top layers. UV-O₃ treatment was found to have no effect on the sealing characteristics. Various methods of overcoming the leaking issue were considered, including physical clamping of the outside of the cell, and selective roughening or plasma cleaning of the mica surface on the section contacting the adhesive.

The first tested approach was addition of stronger supplementary adhesive. It was found that sealing was possible using a two component fast curing epoxy glue (Araldite ARA-400012 Instant). Application of a thin layer of the mixed adhesive onto the hybridisation well, followed by adhering to the cleaved mica and pressure to distribute the glue evenly, led to much better sealing than adhering the well to mica without epoxy. After the glue had been allowed to cure for approximately 5 min the cells were tested using a syringe pump and fittings as described previously.

Whilst there was some variation in the sealing properties of substrates after preparation, with practice all prepared substrates were found to show no leaking at flow rates up to 1 ml/min even after sustained flow for longer than 30 min. At increased flow rates leaking still did occur, presumably due to the higher pressure in the chamber. Removal of the hybridisation well from the mica sheet after testing followed by visual inspection showed that no glue had ingressed into the mica area inside the well, which would have affected the imaged region. This also means contact between solution and glue would be minimised.

Unfortunately planned experiments with these new cells have not yet been able to proceed.

6.4 Future Work

Immediate future work will focus on repeating the experiments discussed here which were originally performed with the sessile drops, with the newly developed chamber cell and continuous flow. This should allow unambiguous determination of what adsorption is 'permanent', rather than readily reversible, and allow bleach recovery measurements to give estimates of the in-plane diffusion constants of surface species.

Another goal is to develop more quantitative analysis, relating fluorescence intensity to adsorbed amount. Careful consideration and calibration would be required but the potential for high throughput isotherm measurements is exciting, conducted in a similar way to QCM experiments but with the ability to chemically resolve adsorbed species and without the complication of solvent replacement. Screening of cations capable of bridging for a given anionic functionality is an example.

The technique as it has been used in this work requires the use of dye molecules. These may be chosen to represent species of interest, which allows easy interpretation and no chance of an added probe perturbing the system, though of course restricts the systems which can be studied. The far more common approach in fluorescence microscopy is to tag structures of interest with a dye. Nile red is a neutral molecule, which is used to stain hydrophobic environments in biological systems²²³. The dye is only sparingly soluble in water, and has very limited fluorescence in polar media²²⁴. It is solvatochromic; the fluorescence characteristics vary depending on the environment of the dye molecule⁹⁴. Use of probes such as this present the opportunity to monitor specific non-fluorescent molecules, such as the DDAB surfactant used in neutron experiments, by labelling the formed structures rather than each molecule.

Chapter 7

Conclusions and Future Work

7.1 Conclusions

Adsorption of Anionic Surfactants onto Mica

The adsorption of the anionic surfactant AOT onto the anionic surface of the mineral muscovite mica was explored, to further the understanding of the effect of cation bridging. Significantly, it was found that the caesium salt of AOT adsorbed to mica at the CMC. This showed that it is possible for monovalent ions to act as bridging ions, in contrast to prior literature assumptions that divalent ions are required. It was postulated that with increasing ionic radius of monovalent ion the decreased ion hydration resulted in a greater likelihood of bridging.

A further study was carried out using the sodium salt of AOT with added cations. It was observed that the addition of potassium, calcium, and magnesium ions all led to adsorption of the surfactant, with different adsorbate structures. The relative concentrations of calcium to the non-bridging sodium ion which still facilitated adsorption was investigated, and it was seen that bridging still occurred even in swamping excess of sodium. This observation might inform composition of flooding water, as it suggests absolute bridging ion concentration is more important than the ratio of relevant ions.

All of the potassium, calcium, and magnesium bridged structures were found to only bind reversibly, and full layer desorption occurred even when ionic strength and bridging ion concentration was maintained. This observation precludes both double layer expansion and multivalent ion exchange as mechanisms of layer removal in this particular system. It

was hypothesised that an effect based on solubility of acid groups in the presence of calcium might be partially responsible for incremental recovery on reduced salinity water flooding.

The adsorption of octanoate and decanoate anions was also probed, and it was found that the sodium salts adsorbed even in the absence of other cations. This was in contrast to the behaviour of AOT, and suggests a difference in interaction based on the nature of the anionic surfactant headgroup. The adsorption was found to be reversible, as with the AOT salts.

Adsorption of a Non-Ionic Surfactant onto Mica

Adsorption of the non-ionic surfactant $C_{12}E_5$ onto the mica surface from aqueous solution was studied. Essentially no adsorption was seen below the CMC, and at the CMC and above a slight change in reflectivity profile was visible. This change could be fitted by a very diffuse or hydrated bilayer, with more hydrated headgroup regions and a less hydrated alkyl tailgroup region.

Adsorption Comparison with Simulation

Through collaboration, MD simulations have been compared with experimental neutron reflectivity data. By calculating the SLD profile for the molecular configuration from the simulation the predictions can be quantitatively compared to the NR data. Initially significant changes were required to the simulation model to be consistent with the recorded NR data, particularly the removal of potassium ions from the simulation.

Once this insight had been determined, good agreement of simulation with experiment reflectivity data was achieved. The optimised simulations can provide molecular information not available from the reflectivity data; it was suggested that the adsorbate structure for the cationic surfactant DDAB on mica is an asymmetric bilayer, with a well ordered layer adjacent to the mica surface, and a more canted and less ordered layer beyond this towards the bulk. This synergy of MD and NR has significant potential.

Surfactant Interaction on the Mica Surface

The behaviour of an adsorbed layer of the cationic surfactant DDAB on mica was studied, on exposure to various solutions of organic molecules. It was found that the DDAB layer, which had previously been thought to be irreversibly bound, could be completely removed

by a solution of the anionic surfactant SDS. DDAB removal only occurred when the SDS concentration was at or above the CMC, suggesting a mechanism for the removal process. No DDAB removal was seen when a non-micellising diacid salt was used instead of SDS, even when the concentration was raised to equal that of the CMC of SDS. This removal of a tightly bound cationic from an anionic substrate, by an anionic surfactant, represents a new insight and approach that could inform a number of applications.

Further work was undertaken to investigate the generality of the removal effect to other surfactants. For the anionic surfactant AOT different behaviour was seen; DDAB was completely removed even at well below the CMC (0.05 CMC). At 0.005 CMC no removal occurred. The difference in behaviour between SDS and AOT was rationalised by the differing structure of the surfactants.

The non-ionic surfactant $C_{12}E_5$ did not lead to DDAB complete removal, even when alternative surface-compensating cations were present in solution. Instead a large amount of the layer was replaced by $C_{12}E_5$, which was labile and was removed when the bulk non-ionic was removed. This left a reduced and modified DDAB layer on the surface, which was still able to template adsorption of the non-ionic into a much thicker and denser layer than for non-ionic adsorption onto a bare mica surface.

Fluorescence Microscopy

Fluorescence microscopy has been demonstrated as a useful tool which has been newly applied to adsorption studies on the mica surface. Some of the capabilities and possibilities have been explored and found to be feasible, including selectively imaging dyes on the surface, and estimating surface diffusion coefficients in an adsorbed layer. There is wide and exciting potential for expansion into numerous further studies.

7.2 Future Work

On Anionic Surfactant Adsorption

There is potential for significant further study into the bridging interaction of cations between anionic surfactant and anionic surfaces, focusing on the key interactions between the substrate, ion, and surfactant. The results in this thesis showed a clear difference between the behaviour

of AOT, which has a sulfonate headgroup, and carboxylates. Ideally, study of a range of surfactants with constant tail groups and as wide a possible range of headgroups, with different charge densities and pKa values, would be tested with a range of cations to give a holistic picture. How the identity of the cations which can cause bridging changes depending on the headgroup is a commercially important question, as is the relative concentrations of non-bridging to bridging ion at which bridging is no longer observed.

The specifics of which cations can lead to bridging is still open to investigation; this work describes a range of inorganic cations for both AOT and carboxylates, but organic ions have not been tested. Organic cations, such as quaternary ammonium ions, might provide a convenient tool to alter cation parameters such as hydration and radius by altering the organic groups. In this way the key properties determining bridging behaviour might be elucidated.

The role of the surface in determining which ions cause bridging is also an area for further study. Mica has a relatively high surface charge density on the scale of clay minerals, and for less charged clays it might be expected that the break point in the monovalent ions which cause bridging might fall lower in the periodic table.

An overall goal, relying on data collected in the ways suggested, would be to condense the bridging interaction to a description of the key parameters involved. These parameters would describe the surface, cation, and anionic species. An example of such a set would be the surface charge density, cation ionic radius, and anionic headgroup pKa, and whether the system was above the CMC. Dividing the parameter space into bridging and non-bridging regions would provide a predictive tool for analysis of a given system.

Some other areas of interest which warrant further investigation include the specific interactions which lead to different structures forming, as was seen for AOT with potassium, calcium, and magnesium in Section 3.1 where it was postulated that anion - cation ratios close to charge neutrality might influence structure. The absolute and relative ion concentrations, and valency, might all play a part in determining the equilibrium structure, whether multilayer or single. Understanding the factors which together cause multilayering is important for applications such as artificial lung surfactants, where multiple surfactant layers are required at the air - liquid interface to facilitate expansion of the lung surface area during breathing.

A further question is whether the bridging interaction can ever be strong enough to lead to either adsorption below the CMC, or irreversible adsorption. Both of these are features observed for cationic adsorption on mica, but not as yet for anionic adsorption.

On Surfactant Interactions at the Mica Surface

The experiments described in this thesis relating to the interaction of a pre-adsorbed DDAB layer exposed to species in solution show a variety of different behaviours, corresponding to different regimes. Future work could focus on understanding what systems will fall into which regimes, based on certain key parameters. The mechanism and dynamics of surfactant removal, where it does occur, are also of interest.

As discussed in Section 4.6, the strength of interaction between surfactants may be quantified by a β parameter. Determining the β parameters for the pairs of surfactants already studied, and observing if there is any relation between the β or β^σ parameter and the observed removal behaviour, would be valuable. For example if the β^σ parameter for DDAB and AOT is significantly more negative than for DDAB and SDS, then the difference in desorption behaviour might be explained. Another possibility is that the ratio of the strength of interaction in the bulk, β , to the strength of interaction in a layer, β^σ , might be the key factor in determining behaviour.

A comprehensive study to elucidate the key characteristics would involve observing behaviour of a range of adsorbed cationic layers from surfactants with different tail groups, when exposed to a range of surfactants in solution with the same headgroup and varying tails, and the same tail group but varying heads. Neutron reflectometry would be a prospective tool for this work. Measurements of the β and β^σ values for these pairs would further inform conclusions about the driving forces for surfactant - surfactant interactions.

Organoclays

Whether many of the effects studied in this thesis still occur in the context of organoclays is an open question. The packing arrangements and coverage of organic molecules between the clay layers is dominated by the effects of the confinement and hydrophobicity of the interlayer, and the structures and total adsorbed amount may differ from those on the basal plane in solution. Further work on whether the use of anionic surfactants may be able to reverse cationic-organically modified clay back into the raw state would be one example of this.

Given the observations of cation bridging of anionic surfactants to the mica surface described here, this behaviour could also be investigated in the clay interlayers. Organically modified clays of this type would be expected to show a higher absorption characteristic for

cationic species in solution. A barrier to forming organoclays with anionic surfactants and relevant cations might be the reversibility of binding seen for cation bridging in the systems studied. It may be the case that irreversible binding is required for a stable organoclay. Organic modification using non-ionic surfactants has however been reported²²⁵, and the adsorption of a non-ionic to mica was found to be only weak and reversible.

In Section 3.1 a potential alternative molecular mechanism for reduced salinity oil recovery was suggested; precipitated carboxylates on mineral surfaces being solubilised as the calcium concentration in solution is reduced. This effect could potentially be applied and tested in the context of organoclays. If it is not possible to produce organoclays from anionic surfactants and bridging cations due to the reversible nature of the binding, then the possibility of initiating the adsorption in a slurry of clay, and then precipitating the carboxylates bound to the surfaces could be explored. Care would need to be taken to separate bulk precipitated organic out of the organically modified clay mixture.

On Comparison of MD Simulations with Reflectivity Data

The collaboration of experimental work with simulations has been demonstrated to be mutually beneficial; without experimental data the MD gives incorrect structures, but once re-directed is capable of giving much more detailed insight and higher spatial resolution structures than possible with NR alone. Comparison of reflectivity data with molecular dynamics simulations of systems more complex than the single adsorbates studied thus far is an obvious next step. When simulations can reliably reproduce experimental results, then their predictive power may be realised, alongside robust theory. Experimentally inaccessible molecular resolution may be gained.

Neutron reflectivity experiments are of course not the only technique where data may be compared to simulations. Physical chemistry is typified by the use of a range of techniques applied to a system to gain different types of information. Perhaps an end goal, admittedly a far reaching one, might be a holistic fitting package capable of analysing and co-refining a model to datasets collected through numerous techniques. It is common to build up a picture of a system from different information in an unstructured manner, but a rigorous scientific method for doing so would be a shift in the manner in which surface science is conducted. A specific example of complementary techniques ideal for such a package might be neutron reflectivity, MD simulation, and sum frequency generation (SFG) spectroscopy.

The specific pitfalls and limitations of each technique would require careful consideration, as would ensuring that the systems under investigation are essentially equivalent in each technique used. The computational power required, in particular for molecular dynamics simulations of the system or DFT simulations of certain interactions within it, is likely a severe limitation on the complexity of systems which this might currently be applicable to.

Sum Frequency Generation Spectroscopy of Organic Species on Mica

Sum frequency generation spectroscopy (SFG) is a non-linear optic technique which can provide surface specific spectra²²⁶. Species in centrosymmetric environments do not generate a signal in the SFG spectrum. Further analysis of the spectra may also be used to provide information on the molecular orientation of surface adsorbed species.

There are examples of SFG being applied to species on mica²²⁷, but many of the systems described in this thesis would lend themselves particularly well to the observations that SFG can provide. The bilayers of DDAB predicted by MD simulations as described in Section 3.4 are highly asymmetric, contrasting with the classical view of a bilayer as two approximately identical layers opposing each other. The arrangement suggested by MD would show a strong signal in SFG, whereas the classical view would likely not, due to the symmetry present.

Described in Section 4.2.3 were efforts to determine the structure formed from a pre-existing DDAB layer on mica when exposed to SDS below the CMC. It was suggested that a two layer system formed, with the SDS including more into the upper layer than into the lower. SFG data of an identical system should provide further information to support or dispute this conclusion. Deuteration of specific species and consideration of the C-H and C-D absorption bands would allow some distinction to be made between the species present.

In analysis of SFG data collected from mica, care would need to be taken to account for any effect on the signal from the inherent birefringence of the mica crystal, which can occur²²⁸.

Surfactant Equilibrium and Partial or Complete Exchange on the Surface: Kinetics

In nearly all surfactant applications, understanding the equilibrium of adsorbed species with species in solution is important. Both neutron reflectivity and SFG provide opportunities for

measuring the speed of exchange of adsorbed layers through selective deuteration; either observing a protonated layer exchanging with deuterated species introduced into solution or vice versa. By observing the change in layer SLD in neutron reflectivity, or the increase or decrease in the C-H or D-H stretches respectively in SFG, the speed of exchange may be calculated. This could be compared to the speed of surface mobility as measured with fluorescence recovery after photobleaching, to observe how the in-plane mobility compares to the equilibrium between bound and free surfactant.

The different exchange speeds of relative components in a layer which has different environments is also of interest. For example the layer structure predicted by simulations in Section 3.4.3, with two distinct sub-layers in the adsorbed structure, might show fast exchange of the outer leaflet, followed by slower exchange with the inner and denser leaflet.

Depending on the speed of exchange these measurements may be beyond the current limitations of time-resolved neutron reflectivity. Many recent developments, including better beam guides and super mirrors, as well as potential for the higher flux of the European Spallation Source currently under development, are all making higher time resolution a greater possibility.

Control of Surface Charge

In this work, initial procedures and data have indicated the ability to produce clay surfaces of intermediate charge. However, it has proved very challenging to quantify this charging behaviour experimentally on flat surfaces.

If robust measurement of surface charge density becomes possible, whether measured by the proxy of zeta potential or through direct means, then tuning of the charge modification techniques discussed in this thesis should be possible to yield a range of surfaces with controlled charges. It is noted that attention must also be given to the resulting surface chemistry, which may influence the adsorption behaviour and in particular any non-electrostatic interactions such as Van der Waals or chemisorption.

These surfaces may then be incorporated into many of the studies described in this thesis, to give a similarly detailed and in-depth assessment of the surfactant systems and the interactions present.

Fluorescence Microscopy

The potential for fluorescence microscopy in physical chemistry is great, and for the most part unrealised. Chapter 6 details the initial steps which have been taken to illustrate the prospects of the method, and the experimental challenges. A major goal is the development of protocols and analysis to make measurements as quantitative as possible; quantitative image analysis is a very advanced field and through careful application a number of physical chemistry challenges may be approached.

One specific objective is the measurement of in-plane diffusion coefficients for a bound layer of cationic species by bleach recovery measurements, and comparison of this with in-plane diffusion measured in other ways, such as with quasi-elastic neutron scattering. The possibility of these measurements has been illustrated in this work. High-throughput adsorption studies are also an opportunity, with the additional advantage of the ability to distinguish components of mixtures.

Fluorescence measurements in this thesis focussed on studies linking with the other work carried out with neutron reflectometry. Studies of surface heterogeneity are however possible in high resolution with fluorescence microscopy, so behaviour of molecules in solution at defect sites on the surface of mica, such as kinks and edges, may be studied. Seeing how behaviour at these sites compares with basal plane behaviour is of great interest to commercial systems. Minerals beyond mica are also of interest, and the possibility of applying the same experimental setup to calcite is being considered.

References

- [1] Neasham, J. J. W. *SPE Annual Fall Technical Conference and Exhibition* **1977**, 8 pp.
- [2] Puntervold, T.; Mamonov, A.; Aghaeifar, Z.; Frafjord, G. O.; Moldestad, G. M.; Strand, S.; Austad, T. *Energy and Fuels* **2018**, *32*, 7374–7382.
- [3] van Olphen, H. *An Introduction to Clay Colloid Chemistry*, 2nd ed.; Krieger Publishing Company: Malabar, Florida, 1991.
- [4] Grim, R. E.; Kodama, H. *Encyclopaedia Britannica*; Encyclopaedia Britannica. inc., 2014.
- [5] Anderson, R. L.; Ratcliffe, I.; Greenwell, H. C.; Williams, P. A.; Cliffe, S.; Coveney, P. V. *Earth-Science Reviews* **2010**, *98*, 201–216.
- [6] Boek, E. S.; Coveney, P. V.; Skipper, N. T. *Journal of the American Chemical Society* **1995**, *117*, 12608–12617.
- [7] Grandjean, J.; Laszlo, P. *Clays and Clay Minerals* **1994**, *42*, 652–654.
- [8] Gulicovski, J. J.; Čerović, L. S.; Milonjić, S. K. *Materials and Manufacturing Processes* **2008**, *23*, 615–619.
- [9] Kosmulski, M. *Advances in Colloid and Interface Science* **2016**, *238*, 1–61.
- [10] De Poel, W.; Pintea, S.; Drnec, J.; Carla, F.; Felici, R.; Mulder, P.; Elemans, J. A.; Van Enckevort, W. J.; Rowan, A. E.; Vlieg, E. *Surface Science* **2014**, *619*, 19–24.
- [11] Schlegel, M. L.; Nagy, K. L.; Fenter, P.; Cheng, L.; Sturchio, N. C.; Jacobsen, S. D. *Geochimica et Cosmochimica Acta* **2006**, *70*, 3549–3565.
- [12] Rojas, O. J. *Encyclopedia of Surface and Colloid Science*; 2002; pp 517–535.
- [13] Secor, R. B.; Radke, C. J. *Journal of Colloid And Interface Science* **1985**, *103*, 237–244.
- [14] Hartwell, J. M. *Clay Minerals* **1965**, *6*, 111–118.
- [15] Hofmann, U.; Klemen, R. *Zeitschrift fur anorganische Chemie* **1950**, *262*, 95–99.
- [16] Nishimura, S.; Biggs, S.; Scales, P. J.; Healy, T. W.; Tsunematsu, K.; Tateyama, T. *Langmuir* **1994**, *10*, 4554–4559.

- [17] Skoubris, E. N.; Chryssikos, G. D.; Christidis, G. E.; Gionis, V. *Clays and Clay Minerals* **2013**, *61*, 83–97.
- [18] Karakassides, M. A. *Clay Minerals* **1999**, *34*, 429–438.
- [19] Atkins, P. W. *Physical chemistry*; Oxford University Press, 2006; p 972.
- [20] Stern, O. *Zeitschrift fur Elektrochemie* **1924**, *30*, 508–516.
- [21] Nakamura, M.; Sato, N.; Hoshi, N.; Sakata, O. *ChemPhysChem* **2011**, *12*, 1430–1434.
- [22] Andelman, D. In *Soft Condensed Matter Physics in Molecular and Cell Biology*; Poon, W, C, K., Andelman, D., Eds.; Taylor & Francis, 2006; pp 97–122.
- [23] Evans, D. F.; Wennerstrom, H. *The colloidal domain: where physics, chemistry, biology, and technology meet*; Wiley-VCH, 1999; pp 99–156.
- [24] Nagarajan, R. *Langmuir* **2002**, *18*, 31–38.
- [25] De Rouffignac, E.; Alldredge, G. P.; Dewette, F. W. *Chemical Physics Letters* **1980**, *69*, 29–32.
- [26] Cao, G.; Zhang, Q.; Brinker, C. J. *Annual Review of Nano Research*; Annual Review of Nano Research; WORLD SCIENTIFIC, 2009; Vol. 3.
- [27] Langmuir, I. *Journal of the American Chemical Society* **1918**, *40*, 1361–1403.
- [28] Meghea, A.; Rehner, H. H.; Peleanu, I.; Mihalache, R. *Journal of Radioanalytical and Nuclear Chemistry* **1998**, *229*, 105–110.
- [29] Inglezakis, V. J.; Pouloupoulos, S. G.; Kazemian, H. *Microporous and Mesoporous Materials* **2018**, *272*, 166–176.
- [30] Buttersack, C. *Physical Chemistry Chemical Physics* **2019**, *21*, 5614–5626.
- [31] Muggeridge, A.; Cockin, A.; Webb, K.; Frampton, H.; Collins, I.; Moulds, T.; Salino, P. *Philosophical Transactions of the Royal Society A: Mathematical, Physical and Engineering Sciences* **2013**, *372*, 20120320.
- [32] Sandrea, I.; Sandrea, R. *Oil & Gas Journal* **2007**, *105*, 1–8.
- [33] Sheng, J. J. *Petroleum* **2015**, *1*, 97–105.
- [34] Rellegadla, S.; Prajapat, G.; Agrawal, A. *Applied Microbiology and Biotechnology* **2017**, *101*, 4387–4402.
- [35] Robbana, E.; Buikema, T. A.; Mair, C.; Williams, D.; Mercer, D. J.; Webb, K. J.; Hewson, A.; Reddick, C. E. *Abu Dhabi International Petroleum Exhibition and Conference* **2012**, 12–14.
- [36] Lager, A.; Webb, K. J.; Black, C. J. J.; Singleton, M.; Sorbie, K. S. *Petrophysics* **2008**, *49*, 28–35.

- [37] Lee, S. Y.; Webb, K. J.; Collins, I.; Lager, A.; Clarke, S.; O'Sullivan, M.; Routh, A.; Wang, X. Low Salinity Oil Recovery: Increasing Understanding of the Underlying Mechanisms. SPE Improved Oil Recovery Symposium Proceedings.
- [38] Pouryousefy, E.; Xie, Q.; Saeedi, A. *Petroleum* **2016**, 2, 215–224.
- [39] Jackson, M. D.; Vinogradov, J.; Hamon, G.; Chamerois, M. *Fuel* **2016**, 185, 772–793.
- [40] Speranza, F.; Pilkington, G. A.; Dane, T. G.; Cresswell, P. T.; Li, P.; Jacobs, R. M. J.; Arnold, T.; Bouchenoire, L.; Thomas, R. K.; Briscoe, W. H. *Soft Matter* **2013**, 9, 7028.
- [41] Striolo, A.; Grady, B. P. *Langmuir* **2017**,
- [42] Penfold, J.; Thomas, R. K. *Current Opinion in Colloid and Interface Science* **2014**, 19, 198–206.
- [43] Pynn, R. *Neutron Scattering—A Non-destructive Microscope for Seeing Inside Matter*; Springer, Boston, MA, 2009; pp 15–36.
- [44] Barker, R. D.; McKinley, L. E.; Titmuss, S. *Advances in Experimental Medicine and Biology*; Springer, Cham, 2016; Vol. 915; pp 261–282.
- [45] Welbourn, R. J.; Clarke, S. M. *Current Opinion in Colloid and Interface Science* **2019**, 42, 87–98.
- [46] Rightor, E. G.; Hitchcock, A. P.; Ade, H.; Leapman, R. D.; Urquhart, S. G.; Smith, A. P.; Mitchell, G.; Fischer, D.; Shin, H. J.; Warwick, T. *The Journal of Physical Chemistry B* **1997**, 101, 1950–1960.
- [47] Coffey, T.; Urquhart, S. G.; Ade, H. *Journal of Electron Spectroscopy and Related Phenomena* **2002**, 122, 65–78.
- [48] Heavens, O. S. *Optical Properties of Thin Solid Films by O. S. Heavens, Ph.D. New York, NY: Dover Publications, INC., 1965; Dover Publications: New York, 1965.*
- [49] Dawidowski, J.; Granada, J. R.; Santisteban, J. R.; Cantargi, F.; Palomino, L. A. R. *Experimental Methods in the Physical Sciences* **2013**, 44, 471–528.
- [50] Cubitt, R.; Fragneto, G. In *Scattering*; Pike, R., Sabatier, P., Eds.; Academic Press, 2002; Chapter 2.8.3, pp 1198–1208.
- [51] Born, M.; Wolf, E. *Principles of Optics Electromagnetic Theory of Propagation INterference and Diffraction of Light 2nd edition by Max Born Emil Wolf New York NY Pergamon Press 1964; Pergamon Press, 1999; pp 1–952.*
- [52] Nénot, L.; Croce, P. *Revue de Physique Appliquée* **1980**, 15, 761–779.
- [53] Nelson, A. *Journal of Applied Crystallography* **2006**, 39, 273–276.
- [54] Zarbakhsh, A.; Querol, A.; Bowers, J.; Webster, J. R. P. *Faraday Discussions* **2005**, 129, 155–167.

- [55] Browning, K. L.; Griffin, L. R.; Gutfreund, P.; Barker, R. D.; Clifton, L. A.; Hughes, A.; Clarke, S. M. *Journal of Applied Crystallography* **2014**, *47*, 1638–1646.
- [56] Griffin, L. R.; Browning, K. L.; Truscott, C. L.; Clifton, L. A.; Clarke, S. M. *The Journal of Physical Chemistry B* **2015**, *119*, 6457–6461.
- [57] Webster, J.; Holt, S.; Dalglish, R. *Physica B: Condensed Matter* **2006**, *385-386*, 1164–1166.
- [58] Dalglish, R. M.; Langridge, S.; Plomp, J.; De Haan, V. O.; Van Well, A. A. *Physica B: Condensed Matter* **2011**, *406*, 2346–2349.
- [59] Saerbeck, T.; Cubitt, R.; Wildes, A.; Manzin, G.; Andersen, K. H.; Gutfreund, P. *Journal of Applied Crystallography* **2018**, *51*, 249–256.
- [60] Cubitt, R.; Saerbeck, T.; Campbell, R. A.; Barker, R.; Gutfreund, P. *Journal of Applied Crystallography* **2015**, *48*, 2006–2011.
- [61] Gutfreund, P.; Saerbeck, T.; Gonzalez, M. A.; Pellegrini, E.; Laver, M.; Dewhurst, C.; Cubitt, R. *Journal of Applied Crystallography* **2018**, *51*, 606–615.
- [62] Taylor, J. et al. *Bulletin of the American Physical Society* **2012**, *Volume 57*,.
- [63] Nelson, A. *Journal of Physics: Conference Series* **2010**, *251*, 012094.
- [64] Parratt, L. G. *Physical Review* **1954**, *95*, 359–369.
- [65] Hamley, I. W.; Pedersen, J. S. *Journal of Applied Crystallography* **1994**, *27*, 29–35.
- [66] Nicklin, C.; Arnold, T.; Rawle, J.; Warne, A. *Journal of Synchrotron Radiation* **2016**, *23*, 1245–1253.
- [67] Björck, M.; Andersson, G. *Journal of Applied Crystallography* **2007**, *40*, 1174–1178.
- [68] Delgado, A. V.; González-Caballero, F.; Hunter, R. J.; Koopal, L. K.; Lyklema, J. *Pure and Applied Chemistry* **2005**, *77*, 1753–1805.
- [69] Lyklema, J. *Colloids and Surfaces A: Physicochemical and Engineering Aspects* **2011**, *376*, 2–8.
- [70] Nishimura, S.; Yao, K.; Kodama, M.; Imai, Y.; Ogino, K.; Mishima, K. *Langmuir* **2002**, *18*, 188–193.
- [71] Bukšek, H.; Luxbacher, T.; Petrinić, I. *Acta Chimica Slovenica* **2010**, *57*, 700–706.
- [72] Anton Paar, SurPASS Electrokinetic Analyzer Instruction Manual. 2015.
- [73] Ohshima, H.; Furusawa, K. *Electrical Phenomena at Interfaces: Fundamentals, Measurements, and Applications*; M. Dekker: New York, 1998.
- [74] Chibowski, E.; Szczes, A. *Adsorption* **2016**, *22*, 755–765.
- [75] Ge, Z.; Wang, Y. *Journal of Physical Chemistry B* **2017**, *121*, 3394–3402.

- [76] Donati, G. L.; Amais, R. S.; Williams, C. B. *Journal of Analytical Atomic Spectrometry* **2017**, *32*, 1283–1296.
- [77] Eastoe, J.; Fragneto, G.; Robinson, B. H.; Towey, T. F.; Heenan, R. K.; Leng, F. J. *Journal of the Chemical Society, Faraday Transactions* **1992**, *88*, 461.
- [78] Eastoe, J.; Robinson, B. H.; Heenan, R. K. *Langmuir* **1993**, *9*, 2820–2824.
- [79] Stahla, M. L.; Baruah, B.; James, D. M.; Johnson, M. D.; Levinger, N. E.; Crans, D. C. *Langmuir* **2008**, *24*, 6027–6035.
- [80] Vig, J. R. *Journal of Vacuum Science & Technology A* **1985**, *3*, 1027–1034.
- [81] ASTM, Standard Test Method for Methylene Blue Index of Clay 1. 2015.
- [82] van Olphen, H.; Fripiat, J. *Data handbook for clay minerals and other non-metallic materials*, 1st ed.; Pergamon Press, 1979; p 346.
- [83] Kahr, G.; Madsen, F. T. *Applied Clay Science* **1995**, *9*, 327–336.
- [84] Patil, K.; Pawar, R.; Talap, P. *Physical Chemistry Chemical Physics* **2000**, *2*, 4313–4317.
- [85] Meier, L. P.; Kahr, G. *Clays and Clay Minerals* **1999**, *47*, 386–388.
- [86] Ammann, L.; Bergaya, F.; Lagaly, G. *Clay Minerals* **2005**, *40*, 441–453.
- [87] Stanjek, H.; Künkel, D. *Clay Minerals* **2016**, *51*, 1–17.
- [88] Borden, D.; Glese, R. F. *Clays and Clay Minerals* **2001**, *49*, 444–445.
- [89] Osman, M. A.; Suter, U. W. *Journal of Colloid and Interface Science* **2000**, *224*, 112–115.
- [90] Sayin, M.; Reichenbach, V. O. N. *Clay Minerals* **1978**, *13*, 241.
- [91] Lim, C. H.; Jackson, M. L. *Clays and Clay Minerals* **1986**, *34*, 346–352.
- [92] Suhling, K.; Hirvonen, L. M.; Levitt, J. A.; Chung, P. H.; Tregidgo, C.; Le Marois, A.; Rusakov, D. A.; Zheng, K.; Ameer-Beg, S.; Poland, S.; Coelho, S.; Henderson, R.; Krstajic, N. *Medical Photonics* **2015**, *27*, 3–40.
- [93] Sydor, A. M.; Czymmek, K. J.; Puchner, E. M.; Mennella, V. *Trends in Cell Biology* **2015**, *25*, 730–748.
- [94] Bongiovanni, M. N.; Godet, J.; Horrocks, M. H.; Tosatto, L.; Carr, A. R.; Wirthensohn, D. C.; Ranasinghe, R. T.; Lee, J. E.; Ponjavic, A.; Fritz, J. V.; Dobson, C. M.; Klenerman, D.; Lee, S. F. *Nature Communications* **2016**, *7*.
- [95] Combs, C. A. *Current Protocols in Neuroscience* **2010**, *50*, 2.1.1–2.1.4.
- [96] Mattheyses, A. L.; Simon, S. M.; Rappoport, J. Z. *Journal of Cell Science* **2010**, *123*, 3621–3628.

- [97] Schneider, C. A.; Rasband, W. S.; Eliceiri, K. W. *Nature Methods* **2012**, *9*, 671–675.
- [98] Rueden, C. T.; Schindelin, J.; Hiner, M. C.; DeZonia, B. E.; Walter, A. E.; Arena, E. T.; Eliceiri, K. W. *BMC Bioinformatics* **2017**, *18*, 529.
- [99] Paria, S.; Khilar, K. C. *Advances in Colloid and Interface Science* **2004**, *110*, 75–95.
- [100] Wang, X.; Lee, S. Y.; Miller, K.; Welbourn, R.; Stocker, I.; Clarke, S.; Casford, M.; Gutfreund, P.; Skoda, M. W. A. *Langmuir* **2013**, *29*, 5520–5527.
- [101] Griffin, L. R.; Browning, K. L.; Lee, S. Y.; Skoda, M. W.; Rogers, S.; Clarke, S. M. *Langmuir* **2016**, *32*, 13054–13064.
- [102] Arnason, T. S.; Keil, R. G. *Marine Chemistry* **2000**, *71*, 309–320.
- [103] Buckley, J. S.; Liu, Y. *Journal of Petroleum Science and Engineering* **1998**, *20*, 155–160.
- [104] Pastré, D.; Piétrement, O.; Fusil, S.; Landousy, F.; Jeusset, J.; David, M. O.; Hamon, L.; Le Cam, E.; Zozime, A. *Biophysical Journal* **2003**, *85*, 2507–2518.
- [105] Hansma, H. G.; Laney, D. E. *Biophysical Journal* **1996**, *70*, 1933–1939.
- [106] Redeker, C.; Briscoe, W. H. *Langmuir* **2019**, *35*, 15739–15750.
- [107] Nave, S.; Eastoe, J.; Penfold, J. *Langmuir* **2000**, *16*, 8733–8740.
- [108] Stocker, I. N.; Miller, K. L.; Welbourn, R. J.; Clarke, S. M.; Collins, I. R.; Kinane, C.; Gutfreund, P. *Journal of Colloid and Interface Science* **2014**, *418*, 140–146.
- [109] Sheu, E. Y.; Lo Nostro, P.; Capuzzi, G.; Baglioni, P. *Langmuir* **1999**, *15*, 6671–6676.
- [110] Fragneto, G.; Li, Z. X.; Thomas, R. K.; Rennie, A. R.; Penfold, J. *Journal of Colloid and Interface Science* **1996**, *178*, 531–537.
- [111] Hellsing, M. S.; Rennie, A. R.; Hughes, A. V. *Langmuir* **2010**, *26*, 14567–14573.
- [112] Hellsing, M. S.; Rennie, A. R.; Hughes, A. V. *Langmuir* **2011**, *27*, 4669–4678.
- [113] Denicolò, I.; Doucet, J.; Craievich, A. F. *The Journal of Chemical Physics* **1983**, *78*, 1465–1469.
- [114] Li, Z. X.; Lu, J. R.; Thomas, R. K. *Langmuir* **1997**, *13*, 3681–3685.
- [115] Lovera, J.; Lovera, P.; Gregoire, P. *Journal of Solid State Chemistry* **1988**, *77*, 40–47.
- [116] Craievich, A. F.; Denicolò, I.; Doucet, J. *Physical Review B* **1984**, *30*, 4782–4787.
- [117] Burgess, J. *Metal ions in solution*; Ellis Horwood: Chichester, 1978.
- [118] Li, N.; Thomas, R. K.; Rennie, A. R. *Journal of Colloid and Interface Science* **2012**, *378*, 152–158.
- [119] Widom, J.; Baldwin, R. L. *Journal of Molecular Biology* **1980**, *144*, 431–453.

- [120] Bloomfield, V. A. *Current opinion in structural biology* **1996**, *6*, 334–41.
- [121] Zhang, F.; Weggler, S.; Ziller, M. J.; Ianeselli, L.; Heck, B. S.; Hildebrandt, A.; Kohlbacher, O.; Skoda, M. W. A.; Jacobs, R. M. J.; Schreiber, F. *Proteins: Structure, Function and Bioinformatics* **2010**, *78*, 3450–3457.
- [122] Zhang, F.; Zocher, G.; Sauter, A.; Stehle, T.; Schreiber, F. *Journal of Applied Crystallography* **2011**, *44*, 755–762.
- [123] Allen, F. J.; Griffin, L.; Alloway, R. M.; Gutfreund, P.; Lee, S. Y.; Truscott, C. L.; Welbourn, R. J. L.; Wood, M. H.; Clarke, S. M. *Langmuir* **2017**, *33*, 7881–7888.
- [124] Li, Z. X.; Lu, J. R.; Thomas, R. K.; Penfold, J. *The Journal of Physical Chemistry B* **1997**, *101*, 1615–1620.
- [125] Chakraborty, A.; Chakraborty, S.; Saha, S. K. *Journal of Dispersion Science and Technology* **2007**, *28*, 984–989.
- [126] Satake, I.; Iwamatsu, I.; Hosokawa, S.; Matsuura, R. *Bulletin of the Chemical Society of Japan* **1963**, *36*, 204–209.
- [127] Thomas, R. K.; Penfold, J. *Langmuir* **2015**, *31*, 7440–7456.
- [128] Tucker, I. M.; Li, P.; Penfold, J.; Petkov, J. T.; Sivia, D. S.; Xu, H.; Thomas, R. K. *Langmuir* **2015**, *31*, 6773–6781.
- [129] Xu, H.; Thomas, R.; Penfold, J.; Li, P.; Ma, K.; Welbourne, R.; Roberts, D.; Petkov, J. *Journal of Colloid and Interface Science* **2018**, *512*, 231–238.
- [130] Kobayashi, K.; Liang, Y.; Murata, S.; Matsuoka, T.; Takahashi, S.; Amano, K.-I.; Nishi, N.; Sakka, T. *The Journal of Physical Chemistry C* **2017**, *121*, 9273–9281.
- [131] Tan, Q.; Zhao, G.; Qiu, Y.; Kan, Y.; Ni, Z.; Chen, Y. *Langmuir* **2014**, *30*, 10845–10854.
- [132] de Poel, W.; Vaessen, S. L.; Drnec, J.; Engwerda, A. H.; Townsend, E. R.; Pintea, S.; de Jong, A. E.; Jankowski, M.; Carlà, F.; Felici, R.; Elemans, J. A.; van Enkevort, W. J.; Rowan, A. E.; Vlieg, E. *Surface Science* **2017**, *665*, 56–61.
- [133] Mohammad Salehi, M.; Omidvar, P.; Naeimi, F. *Egyptian Journal of Petroleum* **2017**, *26*, 301–312.
- [134] Underwood, T.; Erastova, V.; Cubillas, P.; Greenwell, H. C. *Journal of Physical Chemistry C* **2015**, *119*, 7282–7294.
- [135] Serjeant, E.; Dempsey, B. *IUPAC Chemical Data Series*; Pergamon Press, 1979; p 998.
- [136] Andersen, S. I.; Chandra, M. S.; Chen, J.; Zeng, B. Y.; Zou, F.; Mapolelo, M.; Abdallah, W.; Buiting, J. J. *Energy and Fuels* **2016**, *30*, 4475–4485.
- [137] Wellen, B. A.; Lach, E. A.; Allen, H. C. *Physical Chemistry Chemical Physics* **2017**, *19*, 26551–26558.

- [138] Stanley, F. E.; Warner, A. M.; Schneiderman, E.; Stalcup, A. M. *Journal of Chromatography A* **2009**, *1216*, 8431–8434.
- [139] Lee, S. Y.; Welbourn, R.; Clarke, S. M.; Skoda, M. W.; Clifton, L.; Zorbakhsh, A. *Journal of Colloid and Interface Science* **2013**, *407*, 348–353.
- [140] Tanford, C. *The Journal of Physical Chemistry* **1972**, *76*, 3020–3024.
- [141] Israelachvili, J. *Intermolecular and Surface Forces*; Academic Press, 2011; p 704.
- [142] Irani, R. R.; Callis, C. F. *The Journal of Physical Chemistry* **1960**, *64*, 1741–1743.
- [143] Pereira, R. F.; Valente, A. J.; Fernandes, M.; Burrows, H. D. *Physical Chemistry Chemical Physics* **2012**, *14*, 7517–7527.
- [144] Mugele, F.; Bera, B.; Cavalli, A.; Siretanu, I.; Maestro, A.; Duits, M.; Cohen-Stuart, M.; Van Den Ende, D.; Stocker, I.; Collins, I. *Scientific Reports* **2015**, *5*.
- [145] Haagh, M. E.; Siretanu, I.; Duits, M. H.; Mugele, F. *Langmuir* **2017**, *33*, 3349–3357.
- [146] Bera, B.; Duits, M. H.; Cohen Stuart, M. A.; Van Den Ende, D.; Mugele, F. *Soft Matter* **2016**, *12*, 4562–4571.
- [147] Haagh, M. E.; Schilderink, N.; Duits, M. H.; Siretanu, I.; Mugele, F.; Collins, I. R. *Journal of Petroleum Science and Engineering* **2018**, *165*, 1040–1048.
- [148] Skipper, N. T.; Williams, G. D.; de Siqueira, A. V. C.; Lobban, C.; Soper, A. K. *Clay Minerals* **2000**, *35*, 283–290.
- [149] Rosen, M. J.; Kunjappu, J. T. *Surfactants and Interfacial Phenomena: Fourth Edition*; John Wiley & Sons, Inc.: Hoboken, NJ, USA, 2012.
- [150] Inoue, T.; Misono, T. *Journal of Colloid and Interface Science* **2008**, *326*, 483–489.
- [151] Blom, A.; Drummond, C.; Wanless, E. J.; Richetti, P.; Warr, G. G. *Langmuir* **2005**, *21*, 2779–2788.
- [152] Dong, J.; Mao, G. *Langmuir* **2000**, *16*, 6641–6647.
- [153] Rutland, M. W.; Christenson, H. K. *Langmuir* **1990**, *6*, 1083–1087.
- [154] Grillo, I.; Levitz, P.; Zemb, T. *European Physical Journal B* **1999**, *10*, 29–34.
- [155] Mohajeri, E.; Noudeh, G. D. *E-Journal of Chemistry* **2012**, *9*, 2268–2274.
- [156] Deguchi, K.; Meguro, K. *Journal of Colloid And Interface Science* **1972**, *38*, 596–600.
- [157] McDermott, D. C.; Lu, J. R.; Lee, E. M.; Thomas, R. K. *Langmuir* **1992**, *8*, 1204–1210.
- [158] Briscoe, W. H.; Chen, M.; Dunlop, I. E.; Klein, J.; Penfold, J.; Jacobs, R. M. *Journal of Colloid and Interface Science* **2007**, *306*, 459–463.
- [159] Briscoe, W. H.; Speranza, F.; Li, P.; Konovalov, O.; Bouchenoire, L.; Van Stam, J.; Klein, J.; Jacobs, R. M.; Thomas, R. K. *Soft Matter* **2012**, *8*, 5055–5068.

- [160] Tsagkaropoulou, G.; Allen, F. J.; Clarke, S. M.; Camp, P. J. *Soft Matter* **2019**, *15*, 8402–8411.
- [161] Allen, F. J.; Truscott, C. L.; Welbourn, R. J.; Clarke, S. M. *Applied Clay Science* **2018**, *160*, 276–281.
- [162] Cheng, L.; Fenter, P.; Nagy, K. L.; Schlegel, M. L.; Sturchio, N. C. *Physical Review Letters* **2001**, *87*, 156103–156103–4.
- [163] Lamont, R. E.; Ducker, W. A. *Journal of the American Chemical Society* **1998**, *120*, 7602–7607.
- [164] Ducker, W. A.; Wanless, E. J. *Langmuir* **2002**, *12*, 5915–5920.
- [165] Kékicheff, P.; Christenson, H. K.; Ninham, B. W. *Colloids and Surfaces* **1989**, *40*, 31–41.
- [166] Delarios, J. M.; Helms, C. R.; Kao, D. B.; Deal, B. E. *Applied Surface Science* **1987**, *30*, 17–24.
- [167] Griffin, L. R.; Browning, K. L.; Truscott, C. L.; Clifton, L. A.; Webster, J.; Clarke, S. M. *Journal of Colloid and Interface Science* **2016**, *478*, 365–373.
- [168] Fink, C. K.; Nakamura, K.; Ichimura, S.; Jenkins, S. J. *Journal of Physics: Condensed Matter* **2009**, *21*, 19.
- [169] Parker, J. L.; Claesson, P. M.; Cho, D. L.; Ahlberg, A.; Tidblad, J.; Blomberg, E. *Journal of Colloid And Interface Science* **1990**, *134*, 449–458.
- [170] Liberelle, B.; Giasson, S. *Langmuir* **2007**, *23*, 9263–9270.
- [171] Hook, D. A.; Olhausen, J. A.; Krim, J.; Dugger, M. T. *Journal of Microelectromechanical Systems* **2010**, *19*, 1292–1298.
- [172] Dubois, M.; Zemb, T. *Langmuir* **1991**, *7*, 1352–1360.
- [173] Blom, A.; Warr, G. G.; Nelson, A. *Colloids and Surfaces A: Physicochemical and Engineering Aspects* **2007**, *310*, 1–8.
- [174] Sohrabi, B.; Gharibi, H.; Tajik, B.; Javadian, S.; Hashemianzadeh, M. *Journal of Physical Chemistry B* **2008**, *112*, 14869–14876.
- [175] Holland, P.; Rubingh, D. *The Journal of Physical Chemistry* **1983**, *87*, 1984–1990.
- [176] Zhang, R.; Somasundaran, P. *Advances in Colloid and Interface Science* **2006**, *123-126*, 213–229.
- [177] Huang, Z.; Yan, Z.; Gu, T. *Colloids and Surfaces* **1989**, *36*, 353–358.
- [178] Kirby, S. M.; Anna, S. L.; Walker, L. M. *Langmuir* **2015**, *31*, 4063–4071.
- [179] Dan, A.; Kotsmar, C.; Ferri, J. K.; Javadi, A.; Karbaschi, M.; Krägel, J.; Wüstneck, R.; Miller, R. *Soft Matter* **2012**, *8*, 6057–6065.

- [180] Fröberg, J. C.; Blomberg, E.; Claesson, P. M. *Langmuir* **1999**, *15*, 1410–1417.
- [181] Marques, E.; Khan, A.; Miguel, M. D. G.; Lindman, B. *Journal of Physical Chemistry* **1993**, *97*, 4729–4736.
- [182] Marques, E. F.; Regev, O.; Khan, A.; da Graça Miguel, M.; Lindman, B. *The Journal of Physical Chemistry B* **1999**, *102*, 6746–6758.
- [183] Bai, G.; Wang, Y.; Wang, J.; Han, B.; Yan, H. *Langmuir* **2002**, *17*, 3522–3525.
- [184] Zhao, H.; Bhattacharjee, S.; Chow, R.; Wallace, D.; Masliyah, J. H.; Xu, Z. *Langmuir* **2008**, *24*, 12899–12910.
- [185] Kaler, E. W.; Herrington, K. L.; Murthy, A. K.; Zasadzinski, J. A. N. *The Journal of Physical Chemistry* **1992**, *96*, 6698–6707.
- [186] Mukerjee, P.; Mysels, K. J. *Critical Micelle Concentration of Aqueous Surfactant Systems*; 1971.
- [187] Negin, C.; Ali, S.; Xie, Q. *Petroleum* **2017**, *3*, 197–211.
- [188] Grillo, I.; Penfold, J.; Tucker, I.; Cousin, F. *Langmuir* **2009**, *25*, 3932–3943.
- [189] Lee, S. S.; Fenter, P.; Nagy, K. L.; Sturchio, N. C. *Langmuir* **2012**, *28*, 8637–8650.
- [190] Underwood, T.; Erastova, V.; Chris Greenwell, H. *Clays and Clay Minerals* **2016**, *64*, 472–487.
- [191] de Paiva, L. B.; Morales, A. R.; Valenzuela Díaz, F. R. *Applied Clay Science* **2008**, *42*, 8–24.
- [192] Osman, M. A.; Ploetze, M.; Skrabal, P. *The Journal of Physical Chemistry B* **2004**, *108*, 2580–2588.
- [193] Xi, Y.; Ding, Z.; He, H.; Frost, R. L. *Journal of Colloid and Interface Science* **2004**, *277*, 116–120.
- [194] Saitoh, T.; Shibayama, T. *Journal of Hazardous Materials* **2016**, *317*, 677–685.
- [195] Guégan, R. *Comptes Rendus Chimie* **2019**, *22*, 132–141.
- [196] He, H.; Ma, L.; Zhu, J.; Frost, R. L.; Theng, B. K.; Bergaya, F. *Applied Clay Science* **2014**, *100*, 22–28.
- [197] Paiva, L. B.; Morales, A. R. *Brazilian Journal of Chemical Engineering* **2012**, *29*, 525–536.
- [198] Zheng, Q.; Xu, B.; Song, Y.; Yang, H.; Pan, Y. *Journal of Materials Research* **2005**, *20*, 357–363.
- [199] Singla, P.; Mehta, R.; Upadhyay, S. N. *Green and Sustainable Chemistry* **2012**, *02*, 21–25.

- [200] Hwang, J. J.; Liu, H. J. *Macromolecules* **2002**, *35*, 7314–7319.
- [201] Coiro, V. M.; Manigrasso, M.; Mazza, F.; Pochetti, G. *Acta Crystallographica Section C Crystal Structure Communications* **1987**, *43*, 850–854.
- [202] Coiro, V. M.; Mazza, F.; Pochetti, G. *Acta Crystallographica Section C Crystal Structure Communications* **1986**, *42*, 991–995.
- [203] Lide, D. R., Milne, G. W. A., Eds. *Handbook of data on common organic compounds*; CRC Press, 1995; p 1793.
- [204] Khan, A.; Marques, E. F. *Current Opinion in Colloid and Interface Science* **1999**, *4*, 402–410.
- [205] Bumajdad, A.; Eastoe, J.; Griffiths, P.; Steytler, D. C.; Heenan, R. K.; Lu, J. R.; Timmins, P. *Langmuir* **1999**, *15*, 5271–5278.
- [206] Rosen, M. J.; Hua, X. Y. *Journal of Colloid And Interface Science* **1982**, *86*, 164–172.
- [207] Iler, R. K. *The Chemistry of Silica*; John Wiley & Sons: New York, 1979.
- [208] Lafuente, B.; Downs, R. T.; Yang, H.; Stone, N. *Highlights in Mineralogical Crystallography*; de Gruyter: Berlin, 2015; pp 1–30.
- [209] Caseri, W. R.; Shelden, R. A.; Suter, U. W. *Colloid & Polymer Science* **1992**, *270*, 392–398.
- [210] Helmholtz, H. *Annalen der Physik* **1879**, *243*, 337–382.
- [211] E.I. du Pont de Nemours and Company, Surface-Modified Silica Sol - Canadian Patent. 1959.
- [212] Schrader, A. M.; Monroe, J. I.; Sheil, R.; Dobbs, H. A.; Keller, T. J.; Li, Y.; Jain, S.; Shell, M. S.; Israelachvili, J. N.; Han, S. *Proceedings of the National Academy of Sciences of the United States of America* **2018**, *115*, 2890–2895.
- [213] Hoggard, J. D.; Sides, P. J.; Prieve, D. C. *Langmuir* **2005**, *21*, 7433–7438.
- [214] Satoh, K. *BBA - Biomembranes* **1995**, *1239*, 239–248.
- [215] Cumpson, P. J. *Journal of Electron Spectroscopy and Related Phenomena* **1995**, *73*, 25–52.
- [216] Biteen, J.; Willets, K. A. *Chemical Reviews* **2017**, *117*, 7241–7243.
- [217] Hou, J. T.; Ren, W. X.; Li, K.; Seo, J.; Sharma, A.; Yu, X. Q.; Kim, J. S. *Chemical Society Reviews* **2017**, *46*, 2076–2090.
- [218] Ellenberg, J.; Siggia, E. D.; Moreira, J. E.; Smith, C. L.; Presley, J. F.; Worman, H. J.; Lippincott-Schwartz, J. *Journal of Cell Biology* **1997**, *138*, 1193–1206.
- [219] Kang, M.; Day, C. A.; Kenworthy, A. K.; DiBenedetto, E. *Traffic* **2012**, *13*, 1589–1600.

- [220] Soumpasis, D. M. *Biophysical Journal* **1983**, *41*, 95–97.
- [221] Majer, G.; Melchior, J. P. *Journal of Chemical Physics* **2014**, *140*, 94201.
- [222] Toepke, M. W.; Beebe, D. J. *Lab on a Chip* **2006**, *6*, 1484–1486.
- [223] Greenspan, P.; Mayer, E. P.; Fowler, S. D. *Journal of Cell Biology* **1985**, *100*, 965–973.
- [224] Greenspan, P.; Fowler, S. D. *Journal of lipid research* **1985**, *26*, 781–9.
- [225] Zampori, L.; Stampino, P. G.; Cristiani, C.; Dotelli, G.; Cazzola, P. *Applied Clay Science* **2010**, *48*, 97–102.
- [226] Lambert, A. G.; Davies, P. B.; Neivandt, D. J. *Applied Spectroscopy Reviews* **2005**, *40*, 103–145.
- [227] Kunstelj, K.; Spindler, L.; Federiconi, F.; Bonn, M.; Drevenšek-Olenik, I.; Čopič, M. *Chemical Physics Letters* **2008**, *467*, 159–163.
- [228] Backus, E. H.; Garcia-Araez, N.; Bonn, M.; Bakker, H. J. *Journal of Physical Chemistry C* **2012**, *116*, 23351–23361.

Appendix A

Beamtime experiments and DOIs

ISIS

RB1710119

Adsorption of an Anionic Surfactant on Anionic Surfaces in the Presence of Potassium and Ammonium Ions

DOI: 10.5286/ISIS.E.RB1710119

RB1710497

Comparison of Adsorbed Surfactant Behaviour under Poiseuille Flow to Cone-Plate Shear

DOI: 10.5286/ISIS.E.RB1710497

RB1810186

Anionic surfactant induced desorption of cationic surfactants from anionic surfaces

DOI: 10.5286/ISIS.E.RB1810186

RB1820048

Modification of an adsorbed cationic layer by anionic surfactants below the CMC

DOI: 10.5286/ISIS.E.RB1820048

RB1820049

Non-ionic surfactant induced desorption of a strongly bound cationic layer from mica

DOI: 10.5286/ISIS.E.RB1820049

RB1910003

Visualisation of Multi-component Ion Exchange for Oil Recovery

DOI: 10.5286/ISIS.E.RB1910003

RB2010001

Adsorption of Aqueous Carboxylates to Mica in the Presence of Cations

DOI: 10.5286/ISIS.E.RBRB2010001

ILL**9-10-1545**

Adsorption of an anionic surfactant on anionic surfaces in the presence of mono and divalent ions

DOI: 10.5291/ILL-DATA.9-10-1545

9-10-1544

Adsorbed molecular layer of phenol on iron under pressure

DOI: 10.5291/ILL-DATA.9-10-1544

Diamond**SI17724**

Adsorption of an Anionic Surfactant on Anionic Surfaces in the Presence of Cations